

2011

Experimental and computational study of turbulent mixing in a confined rectangular jet

Bo Kong
Iowa State University

Follow this and additional works at: <http://lib.dr.iastate.edu/etd>



Part of the [Mechanical Engineering Commons](#)

Recommended Citation

Kong, Bo, "Experimental and computational study of turbulent mixing in a confined rectangular jet" (2011). *Graduate Theses and Dissertations*. 11961.
<http://lib.dr.iastate.edu/etd/11961>

This Dissertation is brought to you for free and open access by the Graduate College at Iowa State University Digital Repository. It has been accepted for inclusion in Graduate Theses and Dissertations by an authorized administrator of Iowa State University Digital Repository. For more information, please contact digirep@iastate.edu.

**Experimental and computational study of turbulent mixing in a confined
rectangular reactor**

by

Bo Kong

A dissertation submitted to the graduate faculty
in partial fulfillment of the requirements for the degree of
DOCTOR OF PHILOSOPHY

Major: Mechanical Engineering

Program of Study Committee:
Michael G. Olsen, Co-major Professor
James C. Hill, Co-major Professor
Rodney O. Fox
Hui Hu
Shankar Subramaniam
Baskar Ganapathysbramanian

Iowa State University

Ames, Iowa

2011

Copyright © Bo Kong, 2011. All rights reserved.

DEDICATION

I would like to dedicate this thesis to my wife Dong without whose support I would not have been able to complete this work. I would also like to thank my friends and family for their loving guidance during the writing of this work.

TABLE OF CONTENTS

LIST OF TABLES	vi
LIST OF FIGURES	vii
ACKNOWLEDGEMENTS	xiv
CHAPTER 1. Introduction	1
1.1 General introduction	1
1.2 Dissertation organization	3
CHAPTER 2. Population, Characteristics and Kinematics of Vortices in a	
Confined Rectangular Jet with a Co-flow	4
2.1 Introduction	5
2.2 Experimental Facility and Methodology	8
2.3 Swirling Strength Vortex-ID Method	11
2.4 Vortex Characteristics Analysis	13
2.4.1 Instantaneous structures	13
2.4.2 Vortex population	15
2.4.3 Size and strength of vortex cores	17
2.4.4 Deviation velocity of vortex cores	18
2.5 Vortex Tracking Analysis	20
2.6 Spatial correlation functions and linear Stochastic estimation	22
2.6.1 Two-point spatial correlations	22
2.6.2 Linear stochastic estimation	24
2.7 Conclusions	25

CHAPTER 3. Study of Coherent Structures in a Confined Rectangular Wake	46
3.1 Introduction	47
3.2 Experimental Facility and Methodology	51
3.3 Vortex Characteristics Analysis	52
3.3.1 Instantaneous structures	53
3.3.2 Vortex population	54
3.3.3 Size and strength of vortex cores	56
3.3.4 Deviation velocity of vortex cores	58
3.4 Spatial correlation functions and linear stochastic estimation	59
3.4.1 Two-point spatial correlations	59
3.4.2 Linear stochastic estimation	63
3.5 Conclusions	65
CHAPTER 4. Predictive capability of Large Eddy Simulation for pointwise and spatial turbulence statistics in a confined rectangular jet	86
4.1 Introduction	87
4.2 Flow configuration and experimental procedures	90
4.3 Numerical modeling and formulation	91
4.3.1 Governing equations and subgrid models	91
4.3.2 Simulation methodology of the confined rectangular jet	94
4.4 Results and discussion	98
4.4.1 Point-wise (one point) statistics	99
4.4.2 Spatial (two-point) statistics	103
4.5 Summary and conclusions	106
CHAPTER 5. A Comparison Study of Turbulence Statistics in the Mixing Regions of Confined Jet and Wake	127
5.1 Introduction	127
5.2 Experimental Facility	129
5.3 Identification of Inner and Outer Boundaries	131

5.3.1	Geometry of Scalar Boundaries	133
5.3.2	Means and Fluctuations of Passive Scalar and Stream wise Velocity . .	134
5.3.3	Compression and Rotations	139
5.4	Conclusions	140
CHAPTER 6.	Conclusions and future directions	153
6.1	Summary and conclusions	153
6.1.1	Vortex study with a swirling strength based vortex identification method	153
6.1.2	Large eddy simulation of a confined rectangular jet	157
6.1.3	Turbulent statistics in the mixing region of confined jet and wake flows	158
6.2	Future directions	159

LIST OF TABLES

2.1	Flow rates of two cases	11
2.2	PIV Spatial resolution and measurement uncertainty	11
4.1	Dimensionless CPU time comparison between subgrid models.	98

LIST OF FIGURES

2.1	Photograph and schematic of the confined planar jet test section . . .	28
2.2	Schematic of the optical setup for the combined PIV and PLIF experiments	28
2.3	The mean of streamwise velocity. \bullet : $X/d = 1$, \square : $X/d = 4.5$, $*$: $X/d = 15$	29
2.4	Example of vortex identification in an instantaneous PIV velocity field in near-field $0 < X/d < 2.5$ and far-field $6.5 < X/d < 9$ of the jet, at $Re = 20K$. (a) The Galilean decomposition of this instantaneous velocity field with $0.7U_c$, where U_c is the mean velocity of the center stream at each X location. (b) Local Galilean decomposition of vortices with the velocity at each vortex core. The contours of $\Lambda_{ci} = 1.5\Lambda_{ci}^{rms}$ are also shown in the background of the figure (a) and (b).	31
2.5	Local vortex population density of positively and negatively rotating vortices at different streamwise locations. \bigcirc : positively rotating vortices, \cdot : negatively rotating vortices.	32
2.6	Mean populations of positively rotating vortex in the half jet width (1cm) streamwise long region between the centers of the center of center stream ($Y/d=0$) and the center of left side stream ($Y/d = -1$). \bigcirc : $Re = 50K$, \blacksquare : $Re = 20K$	32
2.7	Profiles of the size of vortex cores. \bigcirc : positively rotating vortices, \cdot : negatively rotating vortices.	33

2.8	Mean vortex size in the half jet width (1cm) streamwise long region between the centers of the center of center stream ($Y/d = 0$) and the center of left side stream ($Y/d = -1$). ○: $Re = 50K$, ■: $Re = 20K$	33
2.9	Profiles of the peak swirling strength value of vortex cores. ○: positively rotating vortices, ·: negatively rotating vortices.	34
2.10	Mean the peak swirling strength value of the vortex cores in a half jet width (1cm) streamwise long region between the centers of the center of center stream ($Y/d = 0$) and the center of left side stream ($Y/d = -1$). ○: $Re = 50K$, ■: $Re = 20K$	34
2.11	Vortex deviation velocity in the cross-stream direction. ○: positively rotating vortices, ·: negatively rotating vortices.	35
2.12	Vortex deviation velocity in the streamwise direction. ○: positively rotating vortices, ·: negatively rotating vortices.	35
2.13	Vortex deviation velocity distribution, at $X/d = 1$, $Re = 20K$. X: velocity fluctuation distribution, ○: vortex deviation velocity distribution.	36
2.14	Vortex deviation velocity distribution, at $X/d = 4.5$, $Re = 20K$. X: velocity fluctuation distribution, ○: vortex deviation velocity distribution.	37
2.15	Vortex deviation velocity distribution, at $X/d = 15$, $Re = 20K$. X: velocity fluctuation distribution, ○: vortex deviation velocity distribution.	38
2.16	The trajectories of a positively rotating vortex and a negatively rotating vortex, at the jet outlet, $Re = 20K$. The background contours are the plots of the swirling strength clusters at several different time steps.	39
2.17	The mean tracked vortex maximum strength starting at three different downstream locations.	40
2.18	The mean tracked vortex size starting at three different downstream locations.	40

2.19	Two-point cross correlation $R_{\lambda_{ci}u'}$ (first row), $R_{\lambda_{ci}v'}$ (second row). At $X/d = 1$, $X/d = 4.5$, $X/d = 7.5$ and $X/d = 15$, $Re = 50K$. The black dot indicates the location of swirling strength basis point.	41
2.20	As Fig. 2.19 but at $Re = 20K$	42
2.21	Two-point cross-correlation $R_{\lambda_{ci}\phi'}$. At $X/d=1$, $X/d = 4.5$, $X/d = 7.5$ and $X/d = 15$, for $Re = 50K$ (first row) and at $X/d = 4.5$, $X/d = 7.5$, for $Re=20K$ (second row).	43
2.22	Average of positive and negative peak values of cross correlations. (\square , $R_{\lambda u'}$; \triangle , $R_{\lambda v'}$; \times , $R_{\lambda \phi'}$; —, $Re = 20K$; . . . , $Re = 50K$)	44
2.23	Linear stochastic estimation of velocity field with $U(x_o)$ subtracted from each vector. At $x/d=1$, $x/d=4.5$, $x/d=7.5$ and $x/d=15$, $Re = 50K$ (first row), $Re=20K$ (second row).	45
3.1	Photograph and schematic of the confined planar jet test section . . .	67
3.2	Schematic of the optical setup for the combined PIV and PLIF experiments	67
3.3	The mean and rms of streamwise velocity.	68
3.4	Example of vortex identification in an instantaneous PIV velocity field at $0 < X/d < 2.5$ and $6.5 < X/d < 9$. (a) The Galilean decomposition of this instantaneous velocity field with $0.6U_0$, where U_c is the mean velocity of the center stream at each X location. (b) Local Galilean decomposition of vortices with the velocity at each vortex core. The contours of $\Lambda_{ci} = 1.5\Lambda_{ci}^{rms}$ are also shown in the background of the figure (a) and (b).	70
3.5	Local vortex population density of positively and negatively rotating vortices at different streamwise locations. \bigcirc : negatively rotating vortices, \cdot : positively rotating vortices.	71

3.6	Mean populations of vortices in the half jet width (1cm) streamwise long region between the centers of the center of center stream ($Y/d = 0$) and the center of left side stream ($Y/d = -1$).	71
3.7	Profiles of the size of vortex cores. \bigcirc : negatively rotating vortices, \cdot : positively rotating vortices.	72
3.8	Profiles of the peak swirling strength value of vortex cores. \bigcirc : negatively rotating vortices, \cdot : positively rotating vortices.	72
3.9	Mean vortex size in the half jet width (1cm) streamwise long region between the centers of the center of center stream ($Y/d = 0$) and the center of left side stream ($Y/d = -1$).	73
3.10	Mean the peak swirling strength value of the vortex cores in a half jet width (1cm) streamwise long region between the centers of the center of center stream ($Y/d = 0$) and the center of left side stream ($Y/d = -1$).	73
3.11	Vortex deviation velocity in the cross-stream direction. \bigcirc : negatively rotating vortices, \cdot : positively rotating vortices.	74
3.12	Vortex deviation velocity in the streamwise direction. \bigcirc : negatively rotating vortices, \cdot : positively rotating vortices.	74
3.13	Two-point cross correlation $R_{\lambda_{ci}u'}$ at $X/d = 1$	75
3.14	Two-point cross correlation $R_{\lambda_{ci}v'}$ at $X/d = 1$	76
3.15	Two-point cross correlation $R_{\lambda_{ci}u'}$ at $X/d = 4.5$	77
3.16	Two-point cross correlation $R_{\lambda_{ci}v'}$ at $X/d = 4.5$	78
3.17	Two-point cross correlation $R_{\lambda_{ci}u'}$ at $X/d = 7.5$	79
3.18	Two-point cross correlation $R_{\lambda_{ci}v'}$ at $X/d = 7.5$	80
3.19	Two-point cross correlation $R_{\lambda_{ci}\phi'}$ at $X/d = 1$	81
3.20	Two-point cross correlation $R_{\lambda_{ci}\phi'}$ at $X/d = 4.5$	82
3.21	Two-point cross correlation $R_{\lambda_{ci}\phi'}$ at $X/d = 7.5$	83

3.22	Linear stochastic estimation of velocity field with $U(x_o)$ subtracted from each vector, at $x/d=1, x/d=4.5$ and $x/d=7.5$. First row, on the left side of the wake and second row, on the right side of the wake.	84
3.23	Linear stochastic estimation of velocity field with uniform vector length, at $x/d=1, x/d=4.5$ and $x/d=7.5$. First row, on the left side of the wake and second row, on the right side of the wake.	85
4.1	Photograph and schematic of the confined rectangular jet test section.	108
4.2	Schematic of the optical setup for the PIV experiments.	108
4.3	Mean and rms stream-wise velocity, cross-stream wise rms velocity and shear stress profiles at at the node next to inlet surface.	109
4.4	Stream-wise and cross-stream wise rms velocity profiles at $x/d = 1$ and $x/d = 7.5$ for four different grid resolutions compared with PIV experiments.	110
4.5	Stream-wise and cross-stream wise rms velocity profiles at $x/d = 1$ and $x/d = 7.5$ for linear and cubic interpolation schemes compared with PIV experiments.	111
4.6	Stream-wise and cross-stream wise rms velocity profiles at $x/d = 1$ and $x/d = 7.5$ for Gaussian, second and four order least square gradient schemes compared with PIV experiments.	112
4.7	Stream-wise and cross-stream wise rms velocity profiles at $x/d = 1$ and $x/d = 7.5$ for constant Smagorinsky, dynamic Smagorinsky, one equation eddy, dynamic one equation eddy and mixed Smagorinsky, compared with PIV experiments.	113
4.8	Mean stream-wise velocity profiles at four locations downstream of the splitter plates depicting growth of mixing layer. Experiments are shown as symbols and LES as lines.	114
4.9	Stream-wise rms velocity profiles at four locations downstream of the splitter plates. Experiments are shown as symbols and LES as lines. .	115

4.10	Wall-normal rms velocity profile at four locations downstream of the splitter plates. Experiments are shown as symbols and LES as lines.	116
4.11	Span-wise rms velocity profile at four locations downstream of the splitter plates. Experimental data are not available for comparisons.	117
4.12	Resolved shear stress at four locations downstream of the splitter plates. Experiments are shown as symbols and LES as lines.	118
4.13	Correlation coefficient profiles at four locations downstream of the splitter plates. Experiments are shown as symbols and LES as lines.	119
4.14	Skewness and kurtosis for u - and v -velocity at $x/d = 4.5$. Experiments are shown as symbols and LES as lines.	120
4.15	Skewness and kurtosis for u - and v -velocity at $x/d = 7.5$. Experiments are shown as symbols and LES as lines.	121
4.16	Schematic of measurement plane for two-point velocity correlations. Correlations are obtained at nine points in the plane shown with circles.	122
4.17	Spatial correlations of stream-wise velocity $R_{u'u'}$. Left to right shows correlations at increasing cross-stream wise distance from center of the jet. Bottom to top shows correlations at increasing downstream distance. Experimental data are shown as colored contours and LES data are superimposed as solid lines.	123
4.18	Spatial correlations of cross-stream velocity $R_{v'v'}$. Measurement locations and contours are the same as in Figure 4.17.	124
4.19	Spatial correlations $R_{u'v'}$. Measurement locations and contours are the same as in Figure 4.17.	125
4.20	Spatial correlations $R_{v'u'}$. Measurement locations and contours are the same as in Figure 4.17.	126
5.1	Photograph and schematic of the confined planar jet test section . . .	142
5.2	Schematic of the optical setup for the combined PIV and PLIF experiments	142

5.3	Threshold detection for outer boundary.	143
5.4	Threshold detection for inner boundary.	143
5.5	An example of outer boundary identification, jet, $X/d = 3.5 \sim 5.5$. . .	144
5.6	An example of inner boundary detection, jet, $X/d = 3.5 \sim 5.5$	145
5.7	Averaged inner and outer boundaries.	146
5.8	Distance between inner and outer boundaries, mean and rms.	146
5.9	The mean of passive scalar across the mixing region. a, $x/d = 4.5$; b, $x/d = 7.5$	147
5.10	The mean of streamwise velocity across the mixing region. a, $x/d =$ 4.5 ; b, $x/d = 7.5$	148
5.11	Passive scalar sign-differential fluctuation across the mixing region. a, $x/d = 4.5$; b, $x/d = 7.5$	149
5.12	Streamwise velocity sign-differential fluctuation across the mixing re- gion. a, $x/d = 4.5$; b, $x/d = 7.5$	150
5.13	The mean of principle strain rate across the mixing region. a, $x/d =$ 4.5 ; b, $x/d = 7.5$	151
5.14	The mean of vorticity across the mixing region. a, $x/d = 4.5$; b, x/d $= 7.5$	152

ACKNOWLEDGEMENTS

I would like to take this opportunity to express my thanks to those who helped me with various aspects of conducting research and the writing of this thesis. First and foremost, Dr. Michael G. Olsen for his guidance, patience and support throughout this research and the writing of this thesis. I would also like to thank Dr. Rodney O. Fox and Dr. James C. Hill, their insights and words of encouragement have often inspired me and renewed my hopes for completing my graduate education. To fellow graduate students in the Mechanical Engineering Department and the Chemical and Biological Engineering Department, thank you all for your unconditional support. To my wife, my parents and friends, thank you for your love and support.

CHAPTER 1. Introduction

1.1 General introduction

Turbulent flow is a most important type of fluid flow yet it is one of the least understood. Turbulent shear flows, such as turbulent jets and wakes, are especially of great importance due to its presence in a very wide variety of engineering applications. The presence of turbulent shear in fluid flows can greatly improve mixing efficiency. Particularly in the chemical process industry, proper mixing is necessary to control product formation and therefore a well designed reactor is critical. Thus, studies of mixing in turbulent shear flows are of great importance not only in advancing turbulence theory, but also in engineering practices, such as the design and optimization of various kinds of chemical reactors.

Experimental studies of the modern fluid dynamics research often play two roles, one is to observe phenomena and try to understand the physical principles behind them, the other is to validate and improve computational models. Since much of the turbulent transport, conversion of mean flow energy into turbulent eddies, nonlinear transfer into smaller scales, and eventual dissipation is associated with coherent structures, coherent structures are one of the most popular phenomena to observe and study in turbulent flows. The properties of coherent structures, such as population, size, circulation, and energy, can be useful in the understanding of turbulence and property transport, and also can aid in the development of more efficient and more environmentally benign applications.

In the past two decade, with the advancement of flow visualization techniques, particle image velocimetry (PIV) and planar laser-induced fluorescence (PLIF) have become very popular experimental techniques for the measurements of the instantaneous velocity and scalar distribution in turbulent flows. As a whole-field measurement technique, PIV is superior to

pointwise measurements, such as laser Doppler velocimetry (LDV), because flow field data can be simultaneously collected at a large number of points over a two-dimensional or even three-dimensional domain. The spatial nature of PIV data allows the identification and characterization of coherent structures. Methods of analyzing and interpreting these spatially resolved velocity field data were discussed in Adrian (1999) and Adrian et al. (2000a). Prime examples of using PIV to study coherent structure are provided by Christensen and Adrian (2001, 2002b,a) in the turbulent boundary layers and Agrawal and Prasad (2002a,b, 2003) in turbulent axisymmetric jets. Simultaneous PIV and PLIF measurement has been proven to be a very powerful tool to study turbulent mixing, especially the role of coherent structures in mixing.

As mentioned above, the other role of experiments is to validate computational fluid dynamics (CFD) models. Among turbulent modeling methods of CFD, large eddy simulation (LES) is currently applied in a wide variety of engineering applications. In large eddy simulation, the principal operation is low-pass filtering, which is applied to the Navier-Stokes equations to eliminate small scales of the solution. By resolving the large scales of the turbulent flow, LES provides better fidelity than Reynolds-averaged Navier-Stokes (RANS) methods, which doesn't resolve any scales of the flow, and is much more practical in computational cost than direct numerical simulation (DNS), which resolves every scale of the flow. Therefore, LES has become a popular tool for complex flow calculations. Nevertheless, despite the wide spread acceptance of LES as a flow simulation tool, there are remarkably few reported *detailed* validation studies for complex flows with experimental data. Because the predictive capability of LES is generally attributed to its ability to capture large-scale flow structures (Lesieur and Metais, 1996; Sagaut, 2001), it can be argued that a detailed validation study of LES simulations should also include *two-point* flow statistics (e.g., two-point correlation functions). For this purpose, PIV data are particularly well suited because they capture the same range of large-scale flow structures as the LES models (Adrian, 1991; Agrawal and Prasad, 2002b).

The objectives of the present study are to perform both PIV and PLIF experiments in a confined rectangular reactor, and to use collected data to fulfill the roles of fluids experi-

ments, observing and studying the coherent structures, in both rectangular jet and wake, and performing and validating large eddy simulation models.

1.2 Dissertation organization

The remainder of this thesis is organized as follows: In Chapter 2, vortex behavior and characteristics in a confined rectangular jet with a co-flow are examined using vortex swirling strength as a defining characteristic. Chapter 3 presents the results from the investigation of the vortices in a confined rectangular wake flow. A large eddy simulation study of the confined jet flow with a Reynolds number of 20,000 is presented in Chapter 4. Chapter 5 describes a comparison study of turbulence statistics in the mixing regions of confined rectangular jet and wake. Finally, summary and conclusions are given in Chapter 6. Some future work is also briefly discussed.

CHAPTER 2. Population, Characteristics and Kinematics of Vortices in a Confined Rectangular Jet with a Co-flow

A paper published by Experiments in Fluids

Bo Kong, Michael G. Olsen, Rodney O. Fox and James C. Hill

Abstract

Vortex behavior and characteristics in a confined rectangular jet with a co-flow were examined using vortex swirling strength as a defining characteristic. On the left side of the jet, the positively (counterclockwise) rotating vortices are dominant, while negatively rotating vortices are dominant on the right side of the jet. The characteristics of vortices, such as population density, average size and strength, and deviation velocity were calculated and analyzed in both the cross-stream direction and the streamwise direction. In the near-field of the jet, the population density, average size and strength of the dominant direction vortices show high values on both sides of the center stream with a small number of counter-rotating vortices produced in the small wake regions close to jet outlet. As the flow develops, the wake regions disappear, these count-rotating vortices also disappear, and the population of the dominant direction vortices increase and spread in the jet. The mean size and strength of the vortices decrease monotonically with streamwise coordinate. The signs of vortex deviation velocity indicate the vortices transfer low momentum to high velocity region and high momentum to the low velocity region. The developing trends of these characteristics were also identified by tracing vortices using time-resolved PIV data. Both the mean tracked vortex strength and size decrease with increasing downstream distance overall. At the locations of the left peak of turbulent kinetic energy, the two point spatial cross-correlation of swirling strength with velocity fluctuation and

concentration fluctuation were calculated. All the correlation fields contain one positively correlated region and one negatively correlated region although the orientations of the correlation fields varied, due to the flow transitioning from wake, to jet, to channel flow. Finally, linear stochastic estimation was used to calculate conditional structures. The large-scale structures in the velocity field revealed by linear stochastic estimation are spindle-shaped with a titling stream-wise major axis.

2.1 Introduction

The study of coherent structures in turbulent shear flows is of great importance due to the structures' significant contribution to fluid entrainment and the transfer of mass, momentum and heat. The properties of these structures, such as population, size, circulation, and energy, can be useful in the understanding of turbulence and property transport and can aid in the development of more efficient and more environmentally benign applications. Moreover, detailed measurements of the behavior and characteristics of large-scale structures can be used to validate the predictions of computer modeling techniques, such as large eddy simulation, where the largest scales of the turbulence are resolved. The objective of the work presented here is to use a vortex identification method to analyze the experimental data collected in a confined rectangular liquid jet with a co-flow with regards to the population, size, kinematics and characteristics of vortices within the jet.

In the chemical process industry, liquid jets usually are placed in a confined space, as in a mixer or a reactor, and are commonly applied within a co-flow or cross-flow to improve mixing and chemical reaction between two or more fluids, like a concentric pipeline mixer or a coaxial jet mixer (Lu et al., 1997). A typical geometry for this type of mixer is an axisymmetric jet with a co-flow or cross-flow. However, cylindrical reactors pose challenges in the laboratory with laser techniques such as particle image velocimetry (PIV) due to the curvature and associated image distortion in the measurements. An alternative approach is to use a rectangular configuration (Feng et al., 2005), which can provide much better measurement accuracy and also a much simpler geometry to conduct CFD simulations. When the aspect

ratio of a rectangular jet nozzle (w/h , where w and h are the long and short sides of the nozzle), is not large enough to eliminate the 3D effect, the jet usually can no longer be considered a planar jet, but instead a rectangular jet (Deo et al., 2007a). For example, Pope (2000) pointed out that the aspect ratio of a plane nozzle must be significantly large, typically 50 or more, to ensure that the flow is statistically two-dimensional and free from the effects of sidewalls. For a liquid phase jet, especially when designed to study the mixing process in a high Schmidt number environment, it is not practical to build and study a high aspect ratio planar jet mixer. The aspect ratio of the jet in the current research is 5, which indeed a low-aspect-ratio rectangular jet. But according to Deo et al. (2007b), the sidewalls of the confinement can significantly limit the development of the jet in the spanwise direction, and make the 2-D region extend a longer distance than a rectangular jet without sidewalls. In this study, the farthest observation downstream location was $X/d = 30$, and thus the measured flow fields are more comparable to planar jets, instead of most studies of low aspect ratio rectangular jets in which the focus is mainly on a free jet, in which the 3-D vortex ring structure can break-down faster than in axisymmetric jets due to the presence of sharp corners (Grinstein, 2001; Gutmark and Grinstein, 1999). Although the confined rectangular jet with a co-flow is not common in turbulent jet research, it provides a simple and well defined geometry suitable for both experimental measurements and numerical simulations, especially for PIV experiment and 3-D CFD simulations.

The jet flapping phenomenon first reported by Goldschmidt and Bradshaw (1973) is one of the first indications of large-scale structure in the planar turbulent jet. However, Oler and Goldschmidt (1982) suggested that correlation results indicating the flapping motion can also be explained by the presence of an antisymmetric array of counter-rotating spanwise vortices. Antonia et al. (1983) also performed correlation measurements, which support this concept and showed that the apparent flapping could indeed be explained in terms of the passage of vortical structures past the fixed probe pair and was not associated with bulk lateral displacement of the jet. The existence of a large-scale structural array has also been demonstrated later by the velocity fluctuation two-point correlation fields obtained in different

jet facilities by Mumford (1982), Antonia et al. (1986) and Thomas and Brehob (1986). Such large-scale structural arrays propagate at approximately 60% of the local centerline mean velocity, estimated by Goldschmidt et al. (1981), Antonia et al. (1983) and Thomas and Brehob (1986). Recently, Gordeyev and Thomas (2000) used proper orthogonal decomposition (POD) to analyze experimental data, also suggesting that the presence of planar structures aligned in the spanwise direction as well as three-dimensional structures with asymmetrical shape in the cross-stream direction and pseudo-periodically distributed in the spanwise direction.

Most of the earlier coherent structure investigations on planar jets were focused on the large structures, because they were conducted using point-wise velocity measurements and then analyzed with a correlation technique. In the past two decades, particle image velocimetry (PIV) has become a popular experimental technique for turbulence studies. Since PIV provides instantaneous two-dimensional velocity field data, it is well suited for visualizing and identifying vortical structures. Methods of analyzing and interpreting these spatially resolved velocity field data were discussed in Adrian (1999) and Adrian et al. (2000a). Prime examples of using PIV to study coherent structure are provided by Christensen and Adrian (2001, 2002b,a) in the turbulent boundary layers and Agrawal and Prasad (2002a,b, 2003) in turbulent axisymmetric jets. Of particular interest to the present study. Agrawal and Prasad (2003) and Chhabra et al. (2006) reported results on small-scale vortices present in the axial plane of a self-similar turbulent axisymmetric jet by using a high-pass filter and vortex extraction method based on velocity quadrant and angular variance. These studies include measurements of the vortex characteristics, such as the vortex population, energy, vorticity, and rms of velocity fluctuations. Their studies also show that the centers of a larger vortices spin faster than centers of a smaller vortices. After normalization, vorticity results for different vortex radii collapse upon each other. In contrast, the similar studies of small-scale vortices in planar jets and rectangular jets are lacking.

Besides the geometry of the jet, another new element of current study is the presence of co-flow. Although the vast majority of the turbulent jet research has been focused on jets discharged into ambient fluids, a jet with a co-flow is more commonly seen in industrial appli-

cations. One of the earliest investigations of jets with a co-flow is the analytical study done by Abramovich et al. (1984). He showed the presence of three essential regions in co-flow jets: the initial, principal and transition areas. When the flow is confined, the process of the co-flow driven by the jet is modified and the mixing process depends strongly not only on the velocity ratio, but also on the interaction between the boundary layer, the mixing layer and the main flow (Gazzah, 2010). Gutmark and Wygnanski (1976) found that a jet exhausting into a slow-moving co-flowing stream is narrower than a comparable jet exhausting into quiescent surroundings. Curtet (1958) was interested by recirculation phenomena generated by a considerable pressure gradient, and proposed a parameter of similarity called the parameter of CrayaCurtet, which was formulated by Steward and Guruz (1977). For a CrayaCurtet parameter value greater than 0.8, recirculation can be avoided. Because of its great practical importance, an increasing attention has been given to the jet development and mixing in jets with a co-flow (Bradbury and Riley, 1967; Nickels and Perry, 1996; Chu et al., 1999; Benayad et al., 2001; Enjalbert et al., 2009). Another study of interest is the experimental investigation of an axisymmetric jet discharging in a co-flowing air stream by Antonia and Bilger (2006), which shows that the far jet flow may be strongly dependent on the nozzle injection conditions. Despite all of this previous work, the behavior of turbulent vortices in such a flow remain relatively unstudied. Thus, in the work that follows, the characteristics of vortices in a confined rectangular turbulent jet with a co-flow have been investigated.

2.2 Experimental Facility and Methodology

The flow facility used in the experiments presented here is shown in Fig. 2.1. The measurements are carried out in a Plexiglas test section with a rectangular cross-section measuring 60 mm by 100 mm and with an overall length of 1 m. There are three streams separated by two splitter plates, each emitting from the its own flow conditioning section consisting of a packed bed and turbulence reducing screens and a 16:1 contraction section. The slope of the surface of the splitter plates is 3 degrees along the side channels and 1 degree along the center channel, and the thickness of the tips of the splitter plates are less than 0.5 mm. Two different

flow cases as defined by different bulk flow Reynolds numbers of, 20,000 and 50,000 (based on average velocity and hydraulic diameter), were studied. The volumetric flow rates for the two flow cases are listed in the Tab. 2.1.

Experimental data from simultaneous PIV/PLIF experiments and high speed PIV experiments were collected and analyzed. The simultaneous PIV/PLIF technique has been used to study many turbulent mixing problems, such as Westerweel et al. (2005, 2002) in a turbulent jet. Approximately 24 grams of hollow glass spheres (Spherical, Potters Industries, Inc.) were added to the water reservoir with total volume of 3500 liters in both the regular and high speed PIV measurements. The nominal diameter of the seed particles was $11.7 \mu\text{m}$ and the density of the particles was 1.1 g/cm^3 . The 0.5 mm thick laser sheet used in high speed PIV experiments was produced by a Quantronix Darwin-Duo dual oscillator, single head Nd:YLF CW laser, which passes through the centerline of the test section in the z -direction. A Photron ultima APX-RS high speed 10-bit CMOS camera was used to capture particle images. The image magnification of the CMOS camera was 0.27, and the numerical aperture was 8. The image capturing frequency was 125 Hz for the $\text{Re} = 20\text{K}$ case and 250 Hz for the $\text{Re} = 50\text{K}$ case. A multi-pass cross-correlation technique with decreasing window sizes was used to compute the velocity field. The final interrogation spot size measured 16 pixels by 16 pixels, corresponding to 1.02 mm on each side. With 50% overlap between interrogation windows, the velocity vector spacing was 0.51 mm in both the x - and y -directions. The time interval between two laser pulses was 1 ms in the low flow rate case, and $600 \mu\text{s}$ in the high flow rate case. Since the memory capacity of CMOS camera is limited, 1024 PIV image pairs can be collected in each run. At each observed location, the experiment was repeated 20 times, thus a total of 20480 PIV realizations were collected and analyzed at each locations in both cases.

In the simultaneous PIV/PLIF measurements, illumination was provided by a New Wave Research Gemini PIV laser. PIV and PLIF images were obtained using two 12-bit LaVision Flowmaster 3S CCD cameras. The image magnification of the two CCD cameras was 0.12, and the numerical aperture was 8 for PIV and 5.6 for PLIF. A dichroic mirror (Q545LP, Chroma Technology Corp.) was placed at an angle of 45° to the laser sheet to separate the light paths

and direct them to either the PIV or the PLIF camera. The PLIF camera lens was filtered with a long-pass optical filter (E560LP, Chroma Technology Corp.), and the PIV camera lens was filtered with a narrow-band-pass optical filter (Z532/10X, Chroma Technology Corp.) The seeding method, time interval between two laser pulses and cross-correlation technique in PIV measurement in the simultaneous PIV/PLIF experiments were the same as in high speed PIV measurement. The fluorescent dye Rhodamine 6G was used as a passive scalar in PLIF. In the center stream, the source concentration of Rhodamine 6G was $45 \mu\text{g/l}$, while the other two streams were pure water. The in-plane spatial resolution of the PLIF measurements in the present study was actually limited by the flow area imaged per pixel, which was approximately $56 \mu\text{m}$. The simultaneous PIV/PLIF data at high Reynolds number are a subset of measurements reported by Feng et al. (2007). Since the experimental apparatus and procedure have been described in detail elsewhere (Feng et al., 2005, 2007), the reader is directed to the literature for further information. At each observed location, 3250 simultaneous velocity and concentration realizations were analyzed in high Re cases and 2500 realizations in low Re case. The simultaneous PIV/PLIF experimental data for the low Re case is available at two locations, $X/d = 4.5$ and $X/d = 7.5$, where X is downstream distance and d is the initial jet width, 20mm.

The smallest Kolmogorov scale in the flow field can be estimated based on the exit width of the jet and the turbulent kinetic energy at the tips of the two splitter plates. Although the smallest turbulent scales of the flow cannot be fully resolved, second-order quantities such as velocity fluctuations and characteristics of large-scale structures can be measured accurately. As in Prasad et al. (1992), the random error in the PIV measurements was estimated as one-tenth of the effective particle image diameter. The measurement resolution and uncertainty of the two cases are listed in the Tab. 2.2.

To assist in the understanding of the flow configuration of current investigation, Fig. 2.3 gives the profiles of the mean of streamwise velocity, U , for both Reynolds number cases at 3 different downstream locations, $X/d = 1, 4.5$ and 15 . After normalization by ΔU , which is the average velocity difference between the center stream and two side streams ($\Delta U = 0.2$

Table 2.1 Flow rates of two cases

Reynolds number	Flow rate (Liter/s)	
	Center stream	Outer stream
20K	0.8	0.4
50K	2.0	1.0

Table 2.2 PIV Spatial resolution and measurement uncertainty

	Reynolds number	Spatial resolution (η : local Kolmogorov scale)	Uncertainty	
			Center stream	Outer stream
High Speed	20K	5.4 η	$\pm 1.2\%$	$\pm 2.5\%$
PIV	50K	6.7 η	$\pm 0.8\%$	$\pm 1.6\%$
Sitantaneous	20K	4.6 η	$\pm 1.7\%$	$\pm 3.4\%$
PIV/PLIF	50K	6.0 η	$\pm 1.3\%$	$\pm 2.7\%$

m/s for $Re = 20K$ and $\Delta U = 0.5$ m/s for $Re = 50K$), the profiles of these two flow cases are very similar. Near the channel inlet, at $X/d = 1$, two small wake regions on both sides of the tips of the splitter plates can be observed from the velocity profile. These result from the boundary layers formed on the splitter plates. At the further downstream location, $X/d = 4.5$, the two wake regions disappear and are replaced by two mixing layers regions that quickly grow together, resulting in the potential core in the center jet disappearing for both cases. At $X/d = 15$, the potential cores in the outer streams also disappear, and the flow continues its development toward channel flow because of the confinement by the two walls in cross-stream direction. The wake regions in the near-field of a jet and confinement configuration of the jet are rather uncommon in turbulent jet research. Again, as mentioned in the introduction, the design of the the jet configuration is determined by the practical considerations of simulating flow conditions in an industrial reactor.

2.3 Swirling Strength Vortex-ID Method

Several methods have been suggested and implemented by researchers to identify vortices in instantaneous two-dimensional velocity fields, such as those obtained by PIV. Adrian et al.

(2000a) described a number of vortex eduction techniques and compared their effectiveness in identifying vortices. They found that swirling strength provides a reliable means of extracting the small-scale vortices, including those which are not visible in velocity decompositions. Vollmers (2001) also validated and compared several coherent structure eduction methods. He also concluded that the swirling strength is the best indicator for the presence of vortices in turbulent flow. Thus, the authors have chosen a vortex extraction technique based on swirling strength to analyze the turbulent vortices in a confined rectangular turbulent jet in this paper.

The concept of swirling strength, λ_{ci} , was described by Adrian (1999) as the imaginary part of the complex conjugate eigenvalues ($\lambda_{cr} \pm \lambda_{ci}$) of the local velocity gradient tensor. Physically, λ_{ci}^{-1} represents the period required for a fluid particle to swirl once about the λ_{cr} -axis (Piomelli et al., 1996; Adrian, 1999). Thus, a non-zero λ_{ci} indicates a local swirling motion, and spatially connected regions of non-zero λ_{ci} represent vortices (Wu and Christensen, 2006). Tomkins and Adrian (2003) multiplied λ_{ci} by the sign of the local vorticity to capture the direction of rotation at each location in the flow field. This modified form of swirling strength can be written as (Wu and Christensen, 2006)

$$\Lambda_{ci}(x, y) = \lambda_{ci}(x, y) \frac{\omega_z(x, y)}{|\omega_z(x, y)|} \quad (2.1)$$

This method has two great advantages. First, it is frame independent, meaning a priori information of the bulk motion of the vortex core is not necessary. Second, it only reveals the regions with vortices, which means the flow regions with high vorticity but no local swirling motion, such as shear layers, do not produce non-zero λ_{ci} . However, like other vortex extraction methods based on the velocity gradient, the method does have one important drawback when applied to PIV data. Due to the sensitivity of velocity gradient to noise, this type of method is often not applicable to experimental data if no smoothing has been applied (Vollmers, 2001), since the method may falsely identify measurement noise as vortices. However, too much velocity smoothing may eliminate the small vortices. Thus, in addition to carefully choosing experiment parameters to reduce the measurement uncertainty and applying slight smoothing, we utilized a threshold of $|\Lambda_{ci}| \geq 1.5\Lambda_{ci}^{rms}$ (Wu and Christensen, 2006) to limit the influence of

experiment noise, which only affects the edges of clusters and does not alter the populations appreciably. Further information about this method can be found in the references mentioned above.

2.4 Vortex Characteristics Analysis

2.4.1 Instantaneous structures

Two examples of the instantaneous swirling strength field at near-field $0 < X/d < 2.5$ and far-field $6.5 < X/d < 9$ of the jet at $Re = 20K$, are shown in Fig. 2.4 to illustrate the effectiveness of the swirling strength as a vortex indicator. It is contrasted with the mean-bulk Galilean decomposed velocity field in Fig. 2.4 (a1,a2), which reveals only the vortices moving at their respective spatial convective velocities. The local Galilean decomposed velocity fields are shown in Fig. 2.4(b1,b2), where the local convective velocities have been subtracted from each vortex center. The background contours are the clusters of Λ_{ci} after filtering with a universal threshold of $|\Lambda_{ci}| \geq 1.5\Lambda_{ci}^{rms}$. Where the clusters of filtered Λ_{ci} identified vortices, all of the local Galilean decomposed velocity vectors on Fig. 2.4 (b1,b2) display a clear swirling motion. This demonstrates the effectiveness of using the swirling strength as a vortex identification method, in the present flow field. Due to spatial resolution limitations, clusters of Λ_{ci} with fewer than three grid points across their span in both the x and y directions are not considered.

Comparing the definition of swirling strength above with Robinson’s definition of a vortex, “A vortex exists when instantaneous streamlines mapped onto a plane normal to the vortex core exhibit a roughly circular or spiral pattern, when viewed from a reference frame moving with the center of the vortex core.” (Robinson, 1991), the edges of swirling strength clusters do not necessarily accurately define the very edge of a vortex. By its definition, the swirling strength is the indicator of how strong the swirling motion of a particular local fluid particle is, or how fast the particle rotates. Therefore, the swirling strength clusters are only the parts of vortices that only include fluid particles with distinguishable strong swirling motions. For those vortices with weak rotation at the vortex edge, the filtering process performed to eliminate the effect of the measurement noise will also eliminate the swirling strength signatures of these regions.

A small fluid particle with close to zero swirling strength, with no rotation or swirling motions itself, could be part of large-scale coherent motion. Therefore, the swirling strength clusters identified from the instantaneous velocity fields are only defined as vortex cores, or the highly rotating part of a vortex. As Agrawal and Prasad (2003) argued, vortices in turbulent flows range in size from the integral length scale down to the Kolmogorov scale, and there are always small-scale vortices embedded in large-scale structures. Large-scale vortices account for most of the turbulent energy, while the small scales carry almost the entire vorticity. These swirling strength clusters are those small-scale vortices in their argument.

Fig. 2.4 shows that on the left side of the jet, the positively (counterclockwise) rotating vortices are dominant, while negatively rotating vortices are dominant on the right side of the jet. One may notice from the instantaneous fields of vortices that in both the near-field and the far-field of the jet, the distribution of the vortices seems random and doesn't display as the large-scale structural array in planar jet suggested by the Mumford (1982), Antonia et al. (1986), nor the roller and helical modes revealed by the low-pass filter in axisymmetric jets (Agrawal and Prasad, 2002a). The velocity fluctuation correlation reported by Feng et al. (2007) actually shows, in this jet, there are the chain of large coherent structures in the stream-wise direction, as previous researchers suggested in planar jets. As mentioned earlier, the large-scale coherent motions visualized by the correlation technique are not the swirling motions of the small-scale vortices in the individual instantaneous velocity field. Also, notice that besides those dominant positively rotating vortices, there are also some negatively rotating vortices on the left side of the jet. The counter-rotating vortices are due to the small wake regions downstream of the splitter plates. In the far-field of the jet, the instantaneous vortex fields bear some resemblance to the small-scale vortex field revealed by a high-pass filter in the far-field of an axisymmetric jet (Agrawal and Prasad, 2002b, 2003), where small-scale vortices spread across the jet body. Spatial correlation calculation with the swirling strength were also performed in the present study, like the calculations done by Christensen and Adrian (2001), who found a strong position and angle preference between the vortices in wall turbulence. The results here show that the vortices in entire body of this jet have no strong spatial correlations

with other vortices at all, confirming the high level of randomness observed in the instantaneous fields. In addition to the vortices in the jet region, there are also some vortices in the two boundary layers near the walls, which are not of interest in the current study.

2.4.2 Vortex population

To identify the population trends of the vortices, a similar vortex definition as Wu and Christensen (2006) is used to define the population density of vortices, $\Pi_{p(n)}$. $\Pi_{p(n)}$ is herein defined as the local ensemble-averaged number of detectable positively rotating or negatively rotating vortices whose centers reside at a given PIV grid node. Fig. 2.5 shows $\Pi_{p(n)}$ crossstreamwise profiles at 3 downstream locations for the two different Reynolds numbers investigated. To minimize scatter in the profiles, $\Pi_{p(n)}$ is presented as the vortex population over a half jet width ($d/2 = 1\text{cm}$) long area in the streamwise direction. The plots presented in Fig. 2.5 demonstrate that the distributions of the positively and negatively rotating vortices are nearly axially symmetric at all 3 downstream locations in both two cases.

These profiles confirm the observations from the instantaneous vortices fields above. At $X/d = 1$ in the near-field of the jet, the population density profiles of the dominant direction vortices and counter-rotating vortices both show clear peaks, at the locations on either side of the center of the wake region, according to the streamwise velocity mean profile in Fig. 2.3. The population of the counter-rotating vortices almost disappears completely at $X/d = 4.5$, as the wake regions decay and are replaced by mixing layer-like region population profiles. The population profiles of the dominant vortices also broaden with increasing downstream distance. These vortices are initially confined to the high shear, mixing layer regions with few vortices existing in the free streams, but as the flow develops towards channel flow at the farthest downstream locations, the distribution of the vortices spreads throughout the entire width of the reactor. At $X/d = 15$, the population density profiles approach the vortex distribution of a channel flow. One may notice the remarkable difference between the results here and the small-scale vortex distribution results in far-field of a axisymmetric free jet in Agrawal and Prasad (2002b), which shows that the probability of finding a vortex is uniform up to the edge

of the jet and a substantial number of both clockwise and counter-clockwise rotating eddies exist on both sides of the jet axis. In the far-field of the jet, the two walls on the spanwise direction produces the new source of the turbulence, which reaching into the center of the jet as the flow develops. This causes the small scale vortices distributed as in a channel flow, instead of a free jet.

Also notice that the highest vortex population actually occurs in a very small region of the wall boundary layers, which is not a surprise because of the higher velocity gradient in the wall region. As mentioned earlier, the population here only includes the vortices whose core (swirling strength cluster) diameters are larger than 13.8η in the low Re case and 33.9η in the high Re case.

By adding the number of positively rotating vortices together between the center of the center stream $Y/d = 0$ and the center of the left side stream $Y/d = -1$ in this 1cm long region, the streamwise population changing trend of detectable positively rotating vortex can be more easily observed, as shown in Fig. 2.6. The number of the vortices in the same size region per velocity realization at different different downstream locations initially increased and then decreased. This is reasonable because right after the flow enters the test section, the high velocity gradients produce many vortices. At the same time, the decay and dissipation of these vortices also occurs. As the flow progresses further downstream, the potential cores disappear, fewer vortices are produced. The vortex dissipation process continues, though, and later in the far-field of the jet it eventually overwhelms the jet vortex production. Also notice the population is much higher in the high Reynolds number case than in the low Reynolds case, specially in the far-field of the jet, where the flow approaches a fully-developed channel flow and the boundary layers on the walls play a bigger role in the vortex production than the shear layer caused by the jet. Figure 2.6 also shows that the development towards channel flow is more rapid for the low Re case, which of course makes sense, since the entrance length in a channel or pipe increases with increasing Reynolds number (Sadri and Floryan, 2002).

2.4.3 Size and strength of vortex cores

In addition to the vortex population analysis presented above, other properties of the identified vortices can be obtained from the experimental data. The results of the size of vortex core are presented in a similar manner to the vortex populations. Figure 2.7 shows the mean vortex core size profiles across the channel, and Fig. 2.8 gives streamwise profiles. The values of mean vortex core size appear to be rather small compared to the jet width. Also the smallest size of swirling strength cluster we can identify is $d^2/400$ for both investigated Reynolds numbers.

The cross-stream profiles in Fig. 2.7 show that on both sides of the jet where the dominant direction vortex population is highest, the average vortex size is also the largest, especially at $X/d = 1$. Although the population density of the vortices in the wall boundary layers is highest, the size of the vortices in the boundary layer is small. Figure 2.8 shows that the average vortex core size between the center of the center stream and the left stream monotonically decreases with increasing downstream distance. This might initially seems contrary to what was reported in Feng et al. (2007). In the $Re = 50K$ case, the size of the coherent structures was observed linearly growing almost from $X/d = 1$ through at least $X/d = 15$, which would be expected for jet flow. Glancing back at the instantaneous vortex field in Fig. 2.4, the areas of the identified swirling strength clusters in the far-field are indeed smaller than in the near-field. In the near-field of the jet, the current vortex areas are about two orders of magnitude smaller than in the previous report; in the far-field of the jet, they are almost four order of magnitude smaller than in the previous report. Again, this can be explained based on the difference between the two measurement techniques. In Fig. 2.6, from $X/d = 1$ to $X/d = 7.5$, the populations of vortex cores increase by at least 40%, while the mean sizes only decrease by 15%. Therefore the overall swirling area in the jet grows by approximately 20 %. However, as the jet progresses downstream, there are more small structures with increasing downstream distance, as previously mentioned. The increase in the number of small structures brings the mean size values down. When the flow becomes fully developed channel flow, the mean structure size will remain constant beyond this point. This explains why the vortex core

size becomes smaller with increasing downstream distance and eventually stabilizes as the flow fully develops. This is to be expected as the confined jet flow transitions from a jet-like flow to a channel-like flow, which would have the vortex size independent of downstream location.

The strength of the vortex cores also can be determined. Note that inside the swirling strength clusters, the strength value is not evenly distributed. The highest swirling strength value of the vortex core is used to characterize the vortex, since it gives the maximum rotation speed of the given vortex, according to the swirling strength definition. Figure 2.9 shows cross-stream profiles of the average peak value of the vortex core and Fig. 2.10 gives streamwise profiles. All these profiles were normalized using $\Delta U/d$. In Fig. 2.9, it can be observed that the cross-stream profiles of the maximum strength of vortex core show very similar characteristics as the plot of the size of vortex core. The center of the shear region of the jet has the maximum vortex population density, the largest vortex size, and the strongest swirling motion. Figure 2.10 shows that as the flow develops, the strength of the vortices decreases, then eventually stabilizes, just as the vortex size. Comparing the two Reynolds number cases, the values for the $Re = 20K$ case are higher than the $Re = 50K$ case after normalization, specially at $X/d = 1$. However, the difference between the two Reynolds numbers becomes smaller and smaller as the flow progresses downstream.

The cross-stream and streamwise profiles of both vortex size and vortex strength all indicate that the high Reynolds number case develops more slowly than the low Reynolds number case, just as the profiles of vortex population density show.

2.4.4 Deviation velocity of vortex cores

The instantaneous velocity field data can also lend insight into the motion of the vortices. The velocity of vortex cores can be mapped back to the velocity field once the vortex is identified. By subtracting the mean velocity from the velocity values of the vortex cores, what we define as the *deviation velocity* of the vortex can be obtained, i.e. , the deviation of the instantaneous vortex convection velocity from the local mean velocity. Figure 2.11 and 2.12 show profiles of the average cross-stream (V) and streamwise (U) deviation velocities cross the

channel at three downstream locations, which all are normalized by ΔU .

Figure 2.11 shows that the mean deviation velocity V is zero at the location of the population density peak. Considering the left side of the jet, on the right side of population density peak, vortices tend to move towards the center of the center stream, and on the left side, the vortices tend to move towards the center of center of left side (or outer) stream, which corresponds to the spreading of the shear layers at the center regions of the jet. Particularly, at $X/d = 1$, the deviation velocity V is maximum at the very edge of the potential core of the free streams. Since there are virtually no vortices in the potential core, the average deviation velocity there is zero. In addition, the normalized values of vortex deviation velocity V are higher in the low Reynolds number case than in the high Reynolds number case.

The mean deviation velocity U is also zero at the location of the population density peak as shown in Fig. 3.12. At $X/d = 1$, towards the jet center, the values are negative, and towards the side streams, the values are positive, which corresponds to one of the roles of vortices in the flow: transferring low momentum fluid to the high velocity region and transferring high momentum fluid to the low velocity region. However, at further downstream locations, $X/d = 4.5$ and $X/d = 15$, the profiles of mean deviation velocity U of the counter-rotating vortices overlap with the profiles of dominant rotating direction vortices. Once again, glancing back at the instantaneous vortex field in the far-field of the jet in Fig. 2.4, these small number of counter-rotating vortices are blending with the dominant direction vortices.

The probability density function of vortex deviation velocity was also calculated at three downstream locations, $X/d = 1$, $X/d = 4.5$ and $X/d = 15$ for the $Re = 20K$ case, and compared to the PDF of the velocity fluctuations of the overall flow, which are shown in Figs. 2.13, 2.14 and 2.15. At each downstream locations, three observation points were used, one is at the location of the peaks of positively rotating vortex population density ($Y/d = -0.45$ at $X/d = 1$, $Y/d = -0.42$ at $X/d = 4.5$), one is on the left side and one is on the right side where the middle points of the population density peak declining slopes are. In each case, all the distributions of the deviation velocity appear narrower than the velocity fluctuation distribution. One reason to explain this is the swirling strength vortex identification method

reveals the core of the vortex. It is actually the part of the vortex close to the vortex edge that generates high velocity fluctuations, where the swirling motion could be very weak. Another possible reason is the vortex identification method used here does have spatial limitations, and vortices that are too small to be detected could play some role in the flow unsteadiness. It is also possible that some of the fluctuations are due to other unsteadiness or large-scale coherent motions in the jet flow, such as stream-wise jet pulsing or cross-stream flapping of the jet.

Similar to the mean vortex deviation velocity profiles, at the location of the population density peak, the mean of both the vortex deviation velocities are zero. However, the mean of velocity fluctuations are also close to zero at this location. Interestingly, on both sides of the peak location, the distribution peaks of vortex deviation velocity appear on the opposite side of zero as the distribution peaks of velocity fluctuation. It makes sense that the velocity fluctuation close to the jet center is negative, because low momentum fluid is transferring into the jet center (where the mean velocity is high); and the velocity fluctuation close to the outer stream center (where the mean velocity is low) is positive, because high momentum fluid is transferring in. Notice also, that compared to the distributions at $X/d = 1$, as downstream distance increases, the vortex deviation velocity distributions become closer to the distribution of the velocity fluctuation. (An exception to this is at $X/d = 4.5$ and $Y/d = -0.16$, where the streamwise velocity fluctuation distribution has a much higher peak, which is simply because the location is very close to the jet center). As the flow progresses further downstream, the vortex deviation velocity should become more similar to the distribution shape of the velocity fluctuations, as the mean vortex deviation velocity profiles indicate.

2.5 Vortex Tracking Analysis

From the high speed PIV data, the trajectories of individual vortices can also be determined. After identifying a particular vortex in a pair of velocity realizations, the velocity of the swirling strength cluster can be found from the change in the vortex position between the two frames. Repeating this frame by frame over the high speed PIV data set, the location of the vortex in each frame can be estimated. The vortex on the next frame which has the maximum overlap

with the estimated location is considered the same vortex as the selected vortex from the previous frame. Figure 2.16 shows two trajectories of a positively rotating vortex on the left side of the jet and a negatively rotating vortex on the right side of the jet to demonstrate the effectiveness of this tracking method. Only vortices that newly appear at the bottom of the velocity fields were traced to maximize tracking time because the length of observation window is limited. Once a vortex has been identified in a series of velocity realizations at different time steps, how the size and strength of the vortex changes with time can be determined. Because the vortex property development of one given vortex could be rather noisy, to obtain the main characteristics of vortex development, averaging was performed for certain vortices which traveled through the current watching window, $t \geq 0.2s$ for $Re = 20K$ and $t \geq 0.08s$ for $Re = 50K$. Those vortices which disappeared during this time frame are not included.

The mean vortex size and strength are shown in Figs. 2.17 and 2.18, using observation windows beginning at $X/d = 0$, $X/d = 3.5$ and $X/d = 7.5$. Since the experimental data at these three locations were collected at different times, the vortices that were tracked in one window definitely could not appear in the other windows. The mean tracked vortex maximum strength decreases with increasing downstream distance after the flow enters the channel, the same development as we observed in the previous section. However, the mean tracked vortex size increases slightly after the vortices enter the reactor, and then decreases. The vortices that were tracked close to the jet outlet, must have already existed when the flow entered the test section. They are likely those well organized vortices reported in wall turbulence (Adrian et al., 2000b), and continue to develop for a while before the changing of the flow field affects them. When these vortices meet the counter-rotating vortices on the other side of the splitter plates, and when vortices begin to be produced by the mean shear in the jet, the properties of the vortex core will change. They can be weakened or pushed aside by the counter-rotating vortices. Also, the swirling strength values in the swirling strength clusters could be redistributed, as some parts of the rotating fluid particles can spin off from the cluster, a phenomenon observed in some instantaneous vortices fields from the high speed PIV data.

Also compared to the mean vortex size and strength profiles, at $X/d = 1$ and $X/d = 4.5$,

presented in Figs. 2.7 and 2.9, all the values calculated by tracing individual vortices using high speed PIV data are higher. This is because the averaging here is actually conditional averaging as mentioned earlier. Those vortices chosen here have relatively long life spans, a probable consequence of their being larger and stronger than the “average” vortex.

2.6 Spatial correlation functions and linear Stochastic estimation

2.6.1 Two-point spatial correlations

Normalized by the *rms* of swirling strength and some flow property, σ , the two point spatial cross correlation of swirling strength and the fluctuation of σ can be defined as

$$R_{\lambda\sigma'}(X, Y; x, y) = \frac{\langle \lambda_{ci}(X, Y) \sigma'(x, y) \rangle}{\sqrt{\langle \lambda_{ci}^2(X, Y) \rangle \langle \sigma'^2(x, y) \rangle}} \quad (2.2)$$

where (X, Y) and (x, y) are the coordinates of the basis point (i.e. the point about which the correlation is calculated) and an arbitrary point in the flow field, respectively. In the present study, locations along the left peak of turbulent kinetic energy at different downstream locations were chosen as basis points. This location also corresponds to the peak of the population density of positively rotating vortices. The spatial correlations of $R_{\lambda u'}$ and $R_{\lambda v'}$ for basis points located at four downstream locations for both Re cases are presented in Figs. 2.19 and 2.20. The streamwise flow direction is from the bottom to the top of the figures.

The cross correlation fields of swirling strength and fluctuations of the two velocity components exhibit “butterfly” like shapes. The right wing of $R_{\lambda u'}$ contains positive values and the left wing contains negative values. The symmetry line of this “butterfly” shape in $R_{\lambda u'}$, called “the axis” of these correlation fields hereafter, is oriented vertically in the streamwise direction, which the contour line of $R_{\lambda u'} = 0$ overlaps in the region of the basis point. The symmetry line of $R_{\lambda v'}$ is oriented horizontally with negative values downstream of the basis point and positive values upstream of the basis point. Notice at $X/d = 1$, the axis of $R_{\lambda u'}$ is not oriented vertically as it is at the other downstream locations. Instead, the axis tilts about 30 degree away from the jet center, which is caused by high velocity gradients in this narrow wake region. Once the wake region disappears, the tilting of the axis becomes less significant

due to smaller and smaller velocity gradients. There is a second positively correlated region on the left side of the negative peaks, and a second negatively correlated region on the right side of the positive peaks in the $R_{\lambda u'}$ contours, especially in the low Re case, at $X/d = 1$. Also, there is a weakly correlated negative region upstream of the strong positive region close to the basis point and a weak positive region downstream of the strong negative region in $R_{\lambda v'}$. Assuming the vortex at the basis point is accompanied by vortices upstream and downstream of the basis point location, these two correlation fields indicate locations of accompanying vortices. Also the correlation in the region far from the basis point is actually very weak (that is close to zero), which makes the location of the $R_{\lambda u'} = 0$ contour somewhat random. This agrees with the observation from the instantaneous vortex fields, in Fig. 2.4. Also, as the flow progresses downstream, the correlation areas of both $R_{\lambda u'} = 0$ and $R_{\lambda v'} = 0$ grow larger. Notice the peak values of these correlations in Fig. 2.22. The peak values of $R_{\lambda u'}$ are approximately 0.2 for both cases close to the jet inlet. The peak values of $R_{\lambda v'}$ begin at approximately 0.4 near jet inlet in both cases, and decrease with downstream distance, approaching a value of 0.25 for both Reynolds number cases after the flow passes beyond $X/d = 12$.

Figure 2.21 shows $R_{\lambda_{ci}\phi'}$, the cross-correlation of swirling strength with the concentration fluctuation, for Re=50K and Re= 20K, respectively. Note that simultaneous PIV/PLIF data were only collected for 2 downstream locations for Re= 20K, compared to six locations for Re=50K. There are two correlated areas in the contours; one positively correlated region downstream of the basis point and one negatively correlated region upstream. This shape suggests that the positively rotating (counterclockwise) vortices bring high concentration fluid (i.e., positive concentration fluctuations) from the center stream to the side stream downstream of the vortex core and bring the low concentration fluid from the side stream to the center stream upstream of the core. These two correlation areas are not only comparable in size but also in absolute peak values. As mentioned before, the locations chosen here also are the locations of the peak of positive vortex population density, which means there are predominately positively rotating vortices centered at this location. The contour lines of $R_{\lambda_{ci}\phi'} = 0.1$ and $R_{\lambda_{ci}\phi'} = -0.1$ are nearly symmetrical about the basis point, except at the location $X/d = 1$.

As previously stated, because the axis of positively rotating vortices close to the jet outlet is obliquely oriented, positive $R_{\lambda_{ci}\phi'}$ is located in the second quadrant instead of the first quadrant. Considering these two regions together provides an explanation for the elliptic shape of the $R_{\phi'\phi'}$ with the major axis inclined at 45-degrees, reported in a previous paper (Feng et al., 2007). Also, considering the location of the correlation peaks with respect to the basis point, the results are consistent with the location of the vortex core in linear stochastic estimates of the velocity field given the event of $\phi'(x_o) = +2\phi'_{rms}(x_o)$ (Feng et al., 2007). Notice also that with increasing downstream distance, the size of the correlation area becomes steadily larger. However, the peak values of $R_{\lambda_{ci}\phi'}$, shown in Fig. 2.22, also first increase, then decrease in the high Re case. Compared to the high Re case, the correlation area in the low Re case is considerably larger and the peak values are lower. Also, unlike the high Re case, the negative region not only occupies most of the third quadrant but also the fourth quadrant, with the contour line of $R_{\lambda_{ci}\phi'} = 0$ inclined at approximately 30-degree with respect to the x direction.

2.6.2 Linear stochastic estimation

One useful tool to interpret spatial correlation data is linear stochastic estimation, in which conditional averages are calculated from measured correlation fields (Adrian, 1994; Olsen and Dutton, 2002, 2003). Although conditional averages can be calculated directly from an experiment dataset, this requires either a very large ensemble size or averaging over a large flow region instead of a particular location in the flow, due to the low population density of the vortices. Derived directly from the two point spatial correlation, LSE can give the typical underlying flow structures more precisely with a smaller ensemble size.

Letting $\lambda_{ci}(X, Y)$ be the swirling strength value at location (X, Y) , the linear stochastic estimate of the velocity fluctuation $u'_i(x, y)$ over the entire field given the condition $\lambda_{ci}(X, Y)$ is,

$$\langle u'_i(x, y) | \lambda_{ci}(X, Y) \rangle \approx L_i \lambda_{ci}(X, Y) \quad (2.3)$$

The linear coefficient, L_i , can be determined in the following way,

$$L_i = \frac{\langle u'_i(x, y) \lambda_{ci}(X, Y) \rangle}{\langle \lambda_{ci}(X, Y) \lambda_{ci}(X, Y) \rangle} \quad (2.4)$$

, where $\langle u'_i(x, y) \lambda_{ci}(X, Y) \rangle$ is the (unnormalized) spatial correlation of u'_i and λ_{ci} .

As Christensen and Adrian (2001) argued, since the event of the conditional average is a single scalar value, the character of the conditionally average results remains the same for all values, just the magnitudes are simply amplified and attenuated. Thus, the thresholding of the λ_{ci} is not necessary for just examining the fluctuation field. But to see the real typical structure in the flow field, the estimated fluctuation fields need to be added with the mean field. Thus, the thresholding of the event will only change the size of the structure. Here we chose the event of $\lambda_{ci} = 2\lambda_{ci}^{rms}$ in order to get the features of typical structure in the flow.

Adding the mean field and subtracting $U(x_o)$ from each vector results in Fig. 2.23, which shows the typical velocity field of one vortex at different downstream locations. All the roller structures revealed by the linear scholastic estimation are spindle-shaped with a stream-wise major axis. The tilting of the major axis becomes much more visible here than in the spatial correlation fields. The high momentum of the jet pushes the upper part of the roller structure outwards, and the low momentum fluid was entrained inwards to the center of the jet by the lower part of the structure. In the near-field of the jet, there are two vortices seen adjacent to the vortex at the base point in both upstream and downstream direction. As the flow progresses downstream, the roller structures grow larger. Although the sizes of the vortex cores decrease, the large-scale coherent motions of the flow, which the swirling motions at the base point are part of, are indeed growing. Comparing the two Reynolds number case, the roller structures in $Re = 20K$ are larger than those in the $Re = 50K$ case.

2.7 Conclusions

A vortex identification method based on swirling strength was employed to analyze the properties of vortices in a confined rectangular jet. Experimental data from simultaneous PIV/PLIF experiments and high speed PIV experiments were used in this analysis. Swirling strength fields were computed from velocity fields, and then filtered with a universal threshold of $|\Lambda_{ci}| \geq 1.5\Lambda_{ci}^{rms}$. By identifying clusters of filtered Λ_{ci} , vortex structures were identified.

Instantaneous swirling strength field data indicate that positively (counterclockwise) rotat-

ing vortices are dominant on the left side of the jet and negatively (clockwise) rotating vortices are dominant on the right side. The population density, average size and strength, deviation velocity of vortices were calculated and analyzed, in both the cross-stream direction and the streamwise direction. In the region close to the channel inlet, the population density, average size and strength all show high values on both sides of the center stream. There are some counter-rotating vortices next to the dominant direction vortices, that are indicative of a wake region formed downstream of the splitter plate tips by the boundary layers that form on both sides of the splitter plates. At the further downstream location, $X/d = 3.5$, the wake disappears, as do most of the counter-rotating vortices. As the flow develops towards channel flow at the farthest downstream locations, the distribution of the vortices spreads throughout the entire reactor. The mean size and strength of the vortices decrease continuously downstream from the channel inlet. The mean vortex deviation velocity in both the X and Y directions are zero at the location of the population density peak. The signs of vortex deviation velocity V indicate the vortices move from the high vortex population regions to the low vortex population regions. The signs of mean deviation velocity U are negative on the side near the jet center, and positive on the side of near center of the outer stream, which indicates vortices transfer low momentum fluid to high velocity regions and transfer high momentum fluid to the low velocity regions.

The development trends of vortex size and strength were also identified by tracking vortices using high speed PIV experimental data. Both the average tracked vortex strength and size decrease with increasing downstream distance overall. However the average tracked vortex size increases before it starts to decrease in the area close to the jet inlet.

Two point spatial cross-correlations of swirling strength with velocity fluctuations and concentration fluctuations were calculated at the location of the left peak of turbulent kinetic energy. The cross correlation fields of swirling strength and fluctuations of the two velocity components exhibit a “butterfly” like shape. The right wing of $R_{\lambda u'}$ contains positive values and the left wing contains negative values. The axis of $R_{\lambda u'}$, the contour line of $R_{\lambda u'} = 0$, is oriented vertically in the streamwise direction, slightly tilted toward the outer stream. With increasing

downstream distance, the angle of orientation of the $R_{\lambda u'}$ axis becomes smaller. Also at the $X/d = 1.0$ downstream locations for both Reynolds number cases, there are a weak negatively correlated regions upstream of the strong positively correlated region close to the basis point and a weak positively correlated region downstream of the strong negatively correlated region in $R_{\lambda v'}$. This indicates that a vortex at the basis point is usually accompanied by at least one counter-rotating vortex. The axis of $R_{\lambda v'}$ is aligned with the cross-stream direction with negative values downstream of the basis point and positive values upstream of the basis point. There are also two correlated areas in the $R_{\lambda \phi'}$ correlation field; one positively correlated region downstream of the basis point and one negative upstream of the basis point, indicating that the positively rotating vortices bring high concentration field from the center stream to the side stream downstream of the vortex core and bring the low concentration field from the side stream to the center stream upstream of the core. Finally, linear stochastic estimation was used to calculate conditional structures. The estimation was based on the swirling strength values at chosen locations in the flow. The large-scale structures in the velocity field revealed by linear stochastic estimation are spindle-shaped with a titling stream-wise major axis.

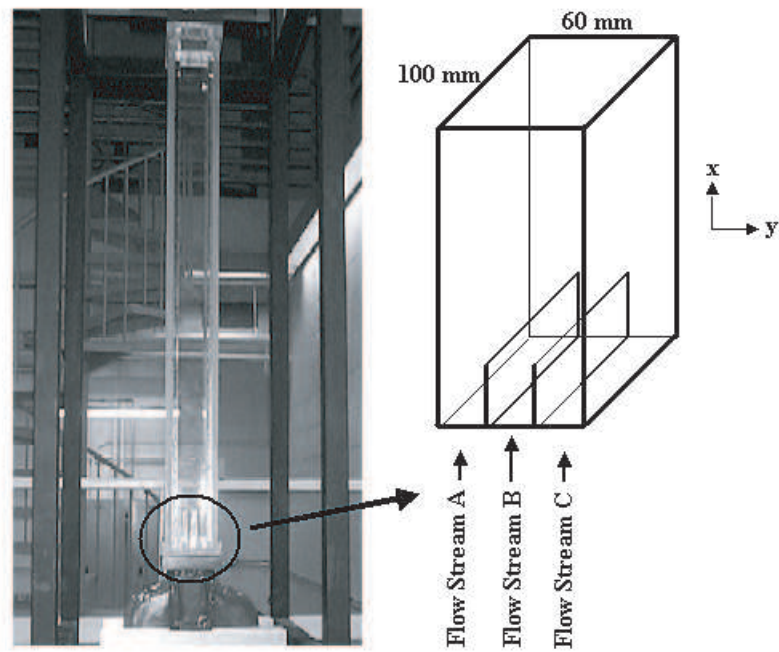


Figure 2.1 Photograph and schematic of the confined planar jet test section

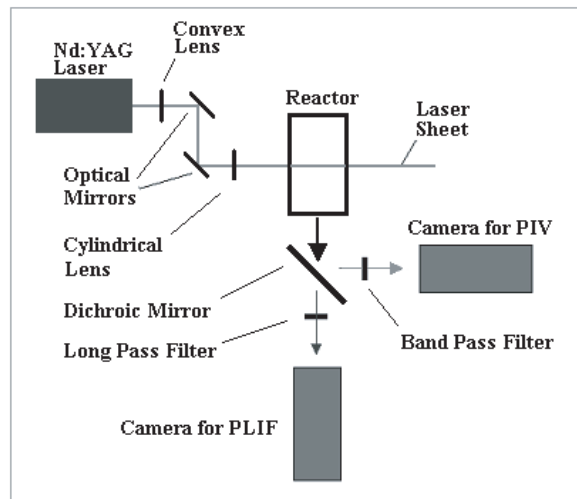


Figure 2.2 Schematic of the optical setup for the combined PIV and PLIF experiments

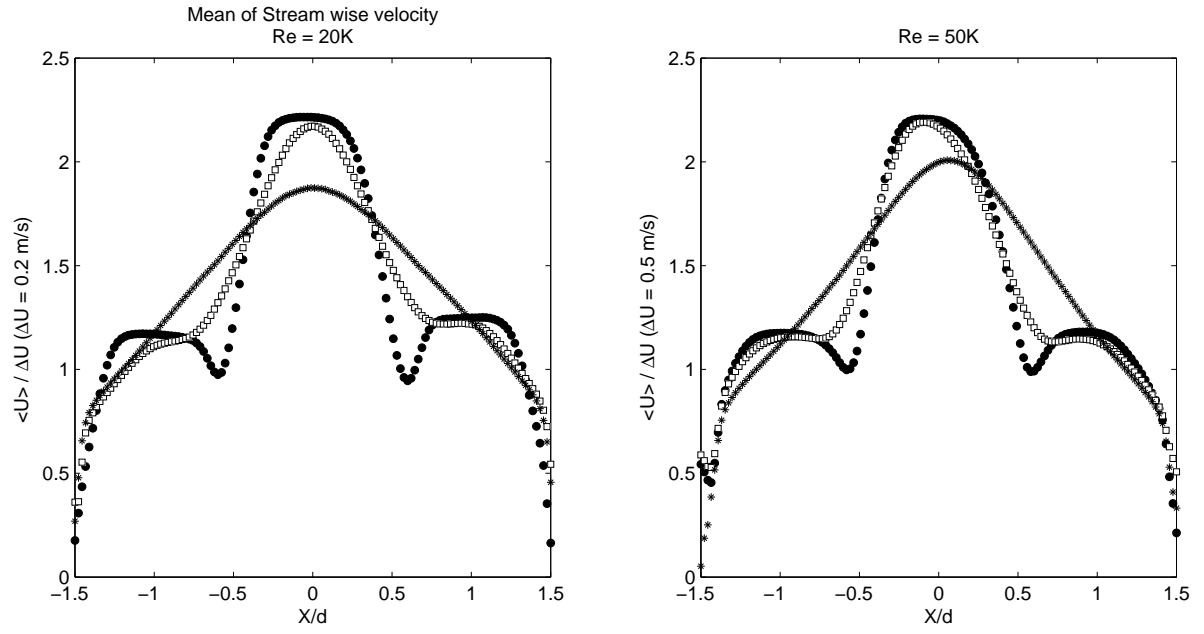
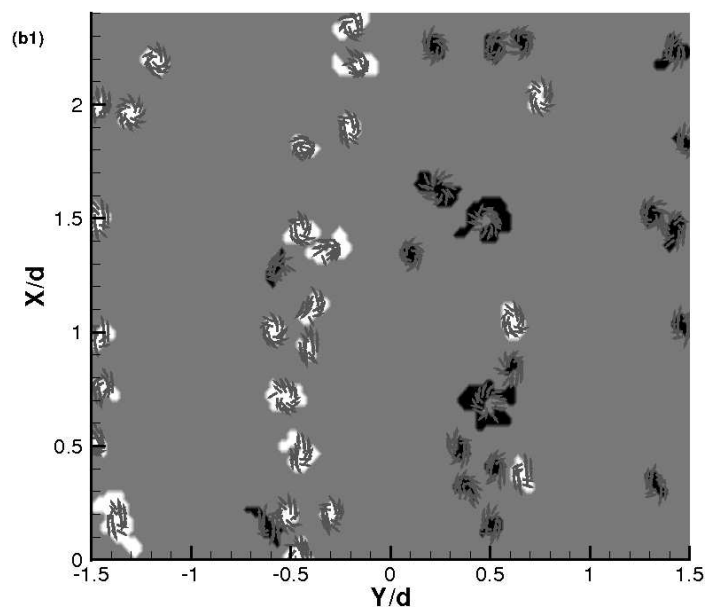
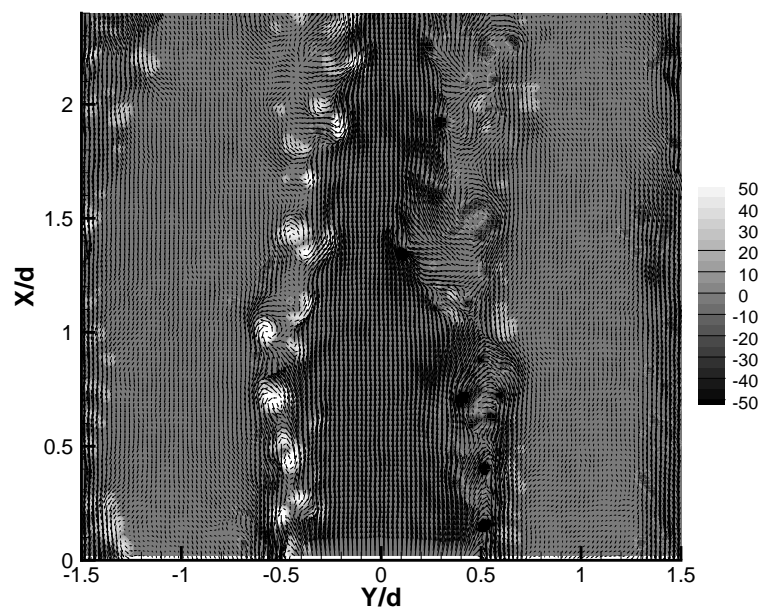


Figure 2.3 The mean of streamwise velocity. \bullet : $X/d = 1$, \square : $X/d = 4.5$, $*$: $X/d = 15$.



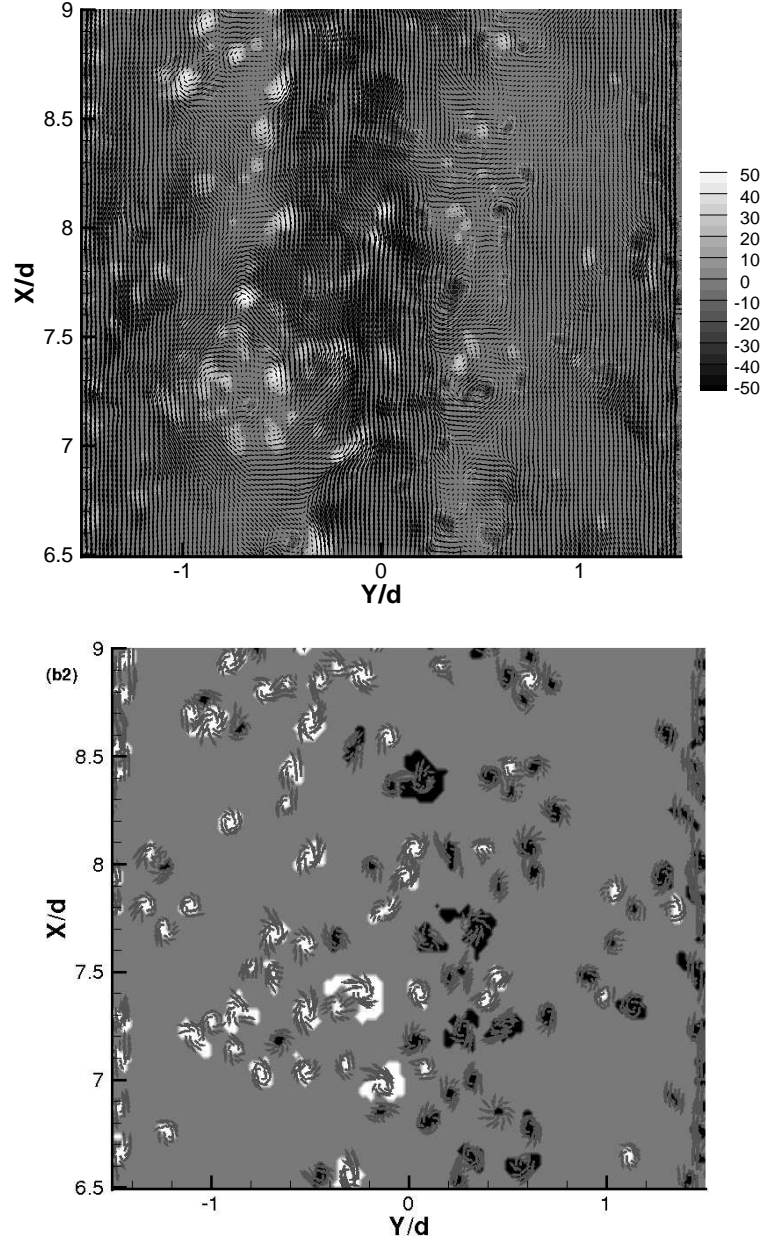


Figure 2.4 Example of vortex identification in an instantaneous PIV velocity field in near-field $0 < X/d < 2.5$ and far-field $6.5 < X/d < 9$ of the jet, at $Re = 20K$. (a) The Galilean decomposition of this instantaneous velocity field with $0.7U_c$, where U_c is the mean velocity of the center stream at each X location. (b) Local Galilean decomposition of vortices with the velocity at each vortex core. The contours of $\Lambda_{ci} = 1.5\Lambda_{ci}^{rms}$ are also shown in the background of the figure (a) and (b).

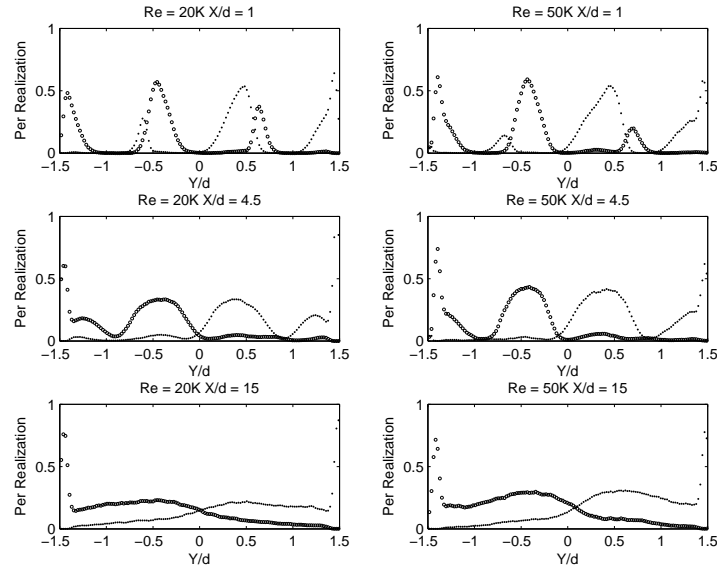


Figure 2.5 Local vortex population density of positively and negatively rotating vortices at different streamwise locations. \circ : positively rotating vortices, \bullet : negatively rotating vortices.

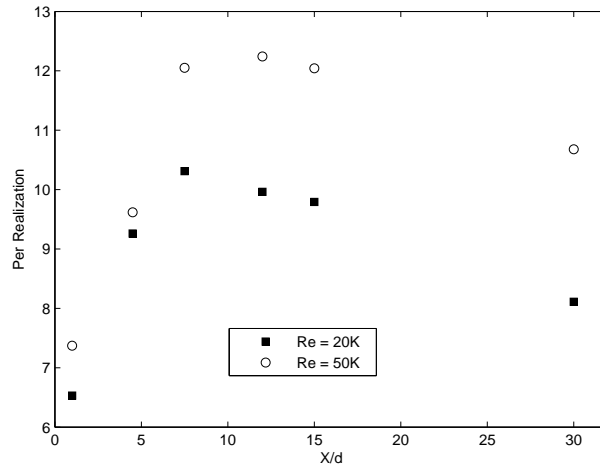


Figure 2.6 Mean populations of positively rotating vortex in the half jet width (1cm) streamwise long region between the centers of the center of center stream ($Y/d = 0$) and the center of left side stream ($Y/d = -1$). \circ : $Re = 50K$, \blacksquare : $Re = 20K$.

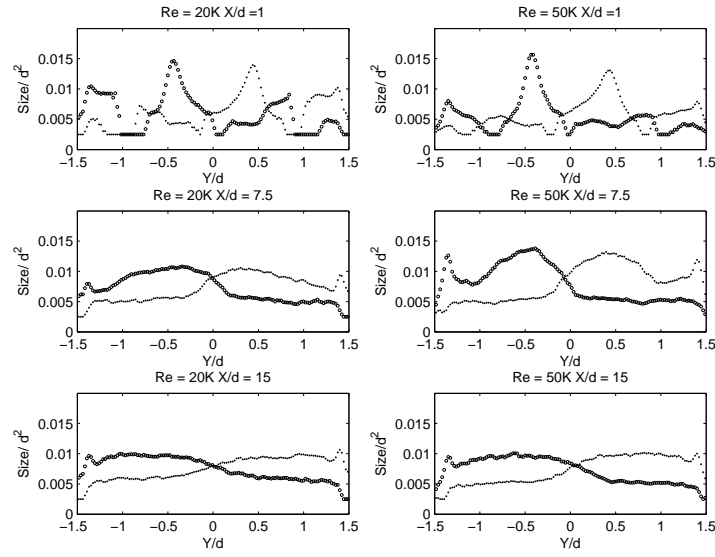


Figure 2.7 Profiles of the size of vortex cores. \circ : positively rotating vortices, \bullet : negatively rotating vortices.

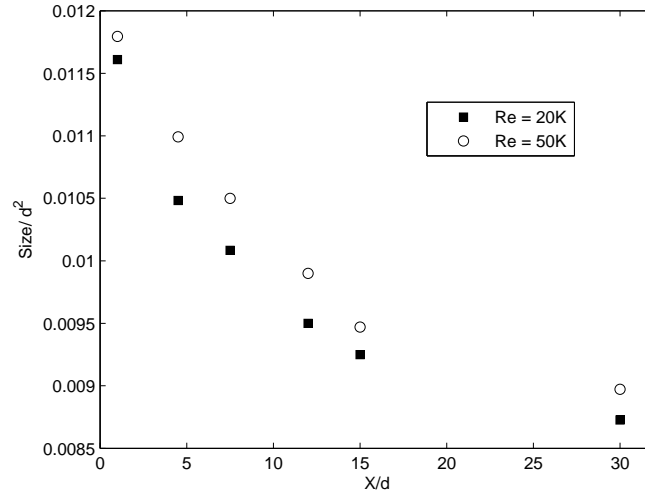


Figure 2.8 Mean vortex size in the half jet width (1cm) streamwise long region between the centers of the center of center stream ($Y/d = 0$) and the center of left side stream ($Y/d = -1$). \circ : $\text{Re} = 50\text{K}$, \blacksquare : $\text{Re} = 20\text{K}$.

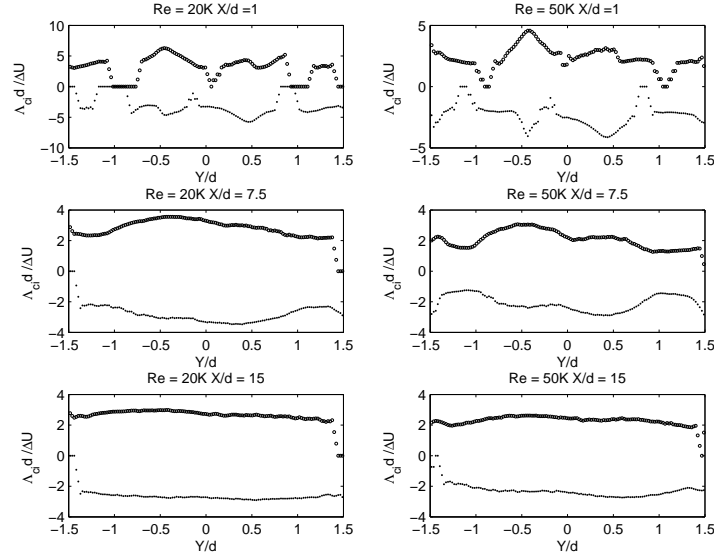


Figure 2.9 Profiles of the peak swirling strength value of vortex cores. \circ : positively rotating vortices, \cdot : negatively rotating vortices.

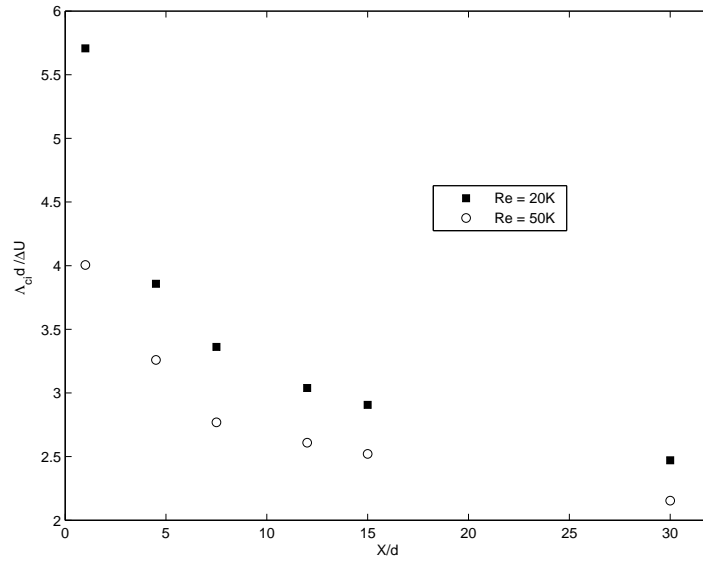


Figure 2.10 Mean the peak swirling strength value of the vortex cores in a half jet width (1cm) streamwise long region between the centers of the center of center stream ($Y/d=0$) and the center of left side stream ($Y/d=-1$). \circ : $Re = 50K$, \blacksquare : $Re = 20K$.

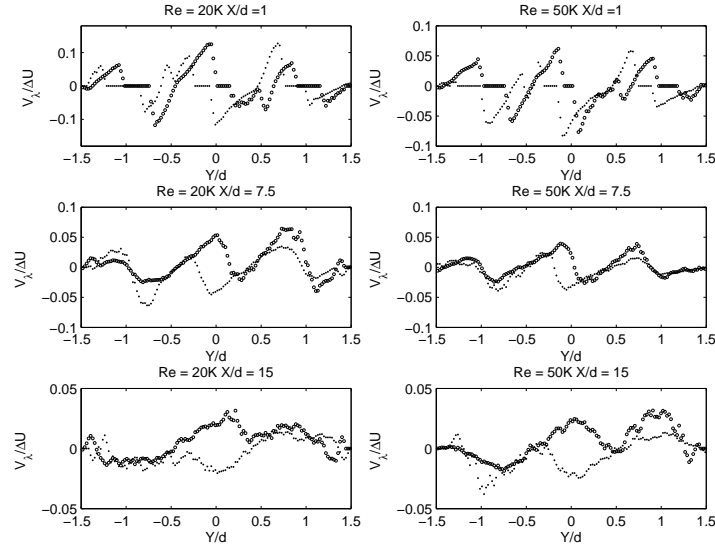


Figure 2.11 Vortex deviation velocity in the cross-stream direction. \circ : positively rotating vortices, \cdot : negatively rotating vortices.

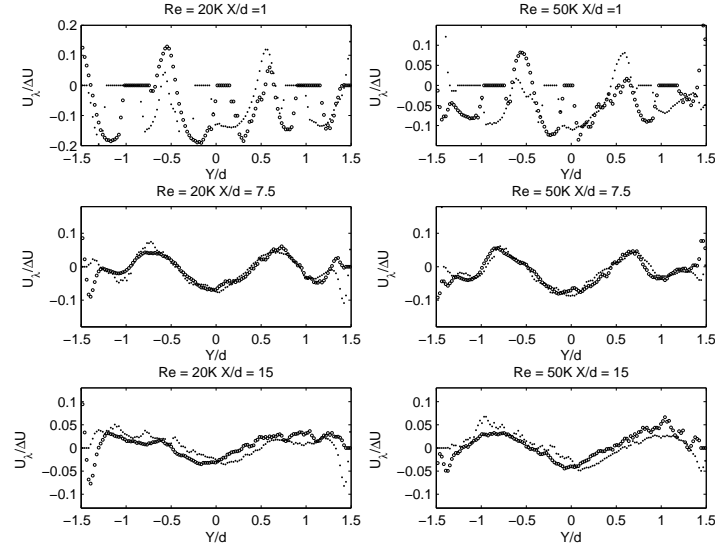


Figure 2.12 Vortex deviation velocity in the streamwise direction. \circ : positively rotating vortices, \cdot : negatively rotating vortices.

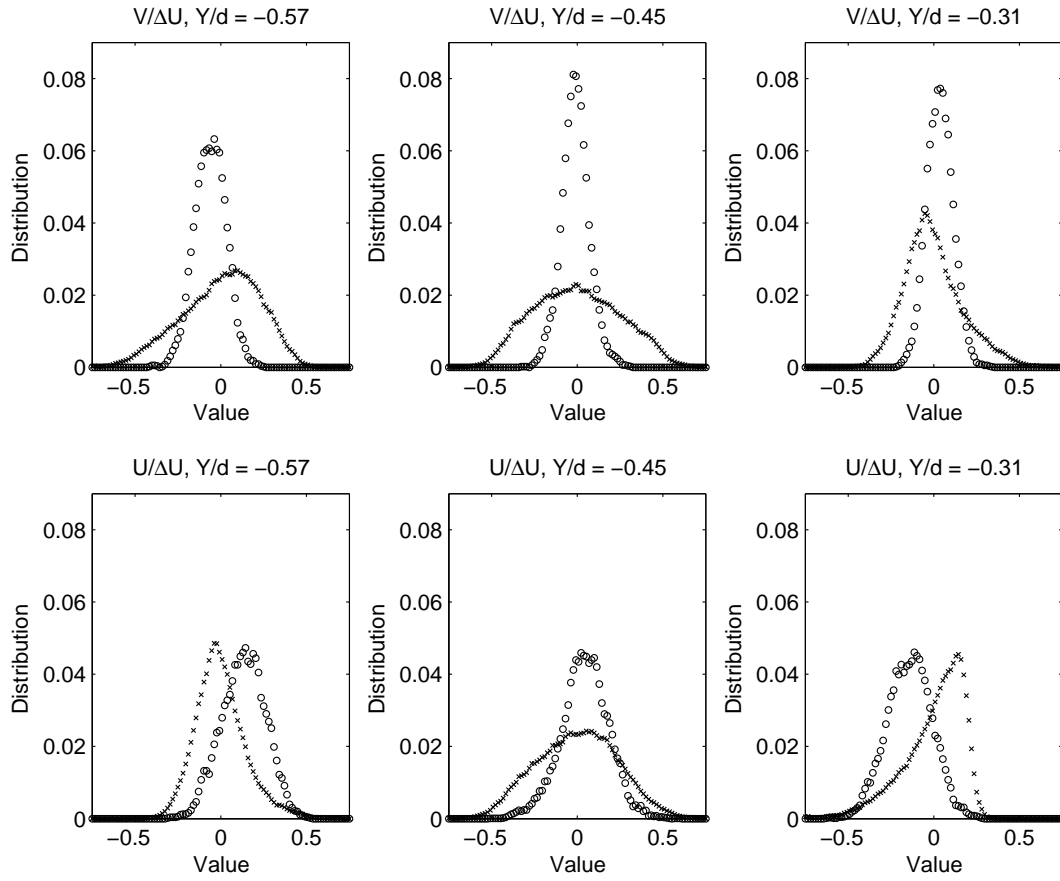


Figure 2.13 Vortex deviation velocity distribution, at $X/d = 1$, $Re = 20K$.
 X: velocity fluctuation distribution, \circ : vortex deviation velocity distribution.

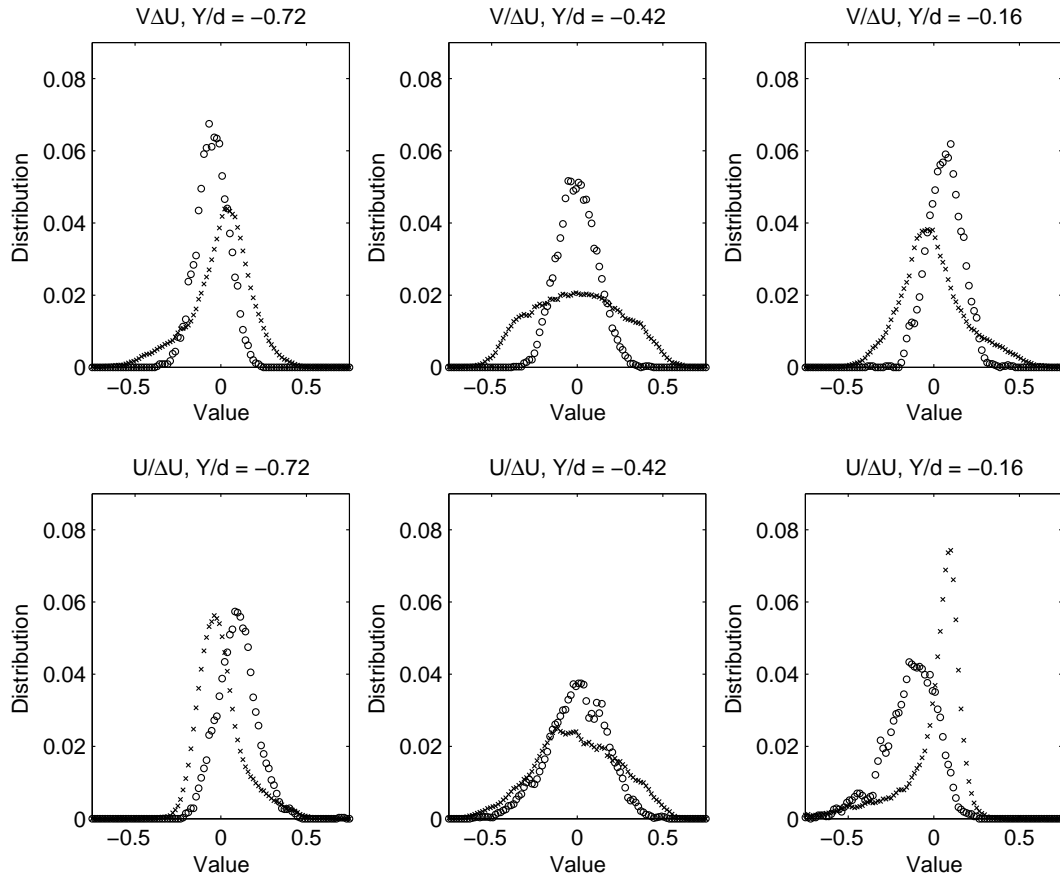


Figure 2.14 Vortex deviation velocity distribution, at $X/d = 4.5$, $Re = 20K$. X: velocity fluctuation distribution, \circ : vortex deviation velocity distribution.

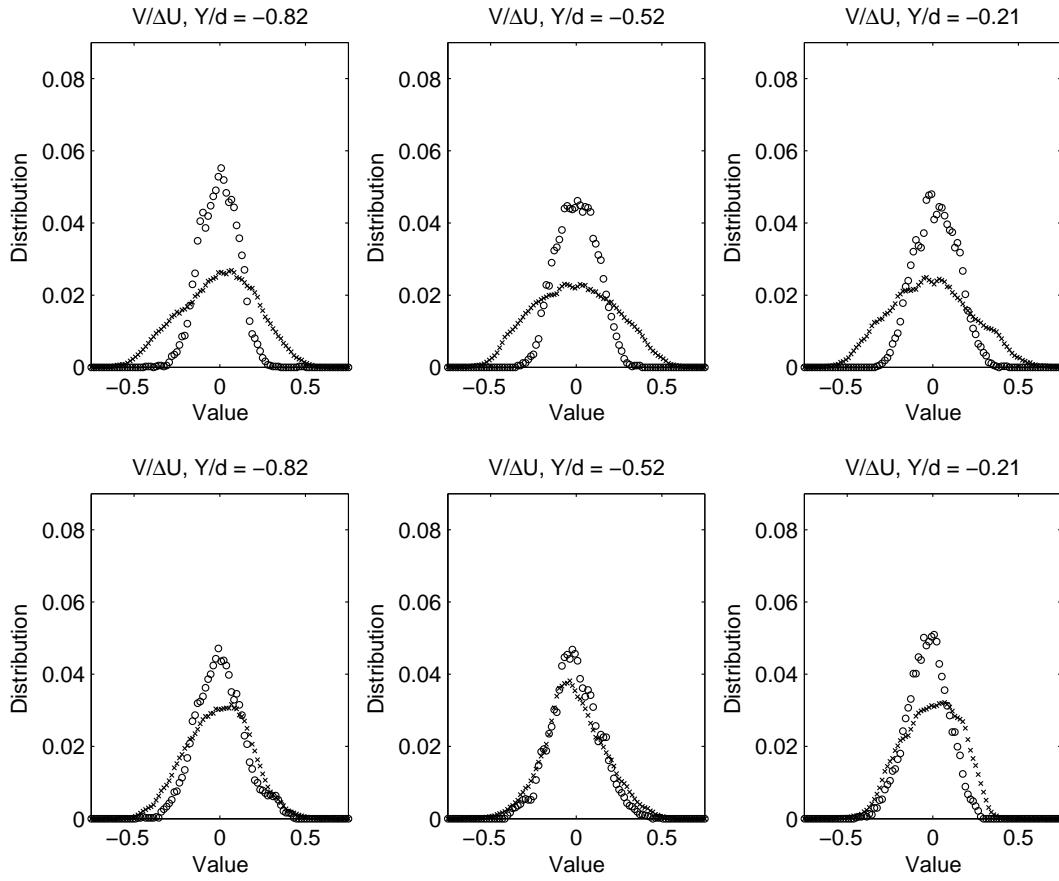


Figure 2.15 Vortex deviation velocity distribution, at $X/d = 15$, $Re = 20K$. X: velocity fluctuation distribution, \bigcirc : vortex deviation velocity distribution.

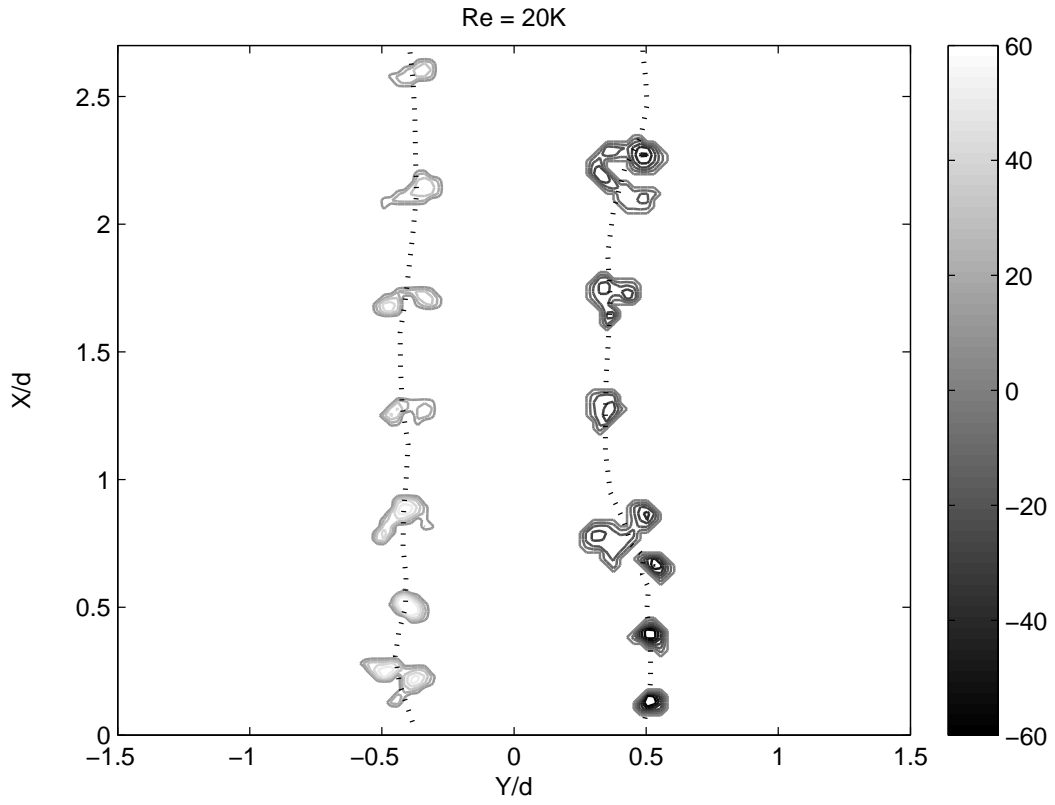


Figure 2.16 The trajectories of a positively rotating vortex and a negatively rotating vortex, at the jet outlet, $Re = 20K$. The background contours are the plots of the swirling strength clusters at several different time steps.

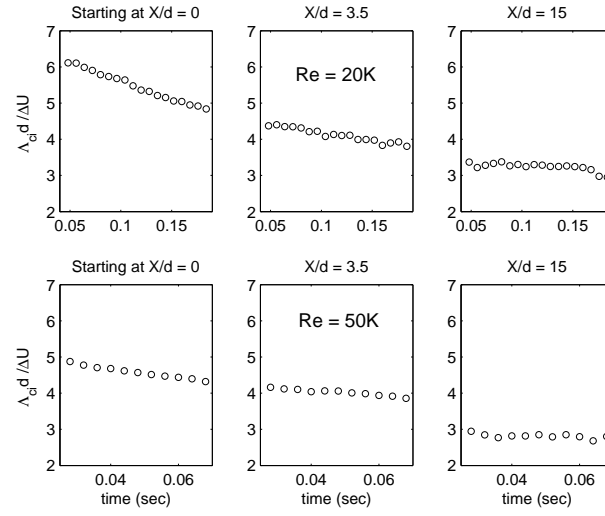


Figure 2.17 The mean tracked vortex maximum strength starting at three different downstream locations.

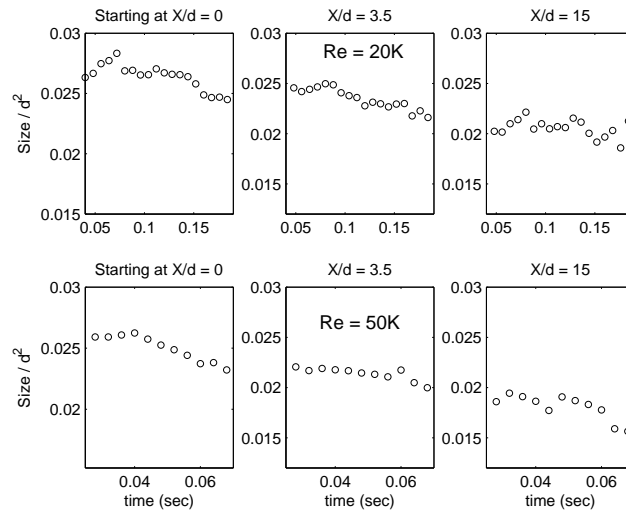


Figure 2.18 The mean tracked vortex size starting at three different downstream locations.

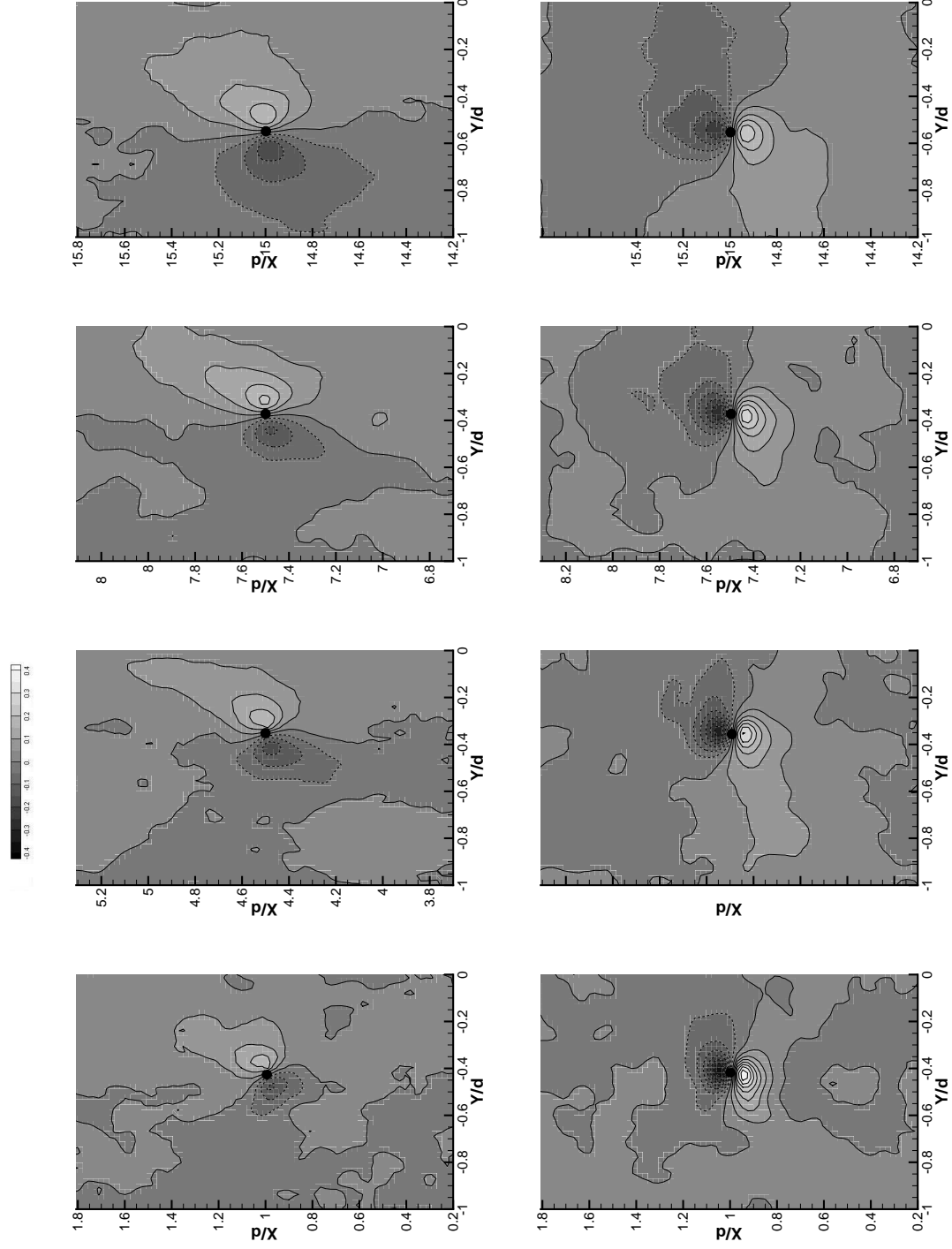
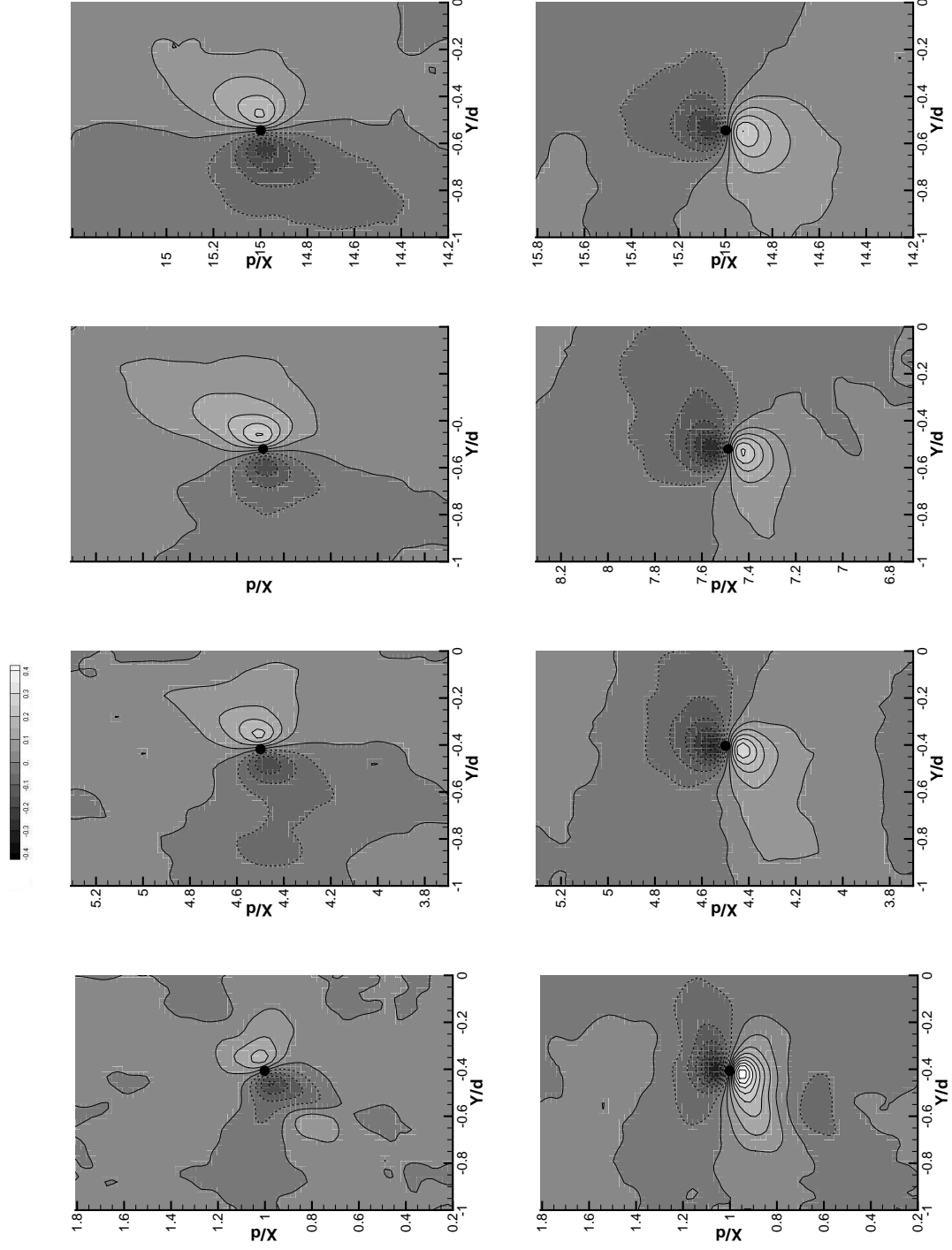


Figure 2.19 Two-point cross correlation $R_{\lambda_{ci}u'}$ (first row), $R_{\lambda_{ci}v'}$ (second row). At $X/d = 1$, $X/d = 4.5$, $X/d = 7.5$ and $X/d = 15$, $Re = 50K$. The black dot indicates the location of swirling strength basis point.

Figure 2.20 As Fig. 2.19 but at $Re = 20K$.

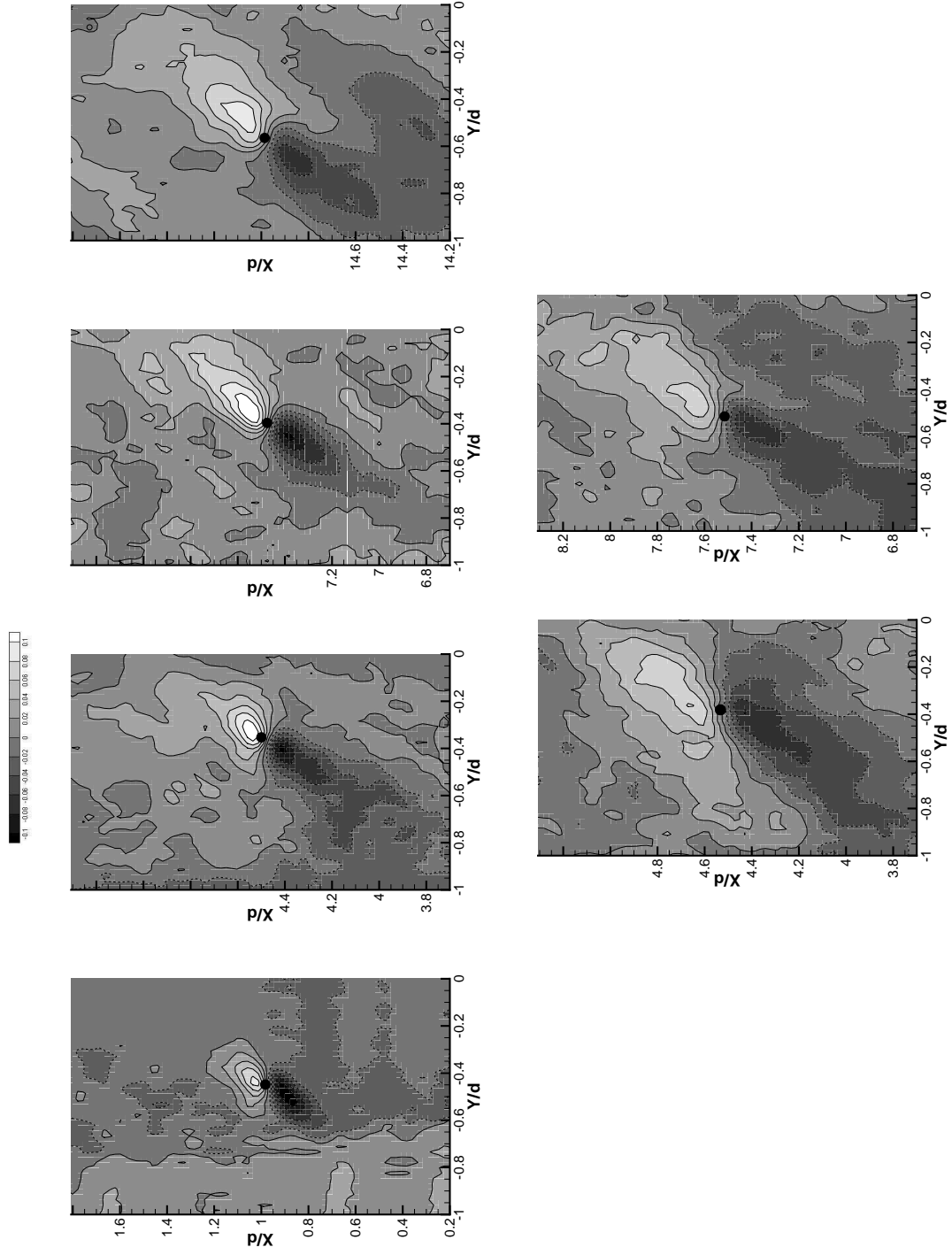


Figure 2.21 Two-point cross-correlation $R_{\lambda_{ci}\phi'}$. At $X/d=1$, $X/d = 4.5$, $X/d = 7.5$ and $X/d = 15$, for $Re = 50K$ (first row) and at $X/d = 4.5$, $X/d = 7.5$, for $Re=20K$ (second row).

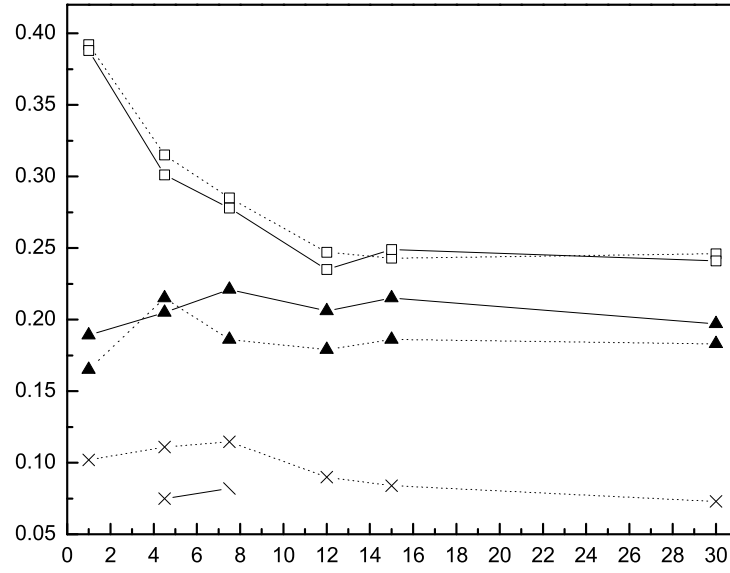


Figure 2.22 Average of positive and negative peak values of cross correlations. (\square , $R_{\lambda u'}$; \triangle , $R_{\lambda v'}$; \times , $R_{\lambda \phi'}$; —, $Re = 20K$; ..., $Re = 50K$)

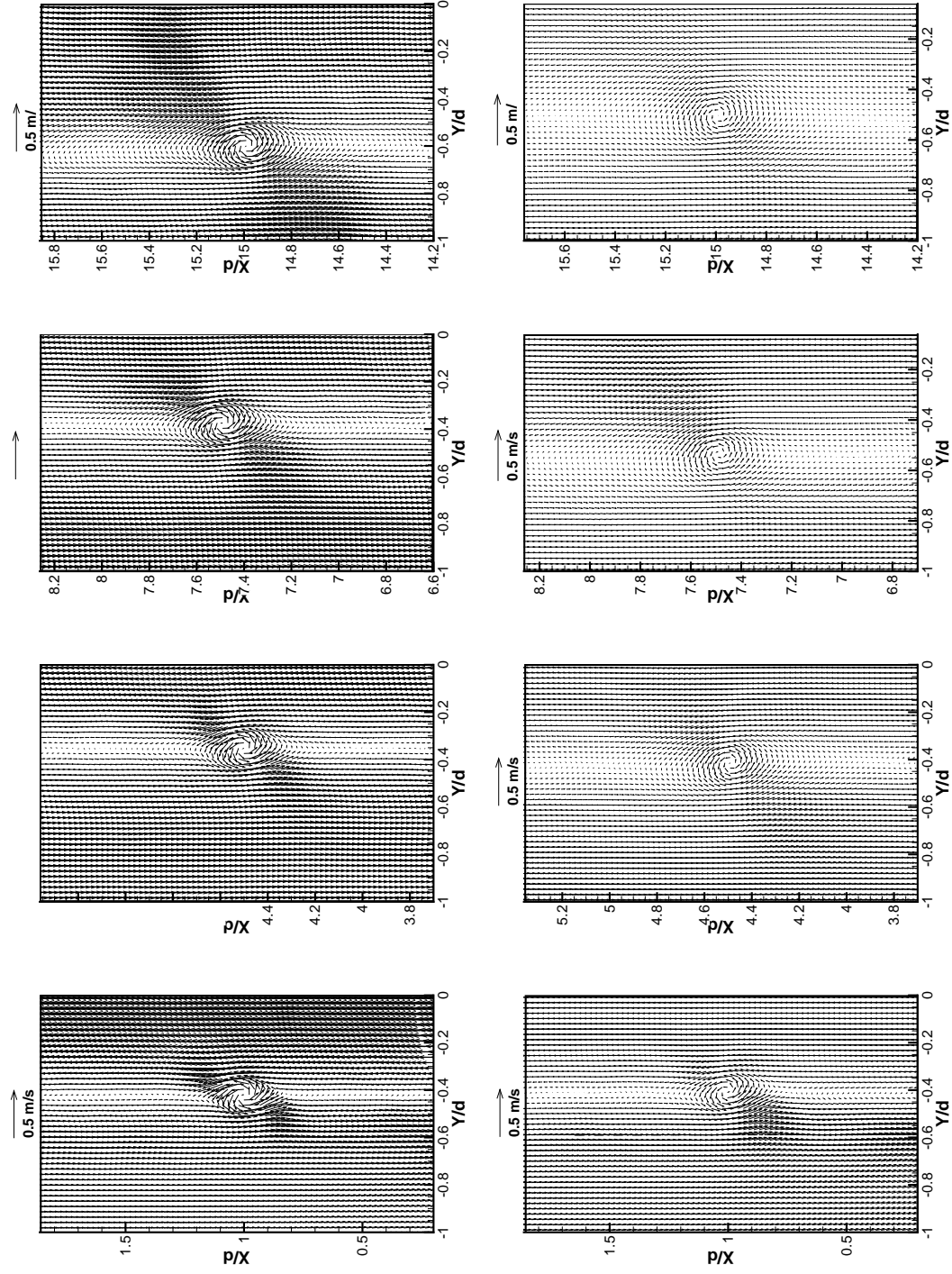


Figure 2.23 Linear stochastic estimation of velocity field with $U(x_o)$ subtracted from each vector. At $x/d=1.5, x/d=4.5, x/d=7.5$ and $x/d=15$, $Re=50K$ (first row), $Re=20K$ (second row).

CHAPTER 3. Study of Coherent Structures in a Confined Rectangular Wake

A paper submitted to Experimental Thermal and Fluid Science

Bo Kong, Michael G. Olsen, James C. Hill and Rodney O. Fox

Abstract

Vortex behavior and characteristics in a confined rectangular wake were examined using swirling strength as a defining characteristic of a vortex. Instantaneous swirling strength field shows that positively (counterclockwise) rotating vortices are dominant on the right side of the wake and negatively (clockwise) rotating vortices are dominant on the left side. The population density, average size and strength of vortex cores all shows high peak values both sides of the wakes, while these peaks decrease quickly and the profiles broaden as the flow progresses downstream. The changing of vortex core maximum strength is seen relatively faster than the change of the core size. The results of mean cross-stream wise deviation velocity of vortex core shows the vortices in the wake spread from the neighborhood of wake to the centers of the free stream, and the mean streamwise deviation velocity indicates that vortices bringing high momentum fluid of the free stream into the the wake. Two point spatial cross-correlations of swirling strength with velocity fluctuations and concentration fluctuations were also calculated. All the cross correlation fields shown here exhibit a “butterfly” like shape, with one “wing” with positive correlation values and the other “wing” with negative values. The axes of correlation fields are oriented in the streamwise direction in $R_{\lambda u'}$ contours, and they tile towards the wake center on the both sides of the wake, while the axes in $R_{\lambda v'}$ are oriented in the cross-stream direction, and they tile downstream on the both sides of the wake. The

$R_{\lambda_{ci}\phi'}$ results show some similarity to those of $R_{\lambda_{v'}}$, indicating the vortices play a similar role in mass transfer as in momentum transfer. Linear stochastic estimation was used to interpret the cross correlation result and visualize the underlining large scale coherent structures. The LSE results show a clear vortex street pattern in far fields of the wake, indicating the vortices, developed independently on both sides of the splitter plates, are reorganized and coherent as the flow develops downstream.

3.1 Introduction

Turbulent shear flows (e.g., wakes, jets and mixing layers) are commonly seen in many engineering applications involving with fluid flows. The coherent structures in these shear flows play key roles due to the structures' significant contribution to noise generation, drag, fluid entrainment and the transfer of mass, momentum and heat. For this reason, the study of coherent structures in turbulent shear flows has long been the focus of the a lot of fluid dynamics researchers. However, the detailed study of properties of these structures, such as population, size, circulation, and energy, is still lacking, which can be useful in the understanding of turbulence and property transport and can aid in the development of more efficient and more environmentally benign applications. Moreover, with increasing feasibility and popularity computer modeling techniques, such as large eddy simulation, where the largest scales of the turbulence are resolved, detailed measurements of the behavior and characteristics of large-scale structures can be used to validate these computation methods on a different perspective. The primary objective of the work presented here is to use a vortex identification method to analyze the experimental data collected in a liquid-phase turbulent confined, rectangular wake with regards to the population, size, kinematics and characteristics of vortices within this wake flow.

Wake flows generated by two-dimensional bluff bodies have been the focus of many fluid researchers since early 1900's. There are some detailed review and bibliography on this type of flow, like Berger and Wille (1972) , Oertel Jr (1990) and Roshko (1993) . The coherent structures in wake flows, like von *Kármán* vortex street, are among the most recognized

structures in fluid flows. Due to its engineering significance and the simplicity in setting up such an arrangement in an experimental or computational laboratory, in the case of the circular cylinder wake alone, there have been literally hundreds of papers published (Williamson, 1996). For example, Cantwell and Coles (Cantwell and Coles, 1983) investigated transport processes in the near wake of a circular cylinder using an X-array of hot wire probes for a Reynolds number of 140,000. Ong and Wallace (Ong and Wallace, 1996) also conducted hot-wire measurements in the wake of a circular cylinder at a Reynolds number of 3900. They noticed that measurements of the streamwise velocity component were inaccurate for such flow fields and the near wake region was pre-dominantly 2-dimensional. Using rectangular and square cylinders as wake generators are also common in wake studies. With laser Doppler velocimetry (LDV), Nakagawa et al. (Nakagawa et al., 1999) measured the unsteady turbulent near wake of a rectangular cylinder in channel flow and found that the turbulent intensities on the centerline of the channel reached their maxima near the rear stagnation point of the recirculation region. Also there are some studies done on the wakes generated by a flat plate normal to the streamwise direction, which is characterized by fixed separation points at the edge of the plate. Najjar and Balachandar (Najjar and Balachandar, 1998) conducted a numerical simulation of a $Re=250$ wake after a normal flat plate and found that except the frequency of the prime vortex shedding, there is a nearly 10 time lower frequency unsteadiness in the wake.

The bluff bodies, like those mention above, educe flow separation behind them when Reynolds number is high enough, which is one of the key issues in most the previous wake studies. However, in chemical engineering applications, the improvement of turbulent mixing and reaction is the main subject, while flow separation is not commonly seen. The wake generated by a flat plate parallel to the streamwise direction, or so called “splitter-plate flows” (Williamson, 1996), can be considered as the simplest form of wake, which is characterized by the absence of a wake producing blunt body with the inevitable local separation and large pressure gradients (Ali and Ibrahim, 1996). This form of wake flow is of great interest to the study of the turbulent mixing process instead of the drag or lift force produced by the flow separation, such as the mixing of reactants in chemical processing. The wake is formed by the

meeting of two boundary layers at the tip of the splitter plate, which are developed on the two side of the plate. Taneda conducted a series studies on the wake behind a flat plate using photograph of wake and hot-wire speed meter. In Taneda (1956), he found that for the pure laminar case, the wake begins to oscillate sinusoidally some distance downstream at about $Re = 700$ (Re is UL/ν , where L is the length of the plate). Later he also found that not only laminar wakes but also turbulent wakes show a strong tendency to form von *Kármán* vortex street Taneda (1958). Another experimental study conducted by Sato and Kuriki (Sato and Kuriki, 1961) was made of the laminar-turbulent transition of a wake behind a thin flat plate which was placed parallel to a uniform flow at subsonic speeds. They also observed that a sinusoidal velocity fluctuation which is axisymmetrical with respect to the centre-line of the wake, and the frequency of fluctuation is proportional to the $\frac{2}{3}$ power of the free-stream velocity, and the amplitude increases exponentially in the direction of flow. When the wake reach turbulent, velocity fluctuations in the non-linear region are still sinusoidal and two-dimensional, but the growth rate deviates from being exponential due to non-linear effects. There are also some analytical instability studies of laminar wake behind flat plate, like Papageorgiou and Smith (1988, 1989). Overall, most of the previous studies were focused on laminar cases. However, the most of the flows in chemical mixers/reactors are turbulent, and the behavior of turbulent vortices in the wake of a flat plate parallel to the streamwise direction remain relatively rare.

A lot of the earlier studies were conducted using some flow visualization techniques or point-wise velocity measurements, such as hot-wire or LDV. In the past two decades, particle image velocitometry (PIV) has become a popular experimental technique for turbulence studies, which is well suited for visualizing and identifying vortical structures, since it provides instantaneous two-dimensional velocity field data . Methods of analyzing and interpreting these spatially resolved velocity field data were discussed in Adrian (1999) and Adrian et al. (2000a). Prime examples of using PIV to study coherent structure are provided by Christensen and Adrian (2001, 2002b,a) in the turbulent boundary layers , Agrawal and Prasad (2002a,b, 2003) in turbulent axisymmetric jets, and also Huang et al. (2006); Perrin et al. (2007); Kim et al. (2004) in wake flow behind a circular cylinder. These scefucessful studies shows the virtue of

PIV technique on coherent structure research. Confined with planar laser induced fluorescence (PLIF), simultaneously measurement of velocity and spicity concentration can be achieved , which has already been proven to be a powerful tool to study the turbulent mixing, such as Westerweel et al. (2005, 2002) in a turbulent jet. . In the current study, the simultaneous PIV/PLIF technique was used in order to study the role of coherent structures in turbulent mixing.

With increasing popularity of PIV techniques, many methods have been proposed and implemented to extracting turbulence information and identify vortices in instantaneous two-dimensional velocity fields, such as those obtained by PIV. One of the prime review on the topic is Adrian et al. (2000a), in which a number of vortex eduction techniques were described and compared on their effectiveness in identifying vortices. They concluded that swirling strength provides a reliable means of extracting the small-scale vortices, including those which are not visible in velocity decompositions. Vollmers (2001) also validated and compared several coherent structure eduction methods. A similar conclusion was reached in his work, which is the swirling strength is the best indicator for the presence of vortices in turbulent flow. The concept of swirling strength, λ_{ci} , was introduced by Adrian (1999); Wu and Christensen (2006) as the imaginary part of the complex conjugate eigenvalues ($\lambda_{cr} \pm \lambda_{ci}$) of the local velocity gradient tensor. The physical meaning of λ_{ci}^{-1} is the period required for a fluid particle to swirl once about the λ_{cr} -axis (Piomelli et al., 1996; Adrian, 1999). Therefore, a non-zero λ_{ci} indicates a local swirling motion, and spatially connected regions of non-zero λ_{ci} represent vortices (Wu and Christensen, 2006). In a two-dimensional flow field, vortices can either positive or negative in the direction normal to two-dimension plane, while the value of λ_{ci} is always be positive by nature, which is inadequate to distinguish the difference. The problem can be solved by multiplying λ_{ci} the sign of the local vorticity to capture the direction of rotation at each location in the flow field, which was proposed by Tomkins and Adrian (2003) . The first advantage of this method is that it is frame independent, meaning the information bulk motion of flow field where the vortex is embedded is not necessary. Also, it only reveals the regions with vortices, which means the flow regions with high vorticity but no local swirling motion, such

as shear layers, do not produce non-zero λ_{ci} . Due to the sensitivity of velocity gradient to noise, vortex extraction methods based on the velocity gradient are often not applicable to experimental data if no smoothing has been applied (Vollmers, 2001), since the method may falsely identify measurement noise as vortices. As (Wu and Christensen, 2006) suggested, in addition to carefully choosing experiment parameters to reduce the measurement uncertainty and applying slight smoothing, a filter with a threshold of $|\Lambda_{ci}| \geq 1.5\Lambda_{ci}^{rms}$ was applied to each instantaneous swirling strength field to limit the influence of experiment noise. A similar study on vortices in a confined rectangular jet with a co-flow used this technique was conducted earlier by the authors, thus more detailed implementation of the technique can be found in Kong et al. (2010).

The remainder of the paper is organized as follows. In Section 2, the rectangular-wake flow facility and the experimental methodology are introduced and Section 3 discusses the properties of vortices in the wake. Then section 4 gives the spatial correlation and linear stochastic estimation results. A summary of results and conclusions is given in Section 5.

3.2 Experimental Facility and Methodology

The experimental data used in the current study was collected by Feng and published in Feng et al. (2010). The following is a brief description of the flow facility and experiment setups, and more detailed information can be found in Feng et al. (2010). The flow facility used in the experiments presented here is shown in Fig. 3.1. The test section in which the measurements were performed was made of Plexiglas, with a rectangular cross-section measuring 60 mm by 100 mm and with an overall length of 1 m. Three flow streams entering the test section were separated by two splitter plates, after passing through its own flow conditioning section consisting of a packed bed and turbulence reducing screens and a 16:1 contraction section. The slope of the surface of the splitter plates is 3 degrees along the side channels and 1 degree along the center channel, and the thickness of the tips of the splitter plates are less than 0.5 mm. Although the splitter plates used in the current study is not ideal flat plate perfectly parallel to the streamwise direction, it provides the same cross-section area for three streams and a

smooth connection between the flow conditioning section and the test section. The volumetric flow rate of each stream was 1.0 l/s, corresponding to a mean velocity of 0.5 m/s. The Reynolds number of this wake flow was 37,500, based on the area-averaged velocity and the hydraulic diameter of the test section.

In the simultaneous PIV/PLIF measurements, a New Wave Research Gemini PIV laser was used to produce a 0.5 mm thick laser sheet, which passes through the centerline of the test section in the z -direction. Approximately 24 grams of hollow glass spheres were added to the water reservoir with total volume of 3500 liters in PIV measurements. The nominal diameter of the seed particles was $11.7 \mu\text{m}$ and the density of the particles was 1.1 g/cm^3 . In the PLIF measurements, Rhodamine 6G was used as fluorescence dye, and added to the water reservoir feeding the center stream, while the other two streams were pure water. The concentration of the fluorescence dye in the center stream is $45 \mu\text{g/l}$. PIV and PLIF images were obtained using two 12-bit LaVision Flowmaster 3S CCD cameras. The image magnification of the two CCD cameras was 0.12, and the numerical aperture was 8 for PIV and 5.6 for PLIF. A dichroic mirror (Q545LP, Chroma Technology Corp.) was placed at an angle of 45° to the laser sheet to separate the light paths and direct them to either the PIV or the PLIF camera. The PLIF camera lens was filtered with a long-pass optical filter (E560LP, Chroma Technology Corp.), and the PIV camera lens was filtered with a narrow-band-pass optical filter (Z532/10X, Chroma Technology Corp.) A multi-pass cross-correlation technique with decreasing window sizes was used to compute the velocity field, and the final interrogation spot size is 16 pixels by 16 pixels. With 50% overlap between interrogation windows, the velocity vector spacing was 0.45 mm in both the x - and y -directions. The in-plane spatial resolution of the PLIF measurements in the present study was actually limited by the flow area imaged per pixel, which was approximately $56 \mu\text{m}$.

3.3 Vortex Characteristics Analysis

To assist in the understanding of the flow configuration of current investigation, the profiles of the mean and r.m.s. (root mean square) of streamwise velocity were given in Fig.

5.10 at 4 different downstream locations, $X/d=1, 4.5, 7.5$ and 12 . Just downstream of the splitter plate tips, at $X/d=1$, the mean streamwise velocity profile shows two wake regions appear just downstream of the tips of the splitter plates as the boundary layers on the splitter plate surfaces merge downstream of the tips. The profiles of rms streamwise velocity displays two peaks in each wake, which show that the high fluctuation peaks in the boundary layers on the walls of splitter plates remain distinct for some distance downstream of the splitter plate tip. The velocity deficit of the two wakes diminishes quickly at the further downstream locations. The two wake regions meet at $X/d=4.5$ near the channel centerline, as seen by the potential core in the center stream disappearing at this position. At the same time the two peaks of rms streamwise velocity become indistinct and only a single peak is observed in each wake. At $X/d=12$, the velocity profile starts to approach the velocity profile of a fully developed turbulent channel flow. More detailed experimental results, such as turbulent fluxes, turbulent viscosity and dissipative, and turbulent Schmidt number, can be found in in Feng et al. (2010) .

3.3.1 Instantaneous structures

The demonstration made in Kong et al. (2010) with the instantaneous swirling strength field in jet flow case showed that the effectiveness of using the swirling strength as a vortex identification method. In the present wake flow, a similar demonstration can be made, which is shown in Fig. 3.4, at near-field $0 < X/d < 2.5$ and $3.5 < X/d < 6$. The contours in Fig. 3.4 (a1,a2) are instantaneous swirling strength fields, which are filtered with a universal threshold of $|\Lambda_{ci}| \geq 1.5\Lambda_{ci}^{rms}$ and the obtained strength clusters are shown in Fig. 3.4 (b1,b2). Note that due to spatial resolution limitations, clusters of Λ_{ci} with fewer than three grid points across their span in both the x and y directions are not considered. The vectors in Fig. 3.4 (a1,a2) are the mean-bulk Galilean decomposed velocity field, which reveals only the vortices moving at their respective spatial convective velocities. And those in Fig. 3.4 (b1,b2) are the local Galilean decomposed velocity vectors, which means the local convective velocities have been subtracted from neighboring points around the vortex centers, which all display a clear

swirling motion. This shows again the swirling strength as a vortex identification method can work effectively in the present wake flow.

Also with Fig. 3.4, some observations can be made on these instantaneous vortices. As expected, on the right side of the both wakes, the positively (counterclockwise) rotating vortices are dominant, while negatively rotating vortices are dominant on the left side of the wakes. However the distribution of the vortices seems quite random and doesn't display as the large-scale structural array, like vortex street, which usually seen in wake flows. Besides the fact that the Reynolds number of the current wake flow is high, meaning the flow itself is quite turbulent, the vortices on both sides of the wake are less coherent, since they are the continuation of the vortices developed independently on both sides of the splitter plates. This is quite rare in commonly studied wake flows, where a flow with a uniform free stream velocity passes a obstacle. However, the type of wake flow is common in the engineering practices, where two flow streams meet together parallelly. The linear stochastic estimated velocity fields based on concentration fluctuation reported by Feng et al. (2010) actually shows the presence of the vortex street in the wakes indeed. As we argued in Kong et al. (2010), the large-scale coherent motions visualized by the correlation technique are not the swirling motions of the small-scale vortices in the individual instantaneous velocity field. And the swirling strength clusters here are the highly rotating part, the core of the vortices. In the other words, although the vortex cores detected by the swirling strength, those highly rotating fluid particles in the instantaneous flow fields seem random and incoherent, they are actually embedded in large scale coherent motions. Compare the two downstream locations, the vortices apparently spread towards the centers of three flow streams. Also notice that there are the positively (counterclockwise) rotating vortices on the left side wall, and negatively rotating vortices on the right side wall. However these vortices on the walls are not of the interest of the present study.

3.3.2 Vortex population

Fig. 3.5 shows $\Pi_{p(n)}$ cross-streamwise profiles at 4 downstream locations, $X/d=1, 4.5, 7.5$ and 12 . $\Pi_{p(n)}$ is herein defined as the local ensemble-averaged number of detectable positively

rotating or negatively rotating vortices whose centers reside at a given PIV grid node, the same definition used in Kong et al. (2010) and Wu and Christensen (2006) . The profiles in Fig. 3.5 are the average vortices numbers on one flow realization over a half stream width ($d/2 = 1cm$) long area in the streamwise direction, instead of the results on just one grid point, to minimize scatter in the profiles.

As the observations from the instantaneous vortices fields above, the population density profiles of the positively rotating vortices show clear peaks on right side of the wake region and also in the regions close to the left wall, and the profile of positively rotating vortices show peaks on the left side of the wake and in the right wall region. At $X/d = 1$, the near field of the wake, the vortices are highly concentrated in the region close to the wake center, where the splitter plates are absent, since these vortices in the wake come from the vortices in the boundary layers on the surfaces of the splitter plate. And there is almost no overlapping between the population density profiles of positive and negative vortices. With increasing downstream distance, the these population peaks decrease quickly while the population profiles also broaden. Also notice that the overlapping of the different direction vortices increases in the wake regions as the flow progresses, indicating the vortices in the wake can move across the center of the wake as the velocity defect of the two wakes diminishes. Compared with the profiles at the center of the three streams, the overlapping of two profiles doesn't appear until the potential cores in the three streams start to disappear. At further downstream location, $X/d = 12$, the peaks of the population density profiles start to diminish and the profiles start to approach the vortex distribution of a channel flow. Also notice that the highest vortex population actually occurs in a very small region of the wall boundary layers, which is not a surprise because of the higher velocity gradient in the wall region. And the profiles in the wall boundary region almost remain unchanged while the flow develops.

Figure 3.6 shows the vortex population in the streamwise direction, which is obtained by adding the number of vortices between the center of the center stream $Y/d = 0$ and the center of the left side stream $Y/d = -1$ in 1cm long region, like from $X/d = 0.75$ to $X/d = 1.25$ on one instantaneous flow realization, And then averaging over all flow realizations . In this way,

the streamwise population changing trend of detectable positively rotating vortex can be more easily observed. The number of the vortices in the same size region per velocity realization at different downstream locations monotonously decreased with increasing downstream locations, and the slope of decreasing is almost linear. Compared to the jet case in Kong et al. (2010), in which the vortex population first increases and then decreases, the results here are reasonable because in the wake flow the driving force of behind vortex generation, the velocity deficit of the wake, only decreases once the flow passes the obstacle, while in the jet there is new shear created once the jet flow is formed. There are still new vortices generated, but the decay and dissipation of these vortices is overwhelmingly dominant on the flow developing process. Also notice that the number of negatively rotating vortices are slightly higher than the number of positively rotating vortices, which can be explained by the mean streamwise velocity profiles in Fig. 5.10. The mean velocity of the left stream is a little bit higher than the center stream, which results in a little more negatively rotating vortices.

3.3.3 Size and strength of vortex cores

In addition to the vortex population density, other properties of the identified vortices can be obtained after the vortices are identified on instantaneous flow realizations, such as the size and strength of vortex core are presented in a similar manner to the vortex populations. Note that the smallest size of swirling strength cluster we can identify is $d^2/400$. Also note that inside the swirling strength clusters, the strength value is not evenly distributed. Since the highest swirling strength value of the vortex core gives the maximum rotation speed of the given vortex, it is used to characterize the vortex strength and averaged to obtain the results here.

Figure 3.7 shows the mean vortex core size profiles across the channel, normalized using d^2 , and Fig. 3.8 gives the mean vortex core strength, normalized by U_0/d . The values of mean vortex core size appear to be rather small compared to the stream width, and the length scale is about one tenth of the stream width, d . The mean size of vortex cores profiles seem similar to the profiles of the vortex population density, and show high peak values in region

of wake and also in the wall boundaries, where the vortex population is highest, the average vortex size is also the largest, especially at $X/d = 1$. As the flow progresses, the values of the size peaks decrease and locations move away from the center of the wake, like the profiles of the vortex population density. Although there is some overlapping between the profiles of different direction rotating vortices in the region of the stream centers, considering the vortices population density in those regions is extremely low, the overlapping is not significant. Also notice that the size of the vortices in the wall boundary region are quite constant, keeping high peak values close to the walls. However, in the near wake, the current vortex areas are about two orders of magnitude smaller than in the previous report Feng et al. (2010) ; in the far wake, they are almost four order of magnitude smaller. Again, this can be explained based on the difference between the two measurement techniques, as we argued in Kong et al. (2010) and also in previous section. In Fig. 3.8, the difference between the strength of vortex cores and the size is quite obvious. At $X/d = 1$, there are still very distinct peaks on the profiles of the strength of vortex cores , at where peak values of population and size are located. The center of the wake has the maximum vortex population density, the largest vortex size, and the strongest swirling motion. However at all the other downstream locations, the peaks disappear, the strength of the vortices are quite uniform, not sensitive to the cross-streamwise locations, which is also observed in the far-field of the jet case Kong et al. (2010). On both the current wake case and the previous jet case, the flow is confined by the two side walls. Once the flow passed the transition stage, it start to approach the fully developed channel flow, the strength of the vortex cores are quite uniform except the small regions close to the walls.

Instead of the showing the average size and strength of vortex cores at different downstream locations, the probability density functions of these properties were calculated and given in . Fig. 3.9 and 3.8 to show how the distribution of these values change in the streamwise direction. In Fig. 3.9 , the number of vortices with large core size decreases and the number of small ones increases as the flow goes down stream, which indicates when those vortices originated from the boundary layers on the surfaces of the splitter plates decay and dissipate, they also break down to small size vortices. As we mentioned earlier, the vortex detection

technique has a lower-limit on spatial resolution, $d^2/400$, which is indicated by the lower end of the pdf profile of the core size. Notice that the locations of the peak values of the profiles of core size pdf remain almost constant in all downstream locations. Although the pdf profiles show vortex number decreases quickly to almost zeros when the size is lower than the peaks, it doesn't mean there population of vortices of that size in the flow is low, which actually is expected to become higher, in the other words, more and more small size vortices as the flow develops downstream. This can be explained by the dual filtering process in the vortex detection procedure to eliminate the effect of PIV measurement noise, which is already described above. The a filter with a threshold of $|\Lambda_{ci}| \geq 1.5\Lambda_{ci}^{rms}$ was applied to the instantaneous swirling strength fields first, and then a filter based on cluster size also was applied to the all the identified swirling strength clusters. Therefore, some of the small vortices could be missed even they are larger than prescribed spatial filter size because their strength is less the strength filter threshold value. Fig. 3.8 shows a similar trend as the core size distribution, the number of high strength vortices decreases and the number of low strength vortices increases as the flow develops. In the other words, the vortices in the near wake region are much stronger than the vortices in the far wake. Also notice that the shape of the core distribution change very rapidly in the near wake region and tends to stabilize in the far wake region as the flow approaches fully developed. The effect of the dual-filtering procedure also can be seen in the core strength distribution in the low value region, as the curves decrease to zeros at the value of the filter threshold. These effect in the low value region is mainly caused by the spatial limitation of the PIV measurements, and also in some degree caused by the high sensitivity of the swirling strength method to measurement noise, since it is based on the velocity gradient.

3.3.4 Deviation velocity of vortex cores

Another very important character of vortices can be examined here how the vortex moves. Once the vortex is identified, the velocity of vortex cores can be obtained by mapping back to the velocity field. Here we used the concept of *deviation velocity* of the vortex, the deviation of

the instantaneous vortex convection velocity from the local mean velocity, which is proposed in our previous study in the jet flow case Kong et al. (2010). It can be calculated by subtracting the local mean velocity from the instantaneous velocity values of the vortex cores. Figure. 3.11 and 3.12 show profiles of the average cross-stream (V) and streamwise (U) deviation velocities cross the channel at four downstream locations, which all are normalized by $U_0 = 0.5m/s$.

Figure 3.11 shows that the mean deviation velocity V is zero at the location of the population density peak for both the positively and negatively rotating vortices. The results here are very similar to the results in the jet flow case. The profiles indicating the vortices in the wake simply move towards where the vortex population density is low, the center of free stream and the other side of the wake. The profiles of the mean deviation velocity U of the positively and negatively rotating vortices are nearly overlap on each other as shown in Fig. 3.12. At the location of the population density peak, the mean deviation velocity U is very close to zero. Both the profiles of positively and negatively rotating vortices shows high positive peaks in the wake center and high negative peaks close to the free stream centers, which corresponds to the vortices bringing high momentum fluid of the free stream to the low velocity region, the wake, and transferring low momentum fluid from the wake to the centers of the free streams, which is the same in the previous jet case.

3.4 Spatial correlation functions and linear stochastic estimation

3.4.1 Two-point spatial correlations

Following the the same definition used in the previous study, the two point spatial cross correlation of swirling strength and the fluctuation of σ is defined as

$$R_{\lambda\sigma'}(X, Y; x, y) = \frac{\langle \lambda_{ci}(X, Y) \sigma'(x, y) \rangle}{\sqrt{\langle \lambda_{ci}^2(X, Y) \rangle \langle \sigma'^2(x, y) \rangle}} \quad (3.1)$$

where (X,Y) and (x,y) are the coordinates of the basis point (i.e. the point about which the correlation is calculated) and an arbitrary point in the flow field, respectively Kong et al. (2010). In the present study of wake flow, instead of locations along the left peak of turbulent kinetic energy, four points at different cross-stream locations on each side of the wake (total

eight points) and three streamwise locations, $X/d = 1, 4.5, \text{ and } 7.5$, were chosen as basis points. Note here the absolute value of swirling strength of λ_{ci} is used, instead of the swirling strength with the sign Λ_{ci} , giving rotating direction, since velocity data used here already carry that information. The spatial correlations of $R_{\lambda u'}$ are presented in Figs. 3.13, 3.15, and 3.17, correlations of $R_{\lambda v'}$ are presented in Fig. 3.14, 3.16, and 3.18, and correlations of $R_{\lambda_{ci}\phi'}$ are presented in Fig. 3.19, 3.20, and 3.21 . In these figures, the first row of figures show the correlation of on the left side of the wake and second row of figures give results on the right side of the wake, with the basis point moving from the left to the right, crossing the center of the left wake in the middle. The streamwise flow direction is from the bottom to the top of the figures.

The cross correlation fields of swirling strength and fluctuations of the velocity at all locations exhibit “butterfly” like shapes with different orientation with respect to the velocity component, similar to the correlations results in our previous jet study Kong et al. (2010) and the results in boundary layer in Christensen and Adrian (2001). The symmetry line of this “butterfly” shape, called “the axis” of these correlation fields hereafter, is oriented vertically (in the streamwise direction) in $R_{\lambda u'}$ contours and oriented horizontally (in the cross-stream direction) in $R_{\lambda v'}$ contours, in which the contour lines of zero correlation overlaps in the region of the basis points. Since on two sides of the wake vortices rotate in different direction, the cross correlation fields carry different signs on the two ”wings” on each side of the wake. On the left side of the wake, the right wing of $R_{\lambda u'}$ contains negative values and the left wing contains positive values, while the the upper wing of $R_{\lambda v'}$ contains positive values and lower wing contains negative values, indicating the vortices in this region dominantly rotate negatively and bringing the high momentum flux to the wake. On the right side of the wake, the correlation fields are almost exact axisymmetric to those on the left side, with the signs on the two “wings” switch sides , since the vortices on the right side of the wake dominantly rotate positively.

In the region close to the center of the wake, the two wings of the correlation fields of $R_{\lambda u'}$ at all three downstream locations are axisymmetric about the their own axis, while those on

each side of the wake strongly tilt towards to the wake center. The tilting of the correlation fields can also be observed in the $R_{\lambda v'}$ fields, with the axis of the correlations slightly tilt upwards on the side closer to the wake center. However, by carefully examining these plots, there is no obvious trend on how the angle of tilting change with locations of the basis points. This tilting of the axis, which is also reported in the previous jet study Kong et al. (2010), suggests the strong momentum transfer in these regions and also the high velocity gradients in this narrow wake region. As the flow develops downstream and the wake decays, the tilting of the axis becomes less significant due to smaller and smaller velocity gradients.

Also notice there is a trend in how the size of the two wings of the correlation fields changes. In the region close to the center of the wake, the upper wings of the correlation fields of $R_{\lambda v'}$ are much larger than the lower wings, while in the far left and far right figures, the lower wings are larger than the upper wings, and in between the two wings are more balanced. The upper wing of the $R_{\lambda v'}$ represents the positive turbulent flux from the free stream to the low momentum wake region, while the lower wing represents the negative turbulent flux from the wake to the free stream. In the far left and far right area of the wake, the high momentum regions, the positive velocity fluctuations are less likely than negative fluctuations, and the negative turbulent flux is more significant, which is also suggested by the very weak correlation values on the wings of $R_{\lambda v'}$ far away from the wake. In the wake center, the positive velocity fluctuations, the positive turbulent momentum flux are very dominant, but they are reduced by both positively and negatively rotating vortices. Thus, the upper wings of $R_{\lambda v'}$ are large and strong, while the two wings of $R_{\lambda u'}$ are quite symmetric.

Notice also, there is a weakly correlated negative region upstream of the strong positive region close to the basis point and a weak positive region downstream of the strong negative region in $R_{\lambda v'}$, which is more noticeable in further downstream locations, like $X/d = 7.5$. This is the indication of the presence of adjacent vortices upstream and downstream of the vortices at the basis points. Last, as the flow progresses downstream, the correlation areas of both $R_{\lambda u'}$ and $R_{\lambda v'}$ grow larger.

Figure 3.19, 3.20, and 3.21 show results of $R_{\lambda_{ci}\phi'}$, the cross correlation of swirling

strength with the concentration fluctuation. The shape and characteristics of the correlation fields of $R_{\lambda_{ci}\phi'}$ are similar to results of the $R_{\lambda v'}$, showing the deep connection between the momentum and mass transfer. There are also two correlated areas in the contours; one positively correlated region and one negatively correlated region, which the distribution of the sign of correlation values are the same as those in the $R_{\lambda v'}$. On the right side of the wake, the positively rotating (counterclockwise) vortices bring high concentration fluid (i.e., positive concentration fluctuations) from the center stream to the left side stream downstream of the vortex core (the basis point) and bring the low concentration fluid from the side stream to the center stream upstream of the core. On the left side of the wake, the negatively rotating (clockwise) vortices bring high concentration fluid upstream of the vortex core and bring the low concentration fluid downstream of the core. Also as the corrections of $R_{\lambda v'}$, in the wake center, the upper wings are larger than the lower wings, and in the far left and far right locations, the lower wings are larger.

However, there are still some difference can be seen. It is noticeable that in near wake, $X/d = 1$, the strong correlation areas of $R_{\lambda_{ci}\phi'}$ are relatively smaller than those of $R_{\lambda_{ci}v'}$, while in the further downstream locations these areas grow quickly, and show nearly the same size as $R_{\lambda_{ci}v'}$. This indicates that the different stages of mass and momentum transfer in the near wake. The mass transfer from the center stream to the side streams only starts right after the flow enters test section, while the momentum transfer already exists on the surfaces of the splitter plates, as those boundary layer vortices. And then as the flow goes downstream, the mass transfer catches on the momentum transfer fast. In Fig. 3.20 and 3.21, the correlations in far upstream and downstream are very weak, unlike $R_{\lambda v'}$ contours showing the neighboring vortices. Also, considering these two horizontally oriented wings of the $R_{\lambda_{ci}\phi'}$ together, one can imagine the auto-correlation of $R_{\phi'\phi'}$ will have a horizontally orientated elliptic shape, which is reported in a previous paper (Feng et al., 2010). Notice also as the corrections with the velocity fluctuations, the size of the correlation area becomes steadily larger with increasing downstream distance.

3.4.2 Linear stochastic estimation

Conditional averages can be calculated from measured correlation fields by using linear stochastic estimation (LSE) technique, which is a useful tool to interpret spatial correlation data above (Adrian, 1994; Olsen and Dutton, 2002, 2003). As we argued in previous jet study Kong et al. (2010), due to the low population density of the vortices, directly calculating conditional averages from an PIV experiment data requires either a very large ensemble size or averaging over a large flow region instead of a particular location in the flow, while LSE can give the typical underlying flow structures more precisely with a smaller ensemble size. The linear stochastic estimate of the velocity fluctuation $u'_i(x, y)$ over the entire field given the condition $\lambda_{ci}(X, Y)$ is, is given by following formula,

$$\langle u'_i(x, y) | \lambda_{ci}(X, Y) \rangle \approx L_i \lambda_{ci}(X, Y) \quad (3.2)$$

The linear coefficient, L_i , can be determined in the following way,

$$L_i = \frac{\langle u'_i(x, y) \lambda_{ci}(X, Y) \rangle}{\langle \lambda_{ci}(X, Y) \lambda_{ci}(X, Y) \rangle} \quad (3.3)$$

, where $\langle u'_i(x, y) \lambda_{ci}(X, Y) \rangle$ is the (unnormalized) spatial correlation of u'_i and λ_{ci} . Again we chose the event of $\lambda_{ci} = 2\lambda_{ci}^{rms}$ in order to get the features of typical structure in the flow, same as the event used in jet vortex study. After $\langle u'_i(x, y) | \lambda_{ci}(X, Y) \rangle$ is calculated, the mean velocity field was added and $U(x_o)$, the velocity values at the basis point the correlations were calculated was subtracted from the all the vectors in the field, resulted in results in Fig. 3.22, which is able to show the typical velocity field of one vortex at different downstream locations.

Here only the results at one basis point at one downstream location on the each side of the wake were presented, while the first row figures in Fig. 3.22 are the results on the left side of the wake and the second row are the those on the right side of the wake, and from left to the right the basis point moving downstream. There are clear roller structures revealed by the linear stochastic estimation at the all six locations, those on the left side of wake rotate negatively and those on the right side rotate positively. All the roller structures are spindle-shaped with a stream-wise major axis. Here, the tilting of the major axis toward the wake center becomes much more visible here than in the spatial correlation fields. As the flow progresses

downstream, the roller structures grow larger. Although the sizes of the vortex cores decrease, as we already concluded in the previous section, the large-scale coherent motions of the flow, which the swirling motions at the base point are part of, are indeed growing. Again this suggesting the vortices detected by the swirling strength are likely the small scale structures embedded in some large scale coherent motions. In the previous jet study, there are no any neighboring structures visible in the LSE velocity fields. However, in Fig. 3.22, there are some weak structures can be seen at the upstream and downstream corner on the opposite side of the wake, especially at the far field of the wake, at $X/d = 7.5$. To make those structures more visible, all the vectors in Fig. 3.22 are made uniform length, shown in Fig. 3.23. This method has been used in the vortex study in wall boundary layer by Christensen and Adrian (2001). At $X/d = 4.5$ and $X/d = 7.5$, the neighboring counter-rotating vortices at the upstream and downstream corner on the opposite side of the wake are very obvious in Fig. 3.23, with nearly the same size as the vortices shown at the basis points. These structures here are very resemble to the von *Kármán* vortex street, which is very common in typical wake flow after blunt bodies. In the current wake study, the vortex street is not visible either in instantaneous velocity fields or identified swirling strength clusters, while it is indeed still present in the flow. There are two combined factors, which can explain this. First, the Reynolds number of the current wake flow is quite high, 37,500, which means the flow is quite turbulent, and the size of the vortices is expected to be rather small and more random, since the Kolmogorov length scale is small. Second, although there is a flow conditioning section for each stream, which is placed before the contraction and the splitter plates, the flow develops again on the walls of contract section and splitter plates after it passes the packed spheres and screens. There are separated boundary layers developed independently before the wake is formed. As we can seen in Fig. 3.23, in the near wake, $X/d = 1$, the vortex street pattern is not quite identifiable, because the vortices on each side of the wake are quite independent, incoherent to each other. However, as the flow develops downstream, these vortices are reorganized and become more and more coherent. Therefore the vortex street pattern is merged in the LSE fields at $X/d = 4.5, 7.5$, which is capable of detecting the large scale coherent structures in turbulent flow.

3.5 Conclusions

As a continuation of the previous jet vortex study, a similar study of the vortices in a confined rectangular wake flow was conducted in the current study, with the same flow rate for all three streams. Experimental data from simultaneous PIV/PLIF experiments were used in this analysis. The swirling strength were computed from instantaneous velocity fields, and the filtered with a universal threshold of $|\Lambda_{ci}| \geq 1.5\Lambda_{ci}^{rms}$. The remaining swirling strength clusters were used as the indicator of a vortex in the flow field. Instantaneous swirling strength field shows that positively (counterclockwise) rotating vortices are dominant on the right side of the wake and negatively (clockwise) rotating vortices are dominant on the left side. In both the cross-stream direction and the streamwise direction, the population density, average size and strength, deviation velocity of vortices were calculated and analyzed. The population density, average size and strength of vortex cores all shows high peak values both sides of the wakes, while these peaks decrease quickly and the profiles broaden as the flow progresses downstream. The change of vortex core maximum strength is seen relatively faster than the change of the core size. The results of mean cross-stream wise deviation velocity of vortex core shows the vortices in the wake spread from the neighborhood of wake to the centers of the free stream, and the mean streamwise deviation velocity indicates that vortices bring high momentum fluid of the free stream into the the wake.

Two point spatial cross-correlations of swirling strength with velocity fluctuations and concentration fluctuations were calculated at three different streamwise locations and eight cross-stream wise locations in the flow field. All the cross correlation fields shown here exhibit a “butterfly” like shape, with one “wing” with positive correlation values and the other “wing” with negative values. The axes of correlation fields are oriented in the streamwise direction in $R_{\lambda u'}$ contours, and they tilt towards the wake center on the both sides of the wake, except those with basis points already located close to wake center oriented exact vertically. The axes in $R_{\lambda v'}$ are oriented in the cross-stream direction, and they tile downstream on the both sides of the wake, except those near wake center. On the left side of the wake, the right wing of $R_{\lambda u'}$ contains negative values and the left wing contains positive values, while the the upper

wing of $R_{\lambda v'}$ contains positive values and lower wing contains negative values, indicating the vortices in this region dominantly rotate negatively. Since on two sides of the wake vortices rotate in different direction, the cross correlation fields carry different signs on the two "wings" on each side of the wake. In the region close to the center of the wake, the upper wings of the correlation fields of $R_{\lambda v'}$ are much larger than the lower wings, while in the far left and far right figures, the lower wings are larger than the upper wings, and in between the two wings are more balanced. The $R_{\lambda_{ci}\phi'}$ results show some similarity to those of $R_{\lambda v'}$, indicating the vortices play a similar role in mass transfer as in momentum transfer. However, in the near wake, the strong correlation areas of $R_{\lambda_{ci}\phi'}$ are relatively smaller than those of $R_{\lambda_{ci}v'}$, while in the further downstream locations these correlations show nearly the same size as $R_{\lambda_{ci}v'}$. The mass transfer from the center stream to the side streams only starts right after the flow enters test section, while the boundary layers are already developed on the surfaces of the splitter plates, thus strong momentum transfer already exist at the inlet. As the flow goes downstream, the mass transfer catches on the momentum transfer. Also, as the flow progresses downstream, all the correlation areas grow larger, indicating the large scale coherent motions grow larger.

Finally, linear stochastic estimation was used to visualize the underlining large scale coherent structures. The estimation was based on the swirling strength values at chosen locations in the flow. The results of LSE show clear roller structures at the basis points, and those on the left side of wake rotate negatively and those on the right side rotate positively. The tilting of the streamwise oriented major axis toward the wake center can be observed easily. As the flow progresses downstream, the roller structures grow larger. Also a vortex street pattern can be seen in these LSE results, which becomes more visible after the length of the vectors were made the same, especially in further downstream locations. The pattern revealed by LSE, which can be seen in instantaneous flow fields actually shows the unique characteristics of the current high Reynolds number wake flow. When the flow enters the test section, there are vortices developed independently on both sides of the splitter plates, which are incoherent to each other. As the flow develops downstream, these vortices are reorganized and become more and more coherent, therefore the vortex pattern becomes visible.

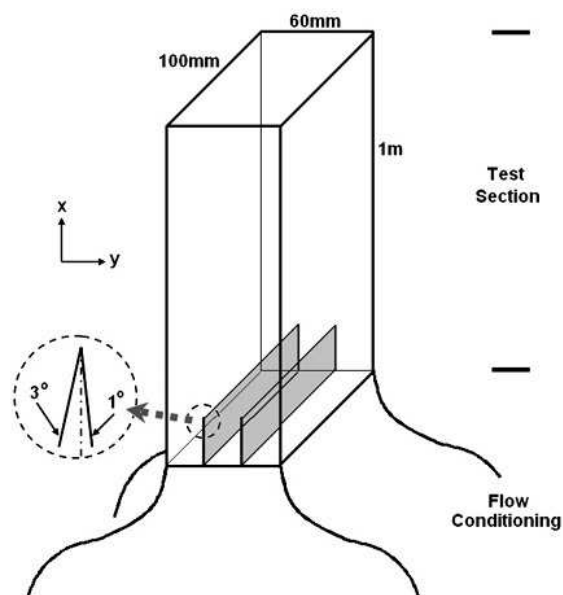


Figure 3.1 Photograph and schematic of the confined planar jet test section

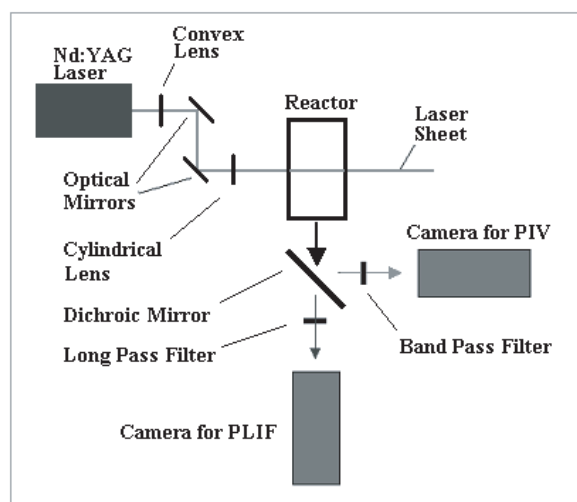


Figure 3.2 Schematic of the optical setup for the combined PIV and PLIF experiments

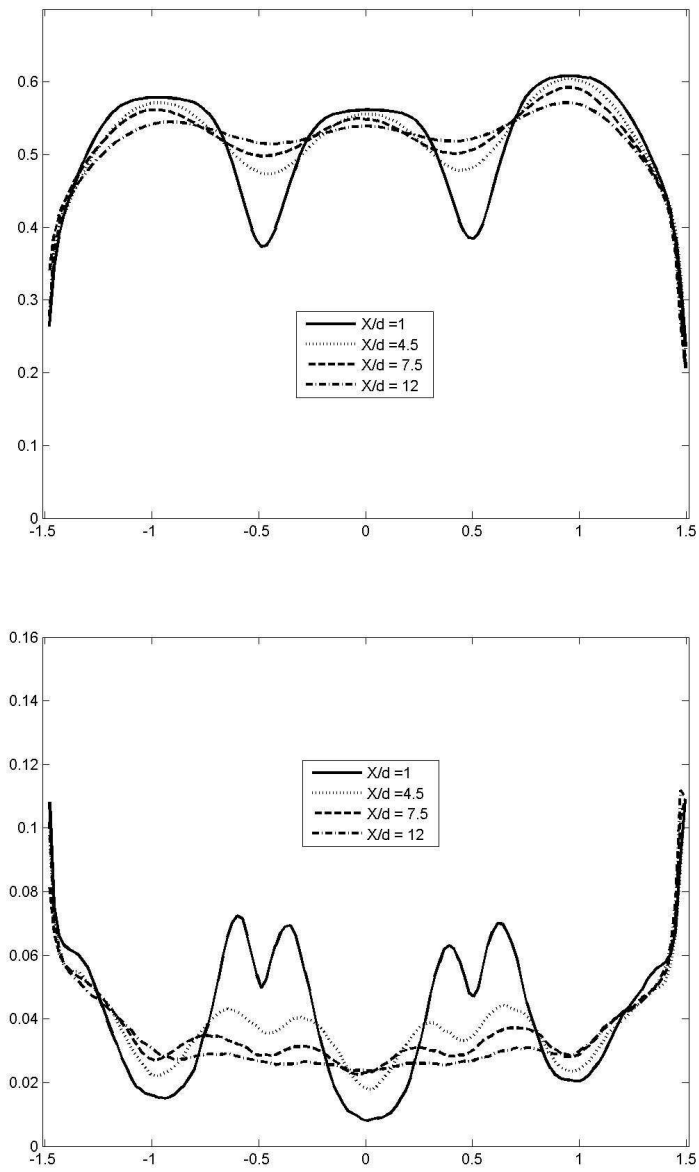
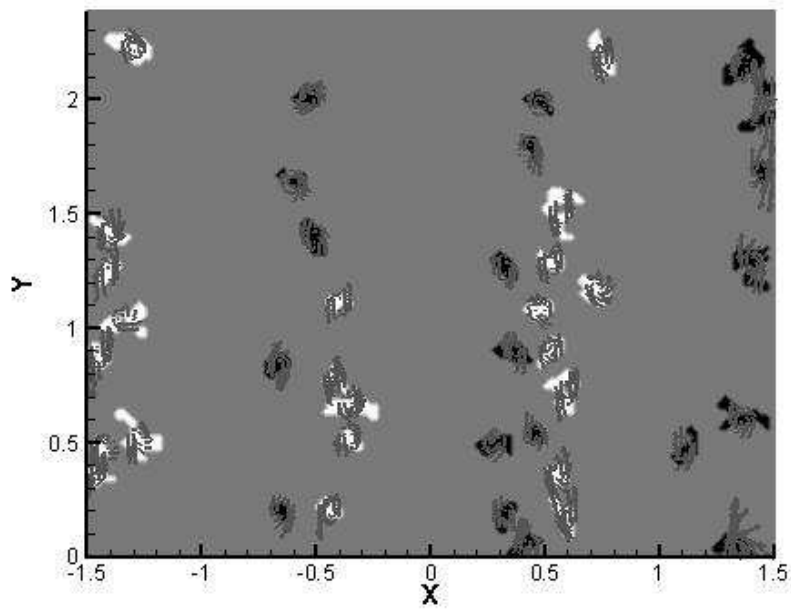
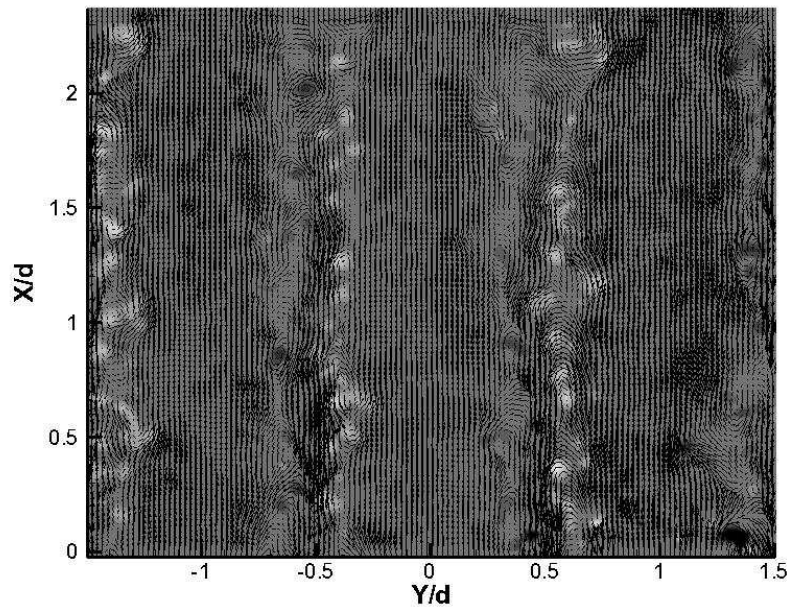


Figure 3.3 The mean and rms of streamwise velocity.



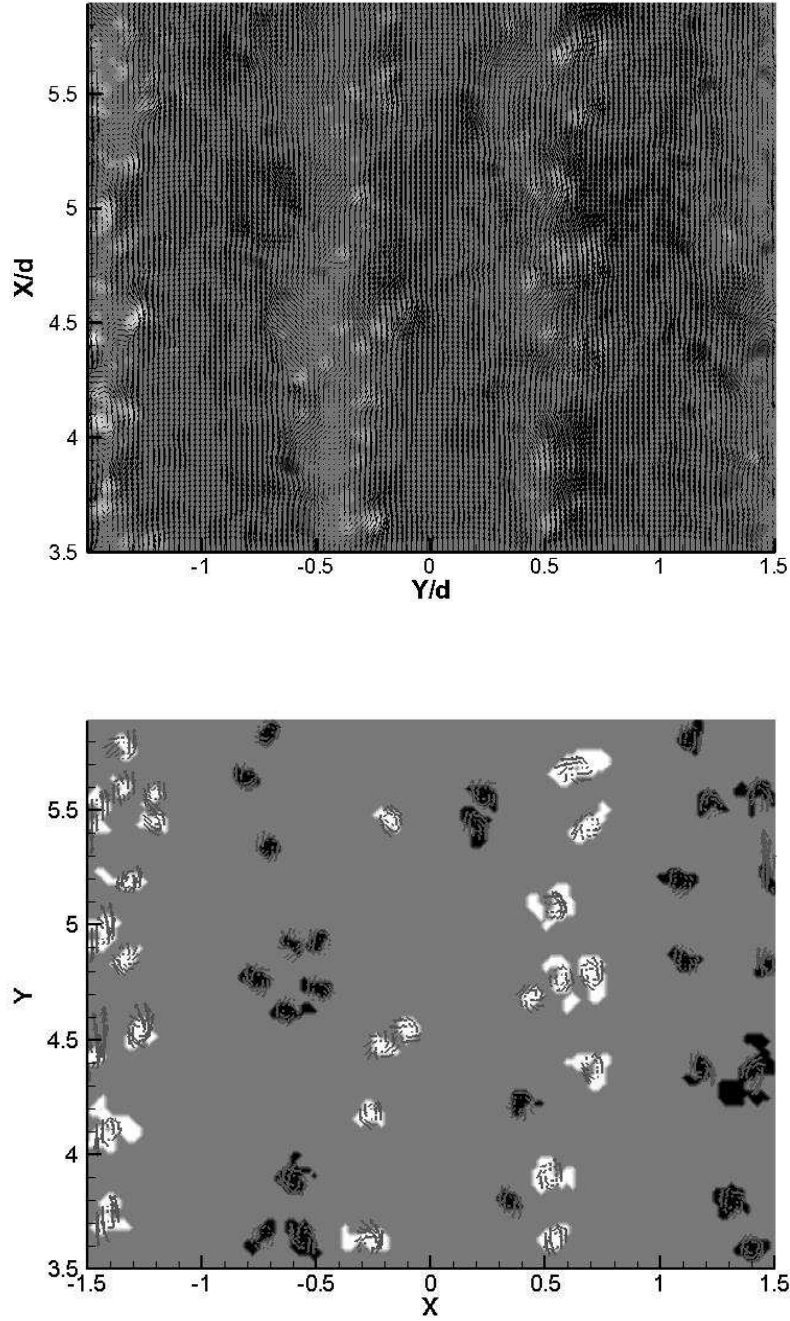


Figure 3.4 Example of vortex identification in an instantaneous PIV velocity field at $0 < X/d < 2.5$ and $6.5 < X/d < 9$. (a) The Galilean decomposition of this instantaneous velocity field with $0.6U_0$, where U_c is the mean velocity of the center stream at each X location. (b) Local Galilean decomposition of vortices with the velocity at each vortex core. The contours of $\Lambda_{ci} = 1.5\Lambda_{ci}^{rms}$ are also shown in the background of the figure (a) and (b).

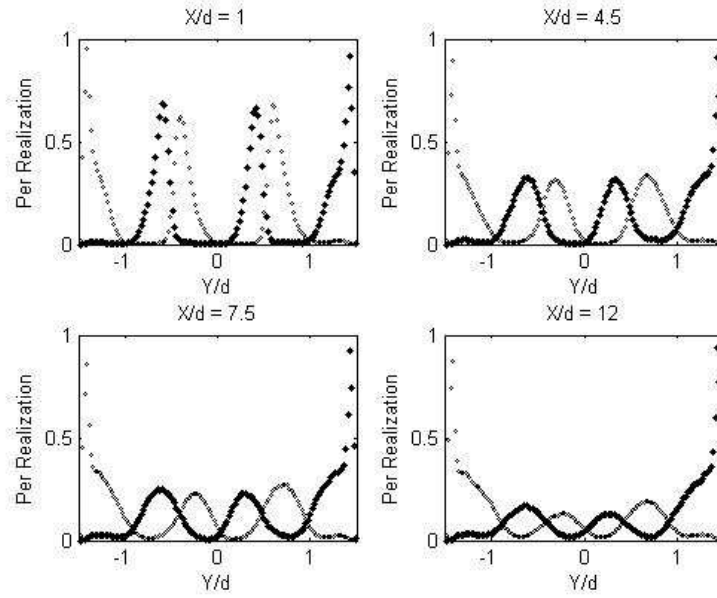


Figure 3.5 Local vortex population density of positively and negatively rotating vortices at different streamwise locations. \circ : negatively rotating vortices, \cdot : positively rotating vortices.

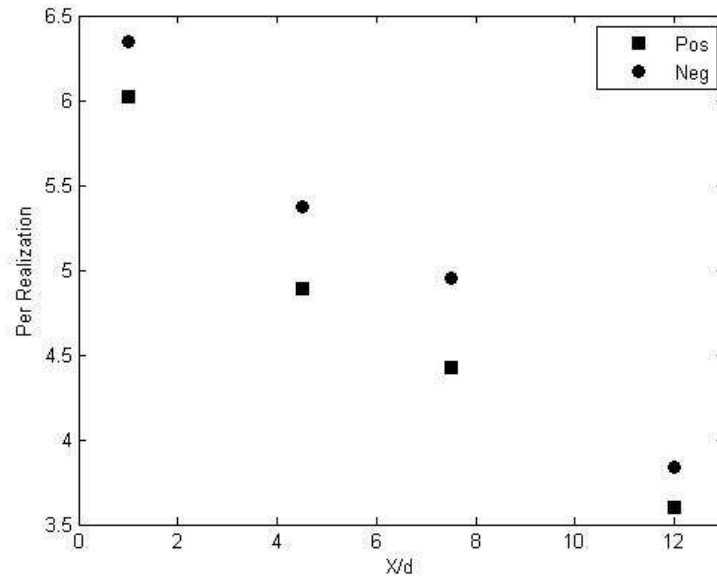


Figure 3.6 Mean populations of vortices in the half jet width (1cm) stream-wise long region between the centers of the center of center stream ($Y/d = 0$) and the center of left side stream ($Y/d = -1$).

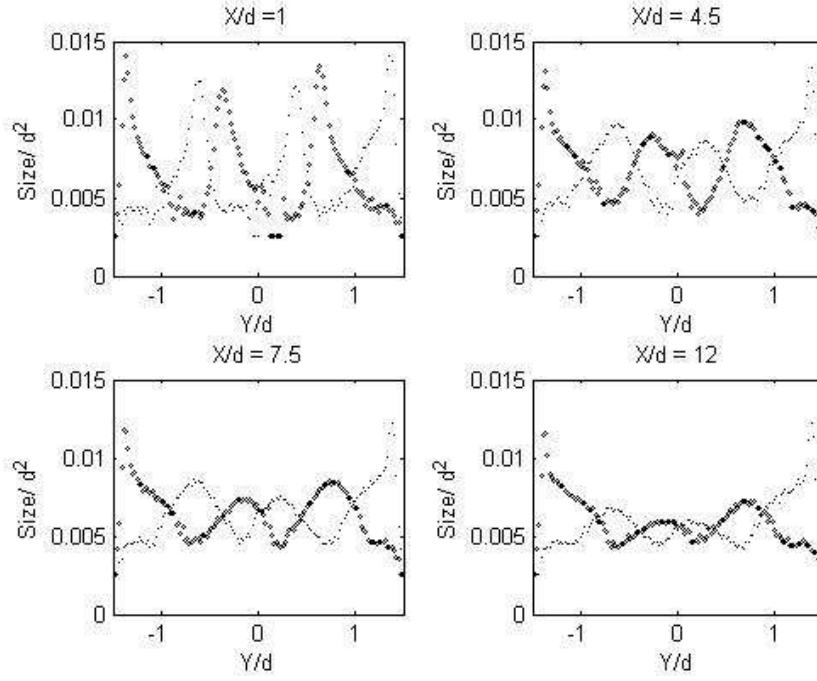


Figure 3.7 Profiles of the size of vortex cores. \circ : negatively rotating vortices, \cdot : positively rotating vortices.

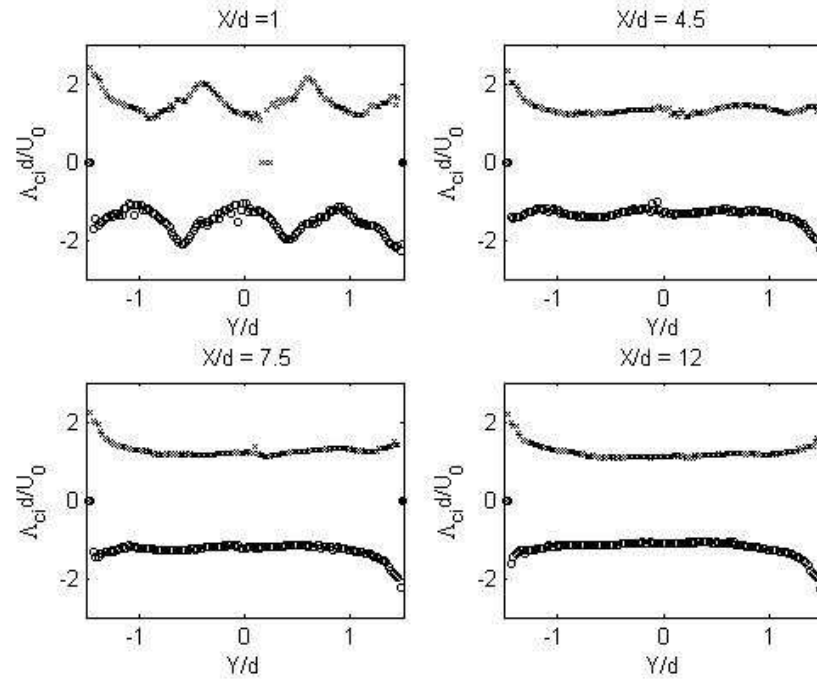


Figure 3.8 Profiles of the peak swirling strength value of vortex cores. \circ : negatively rotating vortices, \cdot : positively rotating vortices.

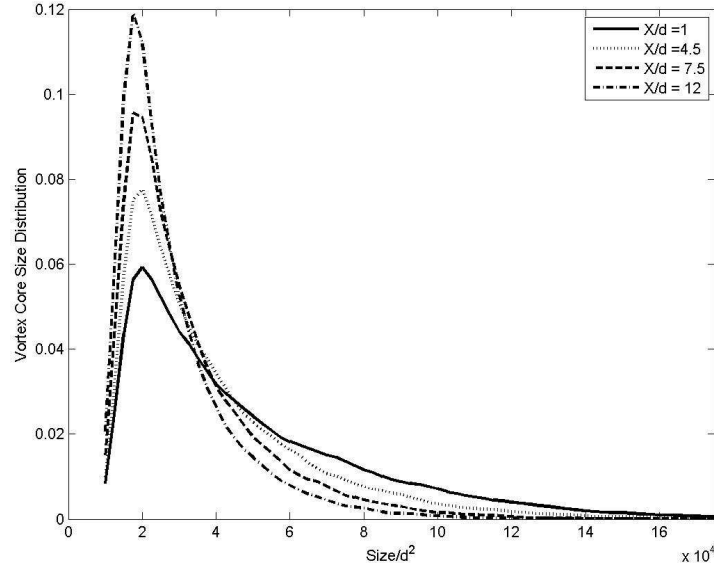


Figure 3.9 Mean vortex size in the half jet width (1cm) streamwise long region between the centers of the center of center stream ($Y/d = 0$) and the center of left side stream ($Y/d = -1$).

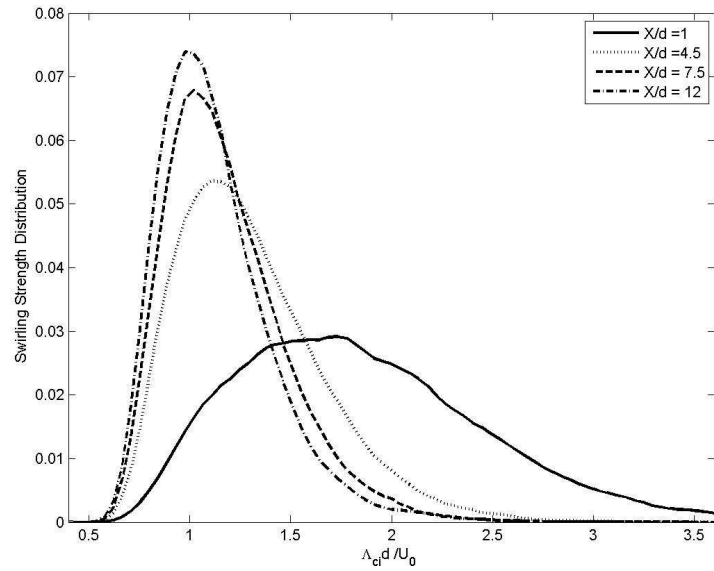


Figure 3.10 Mean the peak swirling strength value of the vortex cores in a half jet width (1cm) streamwise long region between the centers of the center of center stream ($Y/d = 0$) and the center of left side stream ($Y/d = -1$).

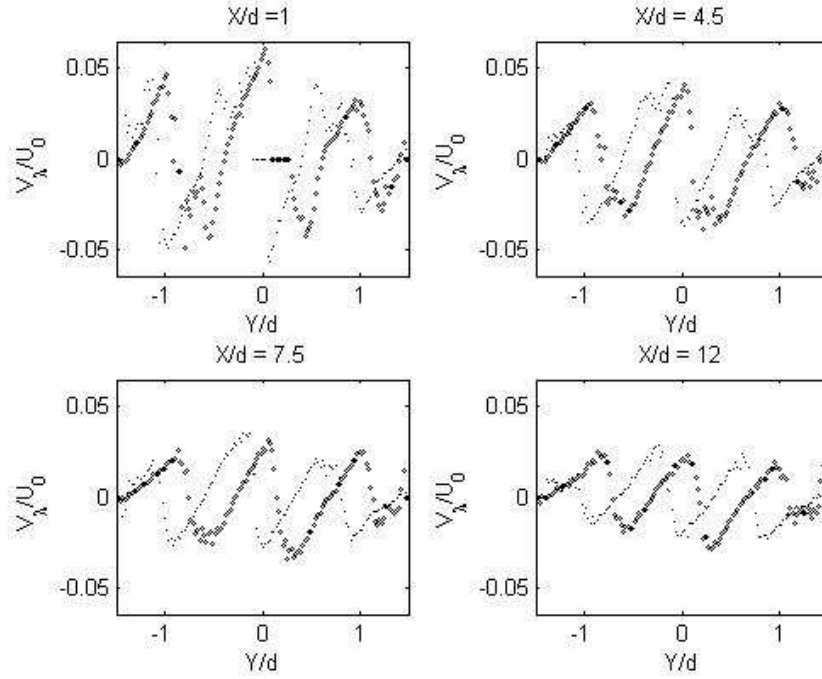


Figure 3.11 Vortex deviation velocity in the cross-stream direction. \circ : negatively rotating vortices, \cdot : positively rotating vortices.

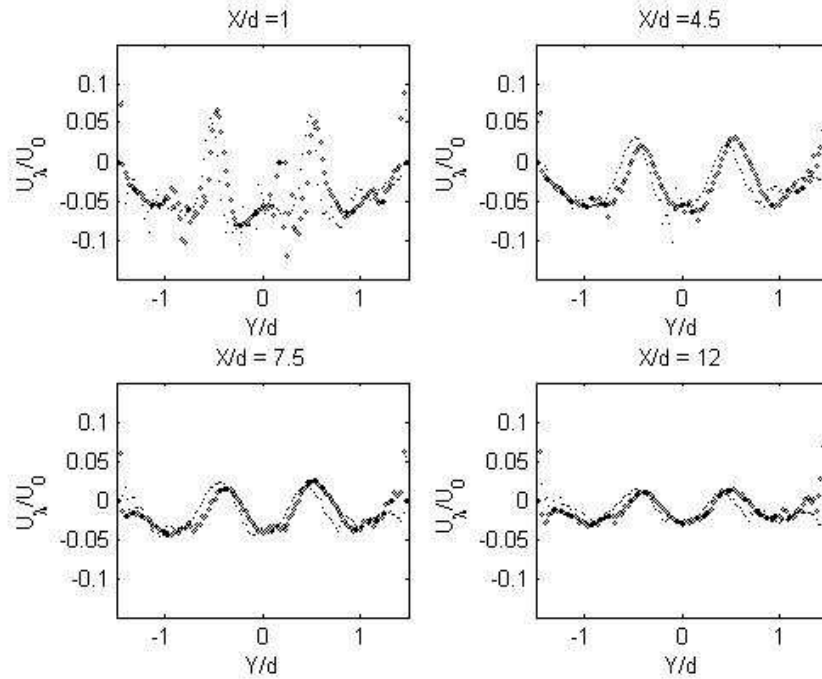


Figure 3.12 Vortex deviation velocity in the streamwise direction. \circ : negatively rotating vortices, \cdot : positively rotating vortices.

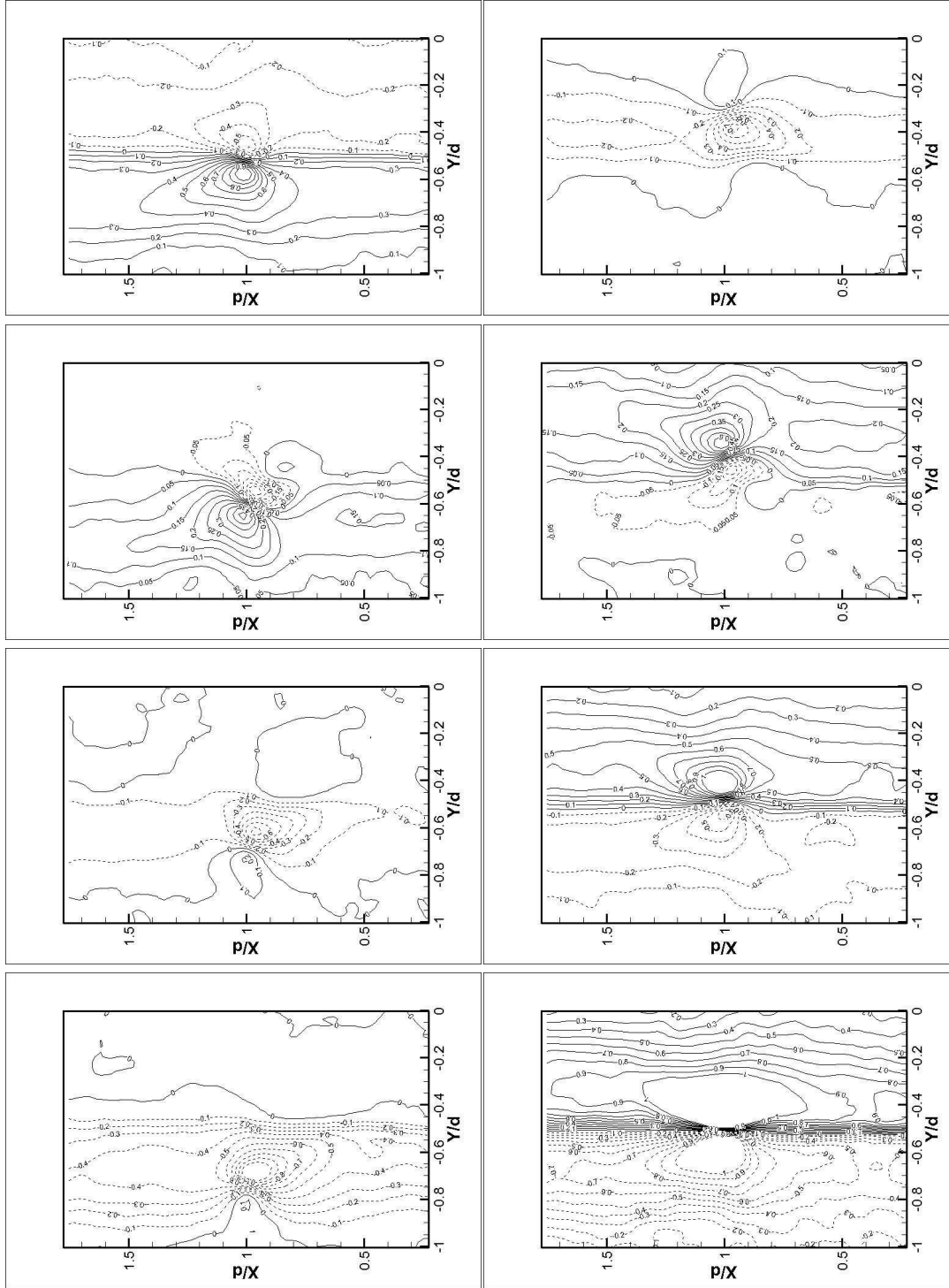


Figure 3.13 Two-point cross correlation $R_{\lambda_{ci} u'}$ at $X/d = 1$.

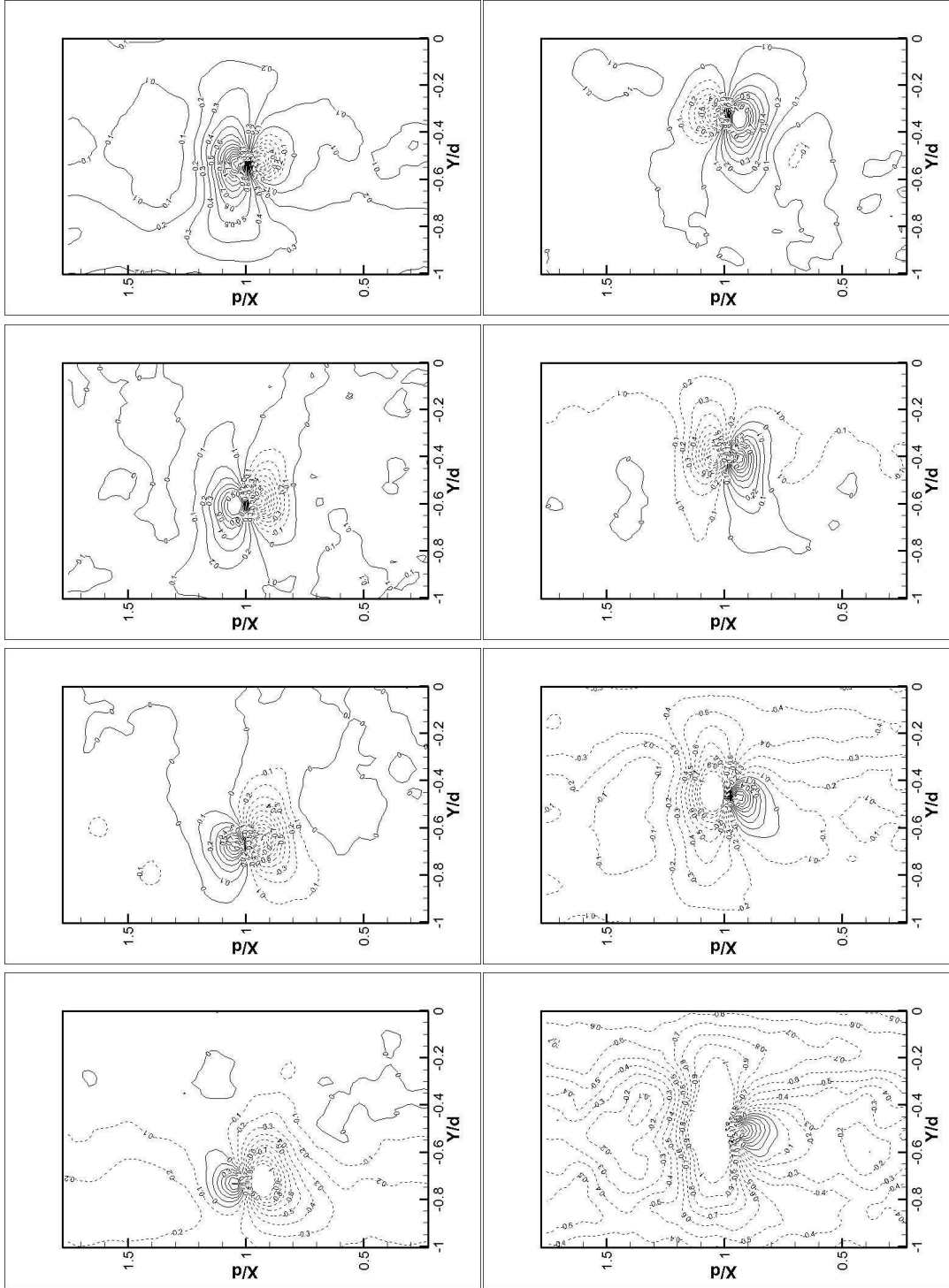


Figure 3.14 Two-point cross correlation $R_{\lambda_{ci}v'}$ at $X/d = 1$.

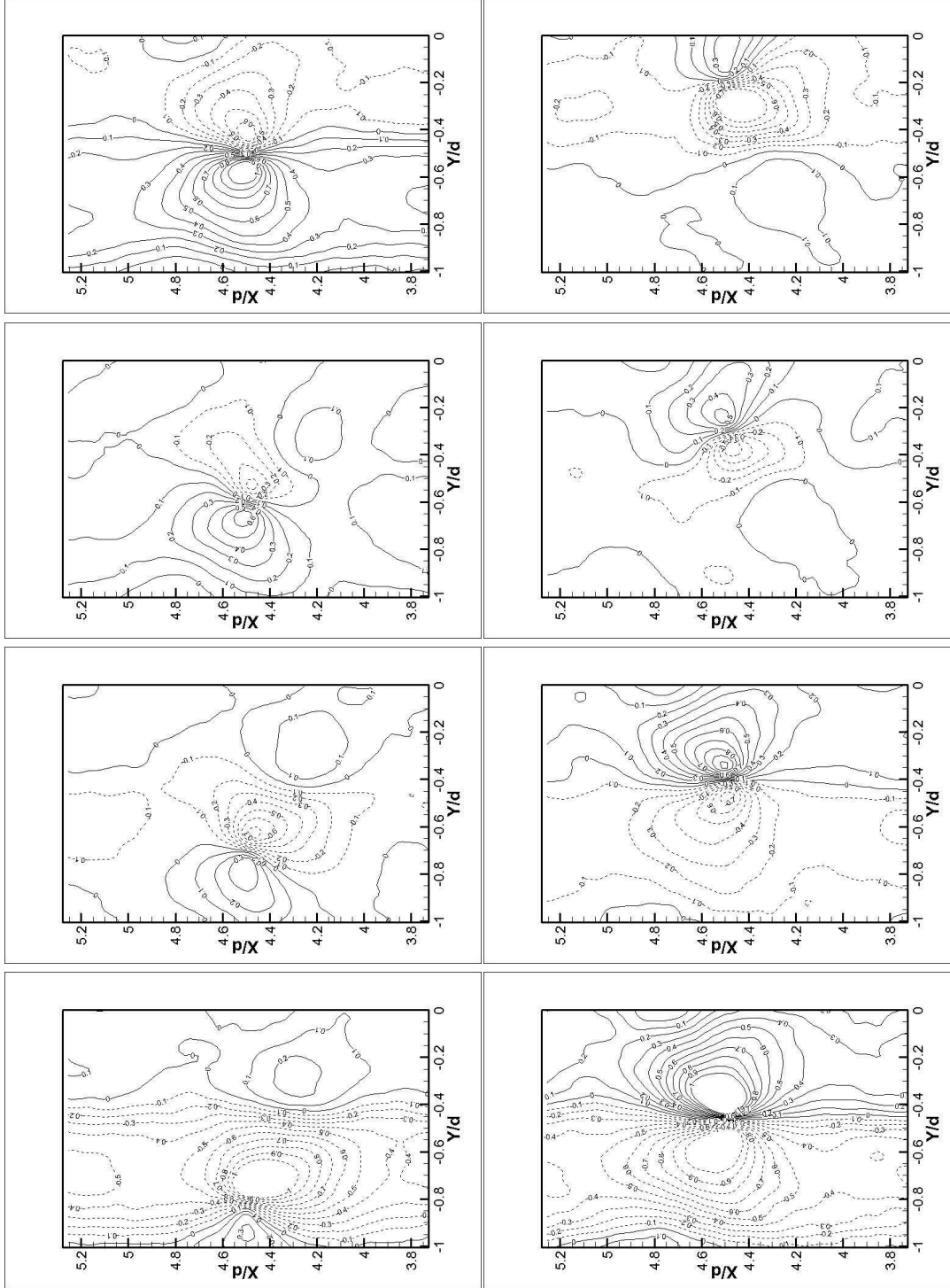


Figure 3.15 Two-point cross correlation $R_{\lambda_{ci} w'}$ at $X/d = 4.5$.

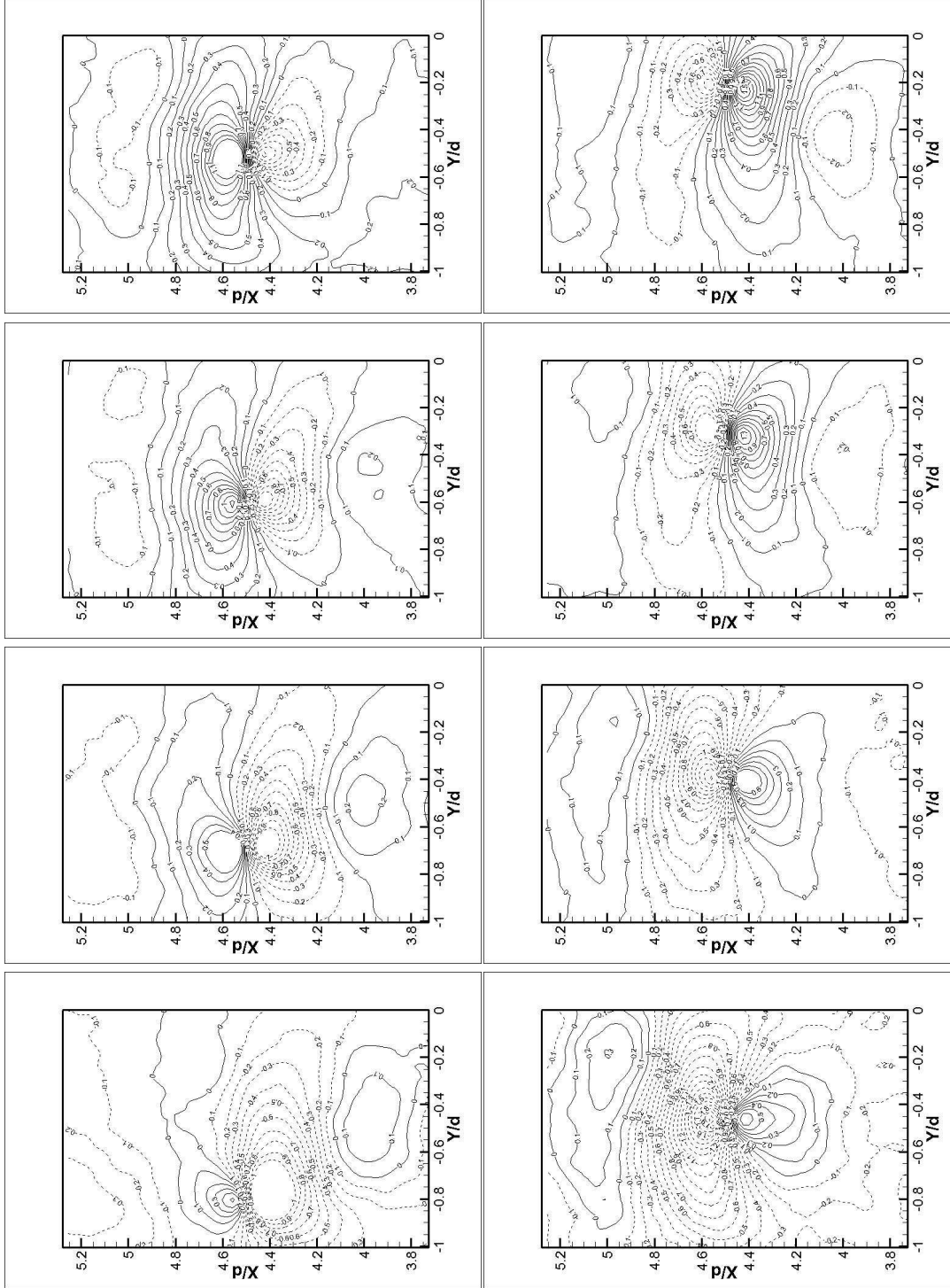


Figure 3.16 Two-point cross correlation $R_{\lambda_{ci}v'}$ at $X/d = 4.5$.

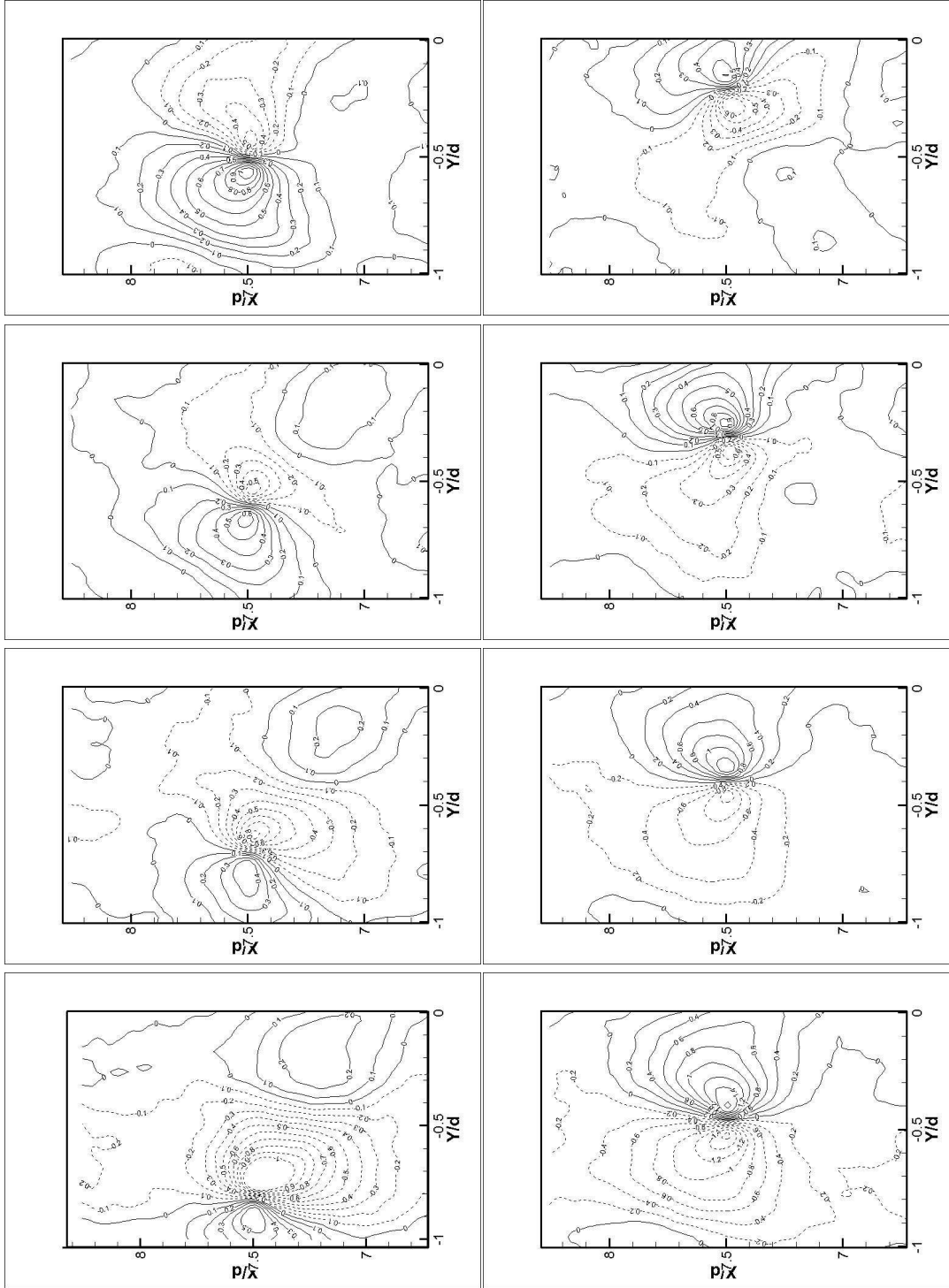


Figure 3.17 Two-point cross correlation $R_{\lambda_{ci}u'}$ at $X/d = 7.5$.

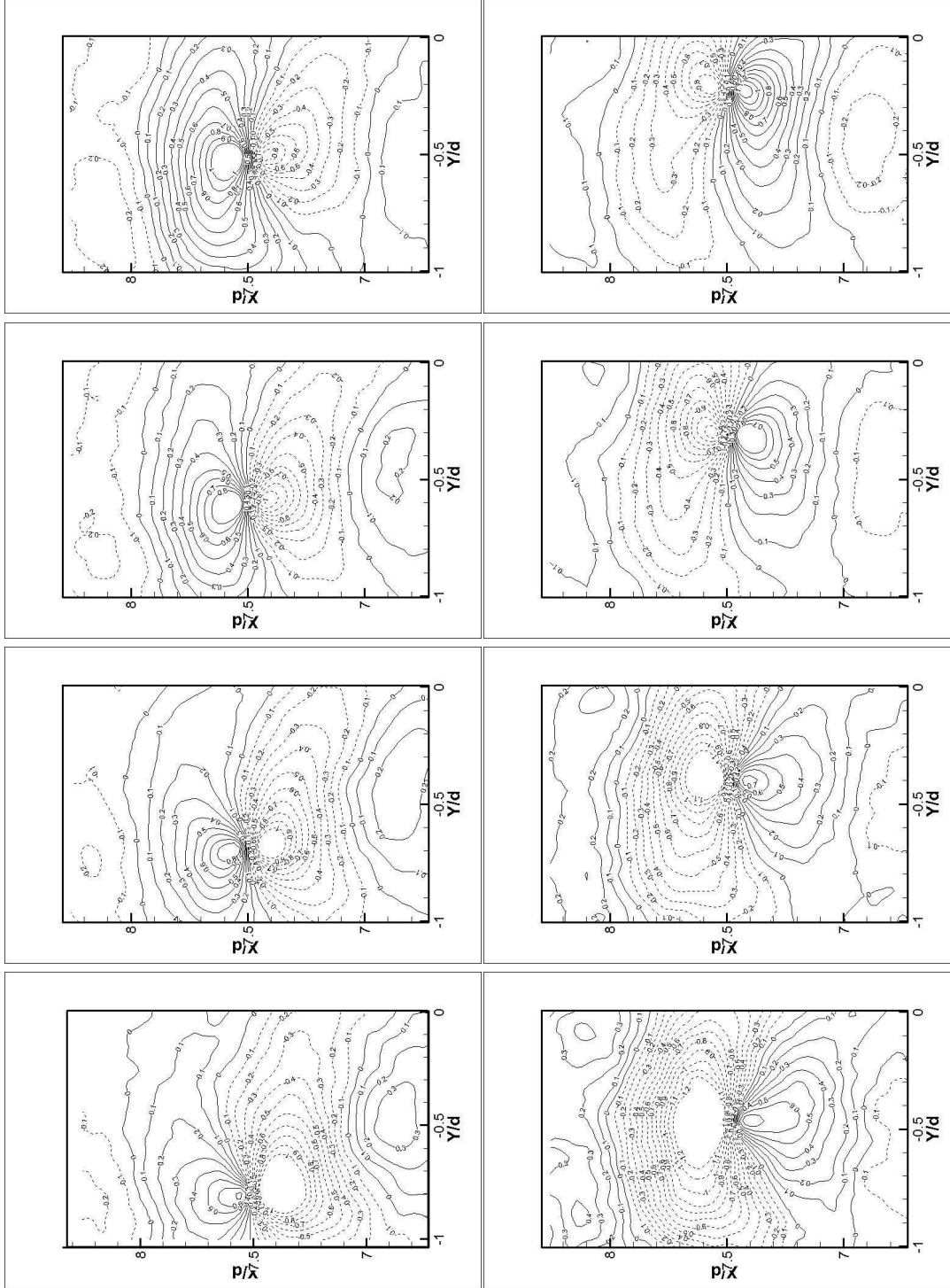


Figure 3.18 Two-point cross correlation $R_{\lambda_{ci} v'}$ at $X/d = 7.5$.

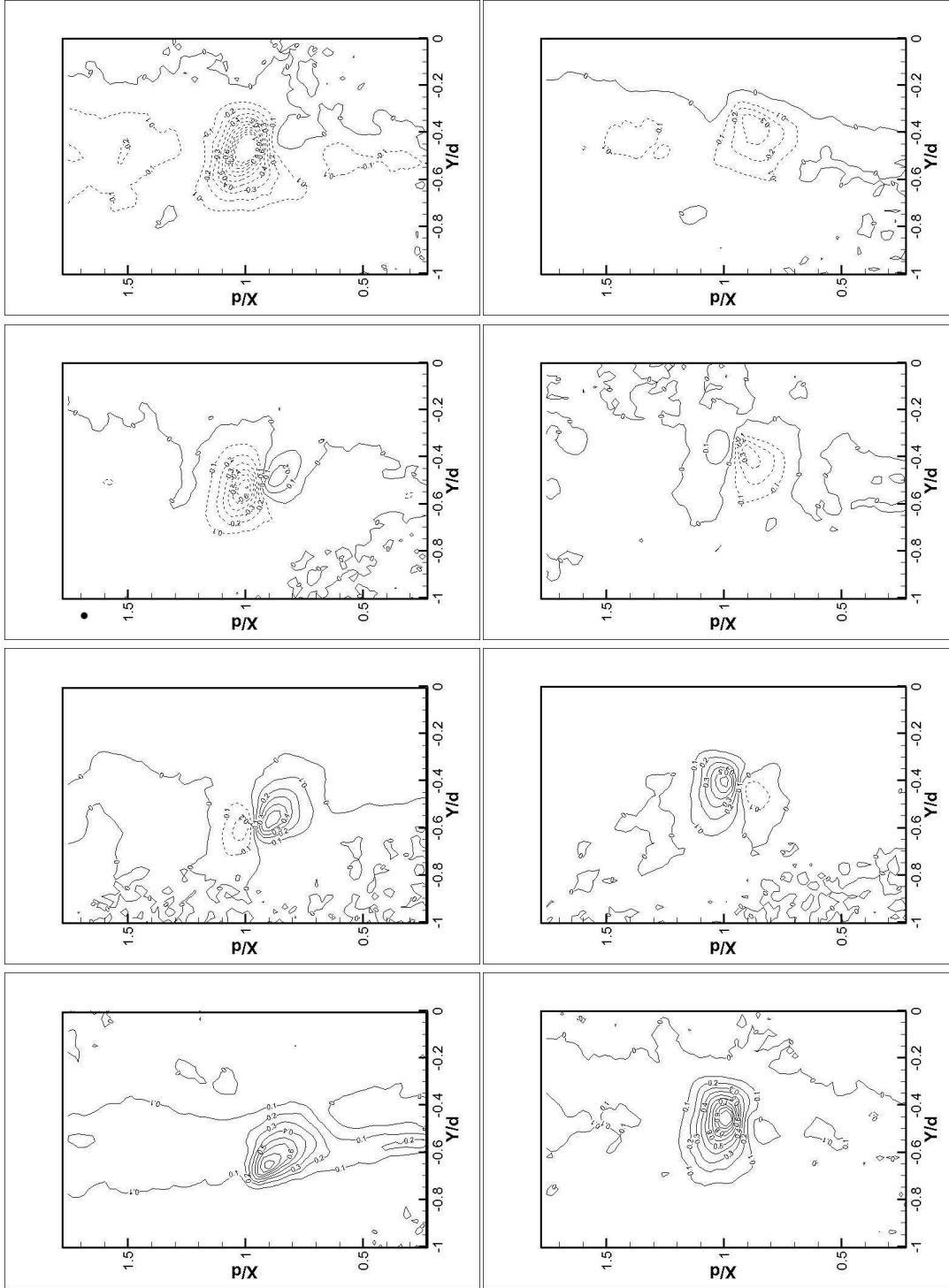


Figure 3.19 Two-point cross correlation $R_{\lambda_i, \phi'}$ at $X/d = 1$.

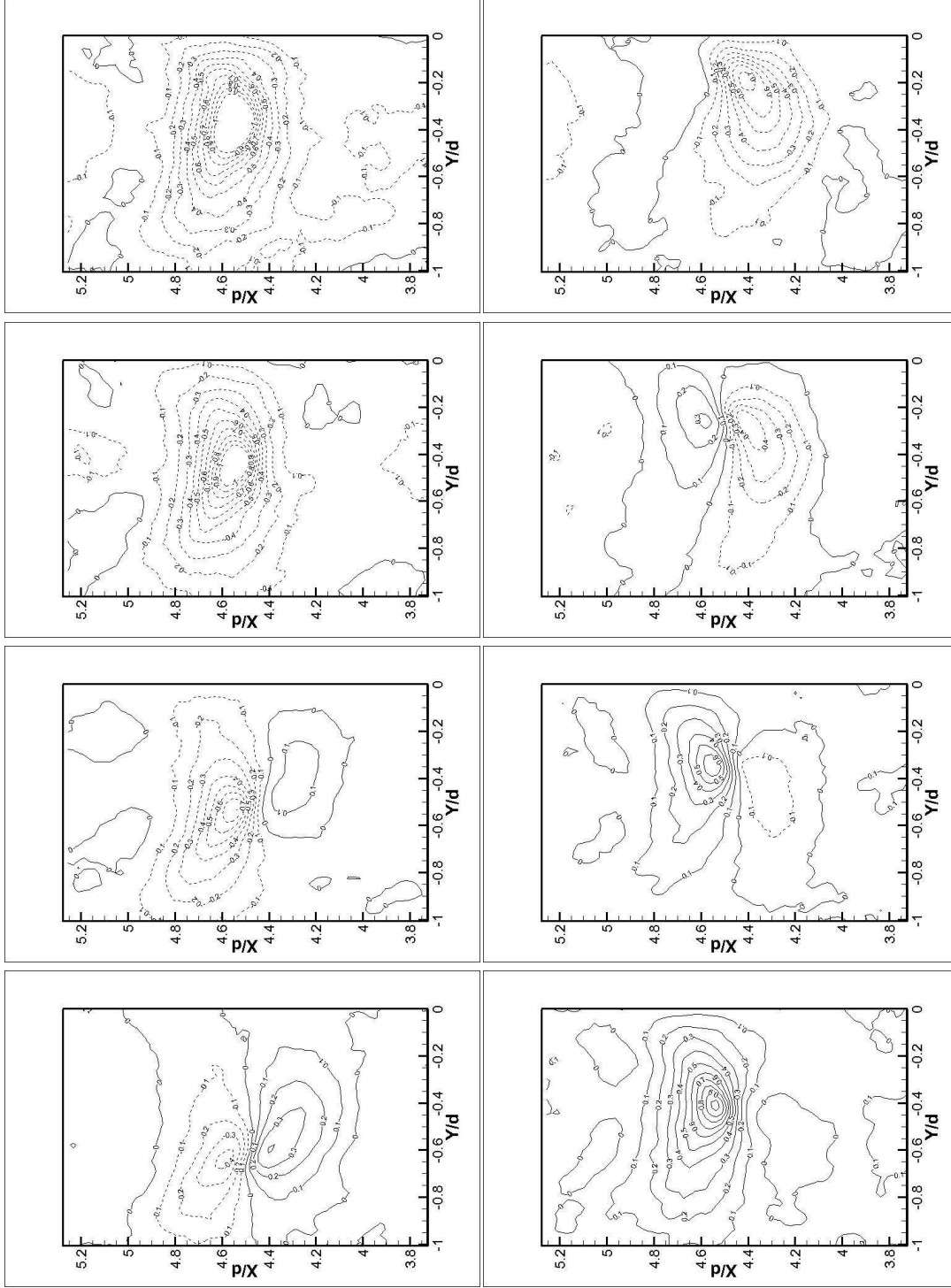


Figure 3.20 Two-point cross correlation $R_{\lambda_i \phi'}$ at $X/d = 4.5$.

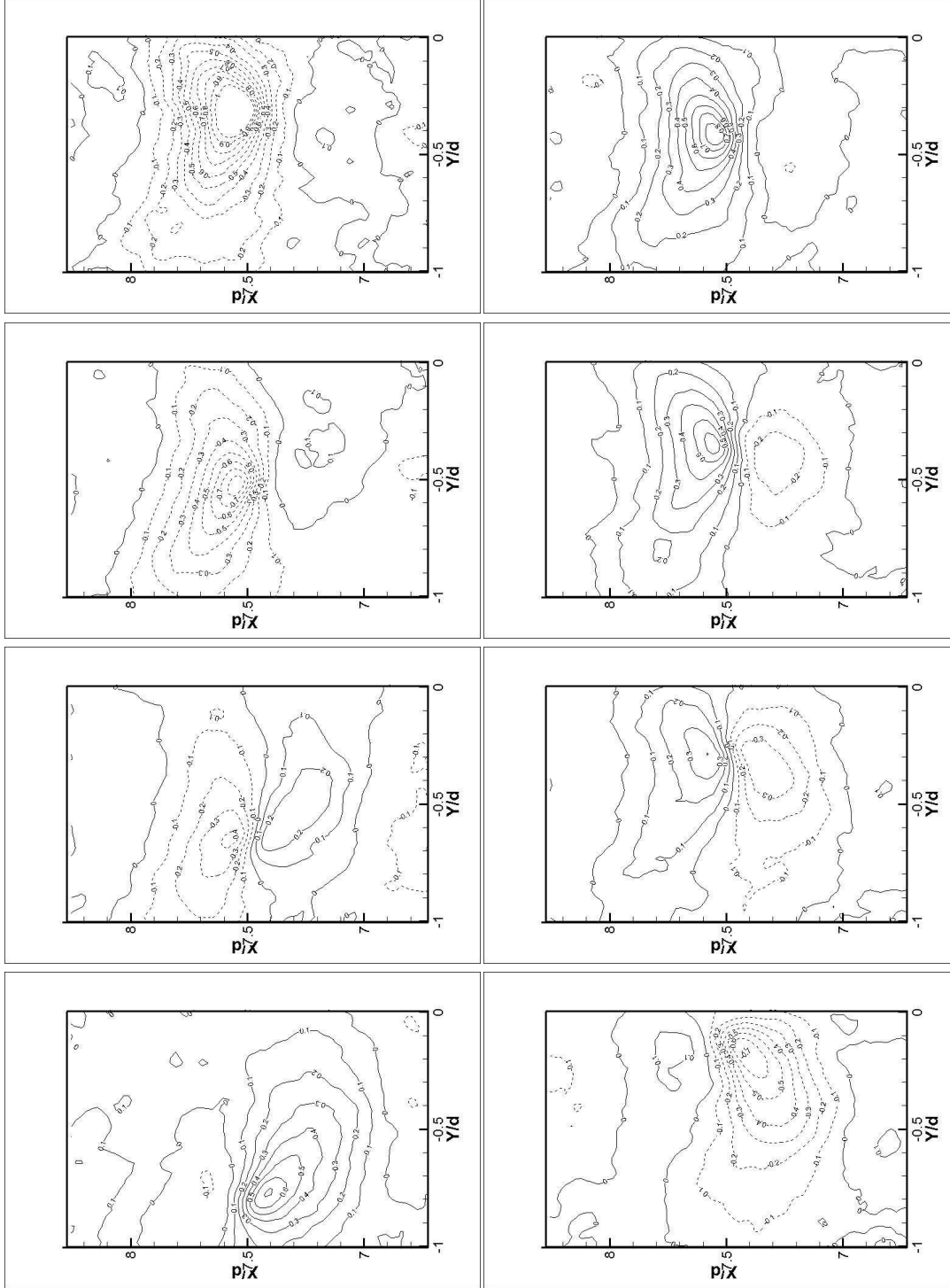


Figure 3.21 Two-point cross correlation $R_{\lambda_{ci}\phi'}$ at $X/d = 7.5$.

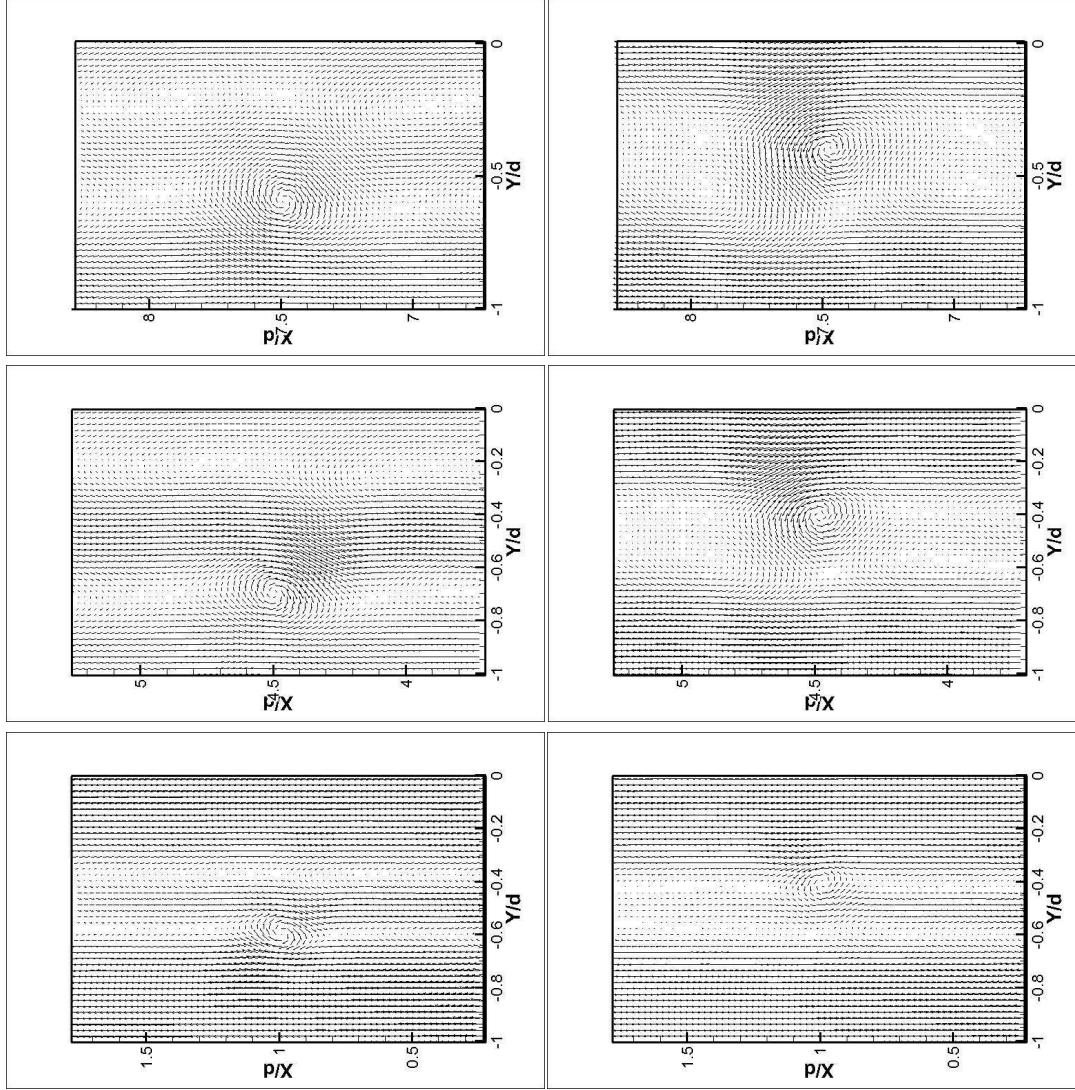


Figure 3.22 Linear stochastic estimation of velocity field with $U(x_o)$ subtracted from each vector, at $x/d=1, x/d=4.5$ and $x/d=7.5$. First row, on the left side of the wake and second row, on the right side of the wake.

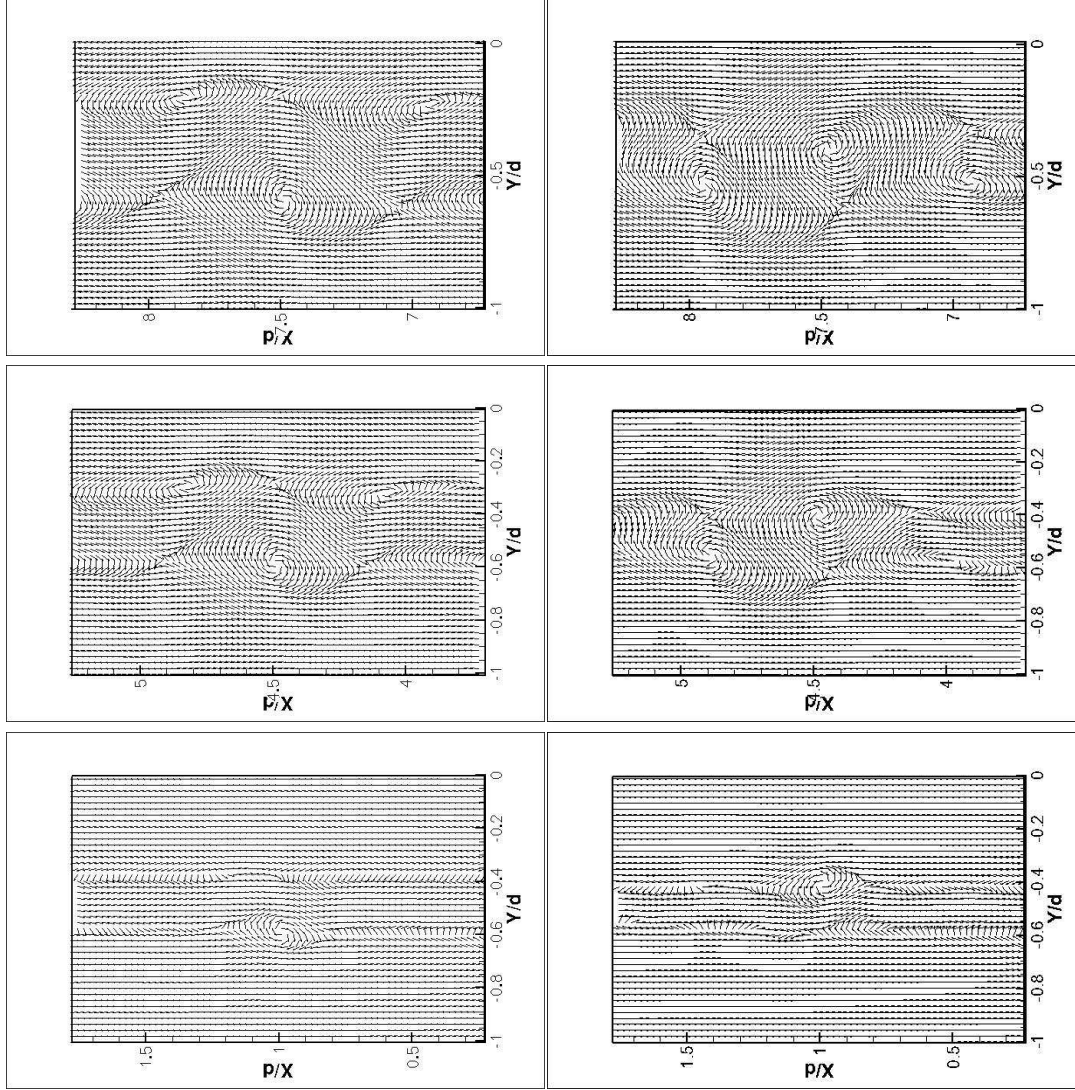


Figure 3.23 Linear stochastic estimation of velocity field with uniform vector length, at $x/d=1$, $x/d=4.5$ and $x/d=7.5$. First row, on the left side of the wake and second row, on the right side of the wake.

CHAPTER 4. Predictive capability of Large Eddy Simulation for pointwise and spatial turbulence statistics in a confined rectangular jet

A paper submitted to Chemical Engineering Science

Bo Kong, Anup Gokarn, Michael G. Olsen, F. Battaglia, Rodney O. Fox and James C. Hill

Abstract

Large-eddy simulations (LES) were performed for a confined rectangular liquid jet with a co-flow and compared in detail with particle image velocimetry (PIV) measurements. A finite-volume CFD library, OpenFOAM, was used to discretize and solve the filtered Navier-Stokes equation. The effects of grid resolution, numerical schemes and subgrid models on the LES results were investigated. The second and fourth order schemes showed the nearly same performance, while the fourth order scheme costs much more computationally. Subgrid model comparison showed that the locally dynamic procedure is necessary for complex flow simulation. Model validation was performed by comparing LES data for the point-wise velocity statistics such as the mean and the root-mean-square velocity, shear stress, correlation coefficient, velocity skewness and flatness with the PIV data. In addition, LES data for the two-point spatial correlations of velocity fluctuations that provide structural information were computed and compared with PIV data. Good agreement was observed leading to the conclusion that the LES velocity field accurately captures the important characteristics of all the turbulent length scales present in the flow, from the fully resolved energy-containing eddies to the subgrid-scale dissipative eddies.

4.1 Introduction

The presence of turbulence in fluid flows can greatly improve mixing efficiency. In the chemical process industry, proper mixing is necessary to control product formation, and therefore a well designed reactor is critical to both maximize reactor efficiency and minimize the formation of pollution. Turbulent mixing in reacting flows is important when the goal is to increase reaction rates by increasing the surface area for molecular contact. Computational fluid dynamics (CFD) can be used as a design tool to improve reactor design since it is a relatively inexpensive approach compared to the costs associated with experiments. However, one challenge that exists with CFD in predicting complex turbulent liquid-phase flows is validating appropriate models due to the lack of available experimental data.

Typical reactor configurations employed for industrial applications are cylindrical, continuously stirred tank reactors Patterson and Passino (1990), coaxial jet stirred reactors Brodkey (1975); Forney et al. (1996) and cross-flow or tee-mixed reactors Lu et al. (1997). Cylindrical reactors pose challenges in the laboratory with flow visualization techniques such as particle image velocimetry (PIV) due to the curvature and associated image distortion in the measurements. An alternative approach is to use a rectangular configuration. Although a rectangular configuration is not common in industrial applications, a rectangular reactor provides a simple geometry suitable for both experimental measurements and CFD simulations.

Large eddy simulation (LES) is a computational methodology that can be used in simulations of turbulent flow problems. The technique aims to reduce the high grid resolution requirements of direct numerical simulation (DNS) by obtaining solutions for the energy containing large scales and modeling the effect of the unresolved small (subgrid) scales. With present computing power still not making DNS feasible except in the simplest turbulent flows, LES is a popular tool of choice for complex flow calculations. Nevertheless, despite the wide spread acceptance of LES as a flow simulation tool, there are remarkably few reported *detailed* validation studies for complex flows such as the one considered in this work. Moreover, even for relatively simple flows (such as fully developed turbulent channel flow), reported LES validation studies are usually limited to point-wise statistical quantities (e.g. mean velocity,

Reynolds stresses), which depend only indirectly on the spatial structure of the flow Kim and Menon (1999); Fureby and Grinstein (2002); Sagaut and Ciardi (2006). Because the predictive capability of LES is generally attributed to its ability to capture large-scale flow structures Lesieur and Metais (1996); Sagaut (2001), it can be argued that a detailed validation study of LES simulations should also include *spatial*, or two-point, flow statistics (e.g., two-point correlation functions). For this purpose, PIV data are particularly well suited because they capture the same range of large-scale flow structures as the LES models Adrian (1991); Agrawal and Prasad (2002b).

In the literature, two distinct approaches to LES can be found: *numerical* and *physical* LES Pope (2000); Fureby and Grinstein (2002). Numerical LES utilizes special numerical schemes to provide an effective viscosity (implicit numerical filtering) Pope (2000), whereas physical LES uses an explicit subgrid stress (SGS) model to close the governing equations. In the present work, a physical LES approach is utilized and an explicit subgrid closure model is used.

Subgrid scale models have improved over the last thirty years, from the simple eddy viscosity model of Smagorinsky Smagorinsky (1963) to the more complex high-order models described by Berselli et al Berselli et al. (2006). The Smagorinsky model is one of the first and simplest closure approximations to the SGS and is of the eddy viscosity type. The length scale and velocity scale are obtained from the filter width (related to grid size) and the resolved strain rate tensor. The proportionality constant C_s is obtained by equating production and dissipation rates in the inertial range for homogeneous isotropic turbulence. The dynamic Smagorinsky model was originally formulated by Germano et al Germano et al. (1991) and then modified by Lilly Lilly (1992). These authors describe a procedure to evaluate the coefficient C_s as a function of space and time, so that the SGS is applied only where required and important effects such as backscatter are accounted for by the model. The scale similarity model described by Bardina et al Bardina et al. (1980) is based on wavenumber asymptotics and is established on the idea that the smallest resolved scale energy is a good representation of the largest subgrid scale energy. The model has been found to be unstable and is often

complemented by an eddy viscosity term (making it a mixed model), illustrated by Zhang et al. (1993). The eddy viscosity type models represent phenomenologically what one generally observes in a turbulent flow, i.e., turbulence is dissipative in the mean. A second approach that has recently received attention is to treat the closure mathematically. One such technique, by Geurts (1997), is the approximate deconvolution method in which one obtains an approximation to the true turbulent field from the filtered field. For further details on the history and development of LES models, one may refer to articles by Metais and Lesieur (1996) and Berselli et al. (2006).

SGS models, when formulated are usually tested for simple canonical flows such as homogeneous isotropic turbulence and turbulent channel flows for which DNS data are available Kim and Menon (1999); Volker et al. (2002). In such flows the models can be validated *a priori* and *a posteriori* Piomelli et al. (1988); Stolz and Adams (1999). Some models have been found to work well in *a priori* tests but not so well in *a posteriori* tests. However, the ultimate test for the subgrid scale models and LES is to compare the simulations with more complex flows similar to those that occur in real applications. An attempt in this direction is made in the present study.

In the present study, LES has been performed for a confined rectangular jet with co-flowing fluid and the results are compared with experimental PIV data collected for the same geometry and flow conditions. The effects of five subgrid scale models are studied: the constant Smagorinsky, the dynamic Smagorinsky, the one equation eddy, the dynamic one equation eddy, and the mixed Smagorinsky model. Grid-resolution studies are also performed to seek a grid size sufficient to represent the flow physics. A thorough validation of the flow is made with experimentally measured data for the velocity field, including point-wise statistics, the mean and the variance of velocity, shear stress, correlation coefficient, skewness and flatness, and two-point statistics, spatial correlations. Two-point spatial correlations based on the LES velocity field provide information about large-scale turbulent structures that to our knowledge have not been previously validated against PIV data in a manner similar to that presented in the current study.

4.2 Flow configuration and experimental procedures

The confined rectangular jet apparatus and experimental setup are shown in Fig. 4.1. As previously mentioned, the rectangular configuration is preferred in order to avoid optical distortion due to refraction, and because it is also easier to model computationally. For the present study, the flow rates in each of the inlet channels are 0.4, 0.8, and 0.4 L/s, corresponding to free-stream velocities of 0.2 m/s, 0.4 m/s, and 0.2 m/s, respectively. The Reynolds number is 20,000 based on the distance (0.06 m) between the two side walls of the test section and the bulk velocity.

A schematic of the measurement system is shown in Fig. 4.2. The laser sheet used in the PIV measurements passes through the centerline of the reactor in the z -direction, and the laser sheet thickness was 0.5 mm. Approximately 24 grams of hollow glass spheres were added to the total reservoir volume of 3500 liters. The nominal diameter of these seed particles was $11.7\ \mu\text{m}$ and the particles' density was $1.1\ \text{g}/\text{cm}^3$. The image magnification of the CCD camera was 0.12, and the numerical aperture was 8. Two distinct images were captured per velocity field with a $1000\ \mu\text{s}$ time delay. A multi-pass cross-correlation technique with decreasingly small window sizes was used to compute the velocity field. The final interrogation spot size measured 16 pixels by 16 pixels, corresponding to 0.9 mm on each side. With 50% overlap between interrogation windows, the velocity vector spacing was 0.45 mm in both the x - and y -directions. At each observed location, 5000 velocity realizations were obtained and analyzed.

The smallest Kolmogorov scale (η) in the flow field is estimated to be approximately $94.5\ \mu\text{m}$, based on the exit width of the jet and the turbulent kinetic energy at the tips of the two split plates Feng et al. (2005). Thus, the spatial resolution of the PIV measurements is approximately 4.6η . Although the smallest turbulent scales of the flow cannot be fully resolved, second-order quantities such as velocity fluctuations and characteristics of large-scale structures can be measured accurately.

According to Prasad et al (1992), the random error in PIV measurements can be estimated as one-tenth of the effective particle image diameter. For the results presented here, the particle image diameter was $8.3\ \mu\text{m}$. Thus, the error relative to the particle

displacement is $\pm 1.7\%$ for the center stream and $\pm 3.4\%$ for the outer streams.

Another important consideration in PIV measurements is the peak locking effect, in which the correlation peak location is biased towards the nearest integer pixel Christensen (2004). The peak-locking effect can be quantified by the peak-locking coefficient, which ranges from 0 to 1: 0 indicates no peak locking effect and 1 indicates strong peak locking effect Stanislas et al. (2005). In the present experiments, this coefficient was found to be 0.05, indicating an acceptably low degree of peak locking. Further details on the experimental apparatus and PIV measurement can be found in Feng et al. (2005).

4.3 Numerical modeling and formulation

4.3.1 Governing equations and subgrid models

In order to separate the large scales from the small scales, a filtering operation is performed to the incompressible Navier-Stokes equations, resulting in the dimensionless filtered equations expressed as,

$$\frac{\partial \bar{u}_i}{\partial x_i} = 0, \quad (4.1)$$

$$\frac{\partial \bar{u}_i}{\partial t} + \frac{\partial \bar{u}_i \bar{u}_j}{\partial x_j} = -\frac{\partial \bar{p}}{\partial x_i} + \frac{1}{Re} \frac{\partial}{\partial x_j} \left(\frac{\partial \bar{u}_i}{\partial x_j} \right) - \frac{\partial \tau_{ij}}{\partial x_j}, \quad (4.2)$$

where the turbulent SGS tensor that requires modeling is

$$\tau_{ij} = \overline{u_i u_j} - \bar{u}_i \bar{u}_j$$

and t represents time, \bar{u}_i is the filtered velocity field, \bar{p} is the pressure and Re is the Reynolds number.

Solutions to the filtered Navier-Stokes equations are obtained by using OpenFOAM (Open Field Operation and Manipulation), an open source Computational Fluid Dynamics (CFD) software package. OpenFOAM is a suite of C++ libraries and applications for manipulating field variables using the finite volume method. In the current study, the *pisoFoam* solver in OpenFOAM is used, which use the PISO (pressure-implicit split operator) Issa (1986) algorithm as its iterative solver.

The choice of a subgrid scale model is a critical aspect in numerical modeling of a turbulent flow using LES. Five SGS models are considered to close the subgrid stress tensor in the current study. The simplest model is the Smagorinsky model Smagorinsky (1963), which is an eddy-viscosity-type model that represents the effect of the subgrid scales as an enhanced diffusivity for the large-scale flow. The SGS tensor is modeled as

$$\tau_{ij} - \frac{1}{3}\tau_{kk}\delta_{ij} = -2\nu_t\bar{S}_{ij}$$

where ν_t is the turbulent eddy-viscosity, δ_{ij} is the Kronecker delta function, and the filtered rate of the deformation tensor is

$$\bar{S}_{ij} = \frac{1}{2} \left(\frac{\partial \bar{u}_i}{\partial x_j} + \frac{\partial \bar{u}_j}{\partial x_i} \right).$$

The turbulent eddy-viscosity is parameterized by equating the subgrid scale energy production and dissipation to obtain $\nu_t = C_s \bar{\Delta}^2 |\bar{S}|$, where $|\bar{S}| = \sqrt{2\bar{S}_{ij}\bar{S}_{ij}}$ and C_s is the Smagorinsky coefficient to be specified. For the constant Smagorinsky model, the coefficient $C_s = 0.17$ was chosen to be consistent with the findings of Lilly (1967) using an energy balance analogy for isotropic turbulence. The effective filter width $\bar{\Delta}$ is a function of the grid resolution and is defined as $\bar{\Delta} = (\Delta_1\Delta_2\Delta_3)^{1/3}$, where Δ_1 , Δ_2 , and Δ_3 represent the filter widths in x , y , and z directions, respectively.

The dynamic Smagorinsky model of Germano et al. (1991) and Lilly (1992) defines the coefficient C_s as a function of space and time. The dynamic model permits the eddy-viscosity to asymptotically approach zero near solid walls and in regimes where the flow is laminar. The model however requires a new filtering operation to be performed within a test filter volume, where the test filter width $\hat{\Delta}$ is assumed to be greater than the grid filter width $\bar{\Delta}$. A Gaussian filter is used for the test-filter operation. On application of the test filter to the Navier-Stokes equations, the sub-test scale stress tensor, T_{ij} , is obtained as

$$T_{ij} = \widehat{\bar{u}_i \bar{u}_j} - \hat{\bar{u}}_i \hat{\bar{u}}_j.$$

The quantities τ_{ij} and T_{ij} are related by the identity of Germano et al. (1991):

$$L_{ij} = T_{ij} - \hat{\tau}_{ij} = \widehat{\bar{u}_i \bar{u}_j} - \hat{\bar{u}}_i \hat{\bar{u}}_j$$

where L_{ij} is the resolved turbulent stress that can be explicitly calculated. The term T_{ij} is also modeled similar to the subgrid scale turbulent stress τ_{ij} using a Smagorinsky model with the same model constant C_s . Using a least squares approach, Lilly (1992) obtained the coefficient C_s as

$$C_s = \frac{\langle L_{ij} M_{ij} \rangle}{\langle M_{ij} M_{ij} \rangle} \quad (4.3)$$

where angled brackets denote averaging over the test filter volume and $M_{ij} = \widehat{\Delta^2 |\bar{S}| \bar{S}_{ij}} - \widehat{\Delta^2 |\bar{S}|} \widehat{\bar{S}_{ij}}$.

The subgrid kinetic energy model was proposed by Yoshizawa (1986), and is also called the one equation eddy viscosity model, since it solves the transport equation for the subgrid kinetic energy, \bar{k} , given as,

$$\frac{\partial \bar{k}}{\partial t} + \bar{u}_i \frac{\partial \bar{k}}{\partial x_i} = \nu_t |\bar{S}|^2 - \epsilon + \frac{\partial}{\partial x_j} \left(\nu_t \frac{\partial \bar{k}}{\partial x_j} \right) \quad (4.4)$$

where the eddy viscosity, ν_t is calculated by $\nu_t = C_k \overline{\Delta k}^{1/2}$ and the dissipation rate, ϵ , is given by $\epsilon = C_\epsilon \bar{k}^{3/2} / \overline{\Delta}$, where the constants C_k and C_ϵ use the suggested values in Fureby et al. (1997), 0.05 and 1.00 respectively. The dynamic procedure used to determine C_s in the dynamic Smagorinsky model also can be used to determine C_k and C_ϵ here, which results in the dynamic subgrid kinetic energy model, first proposed by Kim and Menon (1995). Here, C_k and C_ϵ are calculated using the procedure formulated by Fureby et al. (1997),

$$C_k = \frac{\langle L_{ij} M_{ij}^k \rangle}{\langle M_{ij}^k M_{ij}^k \rangle}, \quad \text{and} \quad C_\epsilon = \frac{\langle \xi m \rangle}{\langle m m \rangle}$$

where, $M_{ij}^k = \widehat{\Delta \bar{k}^{1/2} |\bar{S}|} - 2 \widehat{\Delta \bar{k}^{1/2}} \widehat{|\bar{S}|}$, $\xi = L_{ii}$ and $m = \widehat{\bar{k}^{3/2} / \Delta} - \widehat{\bar{k}^{3/2}} \widehat{1/\Delta}$. There are also other slightly different dynamic procedures proposed, such as Winkler and Rani (2006) and Yoshizawa (1986). When this dynamic procedure is used in the subgrid kinetic energy coefficient, the baseline assumption is that there exists a balance equation for the kinetic energy at the second filter level Fureby et al. (1997).

The scale-similar model was introduced by Bardina et al. (1980), in which it was assumed that the component of the SGS most active in the energy transfer from large to small scales can be estimated with sufficient accuracy from the smallest resolved scales, which can be obtained by filtering the SGS velocity. In other words, it can be simply assumed that the SGS stresses for the full velocity field are the same as the ones corresponding to the resolved field.

$$\tau_{ij} = \overline{u_i u_j} - \bar{u}_i \bar{u}_j \sim \widehat{\overline{u_i u_j}} - \widehat{\bar{u}_i \bar{u}_j}.$$

However, the scale-similar model is inadequate as a stand-alone SGS model, since it is not very robust numerically as it does not introduce enough dissipation in some cases. Therefore, it needs to be combined with a purely dissipative model, e.g., Smagorinsky like, which leads to mixed Smagorinsky model Zhang et al. (1993),

$$T_{ij} = \widehat{\overline{u_i u_j}} - \widehat{\bar{u}_i \bar{u}_j} - 2 \left(C_s \bar{\Delta} \right)^2 |\bar{S}| \bar{S}_{ij} \quad (4.5)$$

.

More information on the implementation of SGS models in OpenFOAM can be found in Fureby et al. (1997).

4.3.2 Simulation methodology of the confined rectangular jet

LES was performed for the confined rectangular jet using the same geometry as in the experiments. There are three inlet streams at the inflow boundary, each separated by splitter plates, and the flow is bounded by walls in the y - and z -directions, thus mimicking the geometry of the experimental apparatus. The flow is numerically complex due to the presence of sharp gradients in the two shear layers that form downstream of the splitter plates and in the boundary layers that form along the walls. At the walls, the no-slip boundary condition is applied, and at the exit a convective outflow boundary condition, as in Ferziger and Peric (2002), is used. For the pressure Poisson equation, a zero normal gradient

condition is used at the inflow and at the walls. At the outflow boundary zero gauge pressure is specified.

In order to compare the LES with experimental data, inflow conditions that are similar to those in the experiments are required. For this purpose, the inflow conditioning technique of Klein et al Klein et al. (2003) is used. The method generates inflow velocity signals that have statistical properties similar to those in the experiments. The inflow velocities are given by

$$\bar{u}_i = \langle u_i \rangle + a_{ij} U_j$$

where $\langle u_i \rangle$ is the mean in flow velocity, U_j is obtained from a random field with a prescribed two-point statistic, and

$$(a_{ij}) = \begin{pmatrix} (R_{11})^{1/2} & 0 & 0 \\ R_{21}/a_{11} & (R_{22} - a_{21}^2)^{1/2} & 0 \\ R_{31}/a_{11} & (R_{32} - a_{21}a_{31})/a_{22} & (R_{33} - a_{31}^2 - a_{32}^2)^{1/2} \end{pmatrix}$$

where R_{ij} is the correlation tensor. $\langle u_i \rangle$ and R_{ij} are obtained from the experimental data at the location of the trailing edge of the splitter plates. This location is denoted as $x/d = 0$ cm and henceforth, all other positions are relative to this location. The third velocity component in the span-wise direction is not measured in the experiments, and an approximation of $\langle w'w' \rangle = \langle v'v' \rangle$ is used. Some statistics at the node next to the inlet surface are presented in Fig. 4.3, which shows that this approximation at the inlet is consistent with the PIV data.

LES results are strongly dependent on the choice of simulation parameters (i.e. grid resolution, finite-difference scheme, SGS model), so a series of “pre-simulations” were carried out to determine the optimal choices needed to adequately capture the flow physics of the rectangular jet. Note the same inflow generator parameters were used in all the ‘pre-simulations’. First, a grid-resolution study using the dynamic Smagorinsky model and the linear (second order central) scheme for interpolation and Gaussian integration for velocity gradient was performed. The effect of increasing grid resolution was investigated. Since the geometry of the test section is strictly rectangular, it is natural to use hexahedral shaped cells. It is important to note that the grid size cannot be changed independently of the filter length scale because the filtering is performed implicitly by the grid. The grid sizes investigated were

1. $160 \times 60 \times 80$ cells in x , y , and z directions, respectively,
2. $240 \times 90 \times 110$ cells,
3. $320 \times 120 \times 134$ cells,
4. $400 \times 150 \times 166$ cells.

Note that all the cells are exactly the same in size for a given resolution. The near wall resolution is commonly expressed in terms of dimensionless units of y^+ , and y^+ for the first off-wall grid point is approximately 10, 8, 6 and 4 for the four grid resolutions above. Figure 4.4 compares the resolved stream-wise and cross-stream rms velocity profiles for the LES (lines) with those obtained from PIV (symbols) at $x/d = 1$ and $x/d = 7.5$. The results of all four grid resolutions show fairly good agreement with the experiment data. However, the cross-stream velocity rms profile of the lowest grid resolution shows significantly lower peak values at the stream interfaces than the experimental results and the results using higher grid resolutions at $x/d = 1$, and higher peak values at $x/d = 7.5$. The difference between the results of the three higher grid resolutions is quite small, thus grid independence can be considered achieved, especially in the jet region. There is indeed some improvement in the wall region using higher grid resolution because at higher resolutions, more of the flow is resolved and the LES is approaching DNS. The role of subgrid models and numerical schemes can be seen to be diminishing with the increasing of grid resolution. Therefore, the LES results reported hence forth are performed using the grid resolution of $240 \times 90 \times 110$ cells in order to observe the different performances of the different subgrid models.

OpenFOAM offers a wide selection of schemes for numerical simulations, which are classified into three basic categories: interpolation, gradient, and component of gradient normal to a cell face. Since all cells are hexahedral shaped, the gradient normal to a cell face scheme is not important for the current study. All the scheme tests here used the dynamic Smagorinsky model, and the second order backward scheme was used to march in time implicitly. It is often argued that a dissipative scheme should not be used for LES since it is difficult to differentiate between numerical and SGS dissipation Mahesh et al. (2004). Since the main role of SGS model

is to dissipate a proper amount kinetic energy, non-dissipative schemes are preferred for LES, therefore central differencing schemes are adopted hereafter. Figure 4.5 shows the velocity rms results using linear (second order) and cubic (fourth order) interpolation schemes with the same gradient scheme, namely, the Gauss integration. There is virtually no difference in the quality of the solutions. However, the cubic scheme costs much more computationally, nearly twice the linear scheme. This agrees with the conclusion of Meinke et al. (2001), which compared the performance of second- and six-order central differencing. Similar conclusions can be found in Breuer (1998). Figure 4.6 gives the results of the different gradient schemes with the linear interpolation scheme, including Gaussian integration, second and fourth order least squares method. No difference can be observed, and the computational costs are almost the same. Therefore, the linear interpolation scheme and second order least squares gradient scheme are used in the simulations performed in this study.

Finally, the constant Smagorinsky, dynamic Smagorinsky, one equation eddy, dynamic one equation eddy and mixed Smagorinsky models were used to compare the effect of the SGS model on the resolved-scale solution (Fig. 4.7). When using the three non-dynamic models, a van Driest wall function van Driest (1956) is used to reduce the SGS viscosity to zero near wall boundaries. Figure 4.7 also shows the rms of velocities in the stream-wise and cross-stream direction, respectively. The mixed Smagorinsky model under predicts the rms velocities in both the shear layers and boundary layers, indicating it generates too much dissipation. The performance of the mixed Smagorinsky model was already found to decrease rather quickly with decreasing grid resolution Fureby et al. (1997). At $x/d = 1$, the constant Smagorinsky and one equation eddy models also under predict the peak values in the stream interfaces significantly. This is because that close to the inlet, the flow is not fully developed yet. However the velocity gradient is quite high in this region, and thus the turbulent viscosity is over predicted without the locally dynamic adjustment. At $x/d = 7.5$, all the other four subgrid models except the mixed Smagorinsky model agree well with the experimental data. In general, the two dynamic models show the best results in the shear layers, showing the importance of dynamically adjusting the coefficient. However in the boundary layers, the two

one equation eddy models (constant coefficient and dynamic model) can capture the sharp streamwise velocity peaks, while the constant and dynamic Smagorinsky can not. The one equation models also show slightly better results in the cross-stream rms velocity profiles in the boundary layer regions. Table 4.1 shows the dimensionless computational time cost of these models, normalized with the values of constant Smagorinsky.

Smagorinsky	dynSmagorinsky	mixedSmagorinsky	oneEqEddy	dynOneEqEddy
1	1.144	1.128	1.134	1.275

Table 4.1 Dimensionless CPU time comparison between subgrid models.

Fureby et al Fureby et al. (1997) found the dynamic models cost 20% more cpu time than their constant coefficient counterparts, and one extra subgrid energy equation also costs 20 % more cpu time. The values in table 4.1 only show a less than 15 % increase. The LES results generated for comparison with experiments in the following section are obtained using the dynamic one equation eddy model, since it gives the best results in the turbulent jet, despite its higher computational costs.

In summary, it is noteworthy that this series of simulations clearly suggests that grid resolution and subgrid models are the important parameters for obtaining accurate simulations of the confined rectangular jet.

4.4 Results and discussion

In this section, LES data from the resolved scales of the simulations are compared with the results from PIV experiments to determine how accurately the LES model predicts both the point-wise and spatial two-point turbulent velocity statistics. As noted in the Introduction, the spatial two-point statistics provide insights into the large-scale turbulent structures in the flow. For these comparisons, the LES code is run for sufficiently long times to allow for the flow to reach a dynamical steady state, after which data are collected at time intervals roughly equal to those used for the PIV experiments. For consistency, the LES data are treated to extract the one- and two-point statistics using the same algorithms as used for the PIV data.

4.4.1 Point-wise (one point) statistics

First, comparisons between the LES and PIV data are made for point-wise flow statistics. These comparisons are made at four different downstream locations in the flow field. One of these locations is at 2cm downstream of the tips of the splitter plates (corresponding to $x/d = 1$), and the other three locations are $x/d = 4.5$, $x/d = 7.5$, and $x/d = 12$ downstream of the tips of the splitter plates. Note that for all of the quantities compared up to second-order moments (i.e., not skewness nor kurtosis), at $x/d = 1$ the LES statistics agree almost exactly with the PIV data since the inflow condition was provided using PIV experimental data. Also note that because the inflow conditions in the experiments are not exactly symmetric about the jet centerline, neither are those used in the LES.

A comparison of the mean stream-wise velocity profiles at the four locations is shown in Fig. 4.8. As in all of the comparison plots, the LES data in Fig. 4.8 are represented by lines, and the PIV data are presented using symbols. As can be seen in Fig. 4.8, initially the flow resembles a planar jet. However, unlike a planar jet, which has unbounded outer streams and can thus approach a self-similar profile, the flow in the present study is confined, and lacking a semi-infinite geometry, does not achieve self similarity. Instead, as both the jet and the boundary layers at the top and bottom walls of the channel grow, the potential core of the outer streams rapidly disappears, and the flow progresses towards fully developed channel flow. As depicted in Fig. 4.8, the LES mean velocity profiles compare well with the experiments for all four locations downstream of the splitter plates. The agreement is especially good in the steep gradients at the wall boundaries, indicating that the LES model is performing very well in the near-wall regions.

The stream-wise rms velocity profiles are shown in Fig. 4.9, and close agreement is observed between the LES predictions and the PIV measurements. For example, at $x/d = 4.5$, $x/d = 7.5$, and $x/d = 12$, the differences between the peak u_{rms} as measured by PIV and computed using LES are 5.8 %, 6.5%, and 7.6 %, respectively. At location $x/d = 1$, the turbulent boundary layers forming along the top and bottom of the splitter plates merge together, resulting in two highly turbulent regions centered at the tips of the splitter plates. Note that there is a

small “dip” in turbulence intensity at $y/d = -1$ and $y/d = 1$. This is indicative of a small wake region formed in the vicinity just downstream of the splitter plates. Also, due to the no-slip condition, within the boundary-layer regions upstream of the splitter plate, the peak in turbulence within the boundary layer occurs some distance above the splitter plate. Thus, just after the boundary layers merge at the trailing edge of the splitter plates, these lower turbulence regions near the walls manifest themselves in the lower turbulence region observed just downstream of the splitter plates at $x/d = 1$. Note that this wake region is short-lived however, as at $x/d = 4.5$ downstream, the “dip” in turbulence intensity is no longer observed.

While the rms peaks at $x/d = 1$ are due to the turbulence in the inlet boundary layers, this turbulence rapidly decays, and at further downstream locations, the turbulence is instead primarily due to the mean shear in the flow. The rapid decay in the turbulence formed from the inlet boundary layers was demonstrated in Liu et al (2006), where PIV measurements were performed in the same geometry as the present study, but with the velocities in all three streams uniform (and thus no mean shear in the flow). Thus, downstream of the splitter plates, the peaks in turbulence fluctuations are most prominent in regions where the mean shear is greatest. The shear is greatest in the near-wall regions (i.e., the boundary layers along the top and bottom walls of the reactor) and in the shear regions formed at the boundaries between the center jet and the outer streams. As the flow progresses downstream, the steep velocity gradients in the boundary region between the jet and outer streams decrease, and consequently, the peaks in turbulence fluctuations in these regions also decrease.

The cross-stream (i.e., wall-normal) rms velocity profiles are shown in Fig. 4.10, and as with the stream-wise rms results there is good agreement between LES and experiment. However, in shear layer flows, such as a jet or wake, the cross-stream velocity are much harder to numerically predict and measure than the stream-wise component, but it is the component actually responsible for the mass and momentum transfer. At further downstream locations, the differences between the peak rms measured by PIV and computed using LES at the stream interfaces are 7.7 %, 1.5%, and 15.4%, at $x/d = 4.5$, $x/d = 7.5$, and $x/d = 12$, respectively. The cross-stream fluctuation profiles exhibit similar behavior to the stream-wise fluctuation

profiles, although the peak intensities for the cross-stream rms velocities are slightly lower than the stream-wise rms velocities.

The span-wise rms velocity w' for the four downstream locations is shown in Fig. 4.11. However, corresponding PIV measurements are unavailable for the span-wise velocity component, since only two-dimensional PIV data were collected. The inlet boundary conditions for the LES were derived from the PIV data with the assumption that $\langle w'w' \rangle = \langle v'v' \rangle$. Note that a comparison of the computed v' and w' fluctuations at the downstream locations shows close agreement between these two quantities, validating the assumption used for the inlet flow conditions for the LES. In a RANS simulation of this flow geometry, Feng et al. (2005) used the same assumption about the cross-stream and span-wise velocity fluctuations to estimate the turbulent kinetic energy from PIV data in order both to obtain inflow conditions for the RANS $k-\varepsilon$ turbulence model and also to compare the PIV results with the RANS predictions. The accuracy of this assumption regarding the cross-stream and span-wise velocity fluctuations has been demonstrated by the present LES study.

A comparison of the resolved shear stress $\langle u'v' \rangle$ is shown in Fig. 4.12. As with the u - and v -velocity fluctuations, the comparison between LES and experiment is quite good. However, this should come as no surprise based on the excellent agreement that was observed in the mean velocity profiles. The Reynolds shear stress is responsible for the spreading and growth of the jet, and the agreement observed in the mean velocity profiles at all three downstream locations implies similar growth behavior for the jet. This similar growth behavior suggests that the Reynolds stresses should be similar, which, indeed they are. Note that the computed LES shear stress is determined purely from the resolved scales and does not include any contribution from the subgrid scales.

Normalizing the Reynolds shear stress in the manner

$$\rho_{uv} = \frac{\langle u'v' \rangle}{\sqrt{\langle u'^2 \rangle \langle v'^2 \rangle}}$$

yields the correlation coefficient ρ_{uv} . Figure 4.13 is a comparison of profiles of the correlation coefficient at the four different downstream locations. The profiles display good agreement between the LES and experimental data, and provide additional confidence in the reliability

the LES methodology. Recall that as the flow progresses downstream, it transitions from a jet flow towards fully developed channel flow. Indeed, at $x/d = 12$, both the LES and PIV correlation coefficient profiles closely resemble the correlation coefficient observed in the fully developed turbulent channel flow simulations of Moin and Kim Moin and Kim (1982).

Further comparisons between the LES and PIV data for the velocity skewness and flatness factors, defined by

$$S(u_i) = \frac{\langle u_i'^3 \rangle}{\langle u_i'^2 \rangle^{3/2}} \quad \text{and} \quad F(u_i) = \frac{\langle u_i'^4 \rangle}{\langle u_i'^2 \rangle^2},$$

are shown in Figs. 4.14 and 4.15 for $x/d = 4.5$ and $x/d = 7.5$, respectively. Skewness is a measure of the asymmetry of the velocity probability distribution. The stream-wise skewness $S(u)$ is consistent with a u -velocity distribution that is symmetric about the centerline at $y/d = 0$, and also symmetric about the shear layers, whose centers are located at approximately $y/d = -1$ and $y/d = 1$, and indeed, the mean stream-wise velocity profiles presented earlier showed this to be the case. The cross-stream skewness, $S(v)$, suggests that the v -velocity distribution is approximately antisymmetric about the centerline. This is consistent with fluid being entrained from the higher velocity jet region into the slower outer streams. Fluid entrained from the jet into the upper outer stream corresponds to a positive cross-stream velocity, while fluid entrained from the jet into the lower outer stream corresponds to a negative cross-stream velocity, resulting in antisymmetry in the cross-stream velocity component around the centerline of the reactor.

Flatness, also known as kurtosis, is a measure of whether the velocity probability distribution is peaked or flat relative to a normal distribution. Data sets with high kurtosis tend to have a distinct peak near the mean, decline rapidly, and have long tails extending far from the mean. Data with low kurtosis tend to have a flat top near the mean. The kurtosis for a standard normal distribution is 3. For the confined jet flow, a kurtosis value close to 3 is observed over much of the channel at $x/d = 12$, where the flow is rapidly approaching fully developed turbulent channel flow. The overall good agreement in the skewness and kurtosis between the LES and experiments is especially encouraging, considering the difficulties associated with the measurement of high-order statistics.

4.4.2 Spatial (two-point) statistics

In the previous section, comparisons between the LES and PIV data were confined to ensemble-averaged quantities determined at one point within the flow field. However, one distinct advantage of LES over ensemble-averaged computational methods (such as Reynolds-averaged Navier-Stokes methods) is that LES fully resolves the instantaneous large-scale turbulent structures in the flow field. Since PIV similarly captures the instantaneous large-scale structures, it is possible to compare the spatial characteristics of the turbulence for both simulations and experiments in addition to point-wise statistics. In this way, the LES model can be validated to both accurately model the point-wise statistical properties of the turbulence and also accurately represent the underlying large-scale turbulent structures.

Much of turbulence theory begins with the concept of an energy cascade where energy from the large scales in the flow is transferred to the small scales and is eventually dissipated by the viscous length scales. Two-point correlations give useful information about this energy cascade and form the basis of spectral theories. Parameters such as the stream-wise and cross-stream length scales based on the two-point correlations are often used to provide an estimate of the eddy sizes involved in the flow Pope (2000). For canonical flows such as isotropic turbulence, the two-point correlation is completely determined by the longitudinal length scale, and *a posteriori* testing of closure models often involves the prediction of these length scales. For more complex flows with no directional homogeneity, eddy structures of different shapes and sizes are prevalent and two-dimensional plots of spatial correlations give a better sense of the energetic eddy structures in the flow. In order to obtain two-point spatial correlations from experiments, measurements with one fixed probe and one moving probe can be simultaneously utilized, as done by Shaw et al Shaw et al. (1995). PIV, however, enables measurement of a complete two-dimensional flow field, making the determination of spatial correlations relatively easy. Spatial correlations can also be easily obtained from LES based on the resolved velocity field to provide information about the characteristic large-scale structures. Similar calculations with LES data can be found in the recent publications, such as the prediction of 2-time features of turbulence in He et al. (2002) and the two-point velocity autocorrelations calculation in

Larchevêque et al. (2004). However, a detailed two-point statistics comparison between an LES model and experiments is still very rare in the LES literature.

The two-point spatial correlations of the velocity fluctuations are defined as

$$R_{u'_i u'_j}(x, y; X_0, Y_0) = \frac{\langle u'_i(x, y) u'_j(X_0, Y_0) \rangle}{\sqrt{\langle u'^2_i(x, y) \rangle \langle u'^2_j(X_0, Y_0) \rangle}}$$

where (X_0, Y_0) are the coordinates of a “basis point” about which the correlation is measured, and (x, y) are displacements from the basis point. Spatial auto- and cross-correlations of velocity fluctuations were calculated at various locations in the flow field from both the LES and PIV data for comparison. Since the PIV data were obtained in the plane $z = 0.05$ m (the center-plane of the reactor), all spatial correlations presented here are for this measurement plane. Within this plane, the spatial correlations were obtained for basis points at three downstream locations, namely $x/d = 4.5$, $x/d = 7.5$, and $x/d = 12$. At each of these stream-wise locations, spatial correlations were obtained for three different cross-stream locations, $y/d = 0$, $y/d = 0.5$, and $y/d = 1$, corresponding to the cross-stream coordinates of centerline of the reactor, the tip of the top splitter plate, and the centerline of the top outer stream, respectively. The locations of these nine basis points are illustrated schematically in Fig. 4.16, where the circles indicate the locations of the basis points.

Figures 4.17–4.20 show the spatial correlations $R_{u'u'}$, $R_{v'v'}$, $R_{u'v'}$, and $R_{v'u'}$, respectively, for the various basis points where the experimentally measured values and those obtained from LES are superimposed on the same plots for comparison. In these figures, the spatial correlations as measured by PIV are shown as colored contours, and the spatial correlations from the LES results are shown by contour lines. Each figure is shown as a matrix of nine sub-figures; moving from left to right, the X_0 basis point changes from $x/d = 4.5$, $x/d = 7.5$, to $x/d = 12$, and moving from top to bottom, Y_0 changes from $y/d = 0$, $y/d = 0.5$, to $y/d = 1$.

Figure 4.17 shows the stream-wise autocorrelation of $R_{u'u'}$ for the nine basis points throughout the flow-field. Strong agreement is observed between the autocorrelation fields measured by PIV and those predicted by LES. At all nine locations $R_{u'u'}$ appears as an ellipse with the major axis aligned in the stream-wise direction with a slight inclination. This shape has been observed previously for mixing layers by other researchers Oakley et al. (1996); Olsen and

Dutton (2002, 2003). The physical dimensions of the correlation for each cross-stream location grow larger as the stream-wise distance of the basis point from the splitter plates increases, indicating that the turbulent structures grow larger in size with increasing downstream distance. Of interest are the additional weak regions of positive correlation upstream and above and below the primary autocorrelation for basis point ($x_0/d = 4.5$, $y_0/d = 0.5$). These positively correlated regions suggest the presence of additional turbulent structures at these locations. Similar behavior was observed in cross-correlation fields of stream-wise velocity fluctuation and concentration fluctuation in an analysis of simultaneous PIV and planar laser induced fluorescence (PLIF) data collected for the same flow geometry by Feng et al (2007), albeit for a Reynolds number of 50,000. These correlation regions are artifacts of a vortex street that forms in the previously described wake region that forms just downstream of the splitter plates. They are displaced obliquely by about 45 degrees from the primary correlation region due to the presence of mean shear in the flow. These additional correlation regions are not visible in the autocorrelation fields for basis points further downstream in the flow since the structures responsible for their presence decay as the flow progresses downstream.

The spatial autocorrelation of the cross-stream velocity fluctuation, $R_{v'v'}$, is shown in Fig. 4.18, and once again, excellent agreement is seen between simulation and experiment. For all nine basis points, this correlation field is a vertically-oriented ellipse, once again consistent with what other researchers have observed in incompressible shear flows Olsen and Dutton (2002). As with $R_{u'u'}$, $R_{v'v'}$ is observed to grow in size with increasing downstream distance for basis points taken at the same y -location, indicating that the large-scale structures grow with increasing downstream distance from the splitter plates.

Finally, the spatial cross-correlations of the stream-wise and cross-stream velocity fluctuations $R_{u'v'}$ and $R_{v'u'}$ are shown in Figures 4.19 and 4.20, respectively, and once again the agreement between the PIV and LES results is quite strong. Note that for $y_0/d = 0$ (the jet centerline), the value of $R_{u'v'}$ is equal to zero, since this is a line of symmetry at which the Reynolds shear stress $\langle u'v' \rangle = 0$. The cross-correlation is antisymmetric about this y -location, since the shear stress is positive above this line of symmetry and negative below. At the other

y -locations about which $R_{u'v'}$ was calculated, the correlation at the basis point is not equal to zero. Also note that as the basis point is moved downstream, the features observed in the cross-correlation fields grow larger, once again indicative of the growth of the largest turbulent structures with increasing downstream distance.

4.5 Summary and conclusions

Large-eddy simulations were performed for a confined rectangular liquid jet, which is an especially challenging flow to model due to the presence of free-shear regions and solid walls at the boundaries of the geometry. Particle image velocimetry experiments were performed in an experimental apparatus of the same geometry as the simulations in order to both provide inlet conditions for the simulations and also to provide detailed one- and two-point velocity statistics that could be used to validate the accuracy of the LES models used in this investigation. It was shown that an *in situ* turbulence generation procedure can represent the experimental data at the inflow boundary quite well once it has been parameterized by the measured inlet turbulence statistics. The effect of grid resolution, numerical schemes, and subgrid turbulence models on the resolved-scale statistics were studied in a systematic manner to determine the effect of these parameters on the simulation results. Four different grid resolutions were tested, the improvement of the two higher resolutions compared to the resolution chosen for the presented simulation is rather small, thus the grid independence was considered obtained. The performance of second and fourth order central schemes for interpolation and second order Gaussian integration, second order and fourth order least square as gradient scheme have been tested, and no noticeable differences were seen. The constant Smagorinsky and one equation eddy model, using the standard value for the constant was found to be overly dissipative, as is generally observed in large-eddy simulations. The two dynamic models, dynamic Smagorinsky and dynamic one equation eddy model, show similar resolved-scale statistics in the jet region, which suggests that they were able to resolve most of the turbulent energy and accurately model the subgrid scales. Although the dynamic one equation eddy model is more computationally expensive than the dynamic Smagorinsky, it gives better agreement with experimental results

in the wall boundary layers, and thus the presented simulations were conducted with the dynamic one equation eddy model.

A comparison of point-wise velocity statistics, including mean stream-wise velocity, rms velocity fluctuations, Reynolds shear stress, and the correlation coefficient showed excellent agreement between the LES and PIV data. Third- and fourth-order point-wise resolved-scale velocity statistics corresponded well with the experimental values, further verifying the accuracy of the LES model used in the present study. In addition to the point-wise statistical comparisons, the capability of LES to model large-scale turbulent structures was evaluated by comparing two-point spatial correlations of velocity fluctuations as derived from the LES data with the corresponding results calculated from the PIV data. Both spatial auto- and cross-correlations were compared. The spatial correlations from the LES data compared very well with the spatial correlations from the experimental data, demonstrating that the LES correctly predicts the length scales and orientation of the large-scale turbulent structures and also correctly models their growth rate. The excellent agreement observed between both the point-wise statistics and two-point spatial correlations of velocity fluctuations demonstrates that the LES model is able to accurately capture the important characteristics of all the turbulent length scales present in the flow, from the fully resolved energy-containing eddies to the subgrid-scale dissipative eddies.

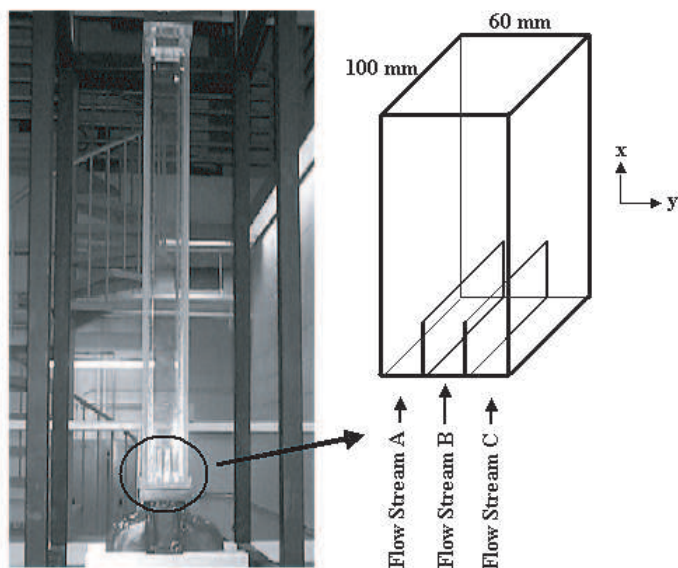


Figure 4.1 Photograph and schematic of the confined rectangular jet test section.

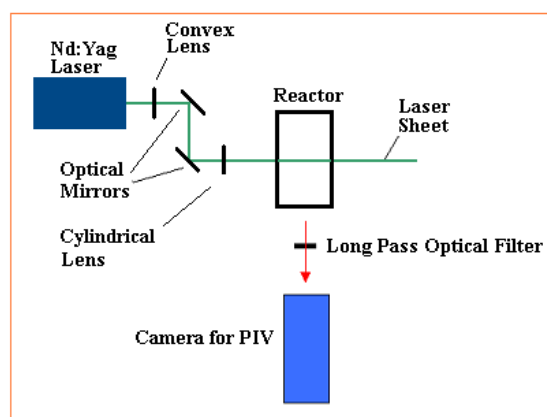


Figure 4.2 Schematic of the optical setup for the PIV experiments.

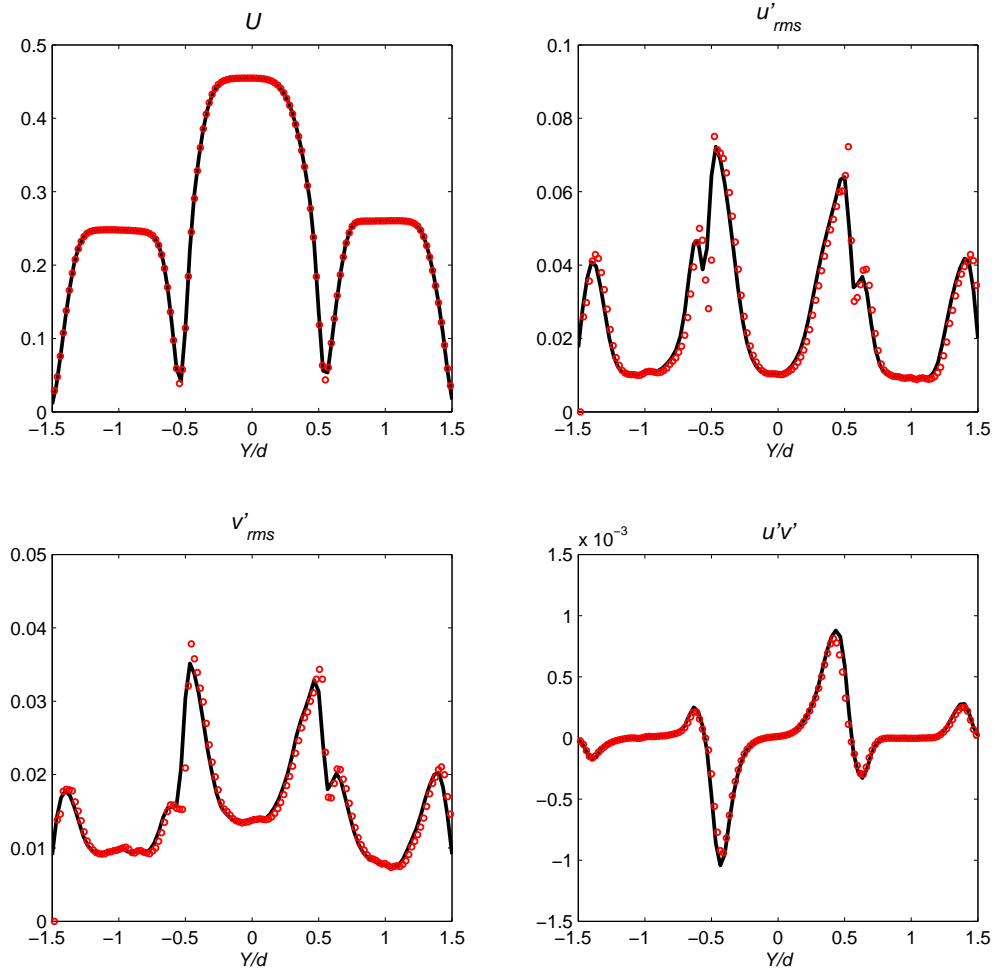


Figure 4.3 Mean and rms stream-wise velocity, cross-stream wise rms velocity and shear stress profiles at at the node next to inlet surface.

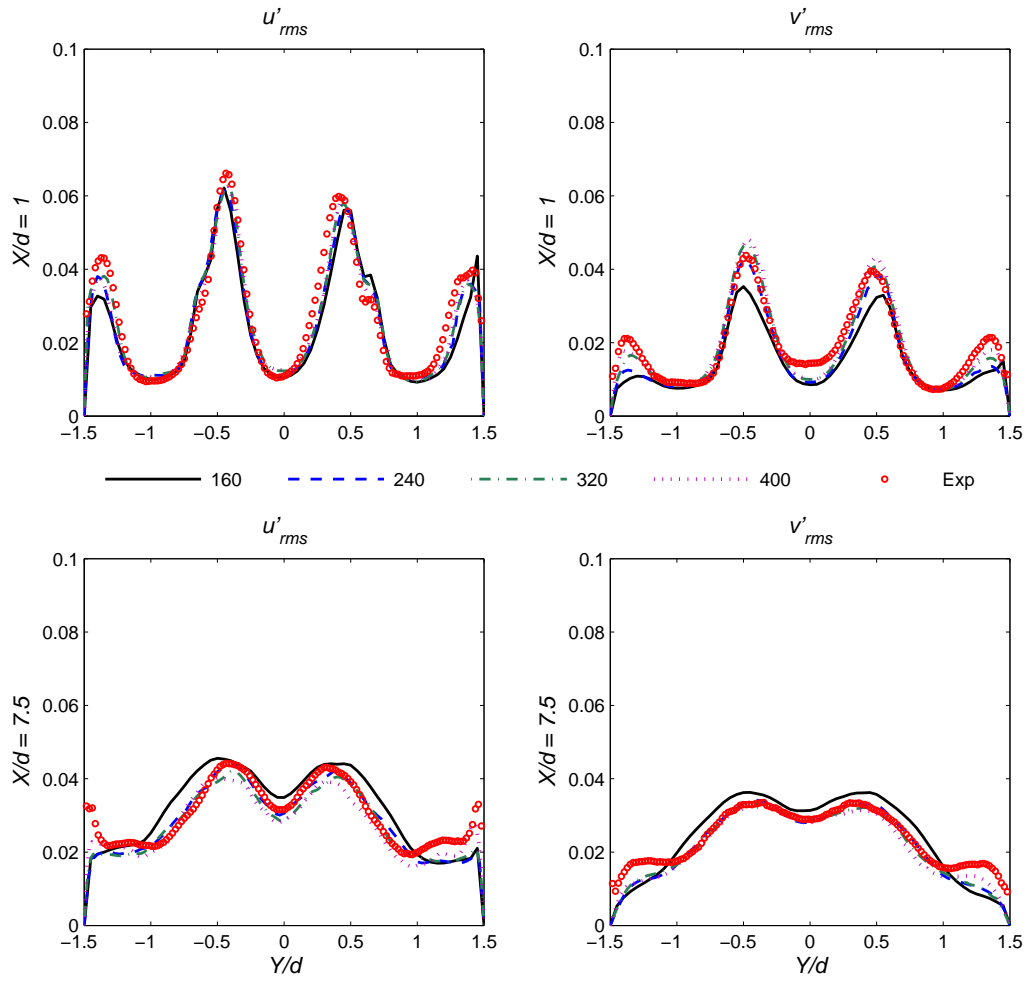


Figure 4.4 Stream-wise and cross-stream wise rms velocity profiles at $x/d = 1$ and $x/d = 7.5$ for four different grid resolutions compared with PIV experiments.

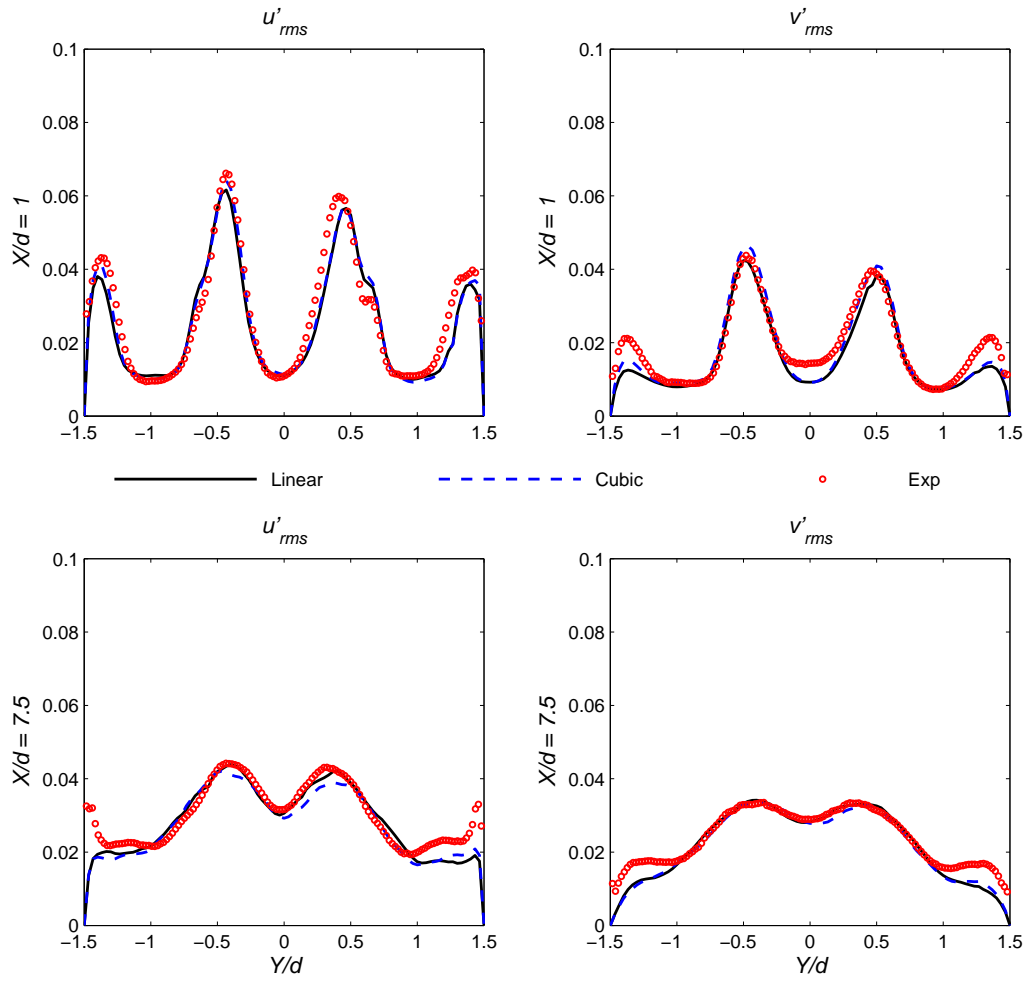


Figure 4.5 Stream-wise and cross-stream wise rms velocity profiles at $x/d = 1$ and $x/d = 7.5$ for linear and cubic interpolation schemes compared with PIV experiments.

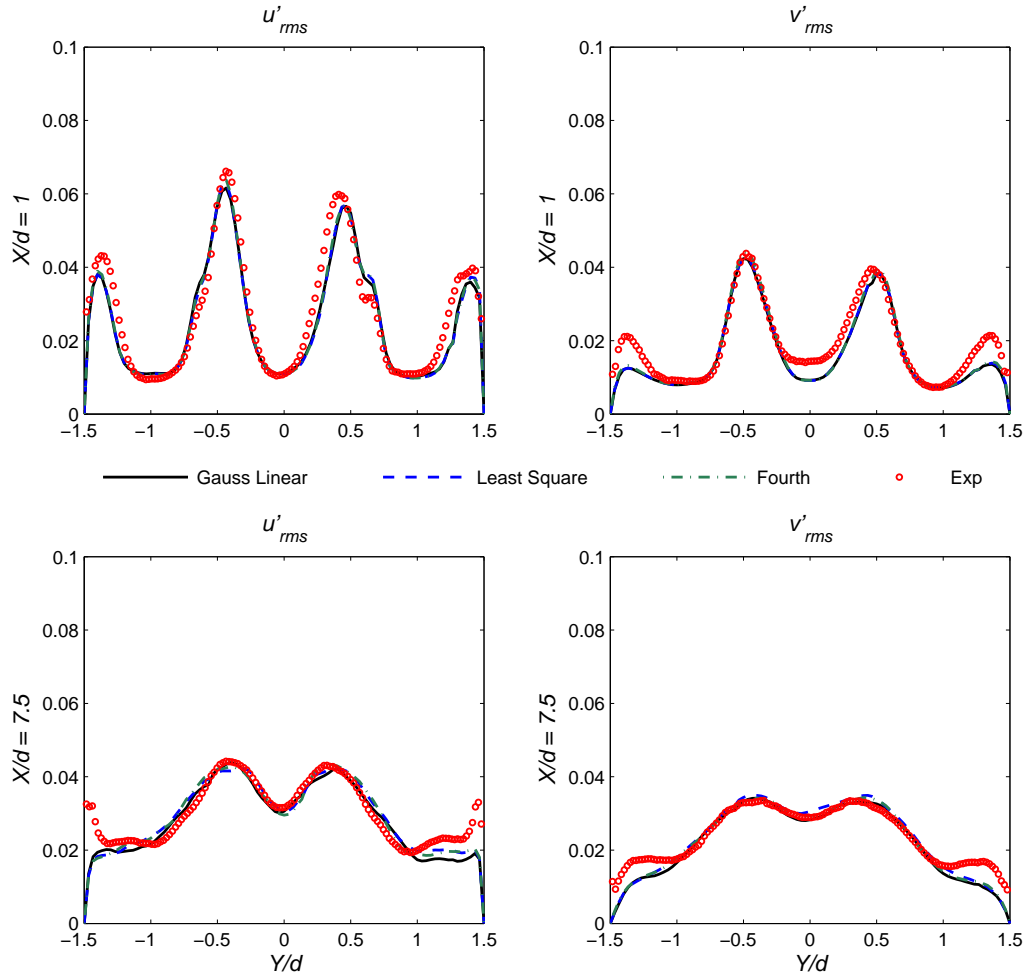


Figure 4.6 Stream-wise and cross-stream wise rms velocity profiles at $x/d = 1$ and $x/d = 7.5$ for Gaussian, second and four order least square gradient schemes compared with PIV experiments.

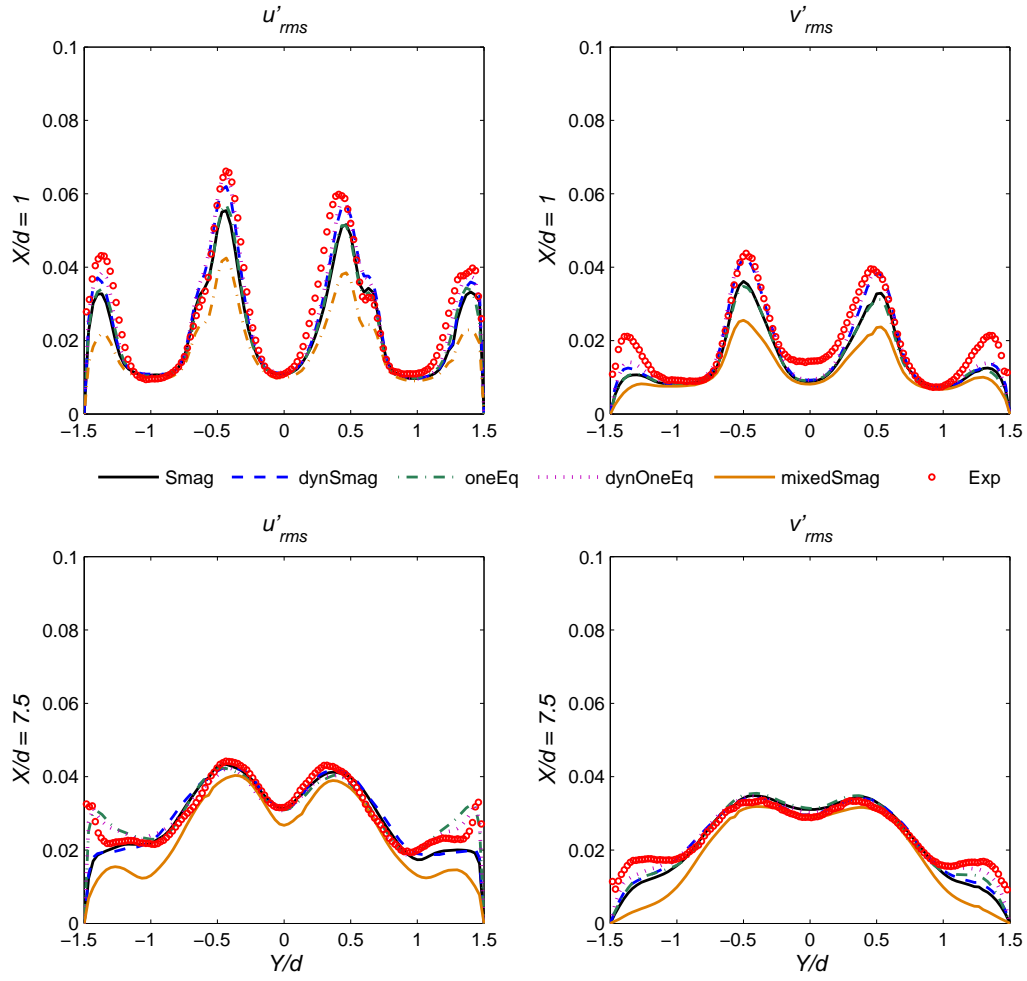


Figure 4.7 Stream-wise and cross-stream wise rms velocity profiles at $x/d = 1$ and $x/d = 7.5$ for constant Smagorinsky, dynamic Smagorinsky, one equation eddy, dynamic one equation eddy and mixed Smagorinsky, compared with PIV experiments.

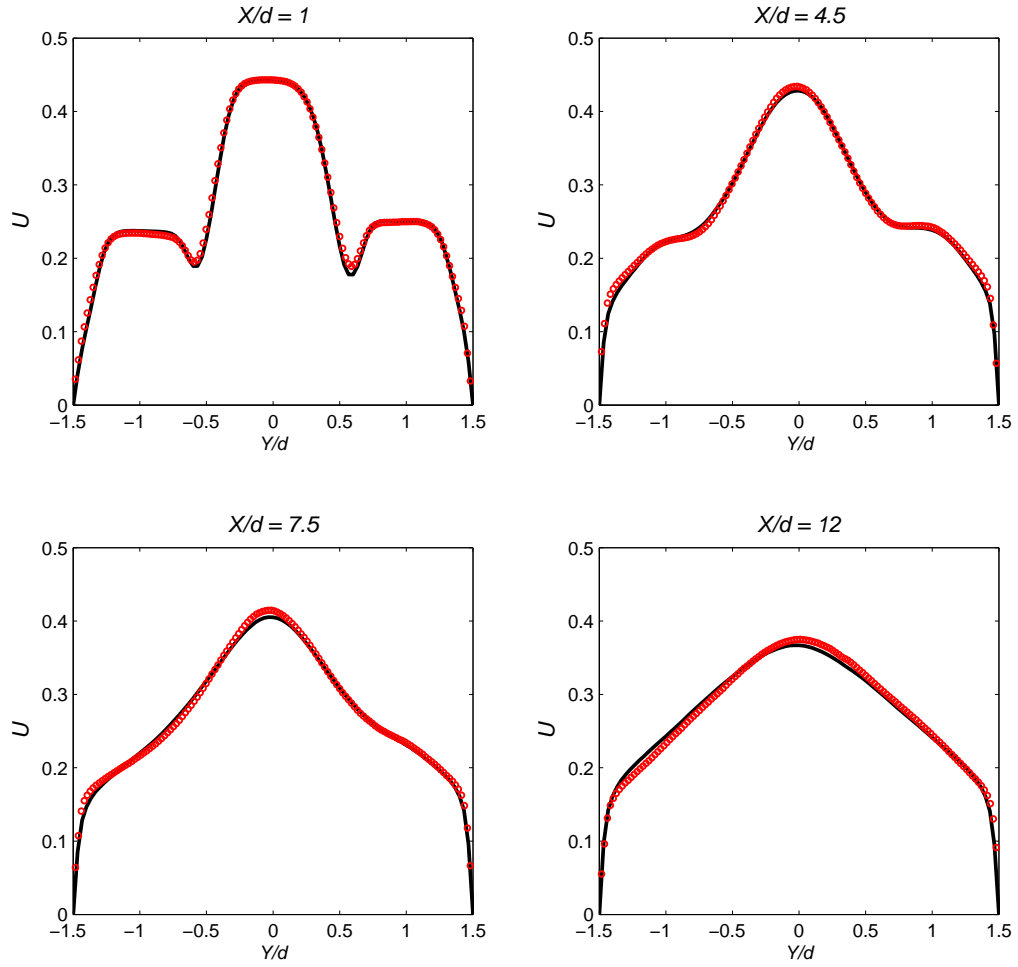


Figure 4.8 Mean stream-wise velocity profiles at four locations downstream of the splitter plates depicting growth of mixing layer. Experiments are shown as symbols and LES as lines.

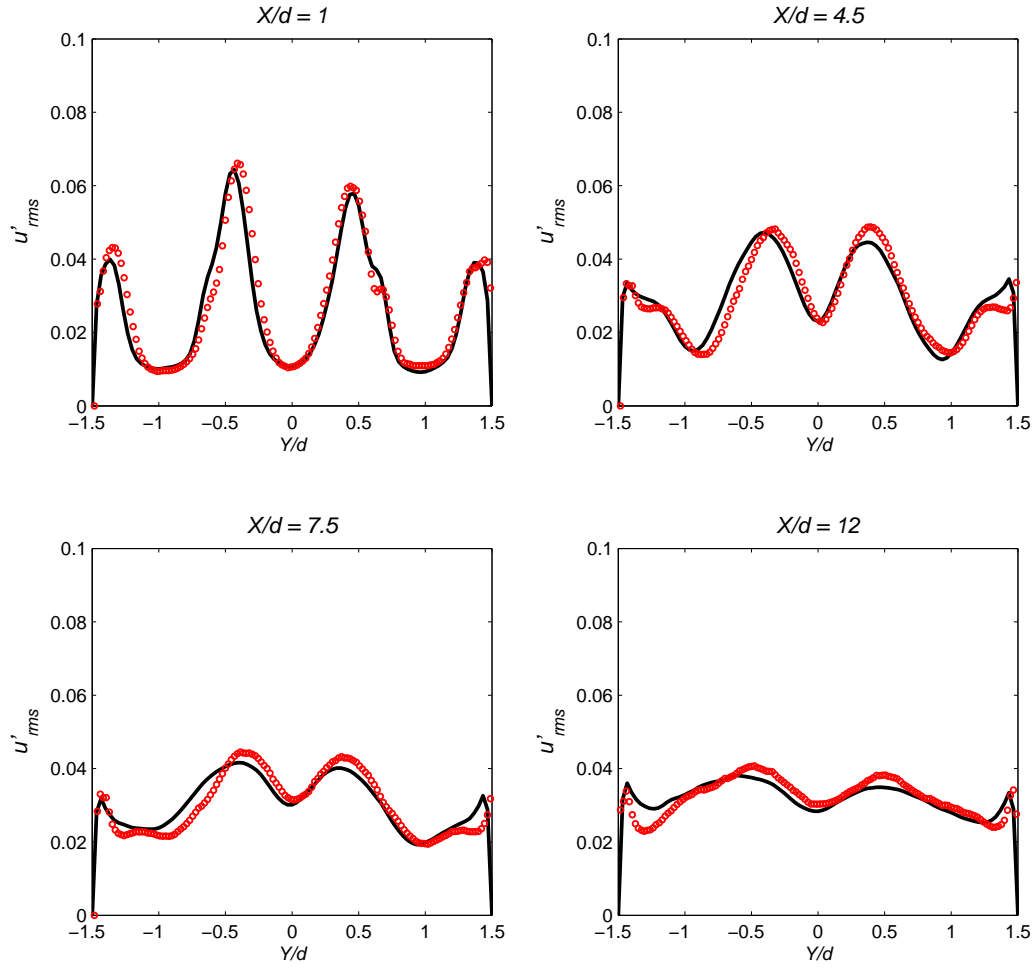


Figure 4.9 Stream-wise rms velocity profiles at four locations downstream of the splitter plates. Experiments are shown as symbols and LES as lines.

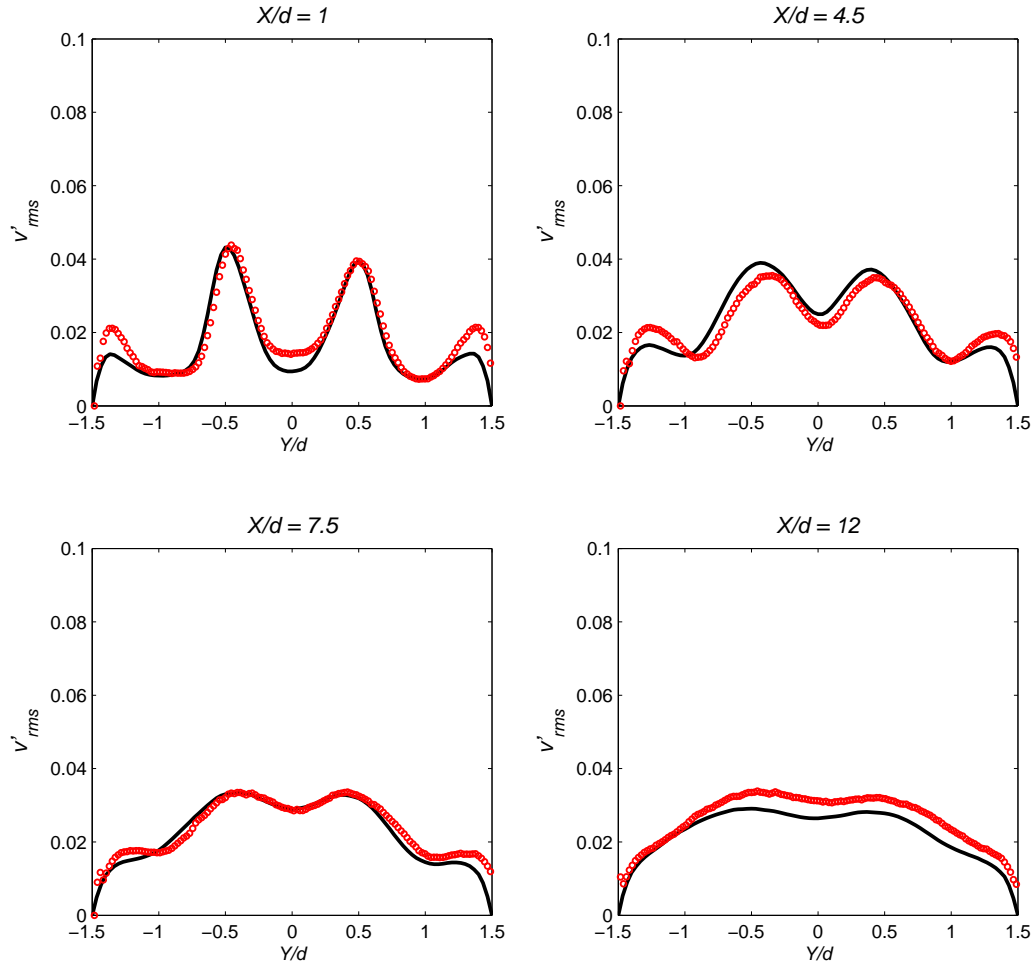


Figure 4.10 Wall-normal rms velocity profile at four locations downstream of the splitter plates. Experiments are shown as symbols and LES as lines.

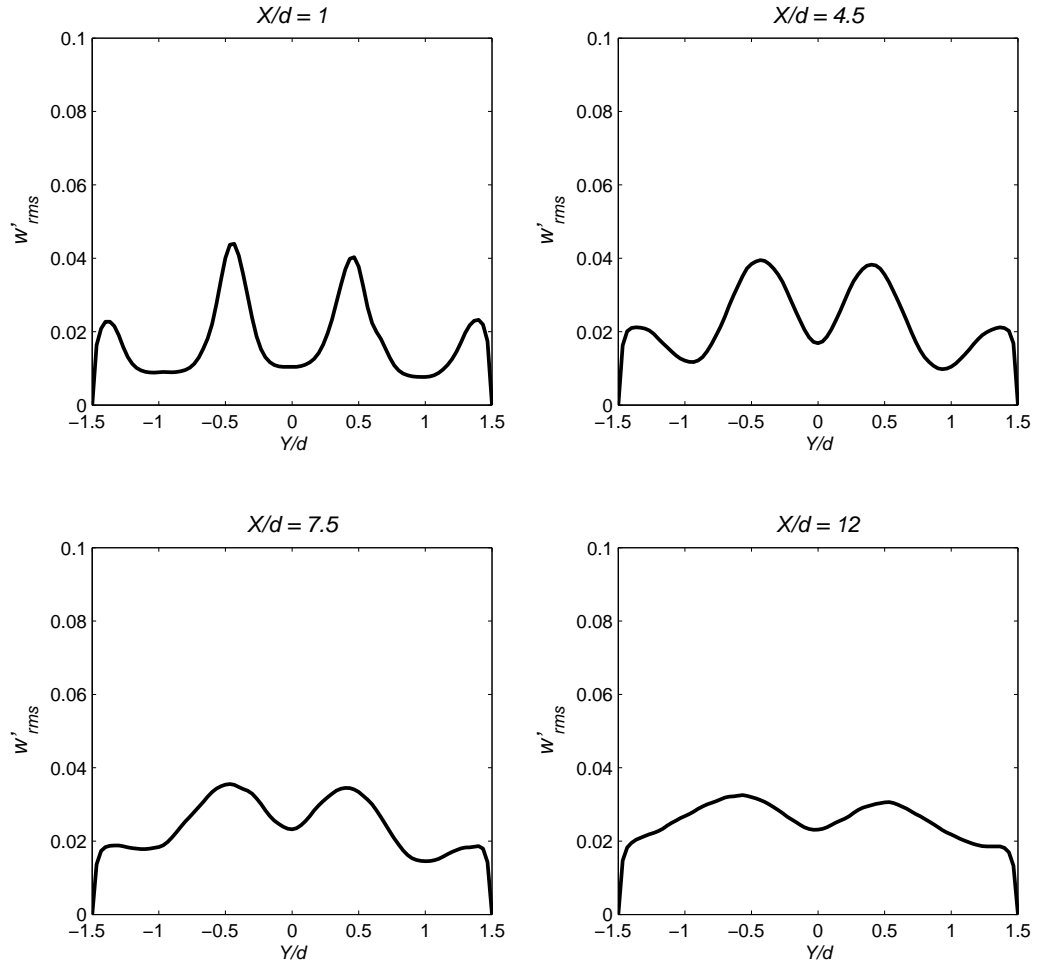


Figure 4.11 Span-wise rms velocity profile at four locations downstream of the splitter plates. Experimental data are not available for comparisons.

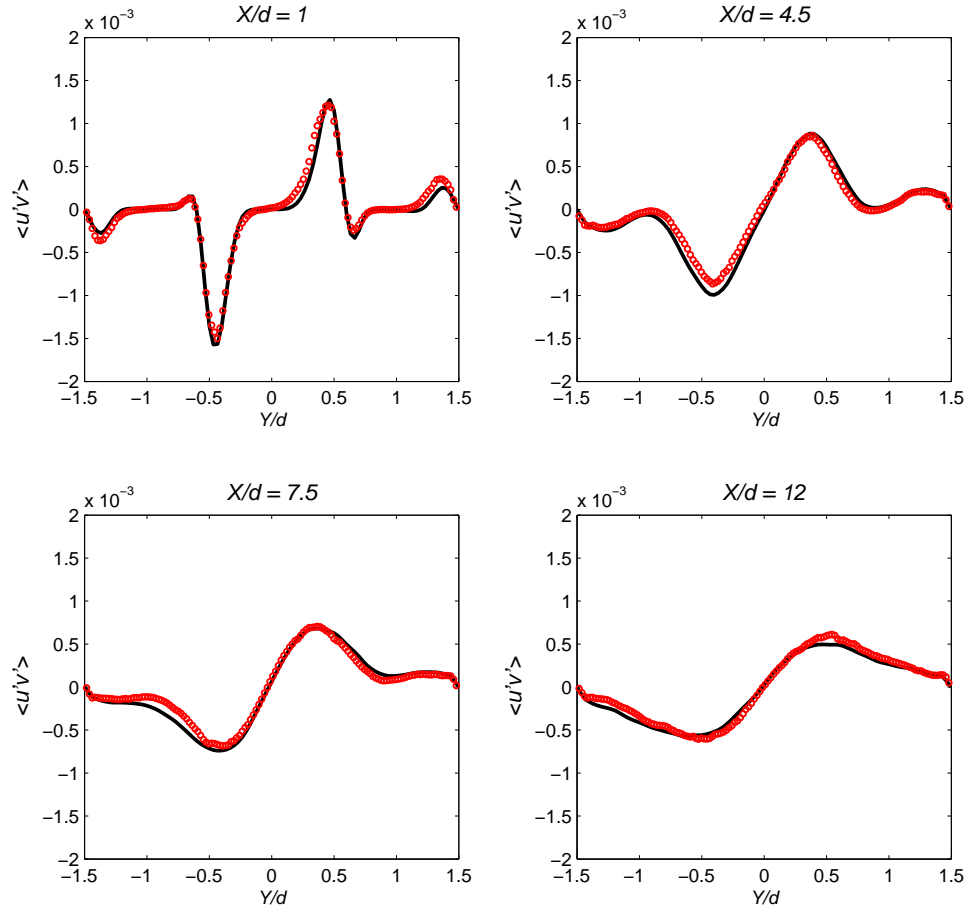


Figure 4.12 Resolved shear stress at four locations downstream of the splitter plates. Experiments are shown as symbols and LES as lines.

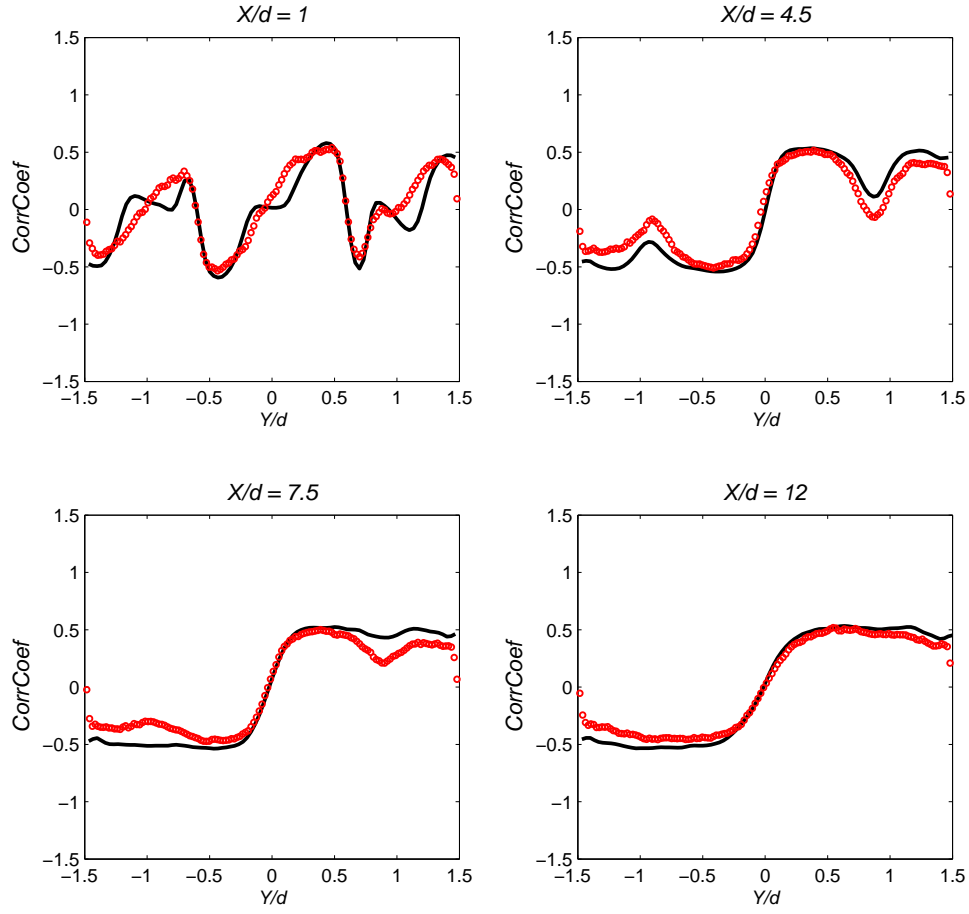


Figure 4.13 Correlation coefficient profiles at four locations downstream of the splitter plates. Experiments are shown as symbols and LES as lines.

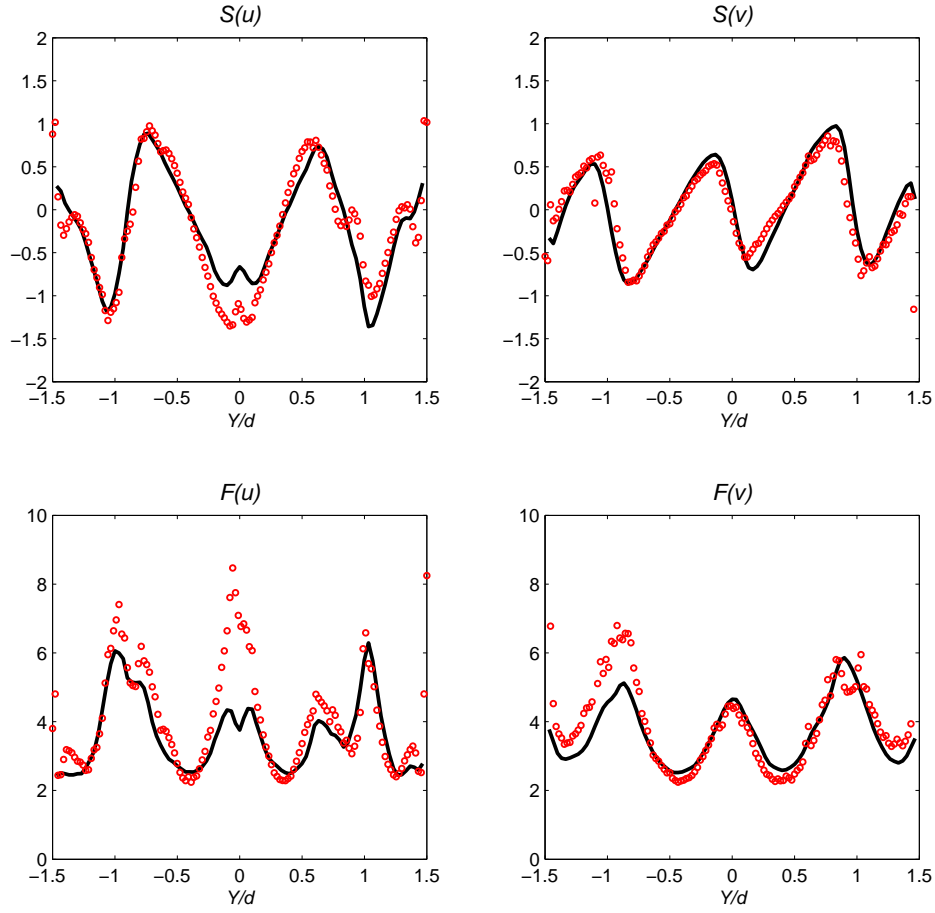


Figure 4.14 Skewness and kurtosis for u - and v -velocity at $x/d = 4.5$. Experiments are shown as symbols and LES as lines.

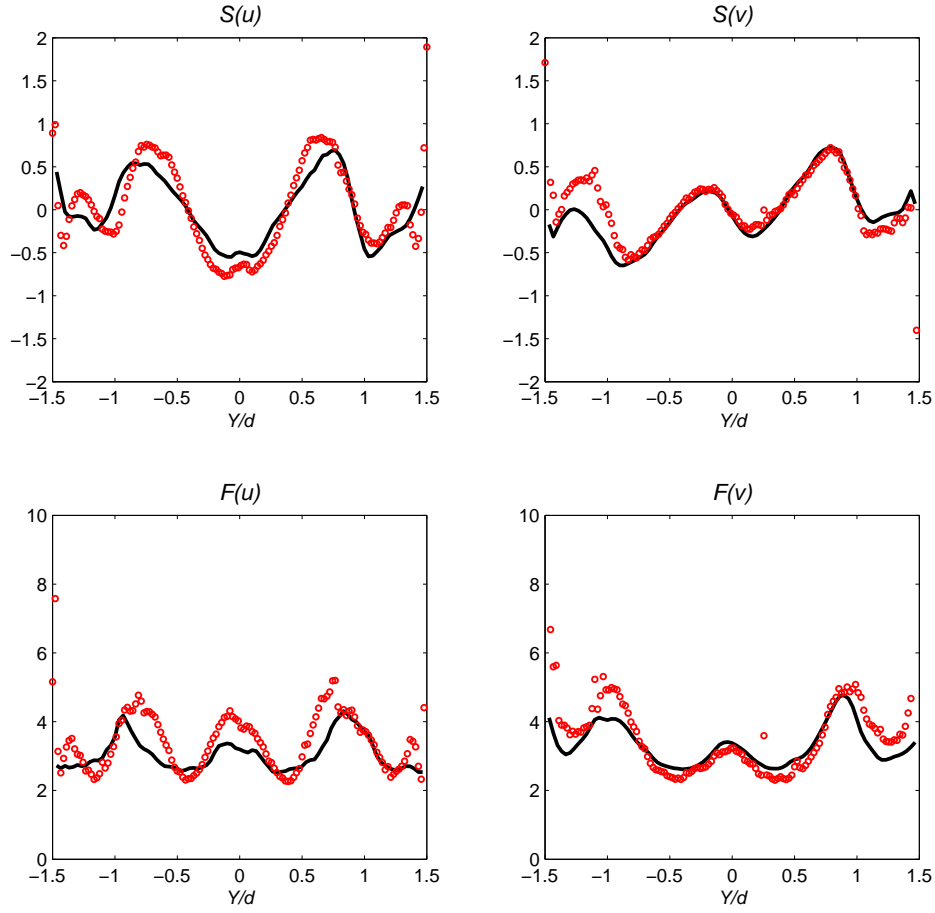


Figure 4.15 Skewness and kurtosis for u - and v -velocity at $x/d = 7.5$. Experiments are shown as symbols and LES as lines.

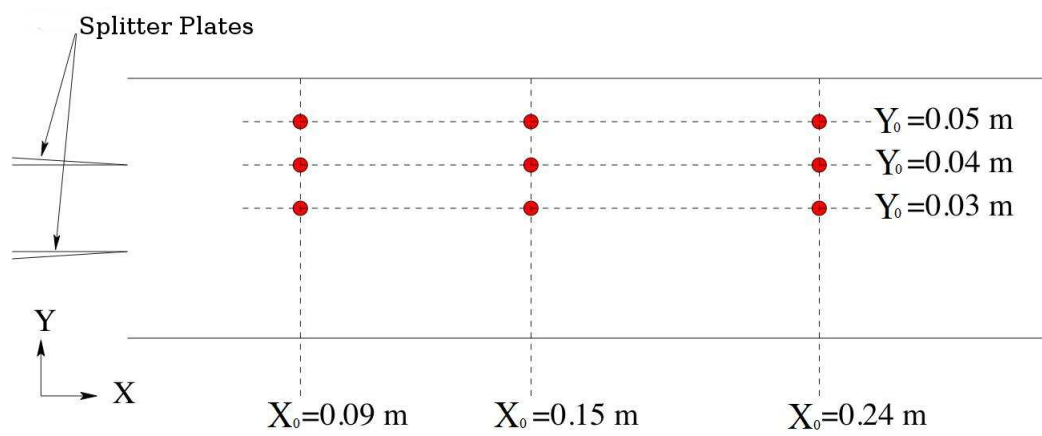


Figure 4.16 Schematic of measurement plane for two-point velocity correlations. Correlations are obtained at nine points in the plane shown with circles.

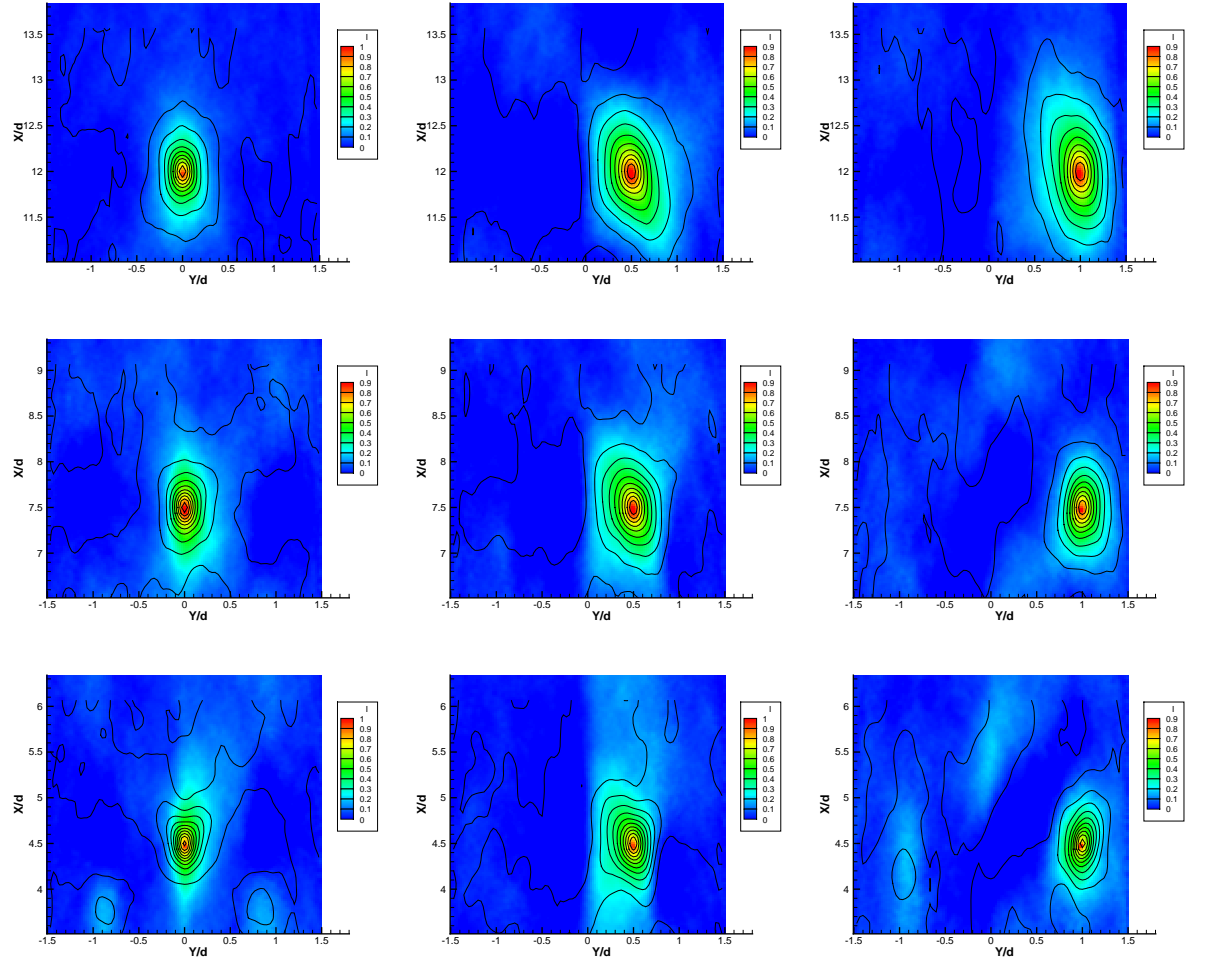


Figure 4.17 Spatial correlations of stream-wise velocity $R_{u'u'}$. Left to right shows correlations at increasing cross-stream wise distance from center of the jet. Bottom to top shows correlations at increasing downstream distance. Experimental data are shown as colored contours and LES data are superimposed as solid lines.

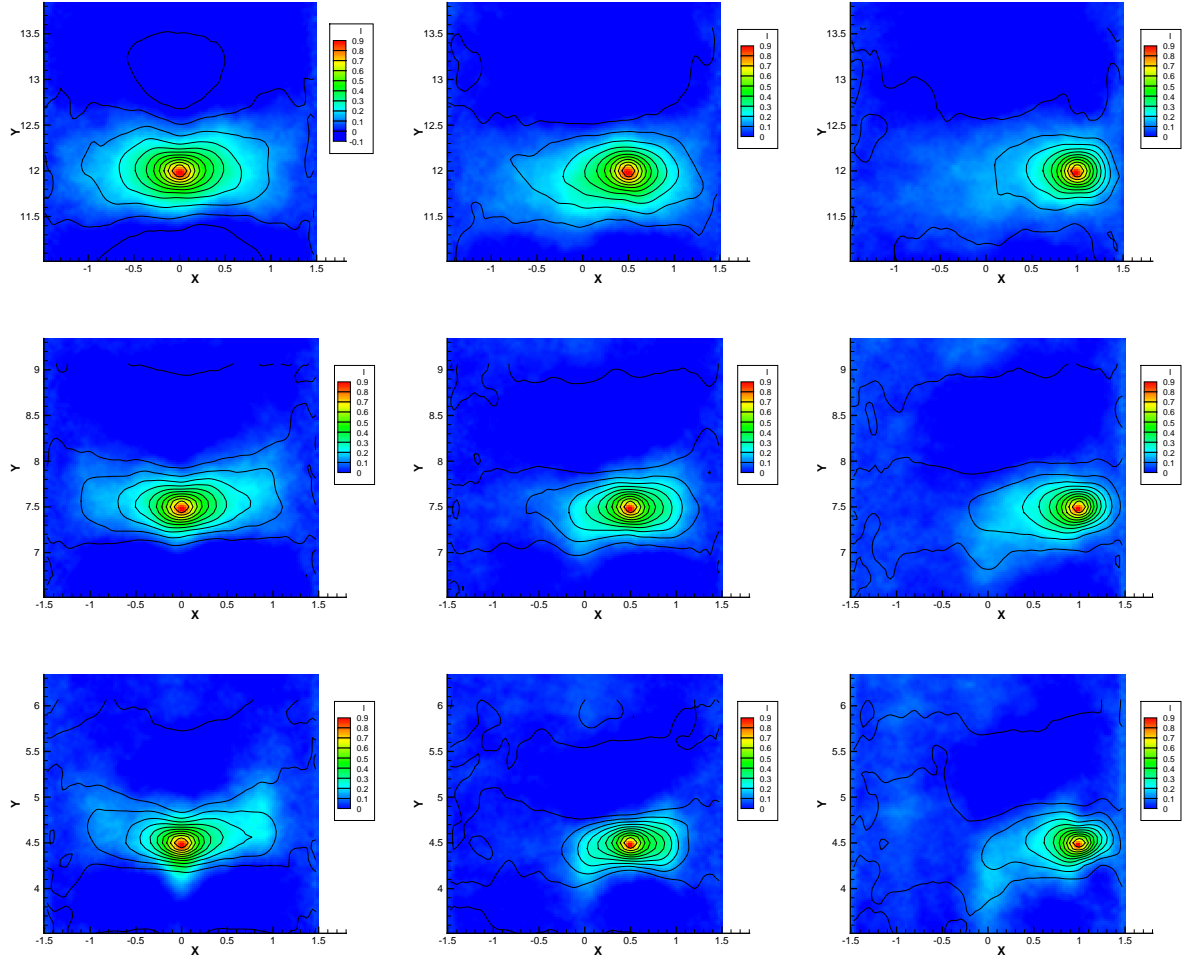


Figure 4.18 Spatial correlations of cross-stream velocity $R_{v'v'}$. Measurement locations and contours are the same as in Figure 4.17.

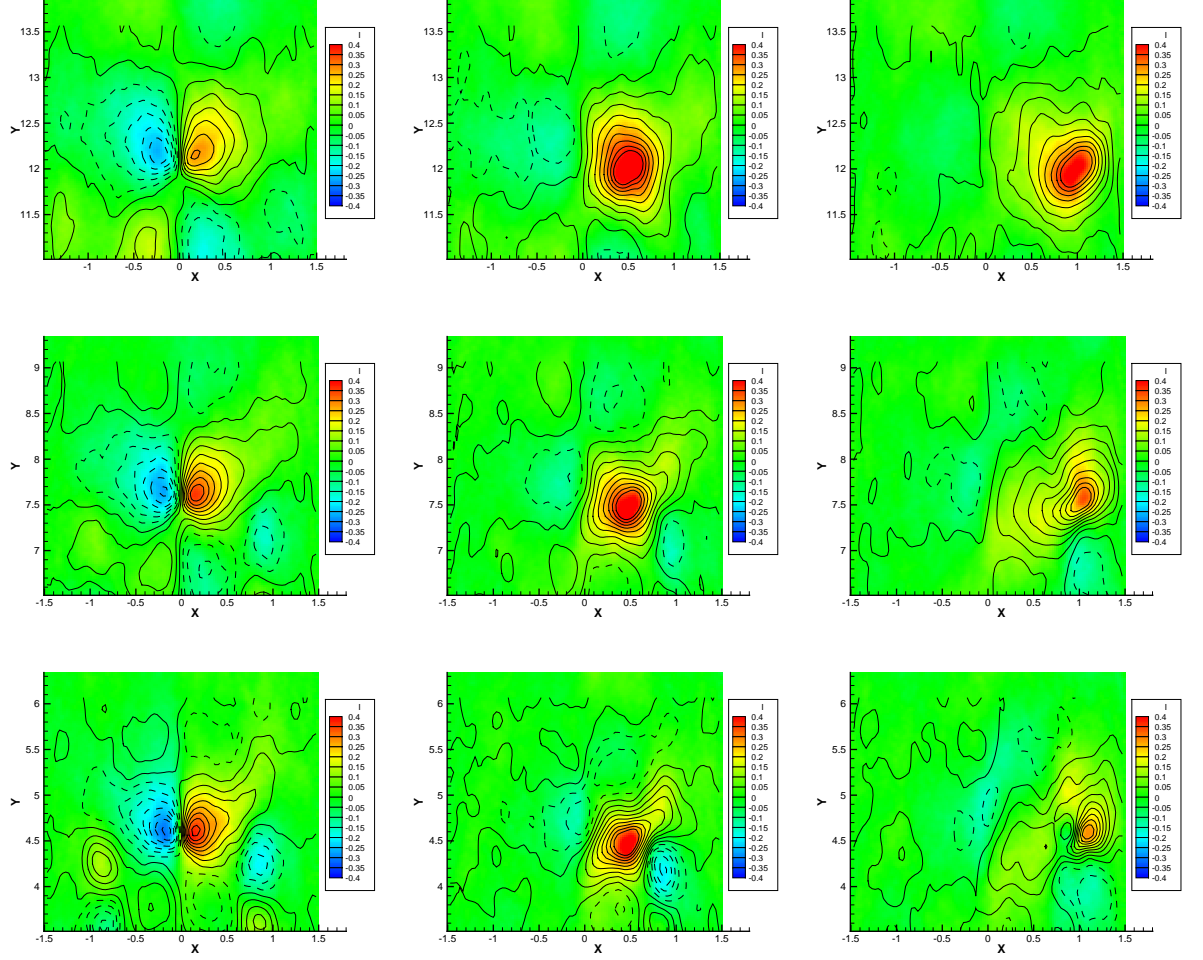


Figure 4.19 Spatial correlations $R_{u'v'}$. Measurement locations and contours are the same as in Figure 4.17.

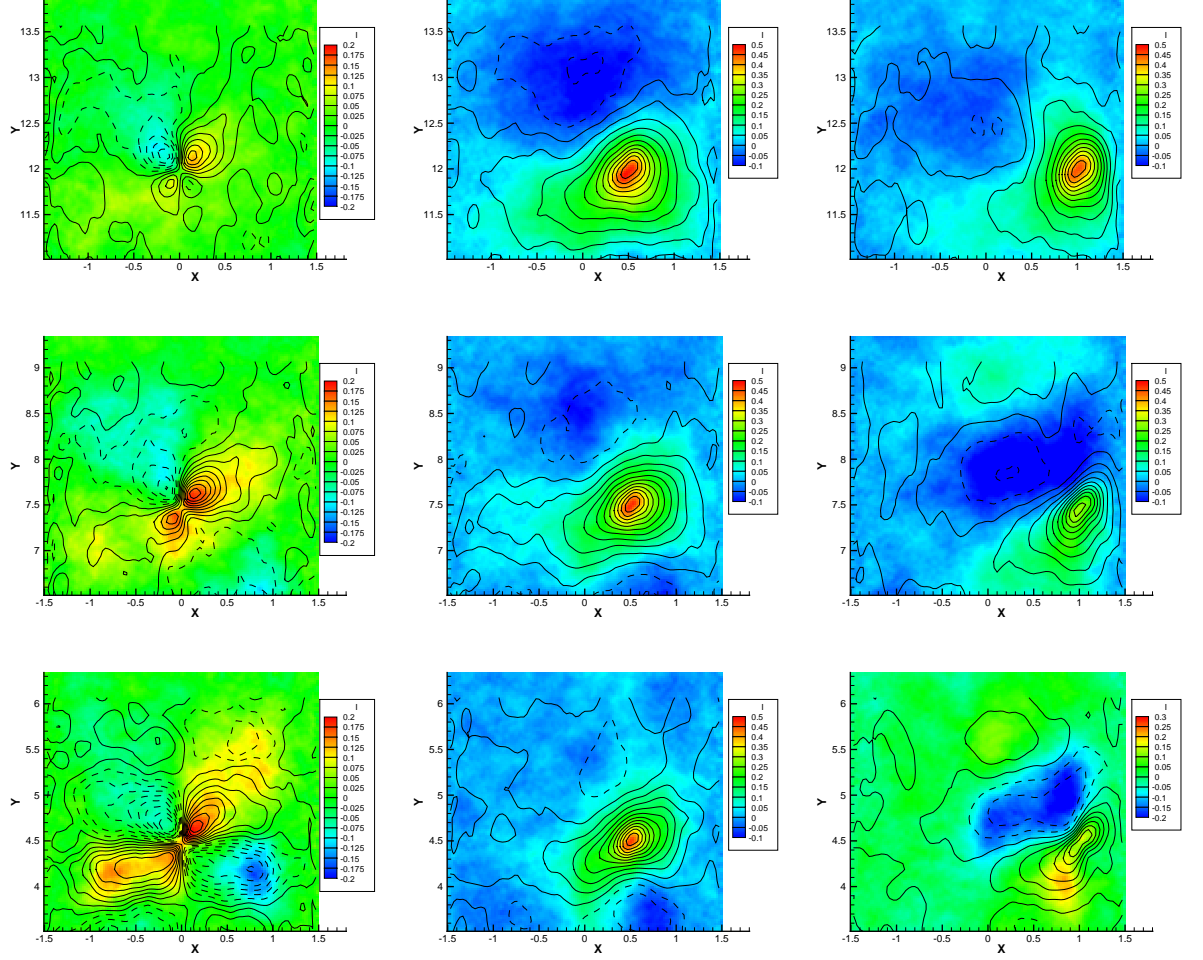


Figure 4.20 Spatial correlations $R_{v'u'}$. Measurement locations and contours are the same as in Figure 4.17.

CHAPTER 5. A Comparison Study of Turbulence Statistics in the Mixing Regions of Confined Jet and Wake

Abstract

Experimental data from combined particle image velocimetry (PIV) and planar laser-induced fluorescence (PLIF) measurements are used to analyze the flow between the two scalar interfaces of a confined turbulent jet and a turbulent wake flow. The fluid of the center stream in both flow cases contains a fluorescent dye, and normalized PLIF images were used to identify the inner and outer boundaries of the center stream. The growth of the boundaries of both flow cases are determined and analyzed. The mean and fluctuations of the passive scalar, velocity, strain rate, and vorticity are determined relative to the locations of the two boundaries. The results show some unique perspectives of this co-flowing confined rectangular jet flow. The fluctuations of the passive scalar show high values close to the outer boundary of the jet, and most of the properties of the velocity fields show high values near the inner boundaries of the jet. The results of the wake case are very symmetrical about the center of the wake, indicating the presence of the vortex street.

5.1 Introduction

The presence of turbulence in fluid flows can greatly improve heat and mass transfer efficiency. Being commonly occurring classes of turbulent flow in engineering applications, turbulent jets and wakes are encountered in numerous components, such as jet pumps, ejectors, combustors, heat exchangers and noise suppression devices.

In the chemical process industry, efficient mixing is necessary to control product formation, maximize efficiency, and reduce the formation of undesired byproducts. Therefore a well-

designed reactor is critical for optimal performance. Consequently, experimental studies of mixing in turbulent shear flows (i.e., wakes, jets and mixing layers) are of great importance not only in advancing turbulence theory, but also in improving engineering practices, such as the design and optimization of various kinds of chemical reactors.

The present research focuses on the turbulent mixing of a passive scalar. In studies involving passive scalar mixing, this passive scalar can be the concentration of a substance (such as a fluorescent dye) or temperature, as long as the effect of variations in the passive scalar itself on the flow kinematics is negligible. The scalar interface, which is the surface separating the scalar-marked regions from the rest of the flow field are of considerable interest (Prasad and Sreenivasan, 1989). Various turbulence properties across scalar interface, such as fluctuations, strain rate, and vorticity, can provide valuable insights into this basic type of mixing process.

This scalar interface is commonly used as the detector of the interface between turbulent and non-turbulent regions of the flow field. For example, Chen and Blackwelder (1978) used temperature as a passive marker to distinguish the turbulent fluid from (cooler) non-turbulent fluid in a turbulent boundary layer flow using an array of cold wires. LaRue and Libby (1974) used a same method to study the wake of a heated cylinder. Some of the most distinguished work on this area was done by Westerweel et al. (2002, 2005). They employed a novel method of performing simultaneous PIV and PLIF experiments on an axisymmetric turbulent free jet. The threshold to detect the scalar interface in their works was determined by using the procedure proposed by Prasad and Sreenivasan (1989). After the interfaces were detected, the PIV data were used to obtain conditionally averaged quantities across the turbulent/non-turbulent interface. In their study, one of the most important discoveries is that nibbling by the small eddies contributes substantially to the total fluid entrained. This technique has also been utilized by Holzner et al. (2007, 2008) to study the process of entrainment and the role of small scale eddies in a flow without strong mean shear with both experimental and direct numerical simulation (DNS) data. da Silva and Pereira (2008) have computed the invariants of the velocity gradient, rate-of-strain, and rotation tensors across the turbulent/non-turbulent interface of a turbulent jet flow in an effort to understand the process of turbulent entrainment

better.

However, in many engineering applications, both of the fluids participating the mixing process are to some degree turbulent already. For example, a jet with a co-flow or a cross-flow is commonly seen in industrial applications. However, investigating the scalar interface can still be a powerful tool to study passive scalar mixing in these types of flow. Thus, in the work that follows, the characteristics of turbulent flow across the scalar interface in a confined turbulent jet with co-flow and a confined turbulent wake have been investigated by using a similar technique described in Westerweel et al. (2002) .

The results of the present study are presented here in the sections that follow. The flow facility and the experimental configuration are described in section 2. The method of stream boundary detection is explained in section 3, and the results and discussion are presented in section 4. Summary and conclusions are given in section 5.

5.2 Experimental Facility

The flow facility used in the experiments presented here is shown in Fig. 5.1. The measurements are carried out in a Plexiglas test section with a rectangular cross-section measuring 60 mm by 100 mm and with an overall length of 1 m. There are three streams separated by two splitter plates, each emitting from the its own flow conditioning section consisting of a packed bed, turbulence reducing screens, and a 16:1 contraction section. The slope of the surface of the splitter plates is 3 degrees along the side channels and 1 degree along the center channel, and the thickness of the tips of the splitter plates are less than 0.5 mm. Three Fisher control valves and feedback control systems with flow accuracy of 0.5 % are used to supply constant flow rates to the three inlet channels. In the jet case, the flow rates for three stream are 1.0, 2.0 and 1.0 liter per second, corresponding to free stream velocities of 0.5 m/s, 1.0 m/s, and 0.5 m/s, respectfully, and in the wake case, the flow rates for all three streams are equally 1.0 liter per second (a velocity of 0.5 m/s). The Reynolds number for these two cases was calculated based on the hydraulic diameter of the test section and the bulk velocity and was 50,000 for the jet case and 37,500 for the wake case.

Simultaneous PIV/PLIF measurements were performed for these two flow cases. This technique has been used to study many turbulent mixing problems, such as Westerweel et al. (2002, 2005) in a turbulent jet. The optical configuration of this combined PIV/PLIF system is shown in Fig. 5.2. The 0.5 mm thick laser sheet was provided by a New Wave Research Gemini PIV laser, which passes through the centerline of the test section in the z -direction. PIV and PLIF images were obtained using two 12-bit LaVision Flowmaster 3S CCD cameras. The image magnification of the two CCD cameras was 0.12, and the numerical aperture was 8 for PIV camera and 5.6 for PLIF camera. A dichroic mirror (Q545LP, Chroma Technology Corp.) was placed at an angle of 45° to the laser sheet to separate the light paths and direct them to either the PIV or the PLIF camera. The PLIF camera lens was fitted with a long-pass optical filter (E560LP, Chroma Technology Corp.), and the PIV camera lens was fitted with a narrow band-pass optical filter (Z532/10X, Chroma Technology Corp.) Approximately 24 grams of hollow glass spheres (Spherical, Potters Industries, Inc.) were added to the water reservoir with total volume of 3500 liters. The nominal diameter of the seed particles was $11.7 \mu\text{m}$ and the density of the particles was 1.1 g/cm^3 . A multi-pass cross-correlation technique with decreasing window sizes was used to compute the velocity field. The final interrogation spot size measured 16 pixels by 16 pixels, corresponding to 1.02 mm on each side. With 50% overlap between interrogation windows, the velocity vector spacing was 0.51 mm in both the x - and y -directions. The fluorescent dye Rhodamine 6G was used as a passive scalar in the PLIF experiments. In the center stream, the source concentration of Rhodamine 6G was $45 \mu\text{g/l}$, while the other two streams were pure water. The in-plane spatial resolution of the PLIF measurements in the present study was actually limited by the flow area imaged per pixel, which was approximately $56 \mu\text{m}$. At each observed location, 3250 simultaneous velocity and concentration realizations were collected and analyzed. Since the experimental apparatus and procedure have been described in detail elsewhere for both the turbulent jet (Feng et al., 2005, 2007) and the turbulent wake (Liu et al., 2006; Feng et al., 2010), the reader is directed to the literature for further information.

5.3 Identification of Inner and Outer Boundaries

Most of the previous studies with scalar interfaces usually focus on the turbulent/non-turbulent boundary (dye/no-dye boundary, in PLIF measurements), and flow quantities have been evaluated across this boundary. For example, in a turbulent free jet flow, this boundary represents the outer most reach of the jet fluid particles into the quiescent fluid in one instantaneous flow realization. However, the mixing process not only involves just one fluid reaching out into the other fluid, but also at the same time the other fluid is passivity entrained into or even actively reaches out into the first fluid. In a typical free jet case, the entrainment of surrounding fluid into the jet body is a commonly recognized phenomenon. Therefore, there exists another type of boundary in jet flow, which identifies the deepest reach of quiescent fluid particles into the jet body. It is of interest to observe how turbulent characteristics across this boundary vary too. To distinguish these two types of the boundary, in this study the first type of boundary is called the outer boundary of the jet flow and the second type boundary is called the inner boundary of the jet flow. In the early stage of jet flow, these two boundaries usually overlap with each other at the places where no entrainment takes place, or no vortices are present. As the jet flow develops, the region between these two boundaries grows. In the present study, the fluorescent dye was carried by the center stream in both confined jet with co-flow and wake flow cases and was transported to the outer streams by turbulent mixing. Thus, we generalized these two flow boundary concepts as the inner and outer boundaries of the center stream. Unlike the other scalar criteria previous researchers have used to detect the scalar interfaces, such as vorticity or stream wise velocity (Anand et al., 2009), the normalized PLIF experiment results, whose range is from 0 to 1, are very suitable for detection of both the inner and outer boundaries.

The outer boundary of the center stream was detected by using a similar procedure used in Westerweel et al. (2002). The instantaneous PLIF images were first rendered into binary form by applying a threshold. The threshold value was determined by the procedure proposed by Prasad and Sreenivasan (1989), which is demonstrated in Fig. 5.3. First, the mean concentrations of all the pixels above one concentration value were calculated and plotted.

The intersection point of the two linear regions is the threshold point. After the images were rendered into binary form by this value, all the holes and islands in the binary images were eliminated so that resulting interface corresponds to only the outer boundary of the center stream. An example of the detection of outer boundary was shown in Fig. 5.5 for the jet case.

The inner boundary of the center stream was detected in a similar manner. Instead of finding the upper averaged mean of the passive scalar function, the inversed upper averaged mean of the passive scalar was calculated. To calculate this, all the concentration values are subtracted from the highest possible concentration values first. In this way, the inner boundary of the jet was treated as the outer boundary of the two side streams. The determination of the threshold for the inner boundary is shown in Fig. 5.4. However, by the nature of the PLIF measurement, the contrast in the images on both sides of the inner boundary is less significant than the contrast on both sides of the outer boundary, since at the inner boundary there is significant fluorescence on both sides of the boundary, but at the outer boundary, the outer stream fluid fluorescence is zero.

Thus, the detection of the inner boundary is more difficult than the outer boundary detection. However, since these boundaries are only representative of large scale motions of the flow (Westerweel et al., 2002), and since the in-plane spatial resolution of the PIV measurement is much lower than the PLIF experiment, the effect of any inaccuracy in the inner boundary detection can be considered very limited. An example of raw and binary PLIF images for inner boundary detection for the jet case is shown in Fig. 5.6.

After both the outer boundary and inner boundary were identified, turbulent quantities that can be derived from the experiment data, such as the velocity, vorticity and turbulence flux, can be calculated as conditional averages along the line connected by these two locations over all PIV/PLIF realizations. Although the PIV/PLIF measurements were taken at 6 different downstream locations, only the three closest to the splitter plates are analyzed here. This is because the interest of the current study is the pure jet/wake region, and after twenty center stream diameters the influence of the boundary layers on the two sidewalls causes the flow in both cases to begin to resemble channel flow. Further information about this method can be

found in the references mentioned above.

5.3.1 Geometry of Scalar Boundaries

Figure 5.7 shows the ensemble averaged inner and outer boundaries at different downstream locations, as detected by using the method described above. The center of the test section is located at $y/d = 0$, and the two sidewalls are located at $y/d = 1.5$ and $y/d = -1.5$. Thus the boundary lines close to the center in Fig. 5.7 are the inner boundaries, and the boundary lines close to the test section walls are the outer boundaries. In both the jet and wake cases, the inner and outer boundaries originate from the tips of the splitter plates. As the fluorescent dye begins to transport from center stream to the two side streams, the mean outer boundaries begin to move towards the walls of the test section. At the same time, low concentration fluid from the outer stream is transported into the center stream, thus the mean inner boundaries begin to move towards the center of the test section. Although the momentum of the center stream in the jet case is twice of that in the wake case, the mean boundary locations in both cases are very close to each other overall. However, there are some noticeable differences. The boundaries of the jet case are located slightly further away from the center of the test section, especially at the observing window, $x/d = 6.5 \sim 8.5$. This is consistent with the common observations in Liepmann et al. (1947) and Olsen and Dutton (2002) that mixing layers are inclined to grow towards the low speed stream.

By the definition of the inner and outer boundaries, the mixing process primarily occurs in the region between these two boundaries. Figure 5.8 shows the mean and rms (root mean square) of distance between boundaries at different downstream locations. In Fig. 5.8, the mean distance initially grows quickly close to the test section inlet, but as the flow progresses, the growth rate decreases. Since the flow is bounded by two sidewalls and not an infinite expanse of fluid like a free jet, the growth of the distance between boundaries cannot grow without bounds since the dye must eventually fill up the entire channel. Since the mean locations of the boundaries are very similar in both the jet and the wake case, the mean values of the distance between the boundaries overlap with each other in Fig. 5.8. However, the rms

of the distance between boundaries in the wake case is larger than in the jet case.

This is due to the jet case having a mean shear, while the wake case does not have a mean shear. In the jet case, the presence of the mean shear results in continuous generation of new turbulent eddies as the flow progresses downstream. Thus, for the jet case, there are turbulent eddies ranging from large to small at all downstream locations and the presence of the small eddies, the nibbling behavior, results in more uniformity in the local distance between the boundaries. In the wake case, the absence of mean shear means the turbulence in this case dissipates as the flow progresses downstream. The smallest scales are the first to dissipate, and as the wake flow progresses downstream, the large scale eddies are the dominant structures in the mixing process. There is a deficiency of small nibbling eddies compared to the jet case, resulting in less uniformity. The inner and outer boundaries can be considered as an indicator of large scale mixing process. Therefore, the higher rms value in wake case shows that there are more large scale motions that predominate the mixing process in the wake case compared to in the jet case at the same downstream locations.

5.3.2 Means and Fluctuations of Passive Scalar and Stream wise Velocity

After identifying the inner and outer boundaries on the instantaneous PLIF images, the simultaneous PIV/PLIF technique allows for the examination of various turbulence properties across these two boundaries, where most of the transport process takes place.

All the measured turbulence properties are presented at the two downstream location, $x/d = 4.5$ and $x/d = 7.5$. Figures 5.9 and 5.10 show the mean of passive scalar concentration and stream wise velocity across the mixing region on the left side of the center stream. In these two figures, the x-coordinate is defined based on the local distance between these two boundaries. $x/D_m = 0$ is the location of the outer boundary and $x/D_m = 1$ is the location of the inner boundary, where D_m is the distance between the inner and outer boundaries.

Figure 5.9 shows that the inner and outer boundaries of the center stream are very sharp for both the jet and wake cases. As suggested in the previous sections, the outer boundary can be considered as the frontier of the center stream (i.e., the high concentration region).

Beyond the outer boundary is the undyed region, consisting almost entirely of pure water. Similarly, the inner boundary can be considered as the frontier of the left side stream, beyond this boundary is the region with almost uniform dye solution of the initial inlet concentration. Also, considering the early stage of development of the flow, large scale coherent motions are dominant here. Therefore, the sudden jumps at the outer/inner boundaries are expected, just like the observed sudden jumps of the mean stream wise velocity across the outer boundary in Westerweel et al. (2002), when velocity and concentration are closely coupled. However, in Fig. 5.10, the mean stream wise velocity profile across these two boundaries does not show a sudden jump for the jet case. One reason could be, as Westerweel et al. (2002) argued, the poorer spatial resolution of the PIV measurements compared to the PLIF measurements. However, it is more likely that this is caused by the fact that in the present experiments, the jet is not discharged into quiescent fluid, but instead discharged into two co-flowing streams. There are very short-lived wake regions between the center and side streams in the jet case. The outer boundaries close to the splitter plates are not the turbulence/non-turbulence interfaces as in the free jet studies. The regions on both sides of the outer boundaries do contain some turbulence and there are still some small turbulent structures outside of the outer boundaries. Therefore, the velocity profiles are more likely to be continuous than show sudden jumps.

Note that at $x/d = 7.5$, the mean passive scalar profile shows lower values beyond the inner boundary, where $x/D_m > 1$, in the wake case than in the jet case, and the mean values also decrease as moving further from the inner boundary. Considering the high rms values of mixing region size of the wake case at this downstream location, the two inner boundaries on both sides of the center stream will have higher probability to be very close, when the low concentration values coming from the right outer stream will be taken into the conditional average calculation. Actually, the mean passive scalar profile of the jet case also begins to slightly decrease at the right end of the x-axis, which is caused by the same reason in the wake case.

Also notice that, in Fig. 5.9, between the jumps at the inner and outer boundaries, the mean passive scalar profiles show obvious differences for the jet and the wake cases. The jet

profile is "fuller" than the wake profile, and the values are higher than the linear connection between the two points at the end of the jumps. However, the right half of the wake profile actually has a similar shape as the jet profile and the left half of the profile is slightly depressed. These features can be explained by the coherent structures in the two flows. In the jet case, on the left side of the jet, the dominant structures are the positively (counterclockwise) rotating vortices. The downstream parts of the vortices are actively out-bursts from the high momentum center stream, which generate the positive turbulent fluxes from the center stream. And the upstream parts of the vortices are caused by the passively entrainment, which reduce the negative turbulent fluxes from the low concentration side stream. Overall, the positive turbulent fluxes are expected to contribute more than the negative flux in the passive scalar transport. Therefore, the values between the two boundaries on the profiles are closer to the values of the high momentum stream.

Compared to the mean passive scalar profiles, there is another difference in the mean stream wise velocity profile in Fig. 5.10 besides the lack of sudden jumps across these two boundaries. For the wake case, there is obviously an already very weak wake region between the inner and outer boundaries. In the profile of the jet case, the mean stream wise velocity beyond outer boundary is close to the potential core velocity of the side stream. This is not the case beyond the inner boundary where the potential core of the jet has almost disappeared, unlike the passive scalar profile. Again, this is another sign of the decoupling between the momentum transport and passive scalar transport, caused by the very different inlet conditions. Before the flow enters the test section and the mixing process starts, there are already boundary layers formed on the sidewalls of the splitter plates. Thus, the velocity potential disappears much earlier than the potential of the passive scalar. Also notice that the highest velocity gradient takes place at the left side of the inner boundary, whereas across the inner boundary, the velocity gradient decreases very quickly. Also, the mean velocity values for the jet case at further downstream location, $x/d = 7.5$, begin to decrease approaching $x/D_m = 1.5$, just like the mean passive scalar profile. This indicates that the potential core of the jet is beginning to disappear at this location. Also notice that at the left side of the profiles of both the jet and

wake case, the mean velocity profile is also begins to decrease, which shows the effluence of the boundary layer along the left wall of the test section. Moreover, the mean velocity profile also shows that velocity deficit in the wake flow almost disappears here.

In addition to the mean properties, the fluctuations of the flow properties provide information on the behavior of turbulence field. Figures 5.11 and 5.12 shows the mean value of the positive and negative fluctuations of the passive scalar and stream wise velocity. The data are presented in this way is to observe the response of positive or negative fluctuations at the two boundaries. For the jet case, at $X/d = 4.5$, as seen in Fig. 5.11, the positive profile shows very few fluctuations beyond the outer boundary, a very sharp jump at the outer boundary, a significant peak at the region close to the outer boundary and then approaching to the jet center, the fluctuation level decreases. As was argued for the mean passive scalar profile, at this stage of flow development, the outer boundary is usually the edge of a high concentration fluid pocket, representing an outburst from the high concentration center stream. Therefore the sharp jump at the outer boundary and high values close to the outer boundary are expected. The negative profile for the jet displays nearly the opposite behavior to the positive profile, which is much more responsive to the inner boundary. However the highest values on the negative profile are located closer to the outer boundary, instead of closer to the inner boundary. This indicates that the low concentration fluid pockets entrained into the center stream from the outer streams are less able to penetrate deep into the high concentration region than are high concentration fluid pockets from the center stream able to penetrate into the low concentration regions. At the further downstream location, $x/d = 7.5$, the fluctuation level in the jet case slightly increases; while in the wake case it slightly decreases. This is another piece of evidence demonstrating that the mean shear in the jet is still generating turbulence and enhancing mixing at this further downstream distance, while the turbulence in the wake flow just keeps decaying. Also here the negative passive scalar fluctuation in the wake case begins to increase in magnitude approaching $x/D_m = 1.5$, which indicates that the decay of mean passive scalar value here is indeed caused by the negative fluctuation from the other side of the center stream.

The stream wise velocity fluctuation profiles for the jet case, shown in Fig. 5.12 display very different characteristics compared to the passive scalar fluctuation profiles. The positive and negative fluctuation profiles are nearly axially symmetric to each other about $x/D_m = 0.5$. Since the side stream is not quiescent fluid, the fluctuations beyond the outer boundary are small but not close to zero as in the positive passive scalar fluctuation profile. In the study of a jet discharging into quiescent fluid, Westerweel et al. (2002) found the Reynolds stress has a finite value at the interface which indicates the presence of irrotational velocity fluctuations in a region outside the interface. The mean stream wise velocity profile for the confined jet already indicates that the mean shear exists on the right side of the inner boundary, and the velocity fluctuations there are more significant than in the region on the left side of the outer boundary. However, the most noticeable difference here is that the highest velocity fluctuations are located at the region close to the inner boundary where the highest velocity gradient is located, instead of the outer boundary where the highest passive scalar gradient is located.

For the wake case, also shown in Figs. 5.11 and 5.12, both the passive scalar and stream wise fluctuation profiles are very axially symmetric about the $x/D_m = 0.5$ line. Although there are sharp jumps at the boundaries, the peak of the passive scalar fluctuations located at the center of these two boundaries. This is simply because there are counter-rotating vortices on each side of the wake bringing negative passive scalar fluctuations on the downstream side and positive fluctuations on the upstream side, and the vortices in the vortex street of the wake do not penetrate deeply into the other side of the wake. In Fig. 5.12, the stream wise velocity fluctuations for the wake case also indicate the presence of the vortex street in the wake flow. Both the passive and negative velocity fluctuations show high values close to the locations of the boundaries, and are symmetric to the center of the wake. Also notice that the velocity fluctuation profiles in the wake case are almost uniform across the mixing region, especially at $X/d = 7.5$, just like the mean velocity profile, and are further evident of the decay of the wake.

5.3.3 Compression and Rotations

The compression in a two-dimensional (2D) fluid field can be quantified by the minimum 2D principal strain rate, which is the smaller of the two 2D the eigenvalues of the strain rate tensor. Although the strain rate tensor requires three-dimensional (3D) velocity data to compute all of its nine components, Kothnur and Clemens (2005) argued that the 2D PIV data are sufficient to calculate the correct in-plane principal strain rate, since the laser sheet was oriented orthogonal the span wise direction and out-of-plane shear components of the strain rate tensor are expected to be small. Figure 5.13 shows the mean minimum strain rate, which does not exhibit a sudden change at either boundary. In the jet case, the minimum strain rate values in the center of the potential cores are quite constant, 10 1/s for the side stream and 20 1/s for the center stream. Moving from the outer stream towards the center stream, the minimum strain begins to increase before reaching the outer boundary, which shows the transfer of compression in the turbulent flow is faster than the passive scalar convection. The peak value of the profile is located close to the inner boundary and then profile begins to decrease moving towards the center of the jet. The minimum strain rate behavior indicates the high momentum center stream pushes the two co-flowing streams outwards, and this compression reaches a maximum close to the location of inner boundary, where the fluctuations are also the highest. For the wake case, the strain rate is slightly higher in the wake region than in the center of the center and side stream. Although the wake is a low momentum region, the high momentum fluid particles of counter-rotating vortices from the center and side streams collide with each other, generating compression. At the further downstream, $X/d = 7.5$, the profile of the jet case rises on both its left and right ends, again indicating the growing influence of the boundary layer along the sidewall and also the mixing layer on the other side of the center stream.

Figure 5.14 shows the mean vorticity across the inner and outer boundaries, providing information on the rotating motions of the flows. For the jet case, just as Westerweel et al. (2002) observed in their study, at the region beyond the outer boundary of the jet, the vorticity is close to zero. There is a small rise at the far left side of the profile, which indicates the

influence of the boundary layers growing along the sidewalls and that the potential core of the side stream is disappearing. However, here there is no sudden jump at the outer boundary. Instead, the vorticity values increase gradually moving towards the jet center and reach a peak value at the same location as the strain rate peak, where the highest velocity gradient exists. Note that in this analysis, all the averaging is performed after all the instantaneous values are interpolated from the inner/outer boundary locations to the uniform range of $-0.5 \sim 1.5D_m$ in the x-axis plotted here. It is possible that any sudden jumps in vorticity are smoothed away by this interpolation. However, since sudden jumps in the other turbulent properties have been easily observed using this analysis technique, this is not likely to be true. Considering the plots here are taken at locations no more than 7.5 jet diameter from the jet outlet, the jet is still developing and all the vortices generated in the shear regions of the developing jet have yet to move to the side stream. Moving from the outer stream to the jet center, after it reaches its highest value, the vorticity profile decreases quickly until the inner boundary of the jet, and then moving still closer to the center stream it decreases more slowly. Considering the mean stream wise velocity profile, this is not surprising. For the wake profile shown in Fig. 5.14, the negative vorticity values on left side of the wake and positive values on the right side of the wake, are a consequence of the vortex street in the wake flow. As the mixing region grows larger at the further downstream location, $X/d = 7.5$, the vorticity profile of the jet case shows a much sharper jump at the outer boundary and a flatter profile in the middle of the mixing region. While the sharper jump is expected, the quite uniform vorticity value can be explained by the near uniform velocity gradient in the mixing layer formed here.

5.4 Conclusions

A combined particle image velocitometry and planar laser induced fluorescence system was used to conduct simultaneous velocity and concentration measurements for turbulent confined jet and wake flow. The procedure of Prasad and Sreenivasan (1989) was used to detect the inner and outer boundaries of the center stream in PLIF images. The average locations of the inner and outer boundaries were observed to move away the center faster in the jet case than

in the wake case. The mean distance between these two boundaries was nearly the same in both cases, and the rms of the distance shows that the large scale motions in the wake case are more dominant than in the jet case at the same downstream locations.

After the boundaries of the center stream were identified, various turbulent properties were calculated conditionally across these two boundaries. Both the jet and the wake case showed sharp jumps at the boundaries in the mean passive scalar profiles, and the curvatures between the two boundaries showed the different characteristics of the two flows. For the jet case, the positive passive scalar fluctuations show a sharp jump at the outer boundary and higher values moving towards the jet center, and the negative fluctuations show high values at the same locations, with sharp jumps at the inner boundary. The stream wise velocity profiles show no sharp jumps at the boundaries, and the velocity values continue to change beyond the boundaries, showing the effect of co-flowing motion of the jet. Both positive and negative velocity fluctuations are relatively high on the left side of the inner boundary of the jet. Although passive scalar properties in the wake case also show sharp responses at the inner and outer boundaries, the velocity properties do not display sharp response at the scalar interfaces.

The mean minimum strain rate and vorticity profiles across the boundaries were also measured. The jet case shows a higher mean strain than the wake case between the two boundaries, and the peak value of the jet profile is located close to the inner boundary of the center stream. The mean vorticity profile of the jet case also showed the highest values on the outer stream side of the inner boundary, indicating the entrainment of the surrounding fluids of the jet are the results of the large scale vortices. The wake vorticity profiles showed the two different sign rotations on the two sides of the wake that one would expect from a vortex street.

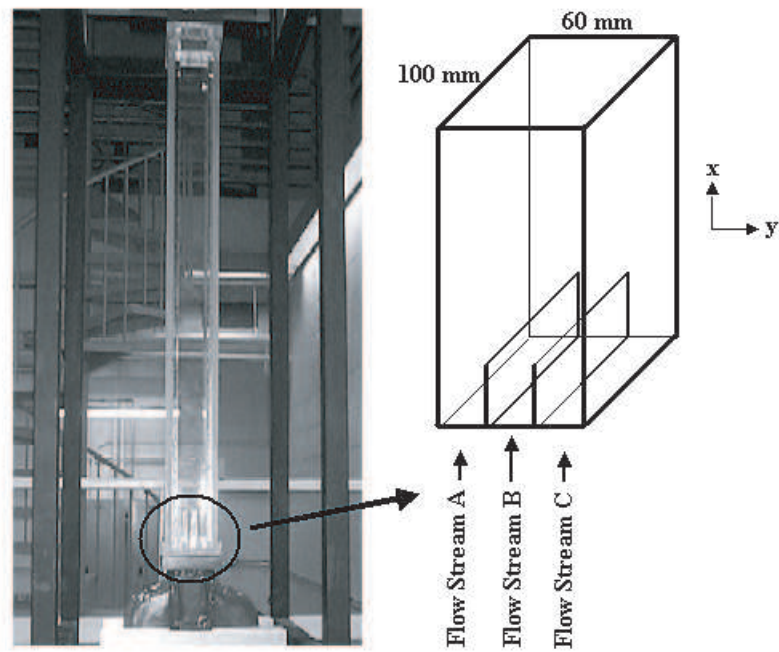


Figure 5.1 Photograph and schematic of the confined planar jet test section

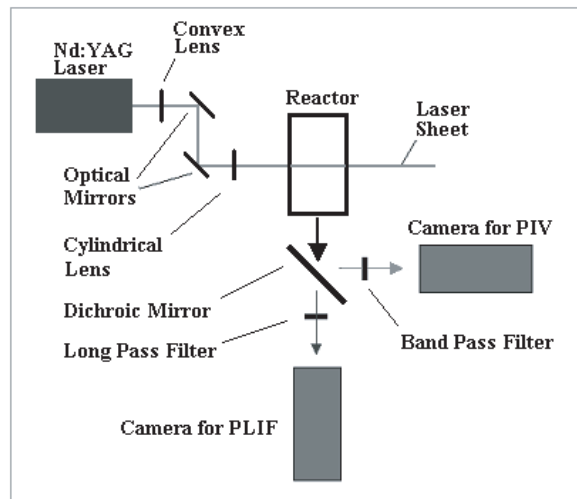


Figure 5.2 Schematic of the optical setup for the combined PIV and PLIF experiments

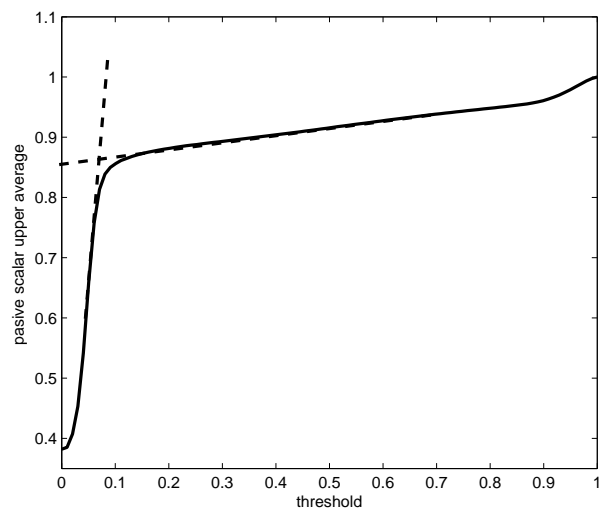


Figure 5.3 Threshold detection for outer boundary.

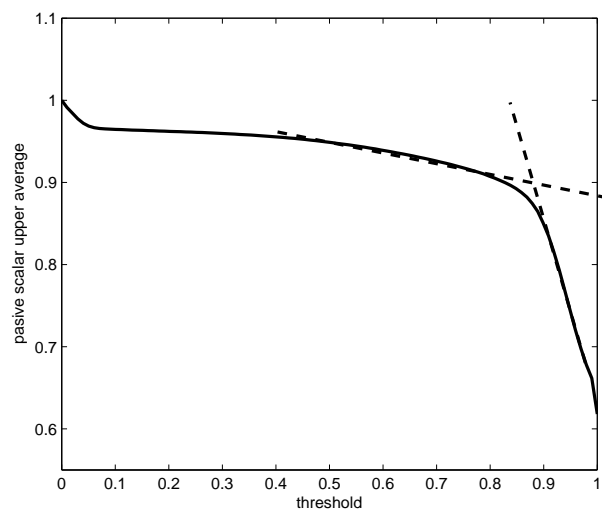


Figure 5.4 Threshold detection for inner boundary.

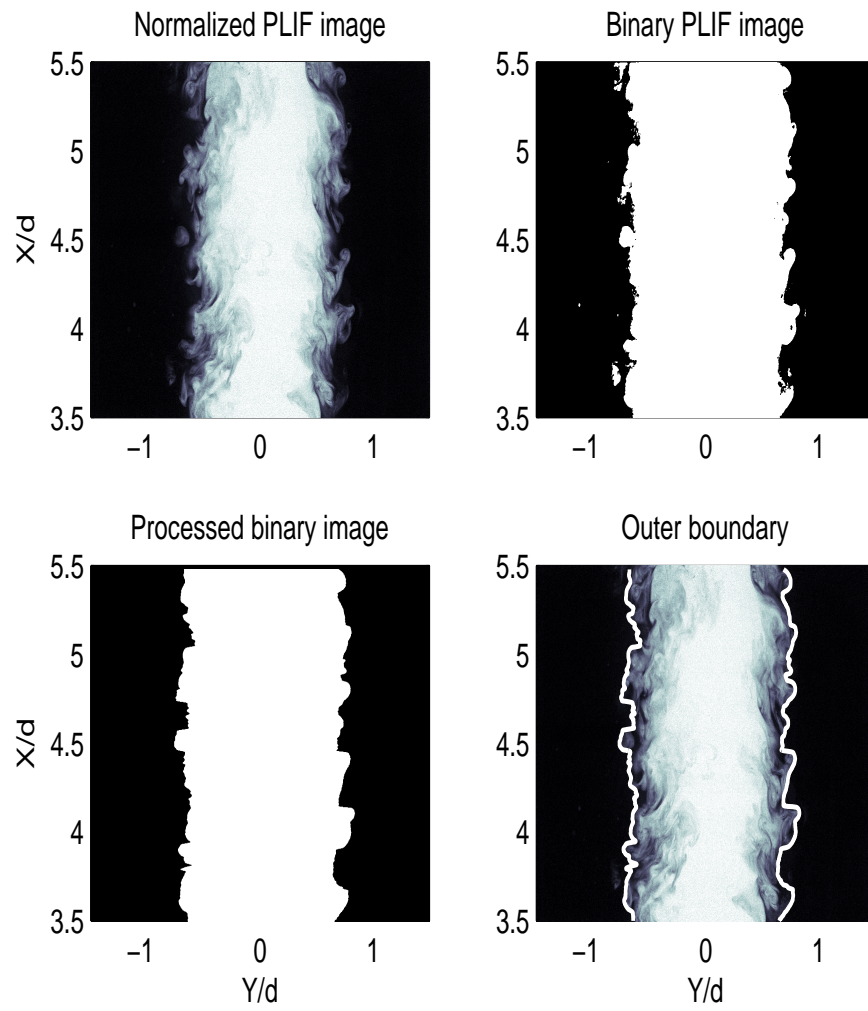


Figure 5.5 An example of outer boundary identification, jet, $X/d = 3.5 \sim 5.5$.

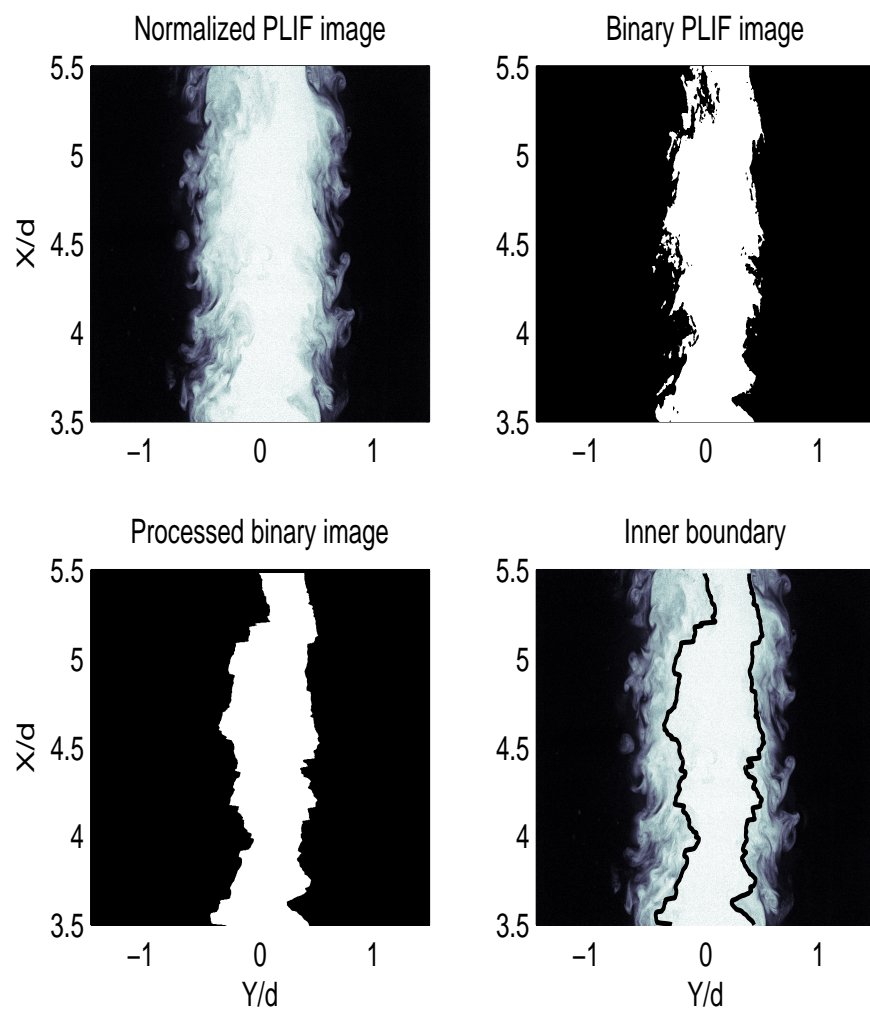


Figure 5.6 An example of inner boundary detection, jet, $X/d = 3.5 \sim 5.5$.

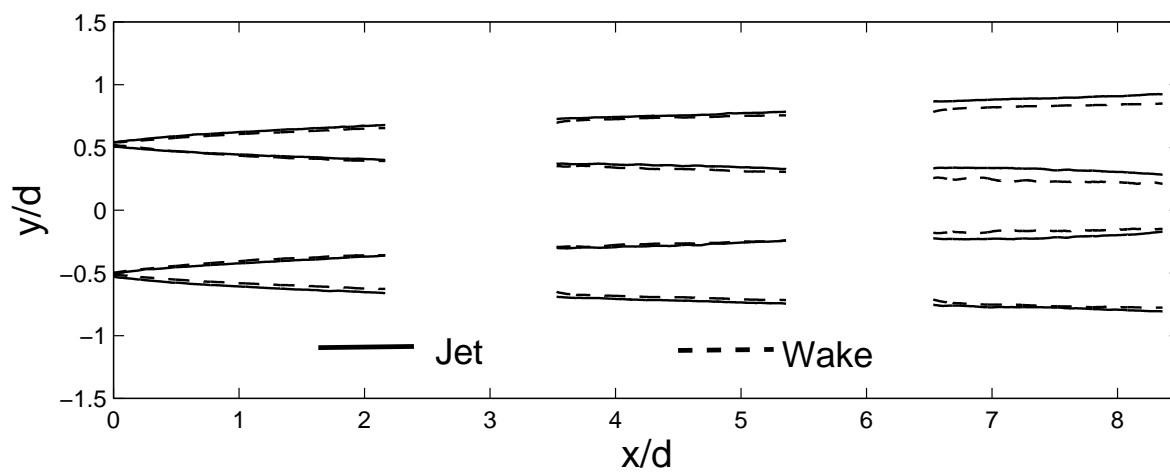


Figure 5.7 Averaged inner and outer boundaries.

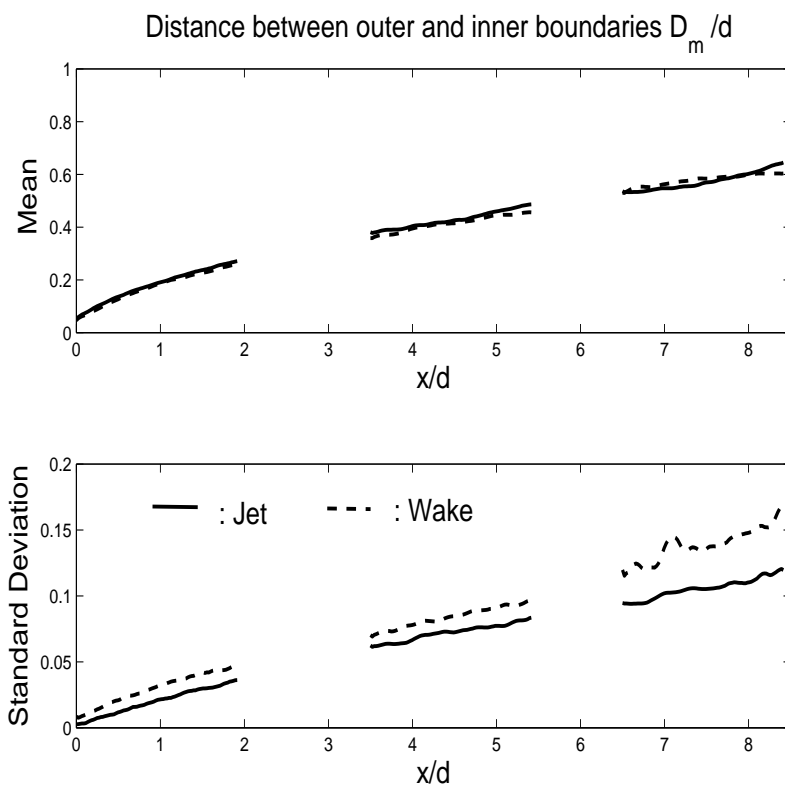


Figure 5.8 Distance between inner and outer boundaries, mean and rms.

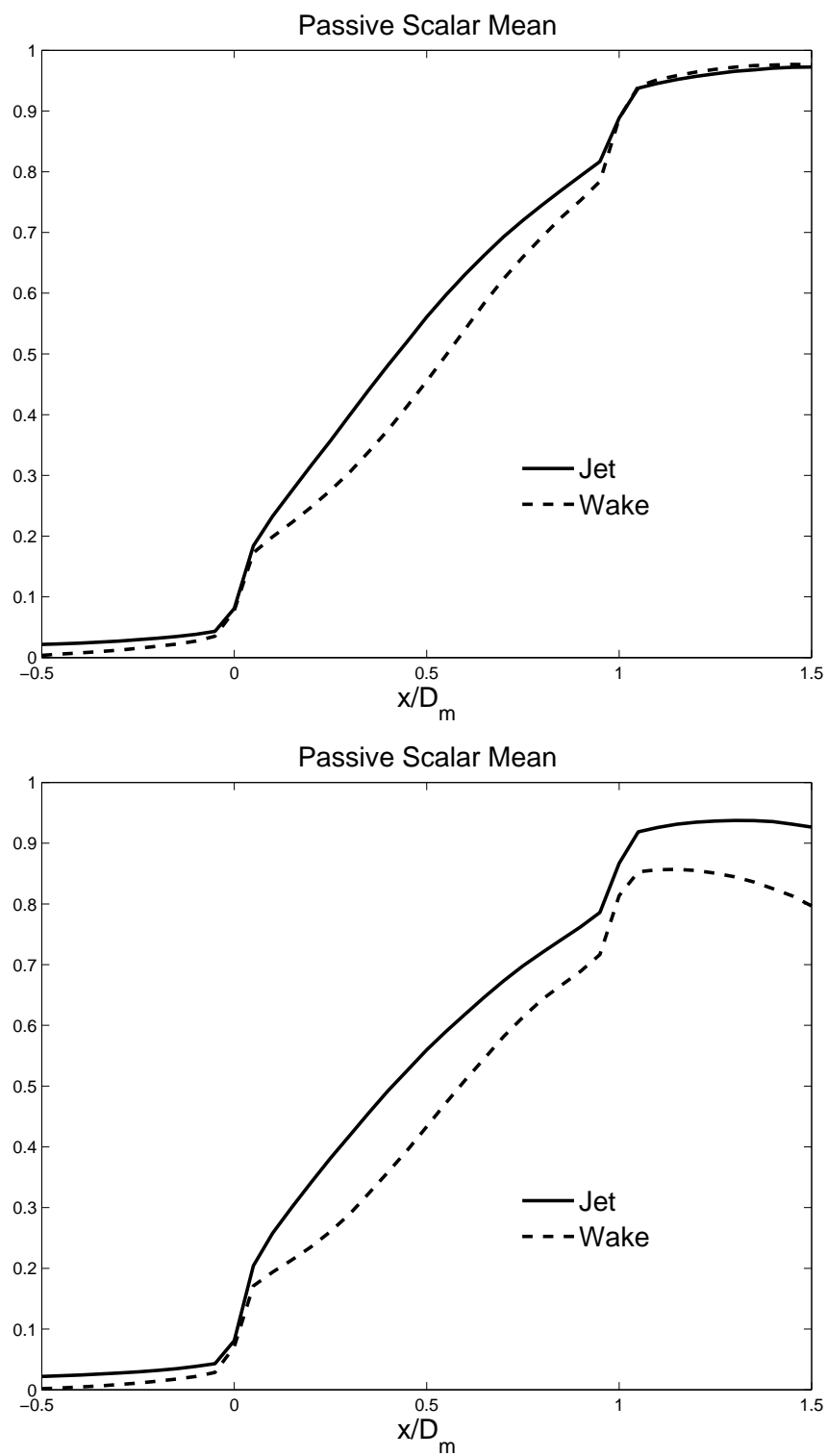


Figure 5.9 The mean of passive scalar across the mixing region. a, $x/d = 4.5$; b, $x/d = 7.5$.

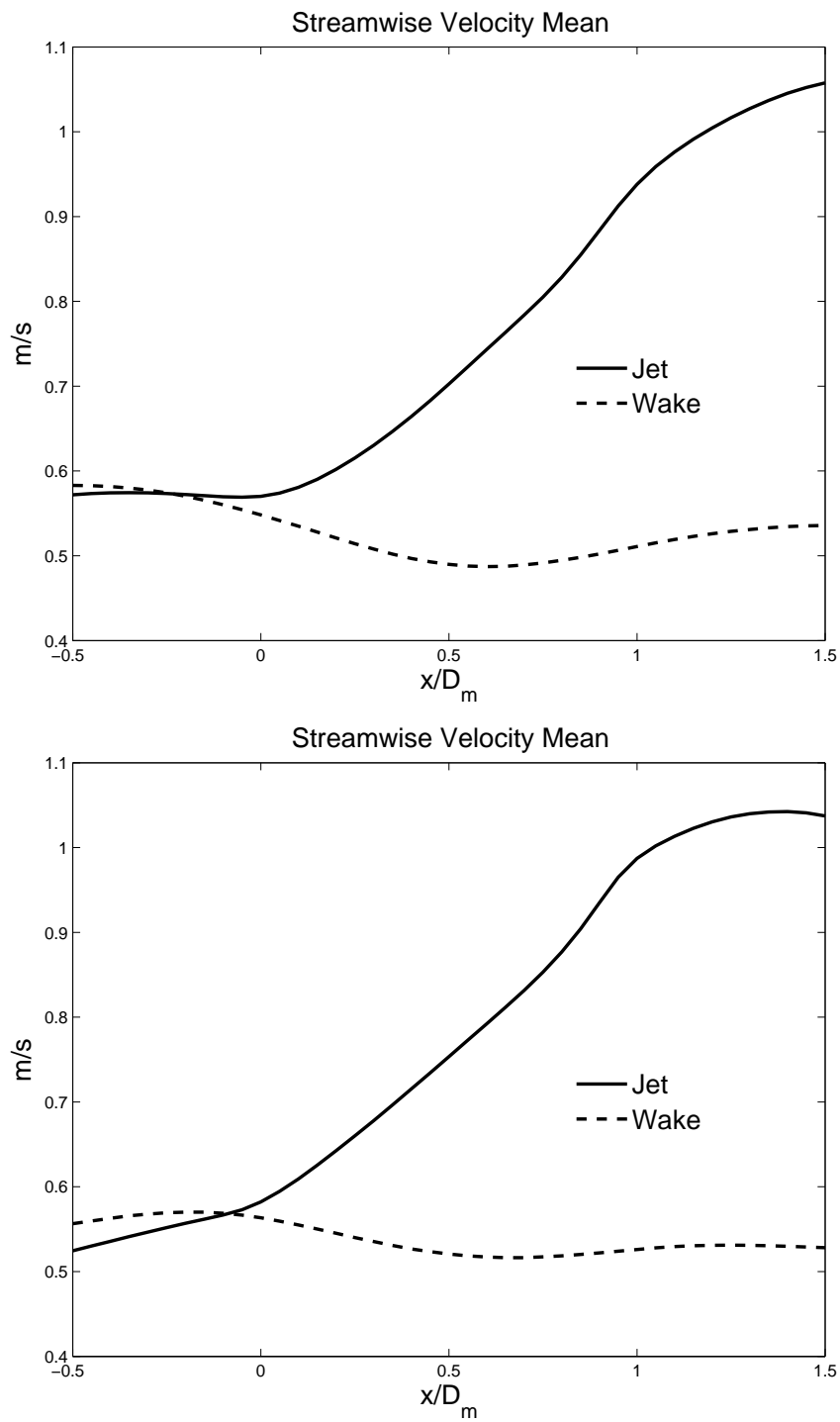


Figure 5.10 The mean of streamwise velocity across the mixing region. a, $x/d = 4.5$; b, $x/d = 7.5$.

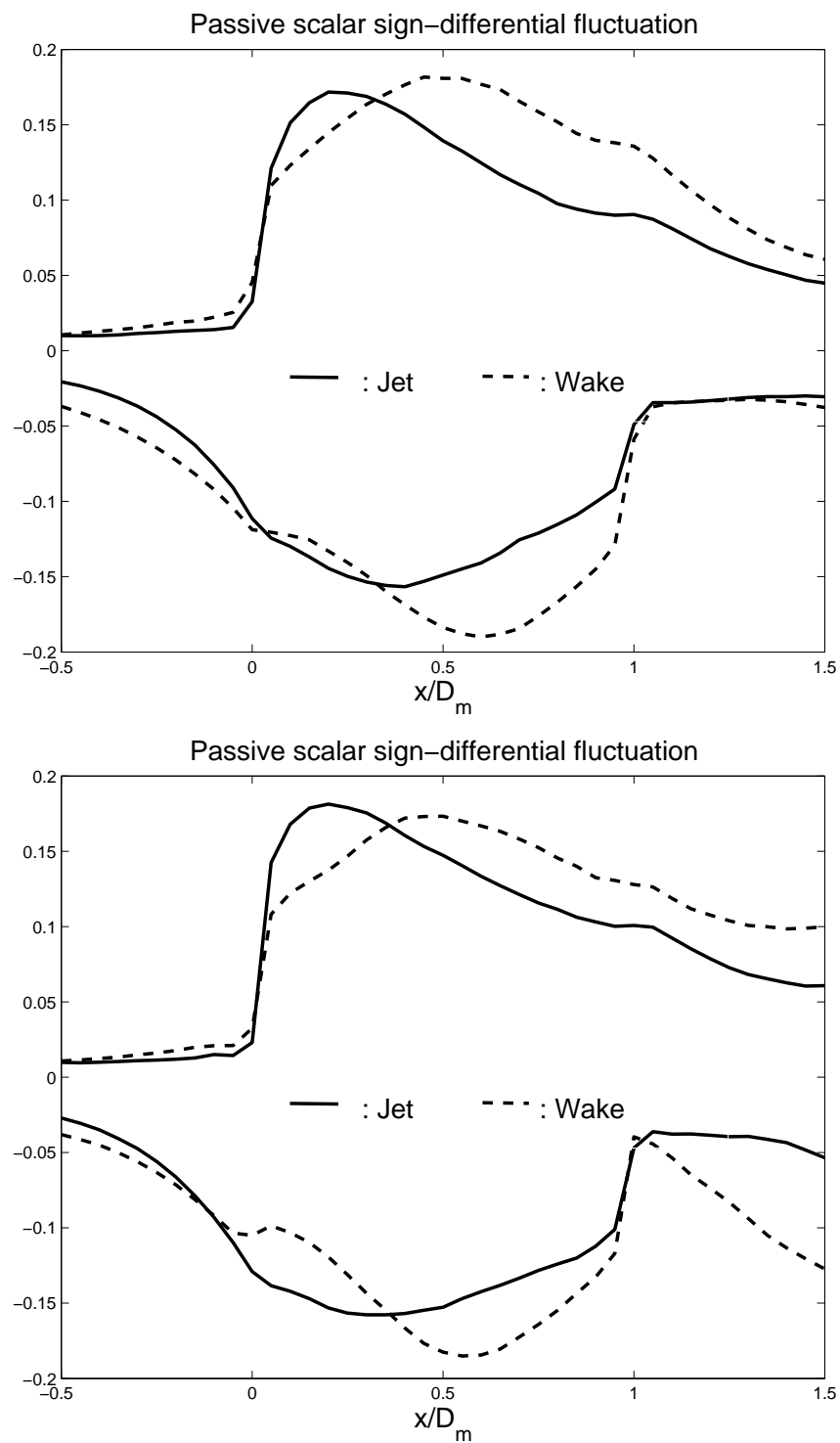


Figure 5.11 Passive scalar sign-differential fluctuation across the mixing region. a, $x/d = 4.5$; b, $x/d = 7.5$.

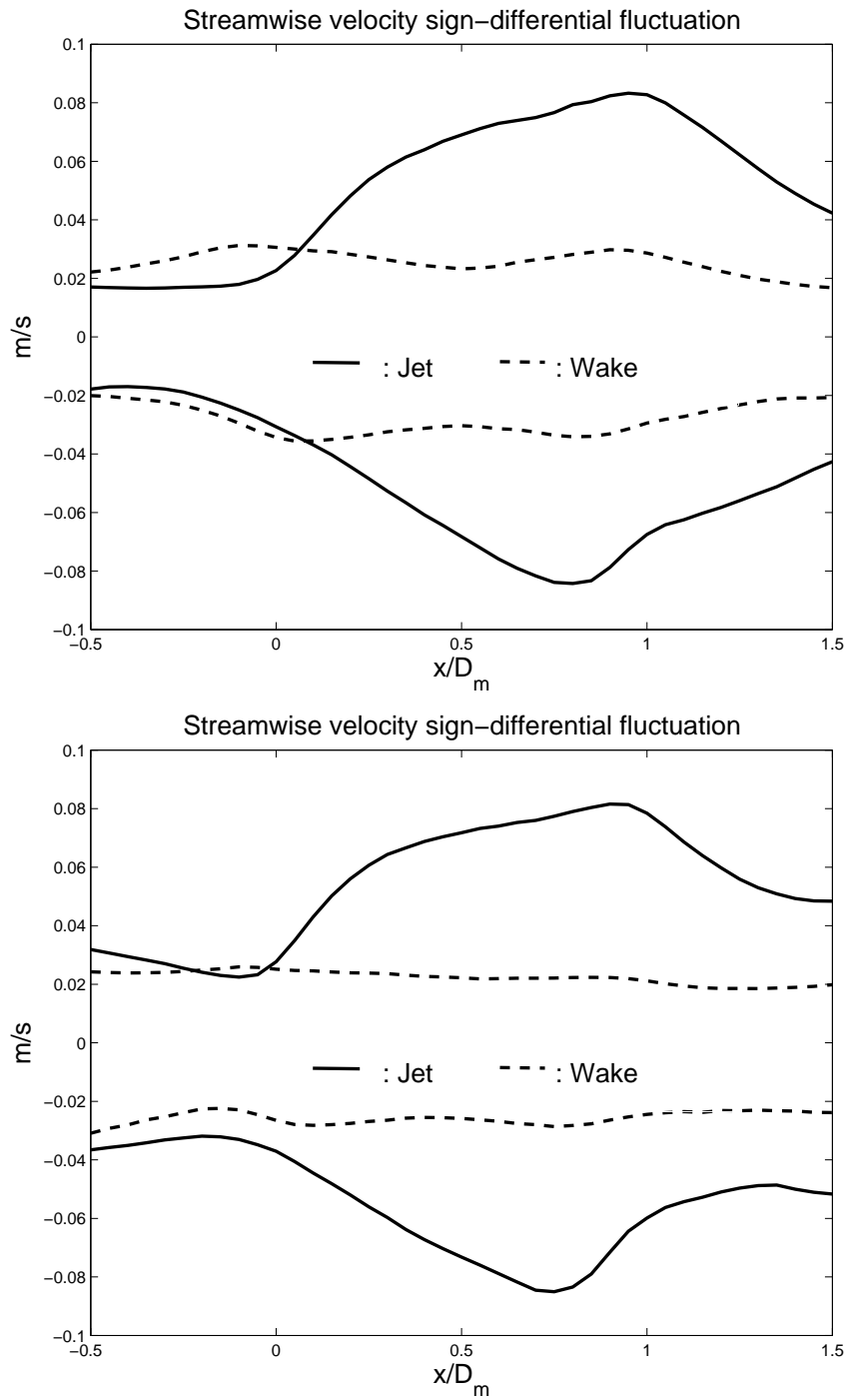


Figure 5.12 Streamwise velocity sign-differential fluctuation across the mixing region. a, $x/d = 4.5$; b, $x/d = 7.5$.

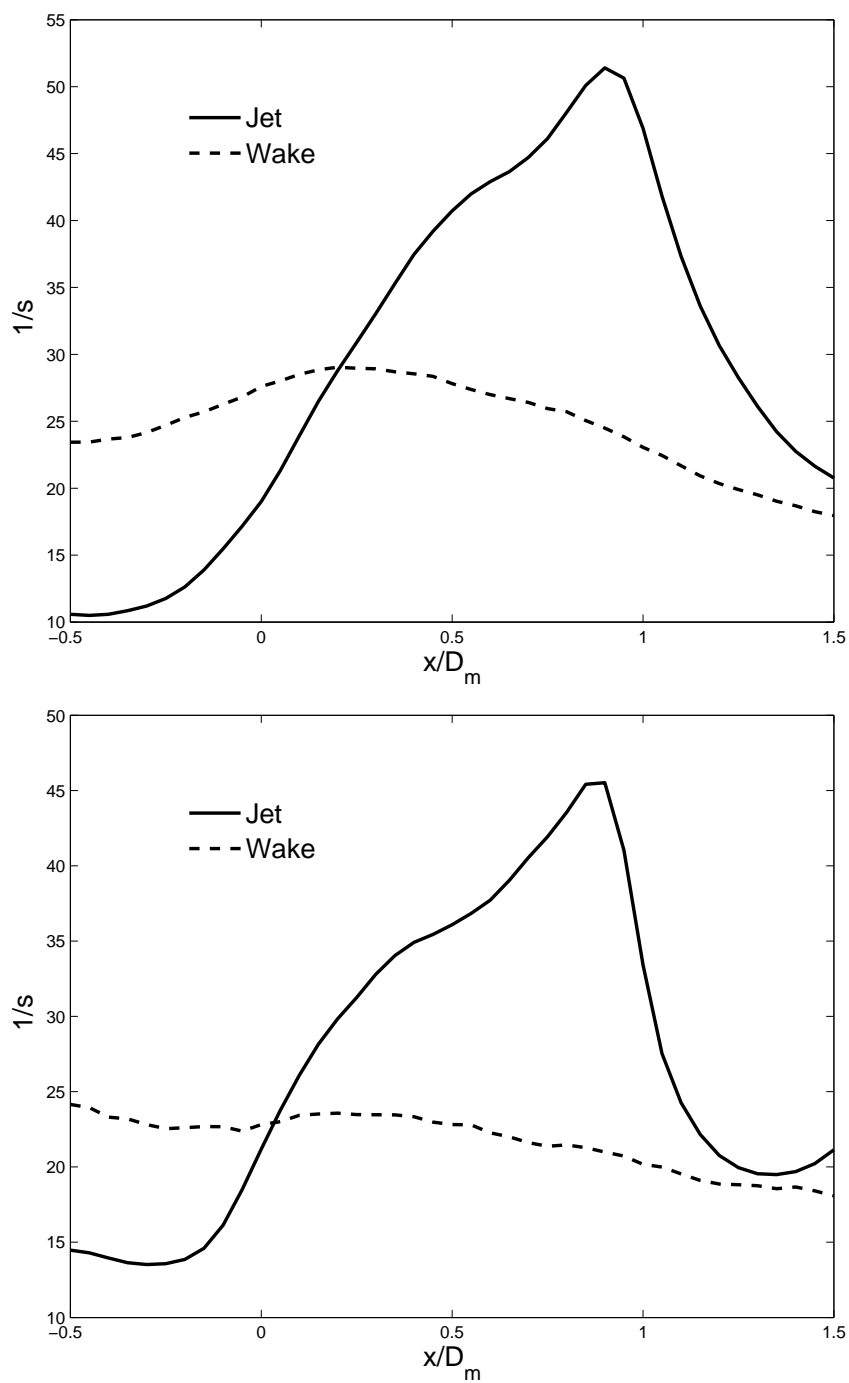


Figure 5.13 The mean of principle strain rate across the mixing region. a, $x/d = 4.5$; b, $x/d = 7.5$.

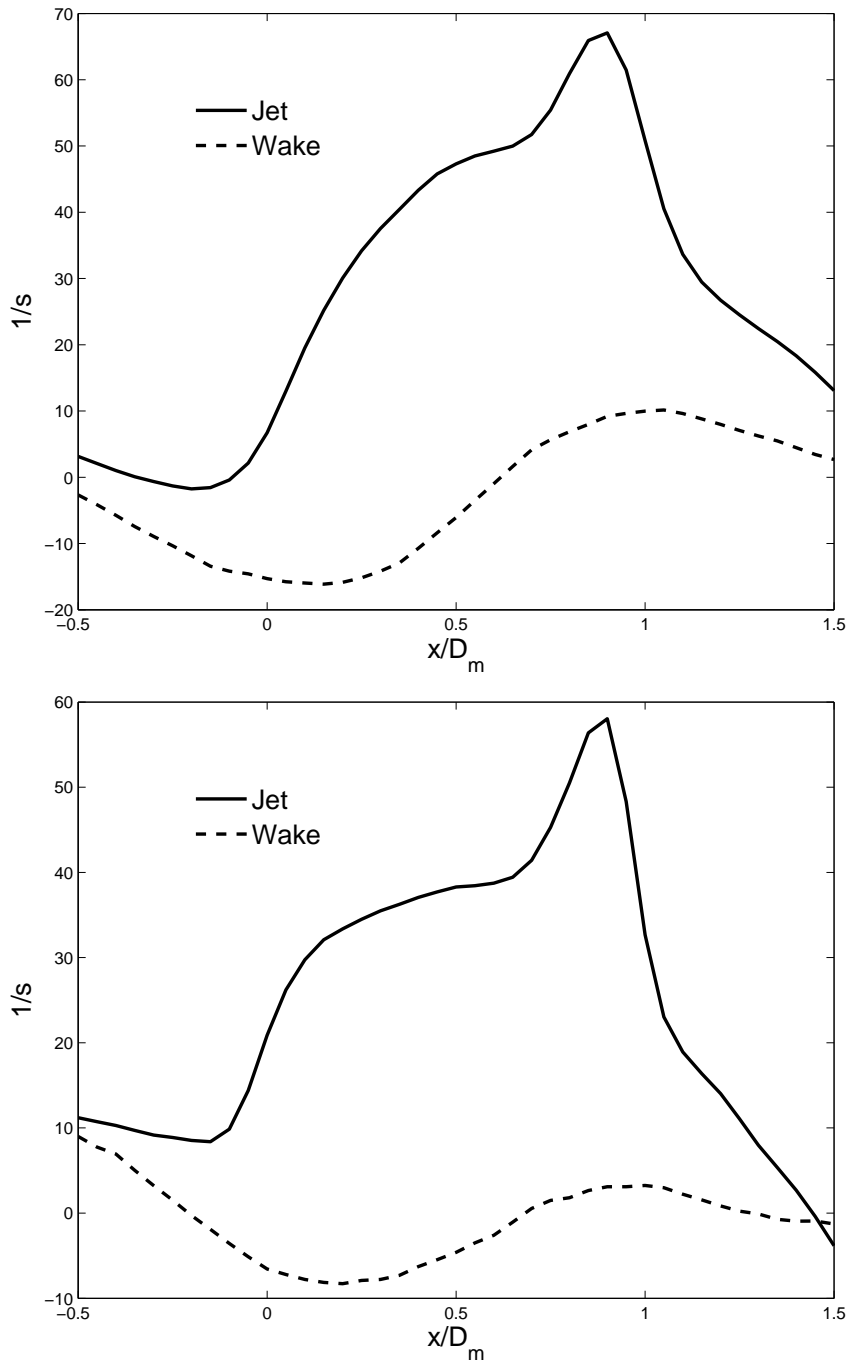


Figure 5.14 The mean of vorticity across the mixing region. a, $x/d = 4.5$; b, $x/d = 7.5$.

CHAPTER 6. Conclusions and future directions

In this chapter, the important findings in this thesis work and the conclusions that can be drawn from the data are summarized. Future directions with the experimental and computational investigation of the turbulent shear flows are also identified.

6.1 Summary and conclusions

6.1.1 Vortex study with a swirling strength based vortex identification method

A vortex identification method based on swirling strength was employed to analyze the properties of vortices in both confined rectangular jet and wake flows. Swirling strength fields were computed from velocity fields, and then filtered with a universal threshold of $|\Lambda_{ci}| \geq 1.5\Lambda_{ci}^{rms}$. By identifying clusters of filtered Λ_{ci} , vortex structures were identified.

In the rectangular jet case, experimental data from simultaneous PIV/PLIF experiments and high speed PIV experiments were used. Instantaneous swirling strength field data indicate that positively (counterclockwise) rotating vortices are dominant on the left side of the jet and negatively (clockwise) rotating vortices are dominant on the right side. The population density, average size and strength, deviation velocity of vortices were calculated and analyzed, in both the cross-stream direction and the streamwise direction. In the regions close to the channel inlet, the population density, average size and strength all show high values on both sides of the center stream. There are some counter-rotating vortices next to the dominant direction vortices, that are indicative of a wake regions formed downstream of the splitter plate tips by the boundary layers that form on both sides of the splitter plates. At the further downstream location, the wake disappears, as do most of the counter-rotating vortices. As the flow develops towards channel flow at the farthest downstream locations, the distribution of the vortices

spreads throughout the entire reactor. The mean size and strength of the vortices decrease continuously downstream from the channel inlet. The mean vortex deviation velocity in both the X and Y directions are zero at the location of the population density peak. The signs of vortex deviation velocity V indicate the vortices move from the high vortex population region to the low vortex population region. The signs of mean deviation velocity U are negative on the side near the jet center, and positive on the side of near center of the outer stream, which indicates vortices transfer low momentum fluid to high velocity region and transfer high momentum fluid to the low velocity region. The development trends of vortex size and strength were also identified by tracking vortices using high speed PIV experimental data. Both the average tracked vortex strength and size decrease with increasing downstream distance overall. However the average tracked vortex size increases before it starts to decrease in the area close to the jet inlet.

Two point spatial cross-correlations of swirling strength with velocity fluctuations and concentration fluctuations were calculated at the location of the left peak of turbulent kinetic energy in the jet case. The cross correlation fields of swirling strength and fluctuations of the two velocity components exhibit a “butterfly” like shape. The right wing of $R_{\lambda u'}$ contains positive values and the left wing contains negative values. The axis of $R_{\lambda u'}$, the contour line of $R_{\lambda u'} = 0$, is oriented vertically in the streamwise direction, slightly tilted toward the outer stream. With increasing downstream distance, the angle of orientation of the $R_{\lambda u'}$ axis becomes smaller. Also at the $X/d = 1.0$ downstream locations for both Reynolds number cases, there are a weak negatively correlated regions upstream of the strong positively correlated region close to the basis point and a weak positively correlated region downstream of the strong negatively correlated region in $R_{\lambda v'}$. This indicates that a vortex at the basis point is usually accompanied by at least one counter-rotating vortex. The axis of $R_{\lambda v'}$ is aligned with the cross-stream direction with negative values downstream of the basis point and positive values upstream of the basis point. There are also two correlated areas in the $R_{\lambda \phi'}$ correlation field; one positively correlated region downstream of the basis point and one negative upstream of the basis point, indicating that the positively rotating vortices bring high concentration field

from the center stream to the side stream downstream of the vortex core and bring the low concentration field from the side stream to the center stream upstream of the core. Finally, linear stochastic estimation was used to calculate conditional structures. The estimation was based on the swirling strength values at chosen locations in the flow. The large-scale structures in the velocity field revealed by linear stochastic estimation are spindle-shaped with a titling stream-wise major axis.

In the study of rectangular wake, experimental data from simultaneous PIV/PLIF experiments were used. In the wake flow, positively (counterclockwise) rotating vortices are dominant on the right side of the wake and negatively (clockwise) rotating vortices are dominant on the left side. In both the cross-stream direction and the streamwise direction, the population density, average size and strength, deviation velocity of vortices were calculated and analyzed. The population density, average size and strength of vortex cores all show high peak values both sides of the wakes, while these peaks decrease quickly and the profiles broaden as the flow progresses downstream. The change of vortex core maximum strength is seen relatively faster than the change of the core size. The results of mean cross-stream wise deviation velocity of vortex core shows the vortices in the wake spread from the neighborhood of wake to the centers of the free stream, and the mean streamwise deviation velocity indicates that vortices bring high momentum fluid of the free stream into the the wake.

Two point spatial cross-correlations of swirling strength with velocity fluctuations and concentration fluctuations were calculated at three different streamwise locations and eight cross-stream wise locations in the flow field in the wake study. All the cross correlation fields shown also exhibit a “butterfly” like shape, with one “wing” with positive correlation values and the other “wing” with negative values, like the results in jet study. The axes of correlation fields are oriented in the streamwise direction in $R_{\lambda u'}$ contours, and they tilt towards the wake center on the both sides of the wake, except those with basis points already located close to wake center oriented exact vertically. The axes in $R_{\lambda v'}$ are oriented in the cross-stream direction, and they tile downstream on the both sides of the wake, except those near wake center. On the left side of the wake, the right wing of $R_{\lambda u'}$ contains negative values and the

left wing contains positive values, while the the upper wing of $R_{\lambda v'}$ contains positive values and lower wing contains negative values, indicating the vortices in this region dominantly rotate negatively. Since on two sides of the wake vortices rotate in different direction, the cross correlation fields carry different signs on the two "wings" on each side of the wake. In the region close to the center of the wake, the upper wings of the correlation fields of $R_{\lambda v'}$ are much larger than the lower wings, while in the far left and far right figures, the lower wings are larger than the upper wings, and in between the two wings are more balanced. The $R_{\lambda_{ci}\phi'}$ results show some similarity to those of $R_{\lambda v'}$, indicating the vortices play a similar role in mass transfer as in momentum transfer. However, in the near wake, the strong correlation areas of $R_{\lambda_{ci}\phi'}$ are relatively smaller than those of $R_{\lambda_{ci}v'}$, while in the further downstream locations these correlations show nearly the same size as $R_{\lambda_{ci}v'}$. The mass transfer from the center stream to the side streams only starts right after the flow enters test section, while the boundary layers are already developed on the surfaces of the splitter plates, thus strong momentum transfer already exist at the inlet. As the flow goes downstream, the mass transfer catches on the momentum transfer. As the flow progresses downstream, all the correlation areas grow larger, indicating the large scale coherent motions grow larger. Linear stochastic estimation was used to visualize the underlining large scale coherent structures. The results of LSE show clear roller structures at the basis points, and those on the left side of wake rotate negatively and those on the right side rotate positively. The tilting of the streamwise oriented major axis toward the wake center can be observed easily. As the flow progresses downstream, the roller structures grow larger. Also a vortex street pattern can be seen in these LSE results, which becomes more visible after the length of the vectors were made the same, especially in further downstream locations. The pattern revealed by LSE, which can be seen in instantaneous flow fields actually shows the unique characteristics of the current high Reynolds number wake flow. When the flow enters the test section, there are vortices developed independently on both sides of the splitter plates, which are incoherent to each other. As the flow develops downstream, these vortices are reorganized and become more and more coherent, therefore the vortex pattern becomes visible.

6.1.2 Large eddy simulation of a confined rectangular jet

Large-eddy simulations were performed for the confined rectangular jet at low flow rate. Particle image velocimetry experiments were performed in an experimental apparatus of the same geometry as the simulations in order to both provide inlet conditions for the simulations and also to provide detailed one- and two-point velocity statistics that could be used to validate the accuracy of the LES models used in this investigation. It was shown that an *in situ* turbulence generation procedure can represent the experimental data at the inflow boundary quite well once it has been parameterized by the measured inlet turbulence statistics. The effect of grid resolution, numerical schemes, and subgrid turbulence models on the resolved-scale statistics were studied in a systematic manner to determine the effect of these parameters on the simulation results. Four different grid resolutions were tested, the improvement of the two higher resolutions compared to the resolution chosen for the following simulation is rather small, thus the grid independence were considered obtained. The performance of second and fourth order central scheme as interpolation scheme and second order Gaussian integration, second order and fourth order least square as gradient scheme have been tested, and no noticeable difference were seen, while the fourth order scheme are more costly in computation. The constant Smagorinsky and one equation eddy model, using the standard value for the constant was found to be overly dissipative, as is generally observed in large-eddy simulations. The two dynamic models, the dynamic Smagorinsky and the dynamic one equation eddy model tested show similar resolved-scale statistics in the jet region, which suggests that they were able to resolve most of the turbulent energy and sufficient to model the subgrid scales. Although the dynamic one equation eddy model costs more computation time than the dynamic Smagorinsky, it gives better agreements with experimental results in the wall boundary layers, the detailed simulation results presented here were obtained with the dynamic one equation eddy model.

A comparison of one-point velocity statistics, including mean stream-wise velocity, rms velocity fluctuations, Reynolds shear stress, and the correlation coefficient showed excellent agreement between the LES and PIV data. Third- and fourth-order one-point resolved-scale velocity statistics corresponded well with the experimental values, further verifying the ac-

curacy of the LES model used in the present study. In addition to the one-point statistical comparisons, the capability of LES to model large-scale turbulent structure was evaluated by comparing two-point spatial correlations of velocity fluctuations as derived from the LES data with the corresponding results calculated from the PIV data. Both spatial auto- and cross-correlations were compared. The spatial correlations from the LES data compared very well with the spatial correlations from the experimental data, demonstrating that the LES correctly predicts the length scales and orientation of the large-scale turbulent structures and also correctly models their growth rate. The excellent agreement observed between both the one-point statistics and two-point spatial correlations of velocity fluctuations demonstrates that the LES model is able to accurately capture the important characteristics of all the turbulent length scales present in the flow, from the fully resolved energy-containing eddies to the subgrid-scale dissipative eddies.

6.1.3 Turbulent statistics in the mixing region of confined jet and wake flows

The procedure of Prasad and Sreenivasan (1989) was used to detect the the inner and outer boundaries of the center stream in PLIF images. Simultaneous PIV and PLIF experimental data from the turbulent confined jet and wake flow were used in this study. The mean locations of the inner and outer boundaries are moving away the center faster in the jet case than in the wake case. The mean distance between these two boundaries are almost the same in both cases, and the rms of the distance shows there are more large scale motions in the wake case than in the jet case at the same downstream locations.

After the outer and inner boundaries of the center stream are identified, various turbulent properties are calculated conditionally across these two boundaries. Both the jet and the wake case show sharp jumps at the boundaries in the mean passive scalar profiles, and the curvatures between the two boundaries show the different characteristics of the flows. For the jet case, the positive passive scalar fluctuations show a sharp jump at the outer boundary and high values on the right side of it, and the negative fluctuations show high values at the same locations, while sharp jumps at the inner boundary. The stream wise velocity profiles

show no sharp jumps at the boundaries, and the velocity values continue to change beyond the boundaries, which shows the effect of co-flowing motion of the jet. Both positive and negative velocity fluctuations are relatively high on the left side of the inner boundary of the jet. Although passive scalar properties in the wake case still show sharp responses to the inner and outer boundaries, the velocity properties show no response to the scalar interfaces. The jet case shows a higher mean strain than the wake case between the two boundaries, and the peak value of the jet profile is located close to the inner boundary of the center stream. The mean vorticity profile of the jet case also shows the highest values on the left side of the inner boundary, indicating the entrainment of the surrounding fluids of the jet are the results of the large scale vortices. The wake vorticity profiles show the typical two opposite sign rotations on the two side of the wake.

6.2 Future directions

First, to better observe the behavior of the vortices, high speed PIV experiments are needed for the confined wake flow. Also, since the swirling strength is calculated using velocity gradient tensor, the small development in the velocity fields brings high variance in swirling strength fields. Thus, the experience gained from the vortex tracking study in the jet flow case shows that just resolving down to Kolmogorov time scale seems to not be enough to capture the detail development and dynamics of the vortices. Therefore the high speed PIV experiments with higher frame rates are needed also for the jet flow case. Also, the coherent structure study here can be used to validate the large eddy simulation result, to see if it can correctly produce the vortices fields with similar properties and dynamics. However, a proper procedure to compare the vortex field measured by PIV and simulated by LES is needed to be investigated, since spatial resolution vortex identification is crucial to vortex identification, and this resolution is typically very different in PIV measurement and LES computation. This kind of the LES validation on coherent structures is still very rare in the published literatures, which makes it of great potential interest.

Second, wavelet analysis has been proved to be a powerful tool to study turbulence, since

it is capable of dealing with multi-scale signal locally, and turbulence is certainly a multi-scale phenomenon. With all the experiment and simulation data collected during this study, wavelet definitely can be used to analyze these data and can be very promising. However, the wavelet was primarily designed to deal with one-dimensional signal, which is able to analyze one-dimensional events at different resolutions locally, and the two-dimensional and three-dimensional extensions of wavelet are problematic when dealing with anisotropy turbulent flow, such as jet and wake, since they can not distinguish the orientation or the shape of multi-dimensional object. As newly developments of wavelet, contourlet and surfacelet are well equipped with these capabilities wavelet lacking (Do and Vetterli, 2005), thus they can be very promising to analyze turbulent mixing problem, especially in locally separating turbulent fields by different length scales and at the same time capturing the geometry characteristics of the flow fields at different spatial resolutions. However, since these new techniques have only used in the digital image and video processing area, the proper implement of these techniques with turbulence fields and interpolation of the results will be the key issues.

Third, turbulent mixing problem in Schmidt number environment is the main topic of this study, and the reactive PLIF experiment is the most important part of the research designed to study the subgrid mixing and has been shown to be a very useful tool (Lehwald, A. and Thévenin, D. and Zähringer, K., 2010). However, due to unexpected difficulties, the experiments were not successful and not included in this thesis, but the experiences learned can certainly help us in the future experiment studies. Also, a multi-inlet vortex reactor has been built and ready to set up in the laboratory, as a continuation of the confined rectangular reactor. The PIV and passive, reactive PLIF experimental studies will be carried out with this new reactor.

Finally, the large eddy simulation with OpenFoam on the confined rectangular has been shown to agree with PIV measurement very well. And the simulation studies on high flow rate jet case and wake flow case are also going to be carried out. The performance of some of the currently available numerical schemes and subgrid models have been shown satisfactory. However, when implementing LES in some real engineering applications, there are still some

issues needed to be solved. Choosing a proper inflow generator is one of them, since the inflow is not always uniform or fully developed. The results with the generator used in the current study has been proved to be quite satisfactory. But more detailed study of the inflow generator is waiting to be done, especially with the knowledge obtained from the vortex study in the jet and wake. Base on the good agreement of velocity simulation, simulations of passive and reactive scalar will be the next. With the regular and reactive PLIF experiments, these simulations will also be validated with experiments. A lot more interesting modeling studies like listed here on turbulent mixing will be carried out in the near future.

Bibliography

- Abramovich, G., Girshovich, T., Krashennnikov, S., Sekundov, A., and Smirnova, I. (1984). The theory of turbulent jets. *Moscow Izdatel Nauka*.
- Adrian, R. J. (1991). Particle-imaging techniques for experimental fluid mechanics. *Annual Review of Fluid Mechanics*, 23:261–304.
- Adrian, R. J. (1994). Stochastic estimation of conditional structure: a review. *Applied Scientific Research*, 53:291–303.
- Adrian, R. J. (1999). Uses, analysis and interpretation of piv data. *30th AIAA Fluid Dynamics Conference*.
- Adrian, R. J., Christensen, K. T., and Liu, Z. C. (2000a). Analysis and interpretation of instantaneous turbulent velocity fields. *Experiments in Fluids*, 29:275–290.
- Adrian, R. J., Meinhart, C. D., and Tomkins, C. D. (2000b). Vortex organization in the outer region of the turbulent boundary layer. *Journal of Fluid Mechanics*, 422:1–54.
- Agrawal, A. and Prasad, A. K. (2002a). Organizational modes of large-scale vortices in an axisymmetric turbulent jet. *Flow, Turbulence and Combustion*, 68(4):359–377.
- Agrawal, A. and Prasad, A. K. (2002b). Properties of vortices in the self-similar turbulent jet. *Experiments in Fluids*, 33:565–577.
- Agrawal, A. and Prasad, A. K. (2003). Measurements within vortex cores in a turbulent jet. *Journal of Fluids Engineering*, 125(3):561.

- Ali, S. F. and Ibrahim, E. A. (1996). Coincidence of turbulent-nonturbulent interface and hot-cold interface in a plane turbulent wake. *Mechanics Research Communications*, 23(1):91–102.
- Anand, R. K., Boersma, B. J., and Agrawal, A. (2009). Detection of turbulent/non-turbulent interface for an axisymmetric turbulent jet evaluation of known criteria and proposal of a new criterion. *Experiments in Fluids*, 47(6):995–1007.
- Antonia, R. and Bilger, R. (2006). An experimental investigation of an axisymmetric jet in a co-flowing air stream. *Journal of Fluid Mechanics*, 61(04):805–822.
- Antonia, R. A., Browne, L. W. B., Rajagopalan, S., and Chambers, A. J. (1983). On the organized motion of a turbulent plane jet. *Journal of fluid mechanics*, 134:49–66.
- Antonia, R. A., Chambers, A. J., Britz, D., and Browne, L. W. B. (1986). Organized structures in a turbulent plane jet: topology and contribution to momentum and heat transport. *Journal of Fluid Mechanics*, 172:211–229.
- Bardina, J., Ferziger, J. H., and Reynolds, W. C. (1980). Improved subgrid scale models for large eddy simulation. In *American Institute of Aeronautics and Astronautics, Fluid and Plasma Dynamics Conference, 13th, Snowmass, Colorado*,, page 10.
- Benayad, S., Salem, A., and Legrand, J. (2001). Turbulent mixing in a coflowing liquid jet. *Ind. Eng. Chem. Res*, 40(3):927–932.
- Berger, E. and Wille, R. (1972). Periodic flow phenomena. *Annual Review of Fluid Mechanics*, 4(1):313–340.
- Berselli, L. C., Iliescu, T., and Layton, W. J. (2006). *Mathematics of large eddy simulation of turbulent flows*. Springer, Berlin.
- Bradbury, L. and Riley, J. (1967). The spread of a turbulent plane jet issuing into a parallel moving airstream. *Journal of Fluid Mechanics*, 27(02):381–394.

- Breuer, M. (1998). Numerical and modeling influences on large eddy simulations for the flow past a circular cylinder. *International Journal of Heat and Fluid Flow*, 19:512–521.
- Brodkey, R. (1975). *Turbulence in Mixing Operations: Theory and Application to Mixing and Reaction*. Academic Press, New York.
- Cantwell, B. and Coles, D. (1983). An experimental study of entrainment and transport in the turbulent near wake of a circular cylinder. *Journal of Fluid Mechanics*, 136:321–374.
- Chen, C. and Blackwelder, R. (1978). Large-scale motion in a turbulent boundary layer: a study using temperature contamination. *Journal of Fluid Mechanics*, 89(01):1–31.
- Chhabra, S., Huq, P., and Prasad, A. (2006). Characteristics of Small Vortices in a Turbulent Axisymmetric Jet. *Journal of Fluids Engineering*, 128:439.
- Christensen, K. (2004). The influence of peak-locking errors on turbulence statistics computed from piv ensembles. *Experiments in Fluids*, 36:484–497.
- Christensen, K. T. and Adrian, R. J. (2001). Statistical evidence of hairpin vortex packets in wall turbulence. *Journal of Fluid Mechanics*, 431:433–443.
- Christensen, K. T. and Adrian, R. J. (2002a). Measurement of instantaneous eulerian acceleration fields by particle image accelerometry: method and accuracy. *Experiments in Fluids*, 33(6):759–769.
- Christensen, K. T. and Adrian, R. J. (2002b). The velocity and acceleration signatures of small-scale vortices in turbulent channel flow. *Journal of Turbulence*, 3:1–28.
- Chu, P. C. K., Lee, J. H. W., and Chu, V. H. (1999). Spreading of turbulent round jet in coflow. *Journal of Hydraulic Engineering*, 125(February):193.
- Curtet, R. (1958). Confined jets and recirculation phenomena with cold air. *Combustion and Flame*, 2(4):383–411.

- da Silva, C. B. and Pereira, J. C. F. (2008). Invariants of the velocity-gradient, rate-of-strain, and rate-of-rotation tensors across the turbulent/nonturbulent interface in jets. *Physics of Fluids*, 20(5):055101.
- Deo, R., Mi, J., and Nathan, G. (2007a). The influence of nozzle aspect ratio on plane jets. *Experimental Thermal and Fluid Science*, 31(8):825–838.
- Deo, R., Nathan, G., and Mi, J. (2007b). Comparison of turbulent jets issuing from rectangular nozzles with and without sidewalls. *Experimental Thermal and Fluid Science*, 32(2):596–606.
- Do, M. and Vetterli, M. (2005). The contourlet transform: an efficient directional multiresolution image representation. *Image Processing, IEEE Transactions on*, 14(12):2091–2106.
- Enjalbert, N., Galley, D., and Pierrot, L. (2009). An entrainment model for the turbulent jet in a coflow. *Comptes Rendus Mécanique*, 337(9-10):639–644.
- Feng, H., Olsen, M., Hill, J., and Fox, R. (2007). Simultaneous velocity and concentration field measurements of passive-scalar mixing in a confined rectangular jet. *Experiments in Fluids*, 42(6):847–862.
- Feng, H., Olsen, M., Liu, Y., Fox, R., and Hill, J. (2005). Investigation of turbulent mixing in a confined planar-jet reactor. *AIChE journal*, 51(10):2649–2664.
- Feng, H., Olsen, M. G., Hill, J. C., and Fox, R. O. (2010). Investigation of passive scalar mixing in a confined rectangular wake using simultaneous PIV and PLIF. *Chemical Engineering Science*, 65(11):3372–3383.
- Ferziger, J. H. and Peric, M. (2002). *Computational Methods for Fluid Dynamics*. Springer, New York.
- Forney, L. J., Nafia, N., and Vo, H. X. (1996). Optimum jet injection in a tubular reactor. *AIChE. J.*, 42:3113–3122.
- Fureby, C. and Grinstein, F. (2002). Large eddy simulation of high Reynolds number free and wall-bounded flows. *Journal of Computational Physics*, 181:68–97.

- Fureby, C., Tabor, G., Weller, H. G., and Gosman, A. D. (1997). A comparative study of subgrid scale models in homogeneous isotropic turbulence. *Physics of Fluids*, 9(5):1416–1429.
- Gazzah, M. H. (2010). The dynamic field in turbulent round jet discharging into a co-flowing stream. *Natural Science*, 02(06):635–640.
- Germano, M., Piomelli, U., Moin, P., and Cabot, W. H. (1991). A dynamic subgrid-scale eddy viscosity model. *Phys. Fluids A*, 3:1760–1765.
- Geurts, B. J. (1997). Inverse modeling for large-eddy simulation. *Phys. Fluids*, 9(12):3585–3587.
- Goldschmidt, V. and Bradshaw, P. (1973). Flapping of a plane jet. *Physics of Fluids*, 16:354.
- Goldschmidt, V., Young, M., and Ott, E. (1981). Turbulent convective velocities (broadband and wavenumber dependent) in a plane jet. *Journal of Fluid Mechanics*, 105:327–345.
- Gordeyev, S. and Thomas, F. (2000). Coherent structure in the turbulent planar jet. part 1. extraction of proper orthogonal decomposition eigenmodes and their self-similarity. *Journal of Fluid Mechanics*, 414:145–194.
- Grinstein, F. (2001). Vortex dynamics and entrainment in rectangular free jets. *Journal of Fluid Mechanics*, 437:69–101.
- Gutmark, E. and Wygnanski, I. (1976). The planar turbulent jet. *Journal of Fluid Mechanics*, 73(03):465–495.
- Gutmark, E. J. and Grinstein, F. F. (1999). Flow control with noncircular jets. *Annual Review of Fluid Mechanics*, 31(1):239–272.
- He, G.-W., Rubinstein, R., and Wang, L.-P. (2002). Effects of subgrid-scale modeling on time correlations in large eddy simulation. *Physics of Fluids*, 14(7):2186–2193.

- Holzner, M., Liberzon, A., Nikitin, N., Kinzelbach, W., and Tsinober, A. (2007). Small-scale aspects of flows in proximity of the turbulent/nonturbulent interface. *Physics of Fluids*, 19(7):071702.
- Holzner, M., Liberzon, A., Nikitin, N., Lüthi, B., Kinzelbach, W., and Tsinober, A. (2008). A Lagrangian investigation of the small-scale features of turbulent entrainment through particle tracking and direct numerical simulation. *Journal of Fluid Mechanics*, 598(-1):465–475.
- Huang, J., Zhou, Y., and Zhou, T. (2006). Three-dimensional wake structure measurement using a modified PIV technique. *Experiments in Fluids*, 40(6):884–896.
- Issa, R. (1986). Solution of the implicitly discretised fluid flow equations by operator-splitting. *Journal of Computational Physics*, 62:40–65.
- Kim, W. and Menon, S. (1995). A new dynamic one-equation subgrid-scale model for large eddy simulations. *AIAA Paper*, 356:1995.
- Kim, W. and Menon, S. (1999). An unsteady incompressible Navier-Stokes solver for large eddy simulation of turbulent flows. *International Journal for Numerical Methods in Fluids*, 31:983–1017.
- Kim, W., Sung, J., Yoo, J., and Lee, M. (2004). High-definition PIV analysis on vortex shedding in the cylinder wake. *Journal of Visualization*, 7(1):17–24.
- Klein, M., Sadiki, A., and Janicka, A. (2003). A digital filter based generation of inflow data for spatially developing direct numerical or large eddy simulations. *Journal of Computational Physics*, 186:652–665.
- Kong, B., Olsen, M., Fox, R., and Hill, J. (2010). Population, characteristics and kinematics of vortices in a confined rectangular jet with a co-flow. *Experiments in Fluids*, pages 1–21.
- Kothnur, P. S. and Clemens, N. T. (2005). Effects of unsteady strain rate on scalar dissipation structures in turbulent planar jets. *Physics of Fluids*, 17(12):125104.

- Larchevêque, L., Sagaut, P., Le, T., and Comte, P. (2004). Large-eddy simulation of a compressible flow in a three-dimensional open cavity at high reynolds number. *Journal of Fluid Mechanics*, 516(-1):265–301.
- LaRue, J. and Libby, P. (1974). Temperature fluctuations in the plane turbulent wake. *Physics of Fluids*, 17:1956.
- Lehwald, A. and Thévenin, D. and Zähringer, K. (2010). Quantifying macro-mixing and micro-mixing in a static mixer using two-tracer laser-induced fluorescence. *Experiments in fluids*, 48(5):823–836.
- Lesieur, M. and Metais, O. (1996). New trends in large-eddy simulations of turbulence. *Ann. Rev. Fluid Mech.*, 28:45–82.
- Liepmann, H., Laufer, J., and NACA (1947). *Investigations of free turbulent mixing*. National Advisory Committee for Aeronautics.
- Lilly, D. K. (1967). The representation of small-scale turbulence in numerical simulation experiments. In Lilly, D. K., editor, *Proceedings of the IBM Scientific Computing Symposium on Environmental Sciences*, pages 195–210, Yorktown Heights, New York. Data Processing Division, IBM.
- Lilly, D. K. (1992). A proposed modification of the Germano subgrid scale method. *Phys. Fluids A*, 4:633–635.
- Liu, Y., Feng, H., Olsen, M. G., Fox, R. O., and Hill, J. C. (2006). Turbulent mixing in a confined rectangular wake. *Chemical Engineering Science*, 61(21):6946–6962.
- Lu, Y., Dixon, A. G., Moser, W. R., and Ma, Y. H. (1997). Analysis and optimization of cross-flow reactors with staged feed policies isothermal operation with parallel-series, irreversible reaction systems. *Chemical Engineering Science*, 52:1349–1363.
- Mahesh, K., Constantinescu, G., and Moin, P. (2004). A numerical method for large-eddy simulation in complex geometries. *Journal of Computational Physics*, 197:215–240.

- Meinke, M., Schröder, W., Krause, E., and Rister, T. (2001). A comparison of second- and sixth-order methods for large-eddy simulations. *Computers and Fluids*, 32:695–718.
- Moin, P. and Kim, J. (1982). Numerical investigation of turbulent channel flow. *Journal Fluid Mechanics*, 118:341–377.
- Mumford, J. C. (1982). The structure of the large eddies in fully developed turbulent shear flows. part 1. the plane jet. *Journal of fluid mechanics*, 118:241–268.
- Najjar, F. and Balachandar, S. (1998). Low-frequency unsteadiness in the wake of a normal flat plate. *Journal of Fluid Mechanics*, 370:101–147.
- Nakagawa, S., Nitta, K., and Senda, M. (1999). An experimental study on unsteady turbulent near wake of a rectangular cylinder in channel flow. *Experiments in Fluids*, 27(3):284–294.
- Nickels, T. and Perry, A. (1996). An experimental and theoretical study of the turbulent coflowing jet. *Journal of Fluid Mechanics*, 309:157–182.
- Oakley, T. R., Loth, E., and Adrian, R. J. (1996). Cinematic particle image velocimetry of high-Reynolds-number turbulent free shear layer. *AIAA JOURNAL*, 34:299–308.
- Oertel Jr, H. (1990). Wakes behind blunt bodies. *Annual Review of Fluid Mechanics*, 22(1):539–562.
- Oler, J. and Goldschmidt, V. (1982). A vortex-street model of the flow in the similarity region of a two-dimensional free turbulent jet. *Journal of Fluid Mechanics*, 123:523–535.
- Olsen, M. and Dutton, J. (2003). Planar velocity measurements in a weakly compressible mixing layer. *Journal of Fluid Mechanics*, 486(-1):51–77.
- Olsen, M. G. and Dutton, J. C. (2002). Stochastic estimation of large structures in an incompressible mixing layer. *AIAA Journal*, 40(12):2431–2438.
- Ong, L. and Wallace, J. (1996). The velocity field of the turbulent very near wake of a circular cylinder. *Experiments in fluids*, 20(6):441–453.

- Papageorgiou, D. and Smith, F. (1988). Nonlinear instability of the wake behind a flat plate placed parallel to a uniform stream. *Proceedings of the Royal Society of London. Series A, Mathematical and Physical Sciences*, pages 1–28.
- Papageorgiou, D. and Smith, F. (1989). Linear instability of the wake behind a flat plate placed parallel to a uniform stream. *Journal of Fluid Mechanics*, 208:67–89.
- Patterson, G. T. and Passino, R. (1990). *Metals Speciation, Separation, and Recovery*. Lewis Publishers, Inc.
- Perrin, R., Cid, E., Cazin, S., Sevrain, A., Braza, M., Moradei, F., and Harran, G. (2007). Phase-averaged measurements of the turbulence properties in the near wake of a circular cylinder at high Reynolds number by 2C-PIV and 3C-PIV. *Experiments in fluids*, 42(1):93–109.
- Piomelli, U., Moin, P., and Ferziger, J. H. (1988). Model consistency in large eddy simulation of turbulent channel flows. *Physics of Fluids*, 31:1884–1891.
- Piomelli, U., Yu, Y., and Adrian, R. J. (1996). Subgrid-scale energy transfer and near-wall turbulence structure. *Physics of Fluids*, Volume 8,:215–224.
- Pope, S. B. (2000). *Turbulent Flows*. Cambridge University Press, Cambridge.
- Prasad, A. K., Adrian, R. J., Landreth, C. C., and Offutt, P. W. (1992). Effect of resolution on the speed and accuracy of particle image velocimetry interrogation. *Expt. Fluids*, 13:105–116.
- Prasad, R. and Sreenivasan, K. (1989). Scalar interfaces in digital images of turbulent flows. *Experiments in Fluids*, 7(4):259–264.
- Robinson, S. K. (1991). Coherent motions in the turbulent boundary layer. *Ann. Rev. Fluid Mechanics*, 23.
- Roshko, A. (1993). Perspectives on bluff body aerodynamics. *Journal of Wind Engineering and Industrial Aerodynamics*, 49(1-3):79–100.

- Sadri, R. M. and Floryan, J. M. (2002). Accurate evaluation of the loss coefficient and the entrance length of the inlet region of a channel. *Journal of Fluids Engineering*, 124(3):685–694.
- Sagaut, P. (2001). *Large eddy simulation of incompressible flows: An introduction*. Springer, Berlin.
- Sagaut, P. and Ciardi, M. (2006). A finite-volume variational multiscale method coupled with a discrete interpolation filter for large-eddy simulation of isotropic turbulence and fully developed channel flow. *Physics of Fluids*, 18:115101.
- Sato, H. and Kuriki, K. (1961). The mechanism of transition in the wake of a thin flat plate placed parallel to a uniform flow. *Journal of Fluid Mechanics*, 11(03):321–352.
- Shaw, R. H., Brunet, Y., Finnigan, J. J., and Raupach, M. R. (1995). A wind tunnel study of air flowing in waving wheat: Two-point velocity statistics. *Boundary-Layer Meteorology*, 76:349–376.
- Smagorinsky, J. (1963). General circulation experiments with the primitive equations. part i. the basic experiment. *Mon. Weather Rev.*, 91:99–164.
- Stanislas, M., Okaamoto, K., Khler, C. J., and Westerweel, J. (2005). Main results of the second international PIV challenge. *Expt. Fluids*, 39:170–191.
- Steward, F. and Guruz, A. (1977). Aerodynamics of a confined jet with variable density. *Combustion Science and Technology*, 16(1):29–45.
- Stolz, S. and Adams, N. A. (1999). An approximate deconvolution procedure for large-eddy simulation. *Physics of Fluids*, 11:1699–1701.
- Taneda, S. (1956). Experimental investigation of the wakes behind cylinders and plates at low Reynolds numbers. *Journal of the Physical Society of Japan Vol*, 11(3).
- Taneda, S. (1958). Oscillation of the Wake behind a Flat Plate parallel to the Flow. *J. Phys. Soc. Japan*, 13:418–425.

- Thomas, F. and Brehob, E. (1986). An investigation of large-scale structure in the similarity region of a two-dimensional turbulent jet. *Physics of Fluids*, 29:1788.
- Tomkins, C. D. and Adrian, R. J. (2003). Spanwise structure and scale growth in turbulent boundary layers. *Journal of Fluid Mechanics*, 490:37–74.
- van Driest, E. R. (1956). On turbulent flow near a wall. *Journal of the Aeronautical Sciences*, 23:1007–1011.
- Volker, S., Moser, R. D., and Venugopal, P. (2002). Optimal large eddy simulation of turbulent channel flow based on direct numerical simulation statistical data. *Physics of Fluids*, 10:3675–3691.
- Vollmers, H. (2001). Detection of vortices and quantitative evaluation of their main parameters from experiment velocity data. *Meas.Sci.Tech*, 12:1199–1207.
- Westerweel, J., Fukushima, C., Pedersen, J., and Hunt, J. (2005). Mechanics of the turbulent-nonturbulent interface of a jet. *Physical review letters*, 95(17):174501.
- Westerweel, J., Hofmann, T., Fukushima, C., and Hunt, J. (2002). The turbulent/non-turbulent interface at the outer boundary of a self-similar turbulent jet. *Experiments in Fluids*, 33(6):873–878.
- Williamson, C. (1996). Vortex dynamics in the cylinder wake. *Annual Review of Fluid Mechanics*, 28(1):477–539.
- Winkler, C. and Rani, S. (2006). Evaluation of subgrid scale kinetic energy models in large eddy simulations of turbulent channel flow. *International Journal of Numerical Methods for Heat & Fluid Flow*, 16(2):226–239.
- Wu, Y. and Christensen, K. T. (2006). Population trends of spanwise vortices in wall turbulence. *Journal of Fluid Mechanics*, 568:55–76.
- Yoshizawa, A. (1986). Statistical theory for compressible shear flows, with the application to subgrid modelling. *Physics of Fluids*, 29(7):2152–2164.

Zhang, Y., Street, R. L., and Koseff, J. R. (1993). A dynamic mixed subgrid-scale model and its application to turbulent recirculating flows. *Phys. Fluids A*, 5(12):3186–3196.